The Interactions of Pyroclastic Density Currents with Obstacles – a Large-scale Experimental Study

A thesis presented in partial fulfilment of the requirements for the degree of

Doctor of Philosophy
in
Earth Sciences

At Massey University Manawatū, Palmerston North, New Zealand

Lucas Raphaël Pierre Corna

2023

Abstract

Pyroclastic Density Currents (PDCs) are hot multiphase flows of volcanic particles and gas that are frequently produced during explosive volcanic eruptions. These fast-moving currents show variable runout distances that range from a few kilometres to more than 100 kilometres from their sources. Through their high velocities, large contents of respirable fine ash, temperatures and dynamic pressures, PDCs constitute extreme suffocation, burn and damage hazards for people living around volcanoes. An important additional source of hazard arises from the ability of PDCs to surmount significant topographic obstacles, such as hills and ridges. Because of their ferocity, to date there are no direct observations and measurements of PDCs interacting with obstacles and current knowledge comes from characterizing PDC deposits and PDC damage features across terrain after eruptions. The interaction of dense granular flows and dilute aqueous and gaseous particle-laden gravity currents with simple topographic barriers has been studied in laboratory experiments. These represent dense, non-turbulent or dilute, fully turbulent end-members of PDC behaviour. How the behaviour of dense and dilute end-member flows interacting with obstacles differs from those of real-world PDCs, which encompass a complete multiphase spectrum from dilute to dense transport regimes, remains unknown. This PhD research aims at bridging this gap in knowledge through synthesizing the behaviour of interaction of PDCs with ridge-shaped obstacles in large-scale experiments.

The experiments were designed and conducted at the eruption simulator facility PELE (Pyroclastic flow Eruption Large-scale Experiment) to visualise the processes of PDCs interacting with obstacles, measure the changes in the flow velocity and density structure induced by this interaction, characterise the effects of the interaction on downstream flow behaviour, and study the variations in deposition across obstacles. Three hill-shaped obstacles were designed for these experiments, with the same shape and aspect ratio, but varying sizes compared to the size of the experimental PDC.

The experiments reveal strong changes in the vertical velocity and density structures of the currents immediately before and after obstacles and strong losses in flow momentum. This is associated with flow compression and acceleration along the stoss

side of the ridge, flow detachment with boundary layer separation behind the ridge crest, and formation of a turbulent wake underneath the detached flow before re-attachment. The amount of flow acceleration, the size of the turbulent wake and the flow re-attachment distance increase with obstacle size. High-speed video footage of the interaction shows evidence for a typical sequence of transient behaviour that could be linked to the time-variant velocity and density structure of the head, proximal body, distal body and a tail regions of the experimental PDCs. Four phases of interactions are noted in all three experiments: (1) during head passage - flow acceleration and compression on the stoss side, followed by detachment after the crest, generation of the wake behind the hills and re-attachment downstream; (2) during passage of the proximal body - the development of an alternatively thickening and collapsing turbulent jet structure along the stoss side that forms the base of the detached flow, and which separates and shields the wake from the detached flow above; (3) during passage of the remaining body - an increase in flow density leads to the blocking of a dense underflow forming thick deposits on the stoss side and to the advection of particles from the lower flow region into the detached flow above the wake; (4) during waning flow and passage of the gravity current tail - the velocity field rotates and the angle of attack of the flow approaches the inclination of the lee side of the obstacle. In this situation, the size of the turbulent wake decreases and eventually flow detachment ceases. The compression and acceleration of material on the stoss side of obstacles allow particles at the base of the flow to be conveyed upward back into the detached flow. The higher the obstacle, the stronger the acceleration and the larger the proportion of the flow that is advected.

Ballistic trajectory models, which have been used to predict flow paths of dense and dilute analogues flows across simple obstacles, do not describe well the wake measured in experiments and under-estimate its dimensions. As evidenced by vortex shedding and high detachment angles in a flow with high Reynolds number, PDC-obstacle interactions are instead controlled by boundary layer separation in a turbulent flow. Therefore, they are linked to the drag coefficient of the hill and the drag force exerted by the obstacle onto the flow. A study of the wake dimensions revealed that a lift force assists in maintaining the wake aloft and in countering gravity. The ratio between the drag and lift forces controls the wake dimensions. An empirical scaling relationship between the re-attachment distance of the flow and the height of the

obstacle was derived and tested against natural data of preserved tree patches behind hills.

The experimental measurements also showed that loss in flow momentum due to obstacle drag is associated with complete blocking of the basal granular-fluid underflow and partial blocking of the upper dilute turbulent part of the experimental PDCs. Data from the three experimental runs, in combination with measurements from experiments with no obstacles, allowed extrapolation of the minimum ridge size that leads to complete flow blocking. This relationship agrees well with results from previous laboratory experiments on dilute gas-particle gravity currents and could find application in volcanic hazard estimates.

The increasing loss in flow momentum with increasing obstacle size is associated with a strong reduction in the bulk flow density. Thus, experimental PDCs propagating over larger obstacles show a lower density contrast with the ambient air, and therefore a lower driving force, than currents propagating over smaller obstacles. Despite this, the final runout distances are remarkably similar in experiments with different obstacle sizes. This finding is explained by two different processes. First, flow compression and acceleration on the stoss side of obstacles leads to the acceleration of internal gravity waves. The gravity waves move faster than the surrounding flow, intrude and provide momentum into the PDC head. Initially slower currents behind large obstacles thus accelerate periodically and ‘catch up’ with less compressed and less accelerating currents downstream of smaller obstacles. Second, particles that sedimented below the level of the obstacle crest before the obstacle become advected with the detached flow into flow regions above the height of the crest. Larger obstacles, which induce stronger flow acceleration, advect particles higher into the detached flow than smaller obstacles. The duration and downstream length over which the advected particles re-sediment, deposit and eventually become inactive to drive the flow as excess density therefore increases with obstacle size. With increasing obstacle height, this second process generates increasingly hotter flows with slightly coarser and thicker deposits downstream of obstacles.

The experimental results and relationships derived in this research add critical complexity to the understanding of PDCs interacting with topographic obstacles and resulting downstream hazards. The reported compressibility effects in the

experimental PDCs are currently not captured in PDC flow and hazard models. The local flow acceleration against gravity on the obstacle stoss side warrants caution for the application of kinetic to potential energy conversion models that are used to estimate bulk velocities of PDCs. These findings encourage further experimental and numerical experiments to investigate, for instance, the more complex situations of three-dimensional obstacles, systematic test of different obstacle geometries and series of obstacles in PDC pathways to help development of predictive PDC flow and hazard models.

Acknowledgments

This thesis was supported by Massey University and the ECLIPSE project, who provided funding through the Ministry of Business, Innovation and Employment.

I would like to thank Gert Lube, my main supervisor, who offered me this project and gave me the opportunity to work on pyroclastic density currents. I am grateful for his precious insights and support during the time of the PhD. I would also like to thank my second supervisor Jim Jones for his support and his input who greatly helped this research.

I am thankful to Ermanno Brosch, who really should have been in my supervising panel, for his precious help all throughout the project. I would also like to thank Daniel Uhle for his help running the experiments and with data analysis, Anja Moebis for her support during laboratory analyses, Kate Arentsen for her administrative help, and James Ardo, David Feek and Kevin Kreutz for their assistance running the experiments.

Many, many thanks to my friends in Palmerston North for their support and the great moments and memories I now share with them from these years: Sarah Tapscott, Claire Zucchetta, Micaiah Hunt, Mathieu Quenu, Julien Gaspar, Caio Kenup, Nimeshika Pattaramibaran, Daniel Coulthard, Carmen Requejo, Shannen Mills, Jeff Robert and Juliette Vicente. I will also thank the cast of Critical Role who offered an exciting distraction during long hours of data processing.

Finally, last but not least, I am thanking my sister and my parents for their everlasting support and love. This thesis is dedicated to them.

Table of contents

List of figures

List of tables

List of supplementary material

1. Introduction

This chapter introduces the PhD research by presenting the research problems and establishes the research questions and objectives of this thesis.

1.1. Research preface and problems

Pyroclastic Density Currents (PDCs) are hot, fast-moving, ground-hugging, particle-laden gas flows produced during explosive volcanic eruptions (Druitt 1998; Branney and Kokelaar 2002). PDCs are formed from different mechanisms such as plinian column collapse or dome collapse. In the most violent cases, they can be associated with flank collapse of a volcano (e.g. Moore and Rice 1984) or with the formation of a caldera (Druitt and Sparks 1984; Legros et al. 2000; Roche and Druitt 2001). The lowest volume PDCs usually travel a few kilometres before stopping (e.g. Moore and Rice 1984; Calder et al. 1999; Lube et al. 2014; Capra et al. 2016), but the largest eruptions can produce flows travelling up to >100 km from their source, overcoming topography (Wilson 1985; Cas et al. 2011; Roche et al. 2016; Takarada and Hoshizumi 2020; Roche et al. 2022). PDCs are extremely lethal, with ash loads leading to suffocation and long-term pulmonary diseases (Baxter 1990; Hincks et al. 2006; Dellino et al. 2021) and high temperature causing fatal burns (Mastrolorenzo et al. 2001; Baxter et al. 2017). Their high dynamic pressures can cause severe damage to buildings (Fig. 5 in Tanguy 1994; Baxter et al. 2005) along with impacts of large blocks carried or entrained by the flow (Baxter et al. 2005).

Two end-members of PDCs are generally recognized: dense and dilute PDCs. While dense PDCs tend to be usually confined in valleys, dilute PDCs have the ability to topple topographic obstacles with ease, making impact areas hardly predictable and hazard planning highly difficult. Topographic interactions include changing flow directions (Valentine 1987), overbanking valley walls (Cronin et al. 2013; Risica et al. 2022), or engulfing entire obstacles (Fisher 1990; Fisher et al. 1993; Burgisser 2005; Lube et al. 2014) leading to significant disasters such as the 2010 Merapi and 2018 Fuego eruptions which claimed the lives of 380 and >400 people respectively.

Despite a few studies over the years, the interactions between PDCs and topographic obstacles are still largely misunderstood and need more focus. Some regions are particularly at risk such as the city of Naples and its surroundings, home to 4 million people and located in the immediate proximity of Mt Vesuvius. Hence, quantifying the ability of potentially generated PDCs to surmount the caldera wall of Mount Somma is essential for hazard assessment in this region (Gurioli et al. 2010). Such situations highlight the need to improve our knowledge on the transport processes of PDCs across obstacles and how the flow dynamics are impacted downstream.

However, due to the dangerous nature of PDCs, it is nearly impossible to obtain internal measurements and our knowledge is still only partial (Lube et al. 2020). Hence, the current knowledge on PDCs, and therefore on their dynamics across topographic obstacles, comes from:

- Theorical and numerical modelling (e.g. Valentine 1987; Legros and Kelfoun 2000; Todesco et al. 2002; Doronzo et al. 2010; Gardner et al. 2018; Kelfoun and Gueugneau 2022).
- Field work characterizing facies variations of PDCs deposits across topographic obstacles (e.g. Walker and Wilson 1983; Branney and Kokelaar 1997; Burgisser 2005; Sulpizio et al. 2008; Cas et al. 2011; Jeon et al. 2011; Ogburn et al. 2014; Breard et al. 2015). Field studies have been used to determine the two aforementioned end-members of PDCs by looking at their deposit characteristics and whether deposits were found on ridges or not. Through changes in facies variations across obstacles indicating conversion of kinetic to potential energy, field studies usually suggest that PDCs decelerate by climbing obstacles.
- Laboratory experiments on analogue systems such as aqueous particle-laden gravity currents (e.g. Alexander and Morris 1994; Woods et al. 1998; Abhari et al. 2018; Wilson et al. 2018) and dense granular flows (e.g. Hákonardóttir et al. 2003; Naaim-Bouvet et al. 2004; Viroulet et al. 2017; Chung et al. 2019). However, while these experiments give insights in the basic structure of PDCs, the analogy with PDCs is limited by fundamental differences in the scaling such as the density contrast with the ambient fluid, the fluid viscosity or the turbulence intensity (Burgisser et al. 2005).

- Large-scale experiments (Andrews and Manga 2011; Dellino et al. 2007; Lube et al. 2015), which reproduce PDCs in a controlled, scaled environment, with the possibility to measure internal parameters and link them to the resulting deposits. However, to date, no large-scale experiments were done with hill-shaped obstacles in the flow path.

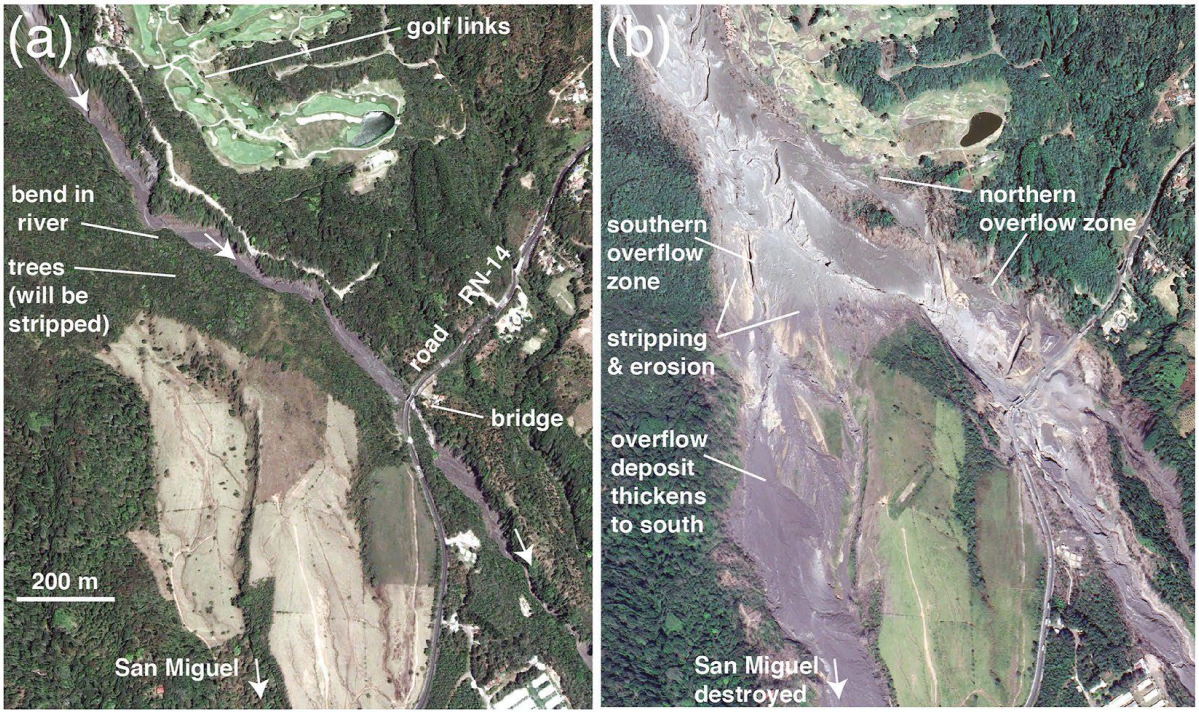

Figure 1.1: satellite view captured (a) before and (b) after the 2018 eruption of Fuego (Guatemala), showing a major overspill zone where the PDC did not stay confined in the valley and rather diverted at the valley bend, leading to the desruction of the entire community of San Miguel Los Lotes. Modified from Risica et al (2022).

This research focuses on the transport and sedimentation processes of PDCs across topographic obstacles. It is motivated by the gaps in the current knowledge and necessity to produce models that would improve hazard mitigation and protect populations and infrastructures. Dynamically and kinematically scaled PDCs were reproduced in the Pyroclastic flow Eruption Large-scale Experiment (PELE, Lube et al. 2015) located in Massey University, New-Zealand. Hill-shaped obstacles of varying size were introduced in the channel to span a range of possible obstacles that can be encountered by a PDC. Through these experiments, this project aims at decrypting the processes occurring inside PDCs as they travel across obstacles, and how the transport and sedimentation processes are affected by the hills, even far downstream.

This work builds on previous works done in PELE for two PhD theses (Breard 2016; Brosch 2020), which respectively focused on dense and dilute PDCs.

1.2. Research questions and objectives

This PhD research is motivated by three main research questions, presented as follows and summarized in Table 1.1:

Question 1: What are the physical processes governing the interactions of PDCs with topographic obstacles?

This will be addressed by:

- Designing and building experimental obstacles that would fit the range of obstacles encountered by a PDC and refining the PELE setup to obtain qualitative results for each experiment.
- Characterizing the dynamic interaction of PDCs across obstacles and linking them to a detailed analysis of flow regimes.
- Determining forces acting on the flow at the obstacle position and their impact on the flow dynamics.

Question 2: Can topographic obstacles modify the internal flow and deposition behaviour of PDCs? How is this reflected in their deposits?

This will be addressed by:

- Defining the changes in flow density, velocity, temperature and momentum before and after the obstacles.
- Quantifying the internal energy of the flows with varying obstacle size.
- Time-resolved analysis of the deposits before and after the obstacles and linking their characteristics to the dynamics of the parent flow.

Question 3: What are the consequences of the interaction of PDCs with topographic obstacles on their runout and hazard behaviour?

This will be addressed by:

- Describing flow processes occurring immediately after the obstacle and their variations with time.
- Characterising flow propagation and how obstacles of different sizes impact the final runout.
- Investigating and comparing the flow density, velocity, grainsize and temperature after each obstacle and the implication for PDC hazards downstream of obstacles.

Question	Methodology	Objective
What are the physical processes governing the interactions of PDCs with topographic obstacles?	Measuring the internal time-variant flow structure, density and velocity, focusing specifically across the obstacles.	Qualitative understanding of the processes occurring when PDCs cross a topographic obstacle.
Can topographic obstacles modify the internal flow and deposition behaviour of PDCs and how is this reflected in their deposits?	Linking the deposit characteristics to flow regimes.	Building a dataset to assess PDC-obstacle interactions with deposit characteristics in the field.
What are the consequences of the interaction of PDCs with topographic obstacles on their runout and hazard behaviour?	Measuring time- and space-variant flow structure, velocity, temperature, density and grainsize after the obstacles up to the end of the flow propagation.	Defining a model that predicts hazards downstream of different obstacle sizes.

Table 1.1: Summary of research question, methods and objectives.

1.3. Thesis outline

This PhD thesis is divided in seven chapters as followed:

Chapter 1

The thesis starts with the present introductory chapter. Here, the focus is centred on the introduction to the research topic and explanations for the reasons behind this project through questions and objectives.

Chapter 2

This chapter focuses on the previous works that were done on PDCs in general, before focusing on their interactions with obstacles. The fundamental processes that are suggested when PDCs encounter topographic obstacles are reviewed through field studies, theoretical models, analogue and large-scale experiments.

Chapter 3

In this section, the methodology used to perform the work presented in this thesis is detailed, from the design of the large-scale experiments and obstacles to a description of the material used for analysis and methods for data processing.

Chapter 4

Here, Questions 1 and 2 are addressed. The interactions of the experimental PDC with the obstacle, and how these interactions vary with time are described in detail. Changes in PDC structure, transport and deposition processes from the stoss side to the lee side are shown.

Authors contributions: L. Corna: conceptualization, methodology, data collection and analysis, investigations, interpretations, writing (first draft, reviewing and editing). G. Lube: conceptualization, methodology, resources, discussions, writing (reviewing and editing). D. Uhle and E. Brosch: experimental and analytical assistance. J. Jones: discussions and assistance.

Chapter 5

This chapter addresses Question 3 and another aspect of Question 1. It is centred on the characteristics of the wake formed behind the obstacle. The link between its physical characteristics and the initial flow structure is investigated and new models are suggested.

Authors contributions: L. Corna: conceptualization, methodology, data collection and analysis, investigations, interpretations, writing (first draft, reviewing and editing). J. Jones: discussions, analytical assistance, writing (reviewing and editing). G. Lube: conceptualization, methodology, resources, writing (reviewing and editing). E. Brosch: experimental assistance and discussions.

Chapter 6

Questions 2 and 3 are investigated in this chapter. It reviews the long-term impacts of the obstacle on the flow structure, runout, density, grainsize and temperature in medial and distal distances. The hazards involved downstream of the obstacles are emphasised.

Authors contributions: L. Corna: conceptualization, methodology, data collection and analysis, investigations, interpretations, writing (first draft, reviewing and editing). G. Lube: conceptualization, methodology, resources, discussions, writing (reviewing and editing). E. Brosch and D. Uhle: experimental and analytical assistance. J. Ardo: experimental assistance. J. Jones: discussions and assistance.

Chapter 7

In this final chapter, the main results of this research and their applications for the field are summarized. This conclusion is then followed by perspectives and suggestions for future work in this field.

2. Literature review

This chapter provides a brief review of PDCs and their hazards with a focus on current knowledge of PDC interactions with topographic obstacles.

2.1. Pyroclastic Density Currents and associated hazards

Pyroclastic Density Currents (PDCs) are gravity-driven hot mixtures of gas and particles travelling at high speed down a volcano (Fig. 2.1). They are produced during explosive eruptions and tend to follow topographic lows, but have the ability to surmount significant topographic obstacles (e.g. Breard et al. 2015; Fisher 1990; Burgisser 2005). Associated volumes of PDC deposits span between less than a million cubic meters to a few cubic kilometres, (Cronin et al. 2013; Lube et al. 2007; Calder et al. 1999; Abdurachman et al. 2000), emplaced during periods of time that can vary between a few minutes (Criswell 1987) and several hours (Roche et al. 2016).

PDCs are driven by the density contrast between the ambient fluid (the atmosphere) and the particle-laden flow. While the mixture is the densest at the onset of the flow, the ingestion of air and sedimentation of particles decrease the bulk density of the flow along the runout. At a critical distance from the source, the bulk flow density can decrease below the density of the ambient air. In this situation, the flow becomes at least partially positively buoyant and lifts off (Druitt 1998).

PDCs are one of the most destructive phenomena occurring on volcanoes worldwide and the main cause of casualties related to volcanic eruptions, claiming the lives of more than 60,000 people since 1783 (Tanguy et al. 1998). Prominent examples are the eruptions of Vesuvius (AD 79), Montagne Pelée (1902) or the more recent eruption of Merapi in 2010, which respectively killed approximately 2,000, 29,000 and 380 people (Gurioli et al. 2010; Sigurdsson et al. 1982; Tanguy 1994; Cronin et al. 2013).

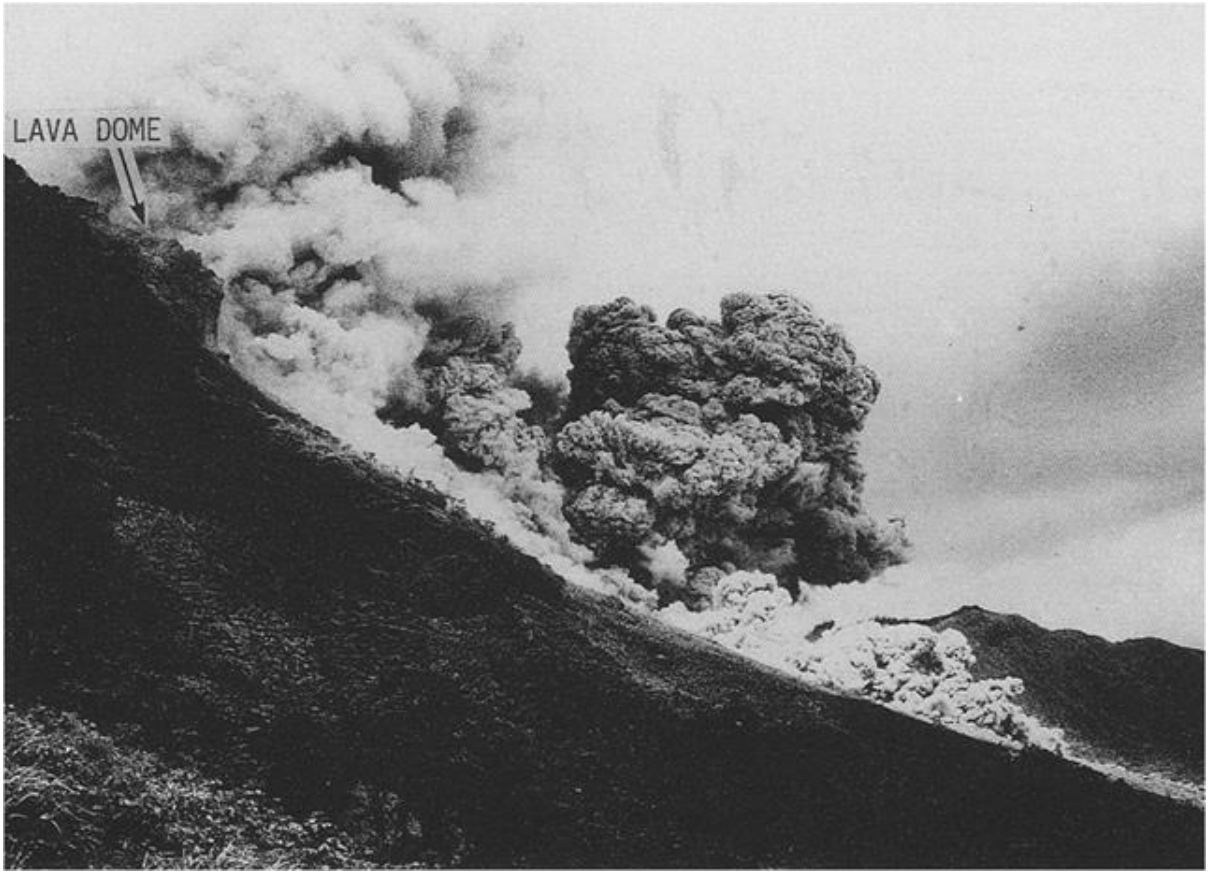

Figure 2.1: View of a PDC generated from dome collapse from the 1991 Unzen eruption (Japan). From Yamamoto et al. 1993.

Hazard impacts of PDCs can be generated by several flow characteristics. On humans, high temperatures can cause severe burn injuries, often lethal (Voight and Davis 2000; Baxter et al. 2017) while the ash load provokes asphyxiation (Baxter 1990; Baxter et al. 2017). Highly populated areas are particularly at risk, even in case of small-scale events (Baxter et al. 1998). As shown in Figure 2.2, the high dynamic pressure generated inside PDCs of several tens to hundreds of kilopascal can cause extensive damage to buildings (Valentine 1998; Clarke and Voight 2000). In the case of dilute PDCs, self-generated dynamic pressure pulses can further exacerbate the destruction potential (Brosch et al. 2021). Important PDC hazards arise from their ability to surmount topographic obstacles (e.g. Lube et al. 2011; Breard et al. 2015), to avulse (i.e. change directions) from channels, channel interfluves and adjacent terrain (e.g. Lube et al. 2011; Risica et al. 2022), and to decouple the mobile dilute PDCs from the main parental flow, thereby increasing the impacted hazard area (e.g. Burgisser 2005). Through the destruction of crops, livestock and infrastructures, the

economic and social consequences can be severe local communities, especially in developing countries (Whiteford and Tobin 2009).

Figure 2.2: Photograph of the Rue Victor Hugo in the town of Saint Pierre (Martinique) after the passage of the deadly lateral blast PDC in 1902. From Tanguy 1994.

2.2. Characteristics of PDCs

2.2.1. Mechanisms of generation

PDCs can be generated though different mechanisms, summarized below.

- ***Dome collapse***, where the gravitational collapse of a solid lava dome produces a highly concentrated basal flow, generally overridden by a dilute, turbulent surge that can decouple and propagate further. These Block and Ash flows mostly stay confined in valleys (Druitt 1998; Abdurachman et al. 2000; Calder et al. 1999), but can potentially overbank in case of valley filling and avulsion, increasing hazard potential (Lube et al. 2011; Cronin et al. 2013; Risica et al. 2022).

- ***Column collapse***, where the density contrast between the atmosphere and the exiting mixture from vent is or becomes too great due to the inability

of the mixture to entrain air. This phenomenon can occur, for instance, through vent widening or decreasing speed of the mixture exiting the vent (Sparks et al. 1978). The column cannot stay buoyant, collapses and produces Pumice and Ash Flows. These flows are often sustained and quasi-steady (Branney and Kokelaar, 2002). For the largest eruptions, this phenomenon can be linked to ignimbrite generation and caldera formation (Druitt and Sparks 1984).

- ***Lateral blast*****,** such as the well-known example of Mount Saint Helens in 1980, where a catastrophic landslide led to the sudden decompression of a crypto dome, forming a powerful directed pyroclastic surge (Christiansen and Peterson 1981; Criswell 1987) and initiating a plinian eruption. This pyroclastic surge travelled up to 24 kilometres unhindered by topography (Fisher 1990; Gardner et al. 2018).

- ***Phreatomagmatic eruptions*** creating base surges, which consist of radial turbulent flows at the base of a volcanic column and can travel for several kilometres (Wohletz and Sheridan 1979). They typically form in shallow submarine and lacustrine phreatomagmatic and phreatic eruptions (Moore 1967). Base surges were emplaced during the eruption of Taal Volcano, Philippines in 1965-1966 (Waters and Fisher 1971), during the Laacher See eruption, Germany (Schmincke et al. 1973), and in the Auckland Volcanic Field, New Zealand (Brand et al. 2014).

- ***Hydrothermal blasts***, which are highly energetic, relatively cold PDCs (<200 °C) generated during hydrothermal eruptions. A typical example of these blasts was described at Bandai volcano, Japan, in 1888 (Yamamoto et al. 1999) or more recently during Te Maari eruption in 2012 at Mt Tongariro, New Zealand (Lube et al. 2014).

2.2.2. Structure of the flow

In order to quantify PDC hazards, it is essential to understand the structure and the transport and deposition mechanisms in these flows. In the past decades, several models have been proposed for the structure of pyroclastic flows and surges, mostly based on field observations and experiments.

Because of the shearing occurring (1) between the base of the flow and the substrate, and (2) with the atmosphere, these flows present a turbulent head with a nose where sits the maximum velocity (Altinakar et al.1996) as shown on Figure 2.3. The head ingests ambient air and leads to a strong dilution of the current in its rear as eddies shed off, creating a dilute wake overriding a gravity-driven body. The body can travel at greater velocity than the head, allowing a constant feeding of particles to the leading part (Andrews 2014; Breard and Lube 2017).

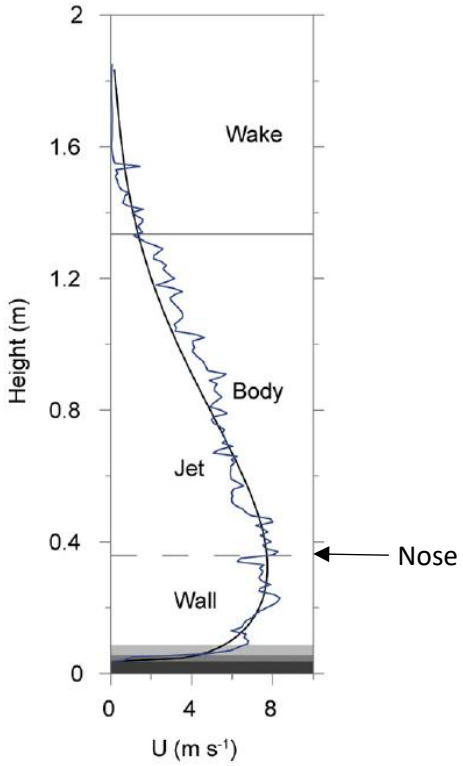

Figure 2.3: vertical velocity (U) profile of a dilute surge (blue curve) fitted by a power-Gaussian function (black curve), showing the wall region (below the nose with maximum velocity) and the jet region (above the nose) as defined by Altinakar et al. (1996). Modified from Brosch and Lube (2020).

The internal architecture of PDCs is still very much discussed because of the lack of direct measurements and observations due to the high destructive power of these

flows. However, it is widely admitted that the internal structure depends on several parameters such as the volume of erupted material, the mass discharge, the grainsize and the nature of the particles. In large-scale experiments, Lube et al. (2015) suggested that whether a dense underflow would occur or not depends on the condition of formation and discharge rate of the flow. Dense pyroclastic flows are overridden by a turbulent ash-cloud that can decouple and travel further distances than the underflow (Burgisser 2005; Abdurachman et al. 2000). However, it remains uncertain whether the transition between the dense underflow and the dilute ash cloud is a sharp contact or a gradual transition (Branney and Kokelaar 2002; Breard and Lube 2017). In the case of dilute PDCs, most of the mass and momentum is carried in the dilute cloud without dense underflow. However, regardless of the initial flow density, vertical density stratification will develop in any PDC (Valentine 1987).

From field studies (e.g. Walker 1985; Sigurdsson et al. 1991; Pollock et al. 2019), numerical modelling (e.g. Brodu et al. 2015; Gueugneau et al. 2019), and more recently with large-scale experiments (Breard and Lube 2017; Brosch and Lube 2020), different transport mechanisms of particles inside PDCs have been suggested. Ballistic, granular-fluid avalanches, traction, saltation and suspension are the main modes of transport and are very similar to the transport mechanism of sediments in aqueous environments such as rivers (Best 1988; Prosser et al. 2001; Branney and Kokelaar 2002). According to the regime of the PDC (mostly dense, mostly dilute or intermediate regime), a certain transport mechanism can dominate the motion of particles (Lube et al. 2020).

Ballistics transport is inferred to occur at the early stages by Walker (1985) while the flow is still not fully formed and contains large dense blocks falling from the collapsing volcanic column. Granular-fluid avalanches are present in the underflow of dense PDCs or in the bedload region of dilute surges where particles accumulate and travel downstream at slower velocities (Rowley et al. 2014), forming shifting sandwaves depositing massive units (Brosch and Lube 2020) where the transport is facilitated by elevated pore pressure and buoyancy (Branney and Kokelaar 2002; Roche 2012). Traction is dominant in the bedload region of pyroclastic surges where particle-particle interactions (friction, collision) and gravity are important. This mode of transport allows large clasts to roll along the substrate. Saltation affects intermediate-size clasts, which are intermittently carried by fluid motion before being deposited again. This phenomenon creates short-lived ballistic trajectories (Wohletz 1998) at the

interface between the bedload and the dilute surge. Suspension occurs in the upper dilute region of dense PDCs or in dilute surges, where particles are coupled with the gas phase. Particle-particle interactions are rare: the fine particles mostly follow the turbulent flow (Burgisser et al. 2005).

2.2.3. Flow properties of PDCs

The dynamics of PDCs have been discussed for many years within volcanology research and remain one of the main challenges to resolve. The particle content or the presence of lobes and lateral levees (Lube et al. 2007) are typical of granular flows with important particle-particle interactions and high friction coefficient. However, their extended runout and their ability to climb slopes suggest a fluid-like behavior explained by different mechanisms such as high pore-pressure (Roche 2012), polydispersity of particles inducing low permeability (Breard et al. 2019), velocity-dependent frictional weakening (Lucas et al. 2014), or gas-particle feedback induced air-lubrication (Lube et al. 2019). The following section summarizes estimates of physical flow parameters in PDCs and tries to build an overview of the influence of each of these parameters on the transport and deposition processes inside these flows.

Temperature

PDCs are generally hot, with temperature ranges going up to several hundreds of degrees, but some types of PDC have been reported to have low temperatures close to that of the ambient air (Moore 1967). Air ingestion and incorporation of relatively cold country rock fragments are important processes that have been suggested to decrease temperature of the flow along its runout (Valentine 1987). The flow cools down until the end of its propagation, when the bulk density becomes too low and the flow lifts off (Druitt 1998). Temperature ranges for some of the PDCs emplaced during the 1997 Soufriere Hills eruption (Montserrat) probably reached 400 to 600°C (Loughlin et al. 2002; Calder et al. 1999) while those emplaced in the Valley of Ten Thousand Smokes (Katmai, Alaska, 1922) likely reached 800°C to 900°C (Lovering 1957).

Velocity

PDCs are known to travel at very high velocities. For example, estimations for flow velocity at Soufriere Hills Volcano are typically several tens of meters per second and can reach 90 m/s (Calder et al. 1999) while they were above 230 m/s at Mount St Helens (Kieffer and Sturtevant 1988). This velocity is partially controlled by the initial over-pressure at source, the type of PDC (dense or dilute) and influenced by parameters such as topography. However, how flow velocities relate to flow runout distance up to 100 km from source and to the ability to surmount very large topographic obstacles remains poorly understood. This is particularly enigmatic for large-volume PDC such as the parent flows of the 232 CE Taupō Ignimbrite, New Zealand (Wilson 1985) or the 18 Ma-old Peach Spring Tuff, USA (Valentine et al. 1989).

Turbulence generation

PDCs are turbulent flows, with Reynolds Numbers (Re) typically greater than 10^6 (Burgisser et al. 2005). In the wall region, where the flow is strongly sheared by the substrate, eddies are small and short-lived, whereas in the jet region where the shearing is caused by free shear with the ambient fluid, eddies tend to be larger and longer-lived (Brosch et al. 2021).

Burgisser and Bergantz (2002) estimated the degree of gas-particle coupling and gas-particle feedback mechanism inside PDCs. Using non-dimensional Stokes (St) and Froude (Fr) numbers, they calculated the Stability Factor (Σ_T), which is the ratio of the Stokes numbers and the Froude Number squared.

$$Fr = \frac{U}{\sqrt{g\delta}} \quad \text{(Eq. 2.1)}$$

$$St = \frac{U_T.\Delta U_{eddy}}{\delta.g} \quad \text{(Eq. 2.2)}$$

And

$$\Sigma_T = \frac{\rho_p.g.d^2}{18\mu.f.\Delta U_{eddy}} = \frac{St}{Fr^2} = \frac{U_T}{\Delta U_{eddy}} \quad \text{(Eq. 2.3)}$$

with U the flow velocity, g the acceleration of gravity, δ the eddy diameter, U_T the terminal settling velocity, ΔU_{eddy} the eddy rotation speed, ρ_p the density of the particles, d the particle diameter, μ the flow viscosity and f the drag factor.

They establish five regimes: “Fall” where particles are fully decoupled from eddies and settle (S_T>1and Σ_T>1), “Unroll” where particle can settle during downward motion of the eddy only (S_T>1and Σ_T~1), “Margins” where particles are concentrated at the periphery of eddies (S_T~1and Σ_T<1), “Turbulent Sedimentation” where sedimentation is modified by turbulences (S_T<1and Σ_T~1), and “Homogeneous Transport” where particles are fully coupled with the gas phase and are carried within the eddies (S_T<1and Σ_T<1).

Concentration

PDC deposits have traditionally been distinguished into two main types: pyroclastic surge deposits and pyroclastic flow deposits. Based on their overall deposit geometry, their sedimentary facies and facies variation, and through an analogy to fluvial and aeolian sediment transport and deposition principles, these two broad classes of PDC deposits are commonly associated with PDCs of either high particle solids concentration (up to several tens of volume percent) or low concentration (< 0.1 vol %) of particles. The concentration profile of PDCs is determined by the Rouse Number (Pn) which describes the ability of a turbulent flow to keep particles in suspension (Valentine 1987; Dellino et al. 2008). If Pn > 2.5, particles have a high settling velocity: they cannot stay in suspension and rapidly settle. If Pn < 2.5, particles are supported by the turbulences and become better mixed vertically with decreasing Pn. The stability of this stratification is described by the Richardson Number (Ri) (Valentine 1987). Flow stratification is stable with Ri < 1, transitional with 1 < Ri < 10, and unstable for Ri > 10.

Dense flows are primarily controlled by gravity, friction and particle-particle interactions. Because of these interactions, slope angles and flow thicknesses have a great importance in the extent of the flow by changing deposition patterns and basal friction (Brown and Branney 2013; Chédeville and Roche 2015; Roche et al. 2021). These parameters are balanced by the low permeability of the mixture (Breard et al. 2019) that allows the retention of pore-pressure (Roche 2012), or basal air lubrication mechanisms limiting basal friction (Lube et al. 2019) that can extend the runout of these flows. Dense PDCs typically deposit thick, massive, poorly-sorted beds, usually confined in valleys (Abdurachman et al. 2000; Loughlin et al. 2002) or forming levees (Lube et al. 2007).

Dilute flows are usually considered fully turbulent gravity flows where particle-particle interactions are rare and where the main mode of transportation is turbulent suspension (Burgisser et al. 2005; Andrews and Manga 2012), even though the flows stay strongly vertically density stratified (Valentine 1987; Brosch and Lube 2020). Air ingestion and settling of particles modify the density of the current and are important for hazard assessment. The Stokes number (St) and Stability Factor (Σ_T) describe the coupling of particles with the turbulent eddies and the residence time of these particles inside them from gravitational force (Burgisser and Bergantz 2002). Dilute PDCs will deposit more typically thinner, finer-grained, stratified or cross-stratified beds draping topography (Druitt 1998).

Some ignimbrites display characteristics such as massive, ponded deposits that indicate a rather dense mode of transportation and deposition (e.g. Valley of the Ten Thousand Smokes, Alaska, Lovering (1957)). Others show stratified, thin deposits even on top of ridges, suggesting a more dilute type of transport and deposition (e.g. Campanian Ignimbrite, Italy, Fisher et al. (1993)). However, other PDC deposits show features compatible with both dilute and dense fluid-particle transport and deposition regimes like the Taupō Ignimbrite, which has fueled several discussions about the transport regime (Dade and Huppert 1996; Druitt 1996; Wilson 1997; Legros and Kelfoun 2000; Roche et al. 2021). Examples of deposit features include close associations of massive, coarse-grained and poorly sorted deposits with intercalation of thin, fine-grained, cross-stratified bed forms. Flow transitions between dilute and dense transport regimes have been inferred to occur in PDCs during the 18th May 1980 eruption of Mount St Helens (Walker 1983; Burgisser and Bergantz 2002; Brand et al. 2014) and they have been observed in the experiments performed by Breard et al. (2018).

Dynamic Pressure

One of the most destructive phenomena associated with PDCs is their high dynamic pressures, which is the product of the flow density and its squared velocity. Effects of dynamic pressure range from breaking small twigs of trees to completely destroying buildings with steel-enforced concrete walls. Dense block and ash flows at Unzen (Japan, 1991) were inferred to have associated dynamic pressures of 8 kPa (Clarke and Voight 2000). Base surges associated with phreatomagmatic eruptions in

the Auckland Volcanic Field (New Zealand) were capable of blowing down 0.5 m wide trees, which necessitate dynamic pressures in the order of 12 to 35 kPa (Brand et al. 2014). The eruption of the Montagne Pelée in Martinique (1902) produced a lateral blast which caused the total destruction of the town of Saint Pierre (Fig. 2.2) located 8 km from the crater, involving minimum dynamic pressures of 30 kPa to inflict the associated damages (Valentine 1998).

2.3. Large-scale experiments

A better understanding of the dynamics, transport and sedimentation mechanisms inside PDCs is necessary to produce accurate models for future events. However, due to the ferocity of these flows, direct measurements of real-world flows are dangerous and impractical. In the past fifteen years, the uncertainties around the flow dynamics of PDCs led to the development of large-scale experiments as a new approach towards quantifying internal flow dynamics of PDCs. Large-scale experiments are a new way to reproduce PDCs in controlled and safe environments. However, ensuring that these flows are dynamically and kinematically scaled to real-world flows is a key condition for these experiments to be relevant and applicable.

2.3.1. Insights into PDC dynamics from past experiments

The first large-scale device was presented by Dellino et al. (2007) from the University of Bari, Italy. It consists of a 2.2 m high cylindrical conduit filled with natural pyroclastic material from Vesuvius (Fig. 2.4). The eruption simulation is triggered by a pressurization system creating a two-phase mixture that is ejected vertically. This ascending column quickly collapses, leading to the formation of asymmetric particle-laden gravity currents (Fig. 2.4) with Reynolds numbers and coupling of particles similar to those estimated for real-world flows. These PDCs spread all around the conduit on a plastic sheet as far as 10 m. By measuring dynamic pressure directly inside the flows, the researchers linked flow dynamics and deposit grainsize

information. They proposed a hazard model showing that only large eruptions would produce PDCs with dynamic pressure high enough (40 kPa) to counterbalance the resistance of a concrete wall (Dellino et al. 2010). Other experiments with this device were run to simulate a diversity of eruption types such as pressurized jets, convective plumes or collapsing pyroclastic fountaining, helping to link conduit conditions and flow regimes (Dellino et al. 2010; Sulpizio et al. 2014).

The setup is scaled to reproduce different eruption styles and dynamisms and gave valuable insights into the generation mechanisms of PDCs and hazard assessment. However, the open non-channelized environment does not allow for the study of internal flow structure and dynamics.

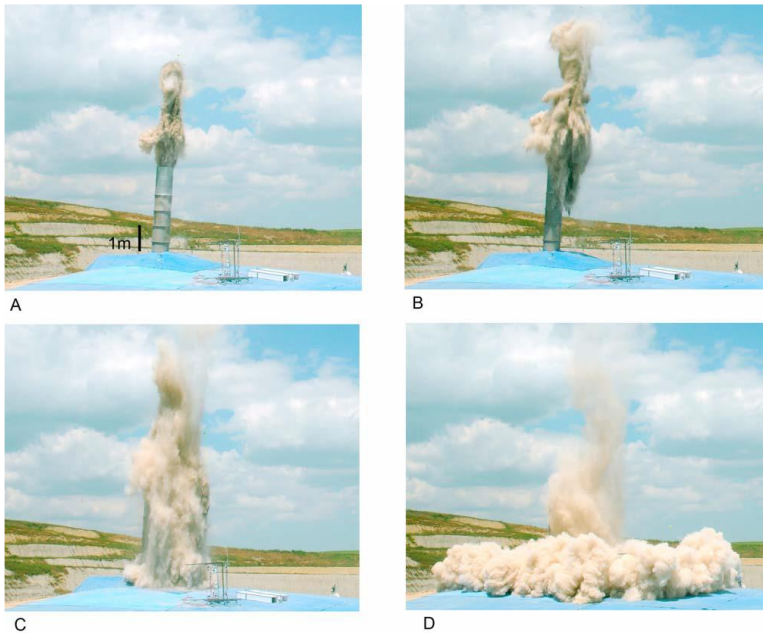

Figure 2.4: large-scale experiment device from University of Bari (Italy). Pictures show the development of a plume (A and B), its collapse (C) and the generation of a radially spreading surge (D). From Dellino et al. (2010).

Andrews and Manga (2011) presented another setup based at the Smithsonian Institution (USA). It consists of an acrylic tank in which synthetic PDCs made of heated talc powder are generated at a known discharge rate, with or without obstacles in the flow path (Fig. 2.5). The flow is visible through a transparent wall and recorded with cameras. The resulting experimental PDCs are dilute, turbulent flows. The authors showed the importance of air ingestion, temperature and kinetic energy during flow transport and how these influence runout distance, while describing flow reversals and sedimentation processes from the co-ignimbrite plume (i.e. the buoyant plume above

a PDC; Andrews and Manga 2012). Experiments performed with topographic obstacles showed that a dilute flow will barely be disturbed by obstacles smaller than 1.5 times the thickness of the head, but cannot cross a higher obstacle and will rather lift-off as a co-ignimbrite plume (Andrews and Manga 2011). Cold currents tend to spread radially and entrain air behind their head, forming a well-defined high-velocity base, whereas hot currents reach their buoyancy reversal earlier and ingest air on their margins, creating narrow flows with a well-defined axis and chaotic velocity profiles (Andrews 2014).

Although this setup gives valuable insights into the runout and formation of co-ignimbrite plumes, the nature of the particles limits the analogy with real-world flow as their transport and sedimentation characteristics are different from those of natural pyroclastic material. Noteworthy, the observations are only valid for fully dilute, fully turbulent flows.

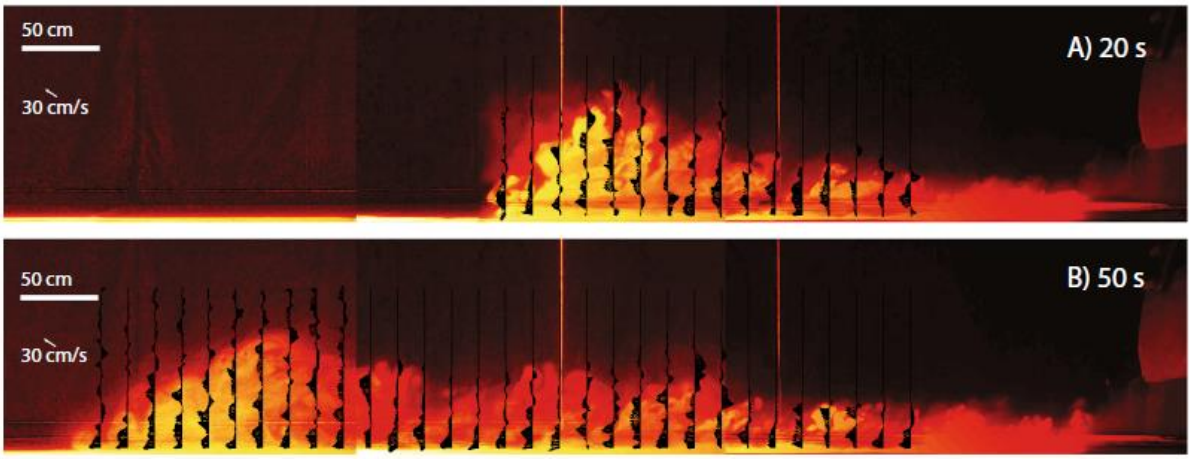

Figure 2.5: Photographs of a talc powder flow in a red laser sheet from Smithonian Institute with velocity profiles in black. Flow direction is from right to left. Modified from Andrews 2014.

2.3.2. Previous work at the PELE facility

The currently largest experimental device for large-scale PDC experiments is located in Massey University, New Zealand (Lube et al. 2015). Past studies using this international facility concentrated on characterising the spatiotemporal flow conditions of dilute, dense and intermediate PDC flow regimes (Breard et al. 2016; Breard and Lube 2017; Breard et al. 2018; Lube et al. 2019; Brosch and Lube 2020; Brosch et al.

2021; Brosch et al. 2022). PELE is capable of creating PDCs in an instrumented channel with a wide range of possible conditions (initial mass and mixture, initial temperature, drop height, channel angle, basal roughness, presence of obstacles). Experimental PDCs generated in the PELE scale well with natural flows as demonstrated through the partial overlap of the range in important non-dimensional numbers characterising experimental and natural PDCs.

Dense pyroclastic flows

The first experimental series focussed on the dynamics of dense flows (Breard et al. 2016; Breard and Lube 2017; Breard et al. 2018). Typical velocities were reached up to 30 m/s with initial flow bulk concentrations of 7.8 vol%, reaching 30 vol% in the lowermost dense underflow (Lube et al. 2015). Breard and Lube (2017) highlighted the different particle transport methods occurring in dense PDCs and evolving with space and time. They focused on the importance of the coupling between the laminar dense underflow and the turbulent dilute ash cloud, showing that the transition is not a sharp boundary, but rather consists of a transitional zone. This intermediate zone hosts the formation and settling of mesoscale structures controlling runout dynamics and lengths (Breard et al. 2016). A second key process responsible for the long runout of these flows was evidenced by Lube et al. (2019) as a retroactive lubrication mechanism happening at the interface between the dense underflow and the substrate. Gas would move into this zone along a shear-generated pressure gradient, lowering effective friction and delaying the deceleration and defluidization of the dense underflow.

However, they also acknowledge the presence of both dense and dilute regimes in a single PDC, and that deposits will only depict the dominant mode of transport just before deposition, without showing the previous ones (Breard et al. 2018). In the same study, they introduced a new non-dimensional number to describe the dominant mode of transport of particles just before deposition. Hence,

$$T_{de-di} = \frac{A^3.d_{S1/2}}{V^{5/3}.L^2} \qquad \text{(Eq. 2.4)}$$

with $T_{de\text{-}di}$ the dense-dilute parameter, A the inundation area, $d_{S1/2}$ the Sauter mean diameter at half runout distance, V the volume of the deposit and L the runout distance.

Dilute pyroclastic surges

In the second experimental series, dilute PDCs were studied in more depth (Brosch and Lube 2020; Brosch et al. 2021). With typical velocities around 9 m/s and initial concentrations around 0.1 vol% (3.4 kg/m^3), their transport and deposition processes were explained by Brosch and Lube (2020) who highlighted the strong density stratification of surges and, again, the importance of mesoscale clusters feeding the transient region. Through their variable settling rate, they are responsible for different modes of transport and deposition in the base of the flow, from erosion to the formation of cm-thick mobile sand avalanches, and therefore different types of deposits. These variable particle settling rates are associated with the largest coherent turbulence structures inside the surge, carrying most of the kinetic energy and dynamic pressure (Brosch et al. 2021).

These two studies lay down the bases for the new experimental series on which this thesis is built. By characterizing the flow initial density, velocity and dynamic pressure, it is possible to compare those obstacle experiments with these previous runs without obstacles.

2.4. Flow propagation over obstacles

The ability of PDCs to surmount topographic obstacles has been documented in many field studies (e.g. Wilson 1985; Fisher 1990; Cas et al. 2011; Burgisser 2005; Breard et al. 2015). However, the lack of quantitative relationships between the parent flow and the resulting deposits is limiting the understanding and potential interpretations. Studies have tried to address the problem with different approaches, from field work to numerical modeling or analogue experiments, but the lack of direct observations limits the ability to fully constrain the parent flow. In this section, different models that have been proposed are reviewed.

2.4.1. Deposit characteristics of PDCs across obstacles in the field and inferred mechanisms of propagation

Studying the deposits of past eruptions is a major branch of volcanology. Through such field studies, it is possible to better understand the transport and deposition mechanisms of PDCs, their architecture and behavior. The study of the deposit structure and grainsize distribution can provide information on the densities and velocities of the parent flow (Branney and Kokelaar 2002). Typically, deposits from dense flows show massive, poorly-sorted, thick deposits mostly confined in valleys. Deposits from dilute pyroclastic surges can be stratified, wavy or cross-stratified on their extended runout, with the possibility of intercalation of massive, poorly sorted beds usually in proximal areas (Druitt 1998), and formation of regressive dune bedforms (Douillet et al. 2013a,b; Brand et al. 2016).

Some field evidences show that obstacles can sometimes completely block PDCs (Yamamoto et al. 1999; Yamamoto et al. 1993), but in most cases, PDCs are able to easily cross topographic barriers (e.g. Capra et al. 2016). In these cases, the deposit type changes according to topography, with thick, massive, ponded deposits in valleys and thinner stratified layers on top of ridges, as described for the 1980 Mount Saint Helens eruption (Hoblitt et al. 1981; Fisher 1990; Druitt 1992; Bursik et al. 1998). Massive, thick, poorly sorted deposits were often identified on the stoss side of topography (Wilson 1985; Bursik et al. 1998; Sulpizio et al. 2008; Burgisser 2005) or buildings (Gurioli et al. 2002, 2007), with high lithics content (Giordano 1998) and sometimes even coarse lithic breccias (Freundt and Schmincke 1985; Macías et al. 1998). Several field studies considered the dynamics of small to moderate-scale PDCs across obstacles and explained their ability to surmount topographic highs through blast-like rapid suspension sedimentation (Breard et al. 2015), valley filling and avulsion (Lube et al. 2011), momentum balance as basal particles accumulate on the slope while the flow compresses and accelerates (Freundt and Schmincke 1985), or sediment trapping and rapid topography modification during flow emplacement (Brown and Branney 2013). The blocking of the basal bedload could lead to a hydraulic jump (or pneumatic jump, Branney and Kokelaar 2002) retreating upstream (Allen 1982, Freundt and Schmincke 1985) and creating a backward motion of the bedload. Valentine (1987) proposes the presence of a dividing streamline in a surge flow, above which particles are able to surmount the obstacle because of their high kinetic energy

and below which they are diverted or blocked, leading to a thickening of deposits in valleys and on the stoss side of hills.

Wilson (1985) describes in the Taupō Ignimbrite lee-side lenses of very coarse pumice in a fines-rich matrix, starting near the crest and thickening downstream, while keeping a relatively low angle compared to the slope. The same observation was made in deposits from the Upper Pollara Eruption (Salina Island, Italy) where topography enhanced the stratified sedimentation of coarse particles and reduced that of fine particles in the lee sides (Sulpizio et al. 2008). The formation of a low dynamic pressure vortex is believed to lead to this layering, entraining particles and reducing potential damages in the lee-sides, causing for example untouched patches of forest (Komorowski et al. 2013; Gardner et al. 2018) as shown in Figure 2.6. However, the length of the coarse lenses is shorter than expected, which would induce a faster filling of this low-pressure zone than expected only by gravity (Wilson 1985). This phenomenon was explained by Gardner et al. (2018) in the case of the Mount Saint Helens eruption in 1980. In order to estimate the reattachment point, they suggested a ballistic trajectory adjusted to a flow front expansion downward, entraining air and decreasing basal density. This corrected trajectory would indeed decrease the reattachment distance and would fit to the extent of the standing trees patches. While this model works for the propagation of the head of the flow, the body would however be more ground-hugging, with lower dynamic pressures allowing trees to stay up in the lee sides of hills (Fig. 2.6, Guinn et al. 2022). In the case where the reattachment would happen before the end of the obstacle, possibly in more proximal areas, coarse lithic breccia deposition would happen in the break in slope due to strong deceleration causing a bulk flow hydraulic jump enhancing sedimentation with fines elutriation (Macías et al. 1998).

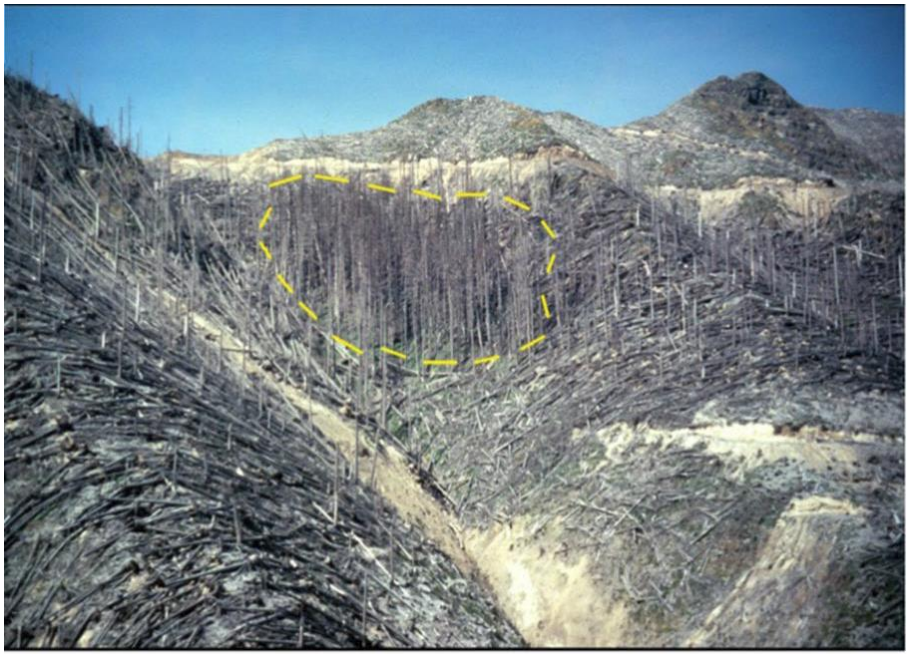

Figure 2.6: Tree patch (circled with yellow dashes) in the lee side of a hill after the 1980 Mount Saint Helens eruption (USA). The photograph was roughly taken facing flow direction. Modified from Guinn et al 2022.

Topography strongly influenced the PDCs of the 1994 Merapi eruption (Indonesia), where it caused abrupt directional changes of pyroclastic surges (Kelfoun et al. 2000) as well as decoupling between dense flow and overriding ash-cloud surge (Abdurachman et al. 2000). The runout distance of these small to moderate scale PDCs is believed to be disturbed by topographic interference as the high resistance of perpendicular ridges creates great loss of momentum in the flow, leading to a decrease in final flow runout (Fisher 1990). By climbing hills, flow velocity would decrease and density stratification would increase up to deposition and strong loss of mass on the stoss side, leaving the downstream flow driven by the residual kinetic energy and the potential energy (Sulpizio et al. 2008).

However, many large-volume PDCs travelled across significant topographic barriers (up to 1000 m above vent) relatively unaffected by their distance from source up to and exceeding 80 km such as the parent flows of the c. 40 ka Campanian Ignimbrite (Italy), the c. 15 ka Neapolitan Yellow Tuff (Italy), the c. 232 AD Taupō Ignimbrite (New Zealand), the c. 2 Ma Cerro Galán Ignimbrite (Argentina), and the c. 22 ka Ito Ignimbrite (Japan) (Wilson 1985; Cas et al. 2011; Fisher et al. 1993; Scarpati et al. 1993; Aramaki 1984). It is still unclear how these flows travel across topographic obstacles, but several hypotheses have been proposed. Burgisser (2005) showed that

the dense underflow produced by the 2050 BP eruption of Okmok Volcano (Alaska) went across obstacles by valley filling and spilling over certain obstacles, while the dilute ash cloud decoupled and travelled across additional and higher obstacles. The Campanian Ignimbrite is thought to have been originated from a very thick dilute flow that was able to cross high topographic obstacles because of its thickness (Fisher et al. 1993). The proposed quasi steady sustained flow for Ataclán Ignimbrite would have slowly deposited in valleys, allowing later parts of the current to deposit further and higher up as evidenced by the absence of disruption in the deposits, and allowing it to overcome topography (Branney and Kokelaar 1997). Wilson (1985) suggests the Taupō Ignimbrite was deposited from a very high-speed dense flow (> 300 m/s) to explain its ability to travel over very large distal obstacles without losing too much momentum. This model however is highly debated (Dade and Huppert 1996; Druitt 1996; Legros and Kelfoun 2000).

2.4.2. Theoretical and numerical models

While field observations are an important approach towards understanding PDC dynamics, they are constrained by the fact that only the deposits of the PDCs can be studied, but direct measurements cannot be carried out. The following section focuses on theoretical, numerical and experimental approaches used to understand PDC dynamics when encountering an obstacle.

In early research, Sparks et al. (1978) argued about the ability of PDCs to cross topographic barriers through their extremely high velocities, reaching values of 300 m/s. More recently, it was proposed that fully dilute PDCs cannot cross a topographic obstacle if it is higher than 1.5 times the thickness of the flow and that a smaller obstacle will have little influence on the PDC runout distance (Andrews and Manga 2011). However, PDCs might not be purely dense or purely dilute flows, but would rather scale on a spectrum between these two end-members, with the recognition of an intermediate regime combining both dense and dilute characteristics (Lube et al. 2020). Hence, the processes responsible for overcoming obstacles might not only reside in the flow velocity (dense flow) or thickness (dilute flow), but also in its sedimentation rate, temperature, mass flux, grainsize distribution, or in the complexity of the topography itself. Woods et al. (1998) suggested that large volume PDCs with

high eruption rates (>10^8 kg/s) can only be blocked by topographic barriers as high as 1000 to 1500 m at several tens of kilometers from their source. Therefore, PDCs of smaller intensity are likely to be blocked and could cross over large obstacles only by spilling over. However, this model only works for a single obstacle. It is important to consider that the more complex the topography, the more sediment loss occurs, decreasing the flow capacity to travel along long distances (Doronzo et al. 2010) or high obstacles. By tracking Lagrangian particles in a “dusty gas”, Doronzo et al. (2010) proposed that by impacting on the stoss side of the obstacle, the velocity of the flow decreases, leading to a density and sediment flux increase forming massive, thick, poorly sorted deposits and a strong sediment loss. After the crest, deposits are thinner than without obstacles, but show a coarser distribution. This phenomenon could be explained by the intense turbulence created by the obstacle remobilizing the finest particles (Doronzo et al. 2010) or because the gas ingested during the flow jump is ejected upward as the flow impacts the substrate again, favouring the elutriation of fine particles back into the overriding surge (Kelfoun and Gueugneau 2022).

The consequences of the flow overcoming topographic obstacles are not limited to the grainsize distribution and the thickness of the deposits. In their numerical simulations of column collapse at Mount Vesuvius at high eruption rate, Todesco et al. (2002) showed that the entire flow runout could be affected by an obstacle (i.e. Mount Somma) by counter-intuitively conserving high temperature and prolongating the final runout of the flow on the long term.

2.4.3. Analogue models using dilute aqueous gravity currents over obstacles

Turbidity currents are dilute gravity flows occurring in marine, lacustrine or fluvial environments, responsible for a wide distribution of marine sedimentary structures (Middleton 1993). They consist of a mixture of water as the fluid phase, loaded with fine sedimentary particles as the solid phase, and move because of the gravity contrast between the current and the surrounding water. In some cases, the particles can be of volcanic origin, sedimenting from the plume (Doronzo and Dellino 2010), from a PDC or a lahar feeding particles into the water body (Schneider et al. 2001;

Trofimovs et al. 2008; Doronzo and Dellino 2013), or even directly from submarine eruptions (White 2000).

Because their structure, transport and deposition mechanisms are similar to those of PDCs, it is possible to compare these two types of gravity flows (Branney and Kokelaar 1992). Several studies have used experimental turbidity currents as analogues of PDCs using lock-exchange experiments in a laboratory environment (Middleton 1966a; 1966b; 1967; Parker et al. 1987; Lee and Yu 1997; Altinakar et al. 1996; Choux and Druitt 2002; Sher and Woods 2017), and more recent works have focused on the transport of these flows across obstacles inserted in the water tanks (e.g. Woods et al. 1998; Farizan et al. 2019; Goodarzi et al. 2020; Wilson et al. 2018; Oshaghi et al. 2013).

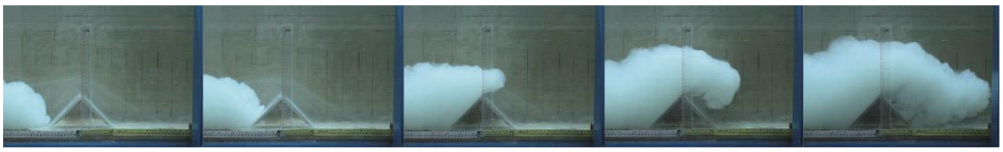

Figure 2.7: Analogue water-tank experiment showing the passage of the flow head over a 10 cm high, triangular-shaped obstacle. Flow direction from left to right. Modified from Oshagi et al (2013)

As the flow climbs the stoss side of the obstacle (Fig. 2.7), its velocity decreases, shifting to a low Froude number subcritical regime (Oshaghi et al. 2013). If the obstacle is small compared to the thickness of the flow, the latter will cross it with little or no difficulty, showing no obvious changes in sedimentary structures (Bursik and Woods 2000; Oshaghi et al. 2013). In case of a larger obstacle, the velocity drops and can even become negative at the base (Wilson et al. 2018; Abhari et al. 2018), reducing the basal shear (Goodarzi et al. 2020) and forming a hydraulic jump before the obstacle travelling upstream as a reflective bore (i.e. backflow), thickening the arriving flow and enhancing sedimentation (Alexander and Morris 1994; Woods et al. 1998; Bursik and Woods 2000). As this bore reaches the source of the flow, it would affect the entire deposition before the obstacle. This effect would increase with obstacle height and concentration as the flow is more density stratified (Farizan et al. 2019). Interestingly, upon reaching the crest, the velocity maximum would be similar regardless of the size of the obstacle, as evidenced by Oshaghi et al. (2013). Immediately after the crest, the flow seems to accelerate again, transitioning back to a high Froude number supercritical regime (e.g. Woods et al. 1998; Oshaghi et al.

2013). However, in the region after the obstacle, the velocity decreases again to values lower compared to a flat runout, leading to the formation of a backflow (Wilson et al. 2018) or a hydraulic jump (García 1993). Sedimentation in the shadow of the obstacle is reduced with increasing obstacle size (Alexander and Morris 1994). Obstacles would increase the average flow deceleration in their wake (Abhari et al. 2018), but their influence on flow propagation seem to be localised and the flow would rapidly readjust (Farizan et al. 2019).

These analogue experiments however have limits in their comparison with PDCs as demonstrated by Burgisser et al. (2005), who showed that these experiments, despite their importance in the understanding of PDC dynamics, are limited in their scaling to PDCs. Aqueous gravity currents display strong differences to PDCs regarding their density contrasts, their temperature, their turbulence generation, the viscosity of the fluid phase and the density and grainsize of their particles. These parameters affect flow processes such as the coupling of particles (affecting the transport and sedimentation mechanisms of the solid phase) or the flow compressibility (influencing on the pressure and velocity changes) when encountering an obstacle, decreasing the accuracy of the comparison.

2.5. Summary

PDCs are complex, turbulent, multiphase flows with the ability to move across obstacles with relative ease, leading to unpredictable paths. Research on their interactions with topography is still at its beginnings and the current understanding emphasises the complexity of these interactions.

Field observations and deposit analyses provide useful insights into these interactions. A consistent asymmetry in the deposit thickness and structure has been shown between thick, massive deposits on the stoss side showing velocity decrease and strong sedimentation rates, and thin, layered deposits on the lee side. In some cases, a relative preservation of the flora was observed, showing lower dynamic pressures. The similarities between PDCs and turbidity currents allow an analogy to

be drawn between these two types of flows and their dynamics when encountering a topographic barrier, highlighting the possible formation of strong acceleration/deceleration processes, hydraulic jumps and backflows. However, the limitations of this analogy raise the importance of a correct scaling to visualise PDC interactions with topography. Hence, experimental models are necessary, but to date, no experimental device has been able to reconstruct a kinetically scaled gas-particle flow interacting with topographic obstacles with direct internal observations.

As variations in flow dynamics are closely related to topography, this research aims to fill the gap in the current knowledge by investigating how the transport and sedimentation processes of PDCs change when encountering topographic barriers of various sizes. This will be achieved by conducting a series of complex large-scale experiments with variable obstacle size.

3. Methodology

This chapter describes the methods used to conduct this research, from the general setup to the design of obstacles and data analysis.

3.1. PELE setup

3.1.1. Introduction to the structure

The Pyroclastic flow Eruption Large-scale Experiment (PELE) is an experimental facility located at Massey University, Palmerston North, New-Zealand. Located inside a former boiler house, it was designed to replicate a wide range of flow conditions in a controlled environment, using a mixture of pyroclastic material as solid phase and air as the fluid phase (Lube et al. 2015). PELE was designed to focus on Pyroclastic Density Currents (PDCs) dynamics and their deposition processes, combining variations in discharge heights, basal roughness, temperature, initial mixture, basal slope, as well as the presence or not of topographic obstacles. A wide range of flows can be reproduced, from dilute, small-volume PDCs to dense flows containing up to 4 tons of pyroclastic material. Flow velocities range from 2 to 30 $m.s^{-1}$ depending on the discharge rate, and flow heights were recorded from 0.75 to 4 m (Lube et al. 2015).

PELE includes four main structures (Fig. 3.1):

- A 13 m high tower that supports two hoppers from which the mixture is dropped. Hopper A has a filling volume of 0.7 m^3 and contains up to nine metallic bars controlling the discharge rate. It is mostly used for dilute and intermediate pyroclastic surges. Hopper B has a filling volume of up to 4.2 m^3 with the ability to drop up to 6 tons of pyroclastic mixture at a discharge rate of several hundreds of cubic meters per second. This allows to reproduce fast moving, high concentrations flows. Both hoppers contain a heating system to remove residual moisture and are fully insulated. A lifting system allows variations of heights from 1.2 to 11 m. During the experiment, the hopper doors instantly open with an electric trigger signal.

- The shrouding is a heat-proof cloth tied to the tower and to the channel which channelizes the dropped mixture into the channel. During the drop, the mixture accelerates, mixes with ambient air and expands.
- The channel is 14.2 m long, 0.5 m wide. Made of steel, it is constrained by steel walls on one side and glass walls on the other side. Walls are 1.8 m high in the most proximal parts of the channel (0 to 6.35 m after impact), 1.2 m high from 6.35 to 10.3 m and 0.6 m high afterwards. The slope of the channel is 6° up to 11.7 m after the impact zone, where it then becomes horizontal.
- The unconfined runout directly follows the end of the channel. In this most distal part of the setup, the flow propagates outside, on a flat concrete, ground, unconfined, for another c. 15 meters before being blocked by a cliff. The total length of the flow is then approximately 30 meters.

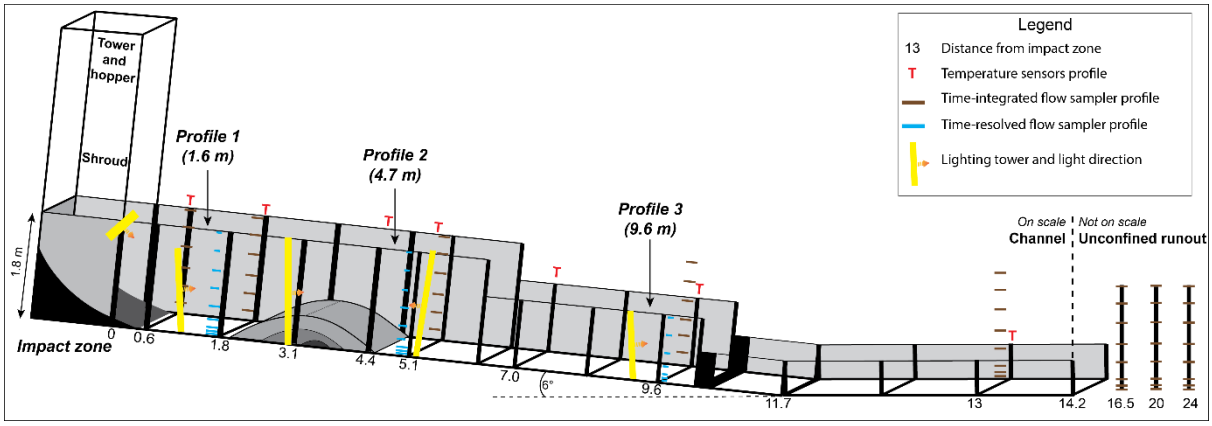

Figure 3.1: Sketch of the PELE setup for all three experiments, showing the position of obstacles in the channel as well as the main control profiles with velocity and density measurements.

Two greenhouse-like structures are built on the window side of the channel to allow observations inside the flows. The first large greenhouse was built between the impact zone (Fig. 3.1) and 6.35 m, where the glass walls are the highest and where the generated flows are most dynamic during propagation. The second small greenhouse is located between 7.8 m and 10.3, where flow propagation transitions to medial-distal reaches.

3.1.2. Obstacle design and positioning

For the purpose of this research, three obstacles were added inside the channel (Fig. 3.1). Obstacles were designed based on real-world ridges found around Mount Saint Helens (USA), Tongariro (New Zealand), Bandai (Japan) and Merapi (Indonesia) using satellite imagery and medium resolution Digital Elevation Models. The average ratio R of the obstacle heights over the flow heights, and the average aspect ratio A_R of the obstacle heights over obstacle lengths were calculated with R = 0.24 and A_R = 0.2. Assuming an experimental flow height of 2 m, the obstacle was scaled for a height of 0.5 m and a length of 2.5 m, with an initial slope angle of 21°.

The demi-shape of the obstacle was then estimated using:

$$H = H_{crest} - \left[\frac{H_{crest}}{\left(\frac{L_{max}}{2}\right)^2}\right] * L^2 \qquad \text{(Eq. 3.1)}$$

with H the height of the obstacle at a distance L from the crest, H_{crest} the height of the obstacle at the crest and L_{max} the total length of the obstacle.

Following the previous works in PELE (e.g. Brosch et al. 2021), the height of the velocity maximum was estimated at c. 0.3 m above the base. In order to span the most possible obstacle sizes encountered during the propagation of a PDC, it was inferred that obstacles could be smaller, larger or of a similar height than the height of the velocity maximum (H_{Umax}). Hence, as the first obstacle was already larger than the H_{Umax}, it was then downscaled, keeping the same aspect ratio and shape but reducing the absolute values of height and lengths. An intermediate and a small obstacle were then designed with H_{crest} = 0.3 and 0.1 m respectively, giving lengths L_{max} of 1.5 and 0.5 m (Fig. 3.2).

Figure 3.2: Photograph of the three obstacles. The smallest one is 10 cm high and 50 cm long, the intermediate one is 30 cm high and 1.5 m long while the largest one is 50 cm high and 2.5 meters long.

In order to characterize the flow before it reaches the obstacles, and to visualize the effects on the obstacle lee sides (i.e. after the crest), the positioning into the channel of each obstacle was carefully thought through and measured. The crests of the large and intermediate obstacles were positioned at 3.3 m after impact, a distance that would allow the flow to fully develop and be well characterized before climbing the stoss slope (i.e before the crest), especially for the largest hill. However, since the small obstacle would allow a good visualisation of both stoss and lee side processes in one single view due to its smaller size, it was decided to shift its crest by 25 cm downstream. This small variation would not change the overall flow dynamic upon reaching the object and would help provide a better characterization of stoss side processes.

3.1.3. Refinement of the setup to focus on flow behaviour along obstacles

Previous works focused on the transport and deposition processes of dense and dilute PDCs in PELE (Lube et al. 2015; Breard et al. 2016; Breard and Lube 2017; Breard et al. 2018; Lube et al. 2019; Brosch and Lube 2020; Brosch et al. 2021; Brosch et al. 2022). In the latest works, PELE was sub-divided in three profiles (proximal, medial and distal) which gave time-resolved information at a static observer location using high-speed, high resolution cameras at 500 fps, thermal sensors with a resolution of 0.1 second as well as time-resolved samplers. Other time-integrated samplers and bulk deposit samplings were used in several locations along the runout, which will be further developed later in this chapter.

For this third phase of large-scale experiments, changes in the setup were necessary in order to focus on the flow transport and deposition processes (1) along the entire length of obstacles and (2) after the obstacle. In order to achieve the goals without downgrading in the quality of measurements, some compromises had to be made to obtain the most qualitative results as the experiments could not be repeated.

Because of the use of high-resolution, high-speed cameras at several profiles along the channelized inclined section of PELE, the necessity of good lighting is crucial for the good quality of the recordings. For that purpose, towers of LED lights were built by stacking up to five flood lights together (references LED Falcon Pro 480W; LDFL650-300W ; Optilum LED 30000 ASYM 4K FLFL300). Each of these LED towers

project up to 170,000 lumens at a colour temperature of 4000 to 5000K. However, to achieve a good exposition of the flows, these towers need to be very close to the windows, obstructing approximately 40 cm of view. Therefore, their number and positions were crucial for the good development of the experiments: too many would obstruct a large field of view and would only allow vertical profiles by hiding most of the obstacles, but too few would result in dark exposition and low-quality results.

A first profile at 1.6 m after impact inside the inclined channel is established as Profile 1 and is used to characterize flow velocity, density, temperature and structure before hitting the stoss slope of the obstacles. A high-speed camera films the flow passage at 1000 fps and is topped by a Gopro™ camera recording at 240 fps. Sets of time-resolved and time-integrated samplers and high-resolution thermal sensors (70 Hz) were also deployed at that position. A similar profile at 4.7 m after impact was established in order to compare the changes in the flow characteristics after the flow has crossed the obstacles. This profile was named Profile 2.

Between these two profiles sit the size-variant obstacles, which added complexity into defining their exact positioning inside the channel. Ideally, the entirety of the obstacle would have been captured, but because of the presence of the LED towers and the limited length of the main observation window (only 1.15 m wide), it was decided to focus mostly on the lee-side of the obstacles. With this objective in mind, the crests were positioned at 3.3 m after impact (i.e. 10 cm after the start of the window, which is enough to limit shadow effects on the crest), allowing the intermediate obstacle to end within this window (4.05 m after impact), and the large obstacle to end close to Profile 2 (4.55 m after impact). Note that for the small obstacle, the crest was shifted by 25 cm in order to capture the stoss side of the obstacle in the same camera view. Three high-speed cameras recording at 1000 fps were stacked and allowed the capture of the entire window length. The first camera records from the base up to 1.15 m, the second camera records from 1.1 m up to 1.35 m, and finally, the third camera records from 1.3 m up to 1.55 m above the channel base.

Finally, a fourth position at 9.6 m after impact (Profile 3) records the flow in medial parts of the channel in order to capture the long-term influence of the obstacles. This profile is similar to profiles 1 and 2, at the difference that the field of view does not go above 1.2 m above channel base.

3.1.4. Experimental preparation

The mixture used for the experiment consists of a very poorly sorted (σ = 3.22 Φ) pumice and ash mix with a low content of dense clasts (juvenile obsidian and banded rhyolites, foreign lithics) and particle size ranging between 2 μm and 16 mm (D_{50} = 422 μm or 1.244 Φ). It is sampled from rhyolitic proximal deposits of the 232 AD Taupō Ignimbrite, about 17 km from vent, within a layer that has been typically described as "Layer 2b" or Valley-Ponded Ignimbrite (Sparks 1976; Wilson 1985).

The mixture is directly sieved on the field in order to remove particles larger than 16 mm and potential organic matter. Interestingly, it contains a great quantity of fine ash <63 μm (26.5 wt%), but also a high percentage of lapilli clasts >2 mm (27.5 wt%). The high fines-content of the mixture and low density of particles allow a good coupling between the particles and the gas phase, necessary to keep the scaling of the experiments representative of real-world PDCs. A fines-poorer mixture (i.e. from pure surge deposits) or denser particles (i.e. basaltic or andesitic composition, or from block and ash flow deposits) would not allow a good coupling between the gas and the particles and would result in the generation of a granular debris flow, unless proper increases by c. one order of magnitude were made in the dimensions of the setup.

Figure 3.3 shows the grainsize distribution of the original mixture.

After sampling, the mixture is dried in an oven for several days at 100 °C in order to remove moisture. It is then carefully placed inside the small hopper to avoid particle segregation and prevent fines to escape. The heating elements inside the hopper are then set to 170°C during 24 hours in order to ensure the evaporation of all residual moisture, before being turned down to 120 °C which is the desired temperature for the experiments. The mixture sits in the hopper for an additional two to three days before the experiment.

For the experiments conducted in this research, a mass of 200 kg of the collected volcanic ash was used. This increase in mass compared to previous pure surge experiments (120 kg) would allow the generation of sustained intermediate flows with features of both surge and dense PDCs to explore a wide range of processes and

study the dynamics of both the turbulent suspension and the thick bedload when encountering the obstacle.

In order to create shear, as well as a realistic base roughness for natural PDCs, the base of the channel was covered in greywacke pebbles of an average size of 6 mm. These gravels were glued onto wooden plates up to 5 meters after the impact zone using epoxy resin, then loosely emplaced until the end of the confined channel. They were equally glued on the obstacles, as well as on sampling trays up to 13 m (see section 3.3.1). Assuming a 500 m thick flow in the real-world and with a 2.5 m thick flow in average in PELE, these gravels are scaled to measure approximately 1 m in diameter, which would correspond to a realistic roughness of bushes, small trees, and rocks found on and around volcanoes.

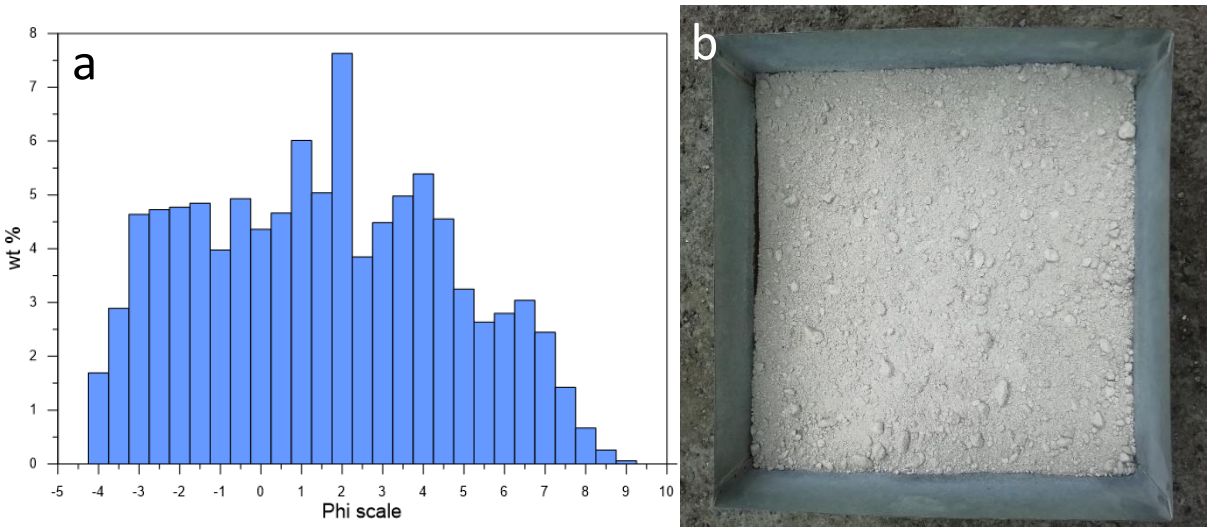

Figure 3.3: (a) Grainsize distribution of the initial mixture, (b) Photograph of the mixture in a tray after drying in the oven to remove moisture. Tray dimensions are 50 x 50 cm.

3.2. Scaling analysis inside PELE

Scaling experiments to real-world flows is essential to produce accurate results depicting natural phenomena. The kinematic and dynamic scaling is not only assured through the overlap of non-dimensional numbers of experimental and real-world flows, but importantly through the overlap of them relative to another. An important example

is the scaling of stress coupling between particle and fluid phases. This is characterized through the Reynolds (Re), Stokes (St) and Stability numbers (Σ_T). This third experimental series in PELE used a different mixture and mass than the previous ones. The reason behind these changes resides in the desired flow dynamics to reproduce flows with an intermediate regime comprising characteristics of both dense (Breard et al. 2016; Breard and Lube 2017; Breard et al. 2018) and surge flows (Brosch and Lube 2020; Brosch et al. 2021). This particularity makes the mixture extremely mobile during flow propagation, with fine particles coupling with the ambient fluid, and the coarse clasts forming thick, dense bedloads leading to deposition of coarse-rich dunes.

A new scaling analysis had to be done to ensure the good kinematic and dynamic scaling o the experimental flows with real-world PDCs. Table 3.1 compares non-dimensional numbers between this experimental series and the previous ones, as well as real world flows.

Scaling parameter	**Symbol**	**Unit**	**PELE intermediate regime with obstacles**	**PELE surges**	**PELE dense flows**	**Nature**
Particle diameter	D	mm	0.002 - 16			0.002 - 1000
Velocity	U	m/s	3 – 12	3 – 9	2 – 30	10 – 200
Density	ρ	kg/m^3	1 – 15	1 – 10		
Reynolds	Re	-	$10^5 – 10^7$	$10^4 – 10^6$	10^4 - 10^7	$10^6 – 10^9$
Richardson	Ri	-	0.5 – 4	0.01 – 10	10^{-3} - 45	0 – 10
Thermal Richardson	Ri_T	-	0.003 – 0.7	0.02 – 4.5		0 – 5
Densimetric Froude	Fr'	-	0.6 – 15	0.75 - 2	0.3 - 10	~1
Stokes	St	-	$10^{-3} – 10^1$	10^{-3} - 1	10^{-5} - 10^4	$10^{-3} – 10^7$
Stability Factor	Σ_T	-	$10^{-2} – 10^1$	$10^{-2} – 10^1$	10^{-7} - 10^5	$10^{-6} – 10^9$
Rouse	Pn	-	1.3 – 20	0.66 - 19		10^{-3} - 10^2
Kinetic Energy density	KE	J/m^3	$10^0 – 10^3$	10^{-2} - 10^2		10^3 - 10^4
Buoyant thermal energy density	TE_b	J/m^3	$10^{-1} – 10^2$	10^1 - 10^2		10^3 - 10^4

Table 3.1: Scaling table between this experimental series and the previous ones at PELE (Brosch and Lube 2020, Lube et al. 2015). Nature data are extracted from Burgisser et al. (2005) and Choux & Druitt (2002).

According to Table 3.1, the flows are dynamically and kinematically scaled with natural flows, regarding the transport method of particles with the fluid (Stokes, Stability Factor, Rouse), their stratification within the current (Richardson), the turbulence generation (Reynolds) or the internal velocity of the flows (Froude). These numbers allow us to be confident in the accuracy of the results by depicting real processes happening inside PDCs when crossing obstacles.

By comparing them to previous experimental series in PELE, the range of the non-dimensional numbers are very similar to pure surge experiments, with only a slight increase for density, Froude, Stokes and Rouse Numbers. This trend suggests that the flows behave as expected by increasing the mass: they generate a turbulent suspension close to a dilute surge, but also allow the generation of a thick, dense bedload at the base of the flow.

3.3. Data analysis

3.3.1. Experimental material

A large number of sensors, cameras and samplers were deployed for each of the three experiments in order to characterise flow internal dynamics as well as its sedimentation processes before, across, and after the obstacles. The following section explains in detail the purpose of each of these devices.

High-speed cameras

Six high-resolution, high-speed cameras recording at 1000 fps were used and are pictured in Figure 3.4b-d (Basler acA2000-340km, NAC HotShot 1280 and NAC Memrecam HX-7 ST-839). The cameras are positioned at four different locations, as explained in section 3.1.3. before, across, and after the obstacles in order to capture most of the processes occurring.

Gopro cameras

A network of 19 Gopro™ cameras (Fig. 3.4e) is deployed along the entire runout of the flow. They have varying purpose, from the recording of time-resolved flow samplers at 60 fps (see allocated paragraph below) to flow overviews (30-120 fps) and high-speed recordings (240 fps). The models used range from Gopro Hero3™ to Gopro Hero8™.

Sedimentation cameras

In order to record local processes of transport, erosion and sedimentation, three cameras were recording in Full HD at 50 fps. Their locations were selected to observe the stoss side of the obstacle, the lee side slope and the end of the hill, as well as a view at Profile 2. Additionally, a fourth camera recording at Full HD and 30 fps was located just after the impact zone to record the first 0.5 m of the flow. They allowed the mapping of time-resolved deposition (Fig. 3.5a).

Thermocouples

A new set of thermal sensors (TC Direct 410-345 Type K) was deployed to replace the old network. These new sensors were used at a high frequency sampling rate of 70 Hz instead of 10 Hz in previous experimental series. They were installed in five fixed profiles at 0.6 m, 1.8 m, 4.7 m, 9.6 m and 13 m. One additional profile shifted between each experiment and was located at the end of the small and intermediate obstacle (i.e. 3.8 and 4.1 m after impact zone respectively). For the large obstacle, since the Profile 2 corresponded to end of the hill, the moving thermocouple profile was set at 7 m from impact.

An additional sensor was added at 20 m after impact zone, at a height of 45 cm to measure the temperature inside the flow propagating outside in the unconfined runout section.

Thermal camera

For the outside unconfined runout between 15 and 30 m after impact, an Infratec VarioCAM thermal infrared camera was used to record flow temperature in distal areas at 50 fps (Fig. 3.4h).

Figure 3.4: Material used for the experiments. a) LED flood lights tower located right before the start of the main window with the obstacles. (b, c, d) high-resolution, high-speed cameras. (e) two models of Gopro™ cameras. (f) deposit tray for the unconfined outside runout. (g) deposit tray of the confined interior channel, covered in glued bed roughness gravels. (h) thermal infrared camera used to measure temperature in the unconfined runout. (i) time-resolved square tube samplers of different size and width. They are graduated per centimetre and their downstream end is closed by layers of very fine mesh as described in Brosch and Lube (2020). (j) time-integrated tube sampler for bulk flow mass and grainsize distribution.

Load cells

Four load cells are located on the hopper and measure the discharge of material during the experiment.

Time-integrated samplers

These samplers consist of glass tubes with a circular opening upstream (Fig. 3.4j). They are mounted on the steel wall and are used to characterise bulk flow grainsize and mass at defined profiles over the runout. Eight different profiles are used at 0.6 m, 1.8 m, 4.7 m, 9.6 m, 13 m, 16.5 m, 20 m and 24 m after the impact zone.

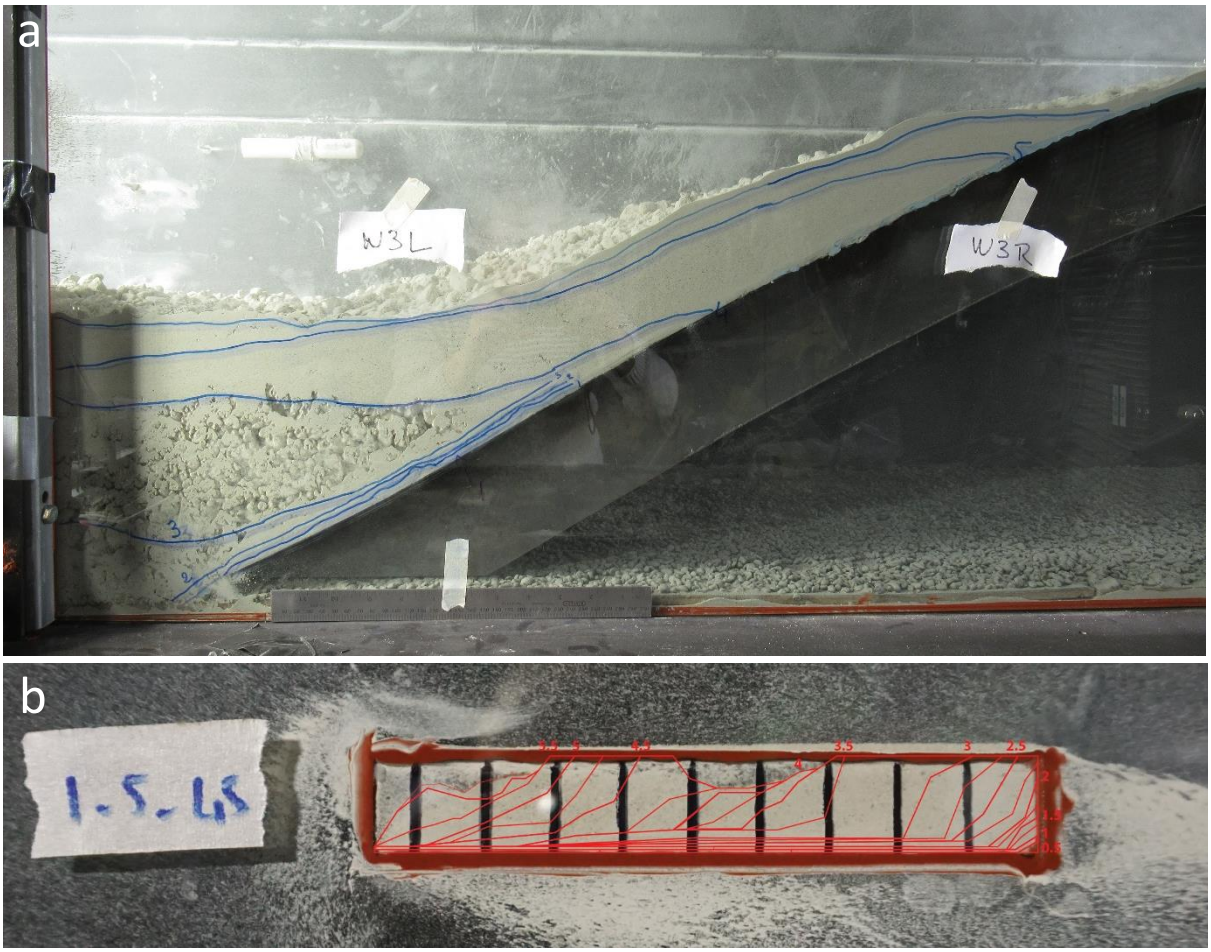

Figure 3.5: (a) Isochrones of deposition at 1 second interval on the stoss side of the large obstacle. T=0 corresponds here to flow arrival at Profile 1. The scale at the base is 30 cm long and the view spans from 1.95 m to 3 m after impact. (b) Filled time-resolved sampling tube at Profile 1, 45 cm above base for Experiment M. Isochrone intervals range between 0.25 and 0.5 second, and t=0 corresponds to flow arrival at the entrance of the sampler.

Time-resolved samplers

As described in Brosch and Lube (2020), these square tubes are glued directly on the glass wall using a heatproof silicon. They are graduated every centimetre, have an internal width of 1.4 or 2 cm and a length from 5 to 15 cm according to the expected mass (Fig. 3.4i). They are open towards the upstream, but different layers of fine mesh

in the downstream end only allows gas to escape while particles are trapped inside the tube. Cameras are recording their filling during the experiment at 60 fps and 2.7K resolution, which allows then to map isochrones of deposition inside (Fig. 3.5b). These isochrones are used to estimate the time-resolved transported mass and, in combination with the calculated internal flow velocities, estimate the spatio-temporal flow density. Each isochrone is carefully sampled and analysed for spatio-temporal grainsize distribution within the flow. Three of these profiles are used at Profiles 1 (1.6 m), 2 (4.7 m) and 3 (9.6 m).

Bulk deposit samples

In the proximal runout where the bed roughness is non erodible and where the obstacles sit, bulk deposit samples were taken using a 15 cm diameter core at the centre of the channel. From 5.5 m onward, 45x37 cm trays were emplaced every 1.5 m, then every 3 m in the unconfined runout. Up to 13 m after impact, greywacke gravels were glued directly onto the trays to allow a fast, efficient sampling after each experiment by washing the trays into a new container. Substrate gravels were loosely emplaced around the trays on the whole length of the confined channel. In the unconfined runout, the trays were simply deposited on the concrete ground without bed roughness and sampled immediately after the experiment.

Time-resolved deposit samples

Using the high-speed cameras as well as the sedimentations cameras, it was possible to map and then sample the isochrones of deposition at specific locations (Fig. 3.5a). These locations include Profile 1, the stoss side of the obstacles, and the zone immediately behind them. To do so, the isochrones are drawn directly on the windows; one person sits in the channel and carefully samples the layers, led by another person outside the channel.

3.3.2. Data acquisition

In the following section, the methods used in the laboratory to analyse the samples taken from the experiments are explained, as well as analytical methods to estimate

flow parameters such as velocities, particle concentration, density contrast, dynamic pressure. These methods are very similar to the ones already described in previous works in PELE (Lube et al. 2015; Brosch and Lube 2020; Brosch et al. 2021) and therefore will only be briefly developed here.

Laboratory methods

Deposit samples were wet sieved with a single 250 µm (2Φ) sieve to separate fine and coarse particles. After drying, the coarse section would be hand sieved in a dry column between 16 mm and 250 µm (-4Φ to 2Φ) with half-phi intervals, and each grainsize would be weighted. The fine section would be splitted in half until a representative sample of approximately 1 gram would be obtained. This sample would be introduced into a Horiba LV-750 Laser-Particle Analyser (LPA). The results from the LPA and the weights would then be combined to obtain to total grainsize distribution of each sample. After combining the total grainsize distribution for each sample, the results would be introduced into Gradistats (Blott and Pye 2001) to obtain statistical values such as their median, d_{90}, d_{10} and sorting using the method of Folk and Ward (1957).

The same method applies for time-integrated and time-resolved tube samples, with the difference that no wet sieving was done: samples were directly hand-sieved in a dry sieve column and separated between coarse and fine particles at 500 µm (1Φ).

Flow mapping

Using the array of cameras deployed for full flow overviews, flow heights and shapes were mapped in two different ways: (1) at static locations across time, using the three main study Profiles 1, 2 and 3 at a temporal resolution of 0.01-0.1 s, and (2) as snapshots of the entire flow at specific times at a spatial resolution of 5-10 cm. In that second case, chosen times were 0.35 s, 1.1 s, 3 s, 5.5 s, 9 s, 12 s and 20 s after impact.

Flow front mapping

The flow front positions were also mapped across time in order to estimate their velocity and associated regimes. The temporal resolution varies between 0.05 and 0.5 seconds.

Particle Image Velocimetry

The obtained high-speed camera videos are analysed with PIVlab (Thielicke and Stamhuis 2014), a Matlab-supported software using Particle Image Velocimetry (PIV) to calculate flow internal velocities. After analysis, the files for each time frame on the obstacle view were inserted into a Python code that would average the data in time and space using a Savitsky-Golay filter (Savitzky and Golay 1964) in order to extract flow parameters such as horizontal and vertical velocities, velocity magnitude, streamlines, vorticity, divergence, acceleration and turbulence fluctuations.

Calculations of particle concentrations, flow density and dynamic pressure

The mapping inside the square time-resolved samplers allowed the definitions of isochrones (typically between 0.1 and 2 seconds intervals depending on the distance and height of each tube) and the calculation of their volume. By interpolating this data at 50 ms interval with a one-way spline and combining with the flow velocity at the desired heights and times, it was possible to estimate the particle concentration within the flow across time with:

$$C = \frac{\varphi.\Delta V_{dt}}{U_{dt}.A.dt} \quad \text{(Eq. 3.2)}$$

with C the concentration is in volume percentage (vol%), φ the porosity of pumice, ΔV_{dt} the volume deposited inside the tube during the time interval dt (here 50 ms), U_{dt} the flow velocity at the tube height during the time interval, A the area of the tube opening.

From particle concentration, calculations of densities and dynamic pressures were produced with

$$\rho = C.\rho_p + (1 - C).\rho_f \quad \text{(Eq. 3.3)}$$

and

$$P_{dyn} = \frac{1}{2}.\rho.U^2 \quad \text{(Eq. 3.4)}$$

with ρ the flow density, ρ_p the density of the solid fraction, ρ_f the density of the ambient fluid, P_{dyn} the dynamic pressure, and U the flow velocity.

The results on each tube were then linearly interpolated at a 1 cm resolution over the entire profile height for each key location.

Time-resolved deposit and bedload mapping

Using the sedimentation cameras as well as the high-speed cameras when possible, the deposit and bedload thicknesses were mapped across time in order to estimate sedimentation rates and deposition processes at static locations (Profile 1, Stoss side, Crest, Lee side, right behind the obstacle and Profile 2). The temporal resolution varies between 0.02 and 0.2 s according to the locations.

Deposit thicknesses

Deposit thicknesses were hand-measured every 5 centimetres from 0 to 5 m after the impact zone. Precise hand-measuring was challenging further downstream because of millimetric or sub-millimetric thicknesses.

4. On the interaction of pyroclastic density currents with hill-shaped obstacles

Corna L., Lube G., Brosch E., Uhle D., Ardo J., and Jones J.

Abstract

Pyroclastic Density Currents (PDCs) are able to cross topographic obstacles, increasing uncertainty in volcanic hazard models. In large-scale experiments we reproduced the propagation of PDCs over hill-shaped obstacles, changing their size while keeping their shape and the experimental conditions unchanged. We measured the spatiotemporal variations in flow velocity, density, temperature and deposition across each obstacle to characterize the differences and similarities of flow dynamics in their vicinity.

Four phases of PDC-obstacle interaction were observed in all experiments: (1) compression and acceleration on the stoss side, followed by flow detachment and generation of a dilute wake behind the obstacle; (2) formation of a turbulent jet above the lee side separating a hot, dense, fast detached flow above a cold, dilute, slow wake; (3) increasing flow density leading to the deposition of a dune on the stoss side and the destabilization of the boundary layer separation above the lee side; (4) flow deceleration and rotation of the velocity field, leading to the disappearance of the wake.

Sedimentation is strongly affected by the obstacles, both on the stoss side, where blocking of the dense underflow occurs, and on the lee side, where the presence of the wake generates local facies in the deposits. Small obstacles do not seem to significantly decrease flow density and momentum. However, larger obstacles cause a strong blocking with a density decrease of c. 60 % and total momentum loss up to c. 72 %. The results suggest that dilute PDCs are fully blocked by obstacles c. 5.45 times higher than the thickness of their boundary layer.

4.1. Introduction

Pyroclastic density currents (PDCs) are hot and mobile multiphase flows of volcanic particles and gas produced during explosive volcanic eruptions (Druitt 1998; Lube et al. 2020). An intriguing characteristic of PDCs is their variable ability to surmount and propagate across significant topographic obstacles. This behavior can lead to PDCs taking unexpected flow paths and engulfing potentially densely populated or cultivated areas behind obstacles that may not have been previously considered in hazard planning. Examples of the real risk associated with such PDC behavior include the burial of the Roman city of Herculaneum in 79 CE, the lateral blasts of Mount St. Helens in 1980 (Moore and Rice 1984) and the 2012 PDC-forming eruption of Te Maari (New Zealand), where low-volume but mobile blast-like PDCs advanced over a series of five ridges to engulf the country's most frequented hiking track and a tourist hut before becoming blocked by a sixth ridge (Lube et al. 2014; Breard et al. 2015). During the lethal 26 October 2010 eruption of Gunung Merapi (Indonesia), PDCs, in their SSE peripheries, crossed a total of four high and steep-sided ridges and completely destroying the village of Kinahrejo. The villagers of the tourist domicile of Kali Urang only narrowly escaped the same fate when the PDCs became locally blocked by a fifth ridge (Cronin et al. 2013; Komorowski et al. 2013). Understanding how PDCs interact with topographic obstacles is thus an important prerequisite to inform hazard modelling approaches and risk mitigation strategies.

Several field studies have addressed this problem through analyses of the characteristics of PDC deposits emplaced across topographic obstacles (e.g. Wilson 1985; Fisher 1990; Dade and Huppert 1996; Bursik et al. 1998; Burgisser 2005; Sulpizio eta l. 2008; Cas et al. 2011; Brand et al. 2016), or through the study of PDC damage to vegetation in mountainous terrain (Kelfoun et al. 2000; Gardner et al. 2018; Guinn et al. 2022). These studies reported strong variation in sedimentary facies and thickness of deposits across obstacles. For instance, in proximal deposits of large ignimbrites, often massive, poorly sorted, and thick deposits on the obstacles' stoss side transition into thin, stratified or laminated deposits on the crest and alternating coarse-rich and fines-rich lenses of PDC deposit on the lee side (Wilson 1985; Sulpizio et al. 2008). These characteristics have been interpreted considering a dominantly

concentrated PDC behavior with the flow adhering and following topography (e.g. Druitt 1998; Branney and Kokelaar 2002). Through a reconnaissance mapping of the blast deposits and tree damage of the 1980 eruption of Mount St. Helens, Gardner et al. (2018) proposed a process of (dilute) PDCs jumping from the crest and re-attaching on the leeside of ridges. They modelled this process as a combination of ballistic flight and downward expansion due to entrainment of ambient air into the basal, 'jumping' flow.

Granular flow experiments revealed that these flows were following ballistic trajectories controlled by the relation between the flow thickness and the obstacle height (Hákonardóttir et al. 2003). Laboratory experiments of aqueous gravity currents that simulated the interaction of PDCs with obstacles reported the formation of hydraulic jumps, backflow on the lee side and upstream-migrating bores on the stoss side of obstacles (e.g Alexander and Morris 1994; Woods et al. 1998; Wilson et al. 2018). In Woods et al. 1998 and Oshaghi et al. (2013), the authors noted that subcritical flows would become supercritical upon crossing an obstacle, before potentially transitioning back to subcritical regime. Andrews and Manga (2011) introduced a large-scale experimental device to simulate the interaction of PDC analogues of hot talcum powder and air with wall-shaped barriers. They demonstrated that such barriers could induce the lift-off of a co-ignimbrite plumes and that dilute PDCs are able to surmount barriers up to 1.5 times their flow thickness.

This study aims to interrogate large-scale PDC experiments of hot volcanic particles and gas to understand better what type of flow processes occur when PDCs flow across and become partially blocked by hill-shaped topographic obstacles; and, if and how these processes modify the PDC flow structure.

4.2. Methods

4.2.1. PELE set-up and scaling

The Pyroclastic flow Eruption Large-scale Experiment (PELE, Fig. 4.1) is an experimental facility to synthesize and study the transport and depositional mechanisms of PDCs at conditions that are dynamically and kinematically scaled to natural PDCs (Lube et al. 2015). The experimental flows constitute multiphase flows of natural, heated pyroclastic material and air.

For the three experiments described here, we used 200 kg of ash-rich material from the CE 232 Taupō ignimbrite that we collected *c.* 17 km northeast of the inferred vent (Wilson 1985). This very poorly sorted mixture (Supplementary material 4.1) is polymodal, contains particle sizes from 2 mm to 16 mm (9 to -4 Φ), a median particle diameter of 422.1 mm (1.2 Φ) and a sorting coefficient of 9.327 mm (3.2 Φ). It contains *c.* 26.5 wt.% fine ash (particle diameter <63 mm) and c. 27.5 wt.% of lapilli clasts (> 2 mm). After field collection, the material was dried in an oven at 100ºC for one week.

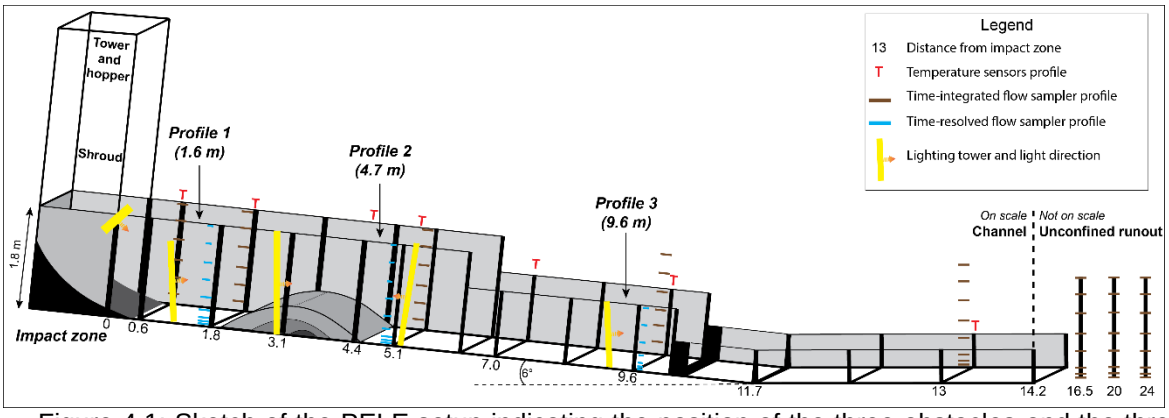

Figure 4.1: Sketch of the PELE setup indicating the position of the three obstacles and the three main profiles labelled 1 to 3.

The pre-dried mixture was transferred into a 0.7 m^3 hopper of the PELE facility, which was suspended 7 m high above an instrumented flow channel and from which the experiment is started. Using a heating system located directly inside the hopper, the mixture was heated at 120°C for three days to remove residual moisture. The hopper trap doors are opened with an electric trigger signal that also provides synchronisation for sensors and cameras to record the flow. The mixture falls and expands by ingesting air in a vertical column enclosed by a heatproof cloth. Upon

impact, it encounters a curved slope leading to a horizontal channel where it is laterally blasted. This channel is 14.2 m long from the impact zone, up to 1.8 m high and is made of steel on one side and heatproof glass windows on the other side, allowing visualisation of the internal dynamics of the flow as it develops. After 14.2 m, the flow continues its propagation across a 16 m-long unconfined runout zone (Fig. 4.1).

More than 200 sensors, samplers and cameras were deployed to characterise each experiment. Two-dimensional velocity fields were measured through the hydraulically-smooth glass walls using an array of 6 high-resolution, high-speed cameras recording at 1000 frames per seconds (fps), and the Particle Image Velocimetry (PIV) software PIVlab (Thielicke and Stamhuis 2014). Measurements of time-integrated flow mass and grain-size distribution were obtained from sediment samplers that were placed on the steel side of the channel as eight vertical profiles (Fig. 4.1). On the glass-wall, vertical profiles of transparent sediment samplers were installed at 3 different profiles (Fig. 4.1). These samplers were open to the upstream side and included a mesh on the downstream side, which is permeable for air but not for particles. Measurements of flow velocity were combined with data of flow sediment filling inside these transparent samplers to compute flow density following the method of Brosch and Lube (2020). The evolving flow shape was recorded with additional cameras (at 30 to 120 fps). The time-variant deposition of the experimental PDCs across flow obstacles were recorded with cameras at 50 fps. Flow temperature was measured in vertical profiles via fast thermocouples sampling at 70 Hz.

To quantify the scaling similarity of natural PDCs and our experimental analogues, characteristic fluid mechanic and thermodynamic non-dimensional numbers are listed in Table 4.1. This table demonstrates the partial overlap in scaling parameters and good scaling experimental PDCs with real-world flows.

Scaling parameters	*Symbol*	*Unit*	*PELE experiment with obstacles*	*Nature*
Particle size	δ	mm	0.002 - 16	0.002 - 1000
Velocity	U	m/s	3 - 12	10 - 200
Density	ρ	kg/m^3	1 - 15	
Reynolds	Re	-	10^5 - 10^7	10^6-10^9
Richardson	Ri	-	0.5 - 4	0 - 10
Thermal Ri	Ri_T	-	0.003 - 0.7	0 - 5
Densimetric Froude	Fr'	-	0.6 - 15	~ 1
Stokes	S_T	-	10^{-3} - 10^1	10^{-3} - 10^7
Stability	Σ_T	-	10^{-2} - 10^1	10^{-6} - 10^9
Rouse	Pn	-	1 - 20	10^{-3} - 10^2

Table 4.1: Table of non-dimensional numbers between the experiments of this study and real-world data extracted from Burgisser et al. (2005) and Choux and Druitt (2002)

4.2.2. Obstacle design, scaling and position

Natural hills and ridges in PDC pathways come in a range of shapes and sizes. Due to the complexity of the large-scale experiments and associated data analysis, a series of three experiments for the situation of partial flow blocking of PDCs by hill-shaped obstacles was designed. In these experiments, the shape of the hill-shaped model was kept constant, while the hill size was varied (Fig. 4.2).

Using medium-resolution Digital-Elevation models of Mount Saint Helens (USA), Tongariro (New-Zealand), Bandai (Japan) and Merapi (Indonesia) volcanoes, the shapes of prominent ridges were analysed. This showed that, on average, the hill or ridge shape is well represented by a demi-shape geometrically defined as

$$H = H_{crest} - \left[\frac{H_{crest}}{\left(\frac{L_{max}}{2}\right)^2}\right] * L^2 \qquad \text{(Eq. 4.1)}$$

with H the height of the obstacle at a distance L from the crest, H_{crest} the height of the obstacle at the crest and L_{max} the total length of the obstacle. The average aspect ratio H_{crest}/L_{max} of the hills is 0.2, and the slope angle is averaged to 21°.

Three hill models of different sizes were built with H_{crest} of 0.1 m, 0.3 m and 0.5 m (associated with lengths L_{max} of 0.5, 1.5 and 2.5 m, respectively). These heights were selected relative to the average height of the velocity maximum (H_{Umax}) of the

experimental PDCs of c. 0.3 m (Fig. 4.2). The crest of the large and intermediate sized hill-shaped obstacles were positioned into the instrumented flow channel at a distance of 3.3 m from the impact zone. Due to lighting requirements for high-speed recording, the position of the crest of the small-sized hill model was positioned slightly downstream (by 0.25 m) from this position.

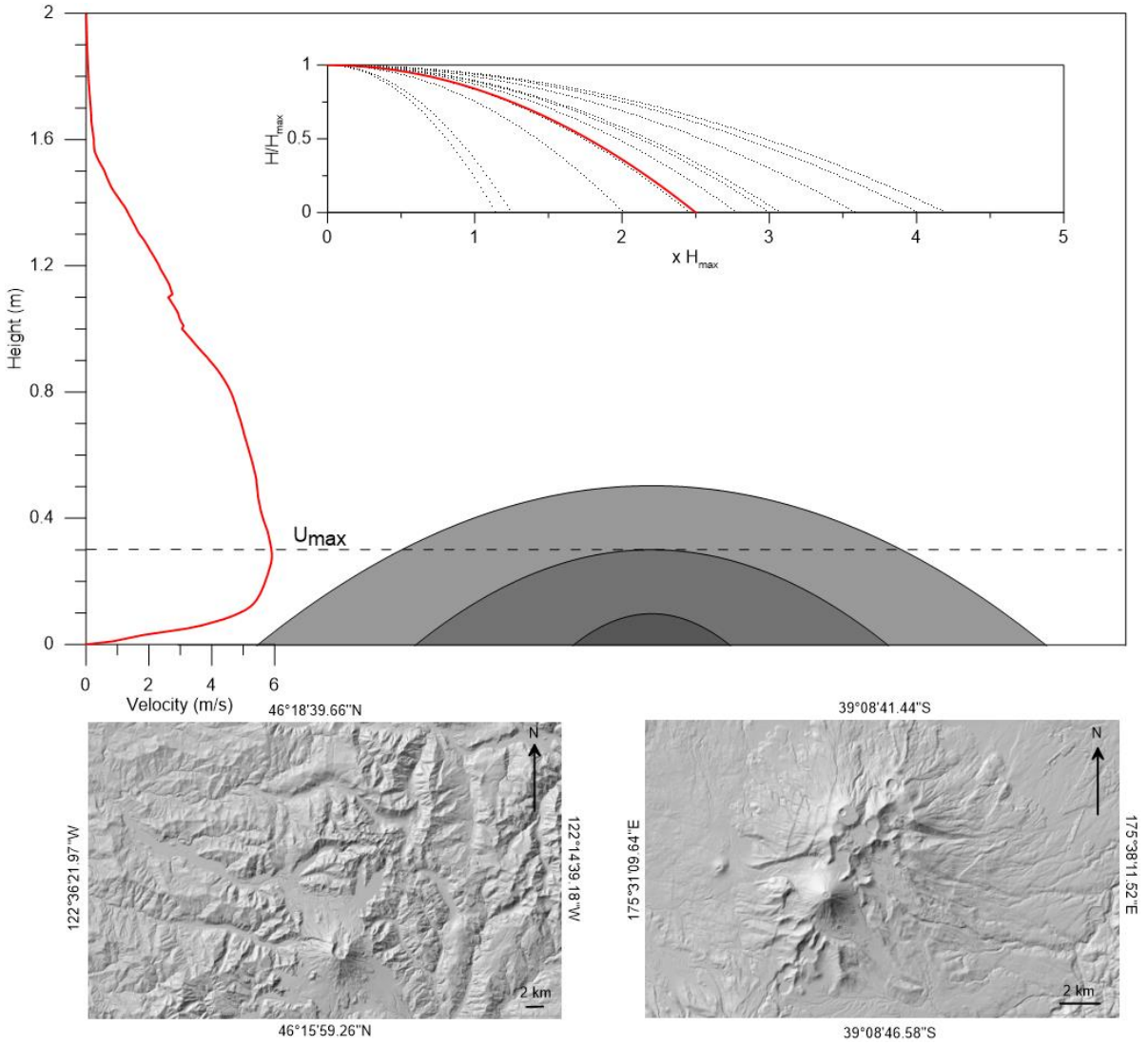

Figure 4.2: Comparison between the heights and shapes of the three different obstacles and the typical time-average velocity profile in a PELE experiment. Obstacles are scaled to be lower, higher or similar height than the height of the maximum velocity (H_{Umax}). In the inset, the natural obstacles are plotted using Eq. 4.1 in dotted curves and scaled to the same height. The red curve shows the average value used in the experiments. Digital Elevation Models of Mount Saint Helens and Tongariro, showing the rough topography around the volcanoes, are shown. The black bars in the bottom right corners represent 2 kilometres, and the arrow points north.

To compare the vertical velocity, density and flow grain-size structure of the experimental PDCs before and after the obstacle, one vertical sensor profile was installed before the obstacle at a runout distance of 1.6 m, which we call the *Profile 1*,

and another one behind the obstacle at 4.7 m, which we refer to as the *Profile 2* (Fig. 4.1). For simplification in this article, experiments are named experiments S, M and L (referring to Small, Medium and Large obstacles).

4.3. Results

4.3.1. General flow characteristics

Figure 4.3a-c shows photographs of the flows crossing the large and intermediate obstacles and propagating in the unconfined outside runout, with a structure of a head and a body overridden by a dilute ash cloud.

At Profile 1, the gravity current structure is fully developed, and is characterized by, from bottom to top, an aggrading deposit, a dense, up to c. 0.1 m-thick, granular-fluid underflow (Fig. 4.3d), and a c. 1.5–2.1 m-thick, fully turbulent dilute upper part. The time- and height-averaged flow density has a value of *c.* 6.5 kg m^{-3} corresponding to a density ratio with the ambient air of around five. The time- and height-integrated density of the dilute part of the experimental PDCs account to c. 3.5 kg m^{-3} corresponding to a density ratio of around three.

As the flow progresses downstream, it reaches the stoss slope of the obstacle, where it compresses and accelerates. The flow then detaches from the hill-shaped obstacles after the crest and decelerates, leading to the formation of a turbulent wake immediately behind the obstacle (Fig 4.3b). In the following, we refer to this local structure as the ‘wake’ to avoid confusion with the gravity current wake region atop the body.

Profile 2, which is situated three metres downstream of the Profile 1, captures both the turbulent wake and the remaining gravity current above. In comparison to Profile 1, the time- and depth-integrated flow density is strongly reduced, by c. 20% for experiment S, and by c. 60% for experiments M and L.

The flow propagates further downstream up to 30 m from the impact zone, where it decelerates and eventually becomes buoyant and lifts off.

The flow duration lasts approximately 20 seconds, and most of the deposition occurs in the first seconds after flow arrival, but the deposition of the phoenix cloud can take several minutes.

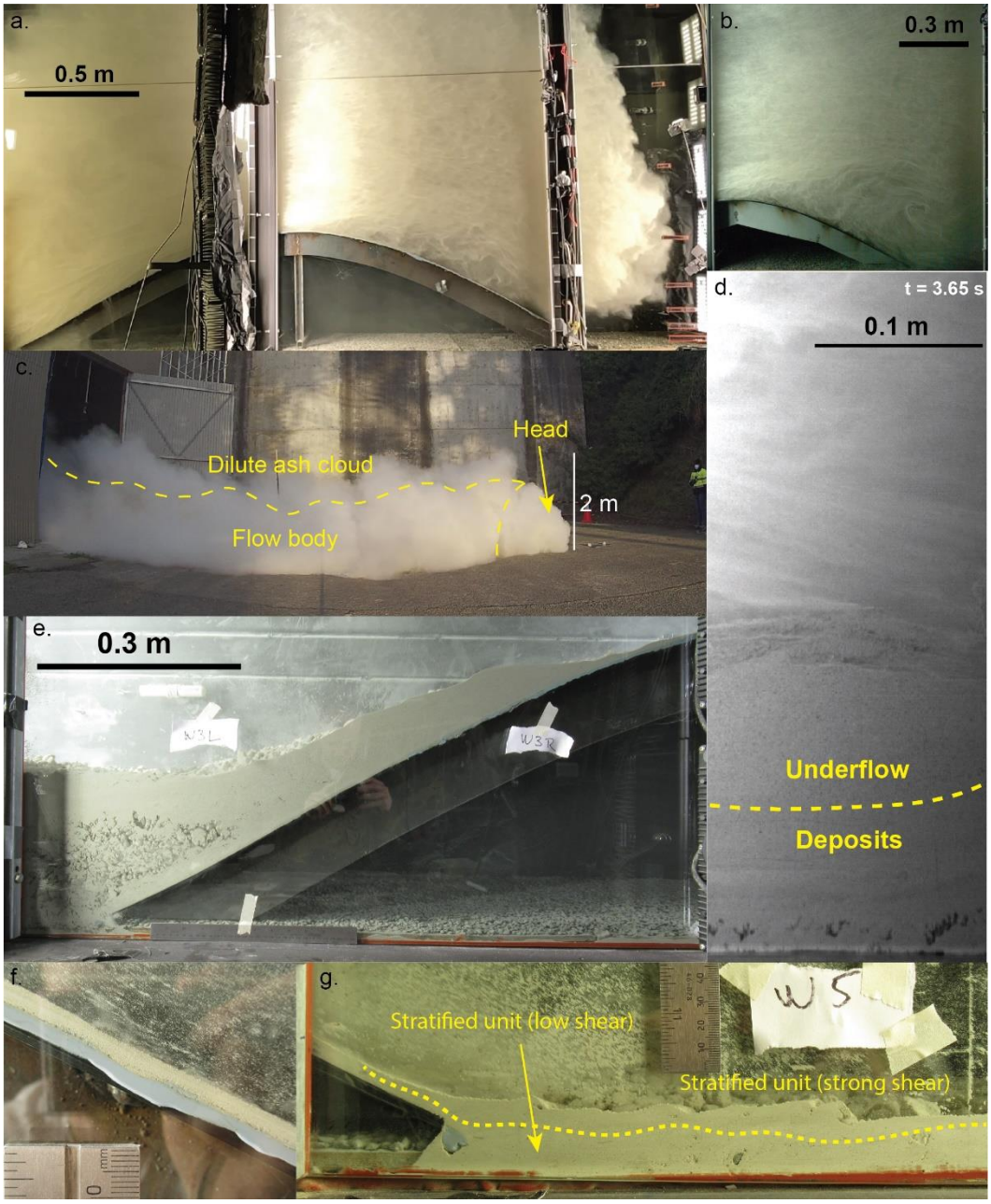

Figure 4.3: Panel showing pictures of the flow and deposits. (a) Flow head crossing the large obstacle. (b) Large rotating vortex in the wake behind the intermediate obstacle. (c) Flow from Experiment S in the outside unconfined section showing a typical structure of a head and a body overridden by a dilute ash cloud. (d) Snapshot at Profile 1 of thick dense underflow emplacing massive, poorly-sorting beds. A dashed yellow line separates the static deposits from the shifting sand wave. The time is taken after flow arrival at the profile. (e) Deposits on the stoss side of the large obstacle showing strong blocking. (f) Thin, thinly stratified or laminated beds on the lee side of the large obstacle showing intense erosion and redeposition. (g) Stratified deposits immediately behind the large obstacle showing thicker deposits than the lee slope, A yellow dashed line separates deposits emplaced with a strong vertical component (low shear) from the deposits emplaced purely from traction (strong shear).

4.3.2. The PDC flow structure before and behind the obstacle

The vertical flow structure was characterized with regards to the height- and time-variant flow velocities, densities and temperatures at Profiles 1 and 2.

Vertical profiles of the time-averaged flow density are depicted for the three experiments in Figure 4.4e, g and i. Due to the same starting conditions, the three experiments show similar time-averaged vertical density profiles, which characterise the strong density stratification of the bi-partite PDC.

Figure 4.4a also depicts the streamwise structure of the gravity currents, which is comprised of a leading gravity current head and a gravity current body region. Turbulent eddies shedding from the head vortex feed an ash cloud above the body. Due to vigorous entrainment of ambient air, the head is more dilute than the trailing body (graph of depth-averaged flow density in Fig. 4.4a). Behind the head, sedimentation leads to the development of a dense bedload region, which grows in thickness over time, and, from c. 3 seconds after flow arrival, transitions into a dense, granular-fluid underflow (Fig.4.3d).

The vertical velocity structure is characterised by strong shear of the dilute, turbulent flow with the lower flow boundary (or slow moving underflow) and weaker free shear with the ambient air above (Fig. 4.4d). The height of the velocity maximum at c. 0.3 m, separates the lower wall-region from an upper jet-region. Time-averaged profiles of the vertical velocity structure for the three experiments are shown in Figure 4.4f, h and j.

In Profile 2, density has strongly decreased due to the blocking of the dense underflow in front of the obstacles, and by an increase in the thickness of the gravity current. The disturbance of the vertical density stratification by the obstacles becomes more enhanced with increasing hill size (Fig. 4.4e, g and i). This can be attributed to two processes. First, for the small hill, a significant proportion of the relatively immobile bedload migrates relatively unhindered over the obstacle. With increasing hill size, however, an increasingly larger proportion of the bedload becomes blocked on the stoss side of the hill. Except for the ‘missing’ underflow, the time-averaged vertical density profile before and after the small hill are largely similar (Fig. 4.4e). Second, the turbulent wake behind the obstacle is increasing in size with increasing hill size.

Because the wake is characterised by lower density stratification, or even lower densities than the detached flow above in the early flow stages, there is stronger reduction of density in the wall and lower jet regions with increasing obstacle size (Fig. 4.4g and i). In addition, for the intermediate and large hill, a region in the upper jet and gravity current wake regions (<1.1 m above the base) becomes more concentrated after the hill. This occurs because of a strong acceleration of the lower proportion of the gravity current that impinges onto the stoss side of the hill. The result of this local flow acceleration is a redistribution of relatively coarse-grained material from the concentrated lower part of the flow into upper flow regions.

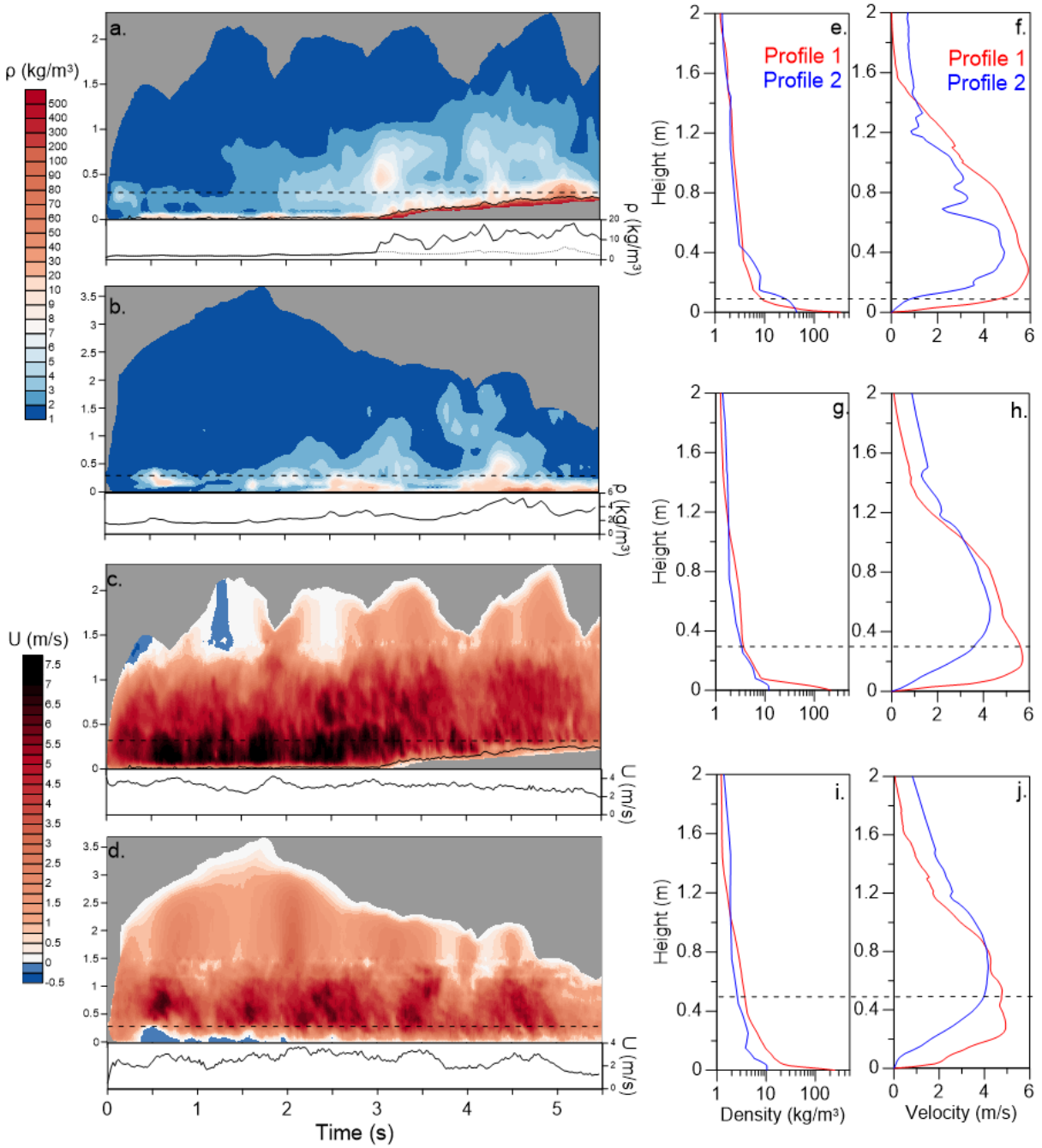

Figure 4.4: Density and velocity of the experimental flows. Time-resolved density plot for (a) Profile 1 and (b) Profile 2 of Experiment M in kg/m3. The grey area at the base shows the building of deposits and the solid line refers to the height of the bedload. The dashed line shows the height of the obstacle. Depth-averaged time series are shown below each plot. (c) Time resolved downstream velocity (U) plot for Profile 1 and (d) Profile 2 for Experiment M. Note the negative velocities in the wake marked with blue colours indicating backflow. Depth-averaged time series are shown below each plot. (e-j) Time-integrated density and velocity profiles for experiments S, M and L at Profiles 1 and 2. The dashed lines refer to the height of the obstacle for each experiment.

The following changes occur to the vertical velocity structure of the gravity current:

- In the turbulent wake behind the hill, low and negative values of downstream component (U) of the velocity fields develop (Fig. 4.4d).

- This leads to a change in the form of the vertical velocity structure. At Profile 1, the vertical velocity profile is characterized by logarithmic, high-shear profiles in the wall region. At Profile 2, the velocity profile has changed to a with a characteristic low basal shear with an inflection point from where a stronger shear region in the upper wall region occurs (Fig. 4.4f, h, and j). Both the inflection point and position of the velocity maximum move significantly upwards with increasing hill size.
- Furthermore, at a height of approximately 0.1-0.5 m above the crest of the obstacle, the flow velocity is characterized by strong and regular oscillations at a period of around one second. While this oscillating pattern also occurs before the obstacles and has been attributed to the occurrence of large-scale coherent turbulence structures (Brosch et al., 2021), it is markedly pronounced immediately behind it.

The densimetric Froude number Fr', which is the ratio of inertial and gravitational forces is given by:

$$Fr' = \frac{U_c}{\sqrt{\frac{\Delta\rho}{\rho_c} g.h.\cos\theta}}. \qquad \text{(Eq. 4.2)}$$

with U_C the flow velocity, Δρ the difference between flow and atmosphere, ρ_c the flow density, g the acceleration of gravity, h the flow thickness and θ the channel slope angle. Fr' was calculated for both Profiles 1 and 2 for the three experiments. At Profile 1, the time average Fr' varies between c. 0.9 and 1, which makes the flows subcritical. After the obstacles, as the flow thickness strongly increases, Fr' takes values between c. 0.7 and 0.8, making the flow more subcritical behind the hills. In Experiment L, Fr' keeps decreasing until distances of up to c. 10 m from the impact zone.

Looking in more details, Figure 4.5 shows a time series of Fr' for Experiment M at both locations. Initially, the head values are strongly supercritical with values of Fr' greater than 2. Fr' decreases steadily at Profile 1, which could be caused by the increasing flow density, followed by the decreasing velocity towards the end of the flow. In comparison, in Profile 2, Fr' is initially high but strongly decreases in the head, before staying relatively constant for the entire propagation. This pattern is supporting the fact that obstacles may be a locally important factor strongly reducing the importance of inertial forces in comparison with buoyancy.

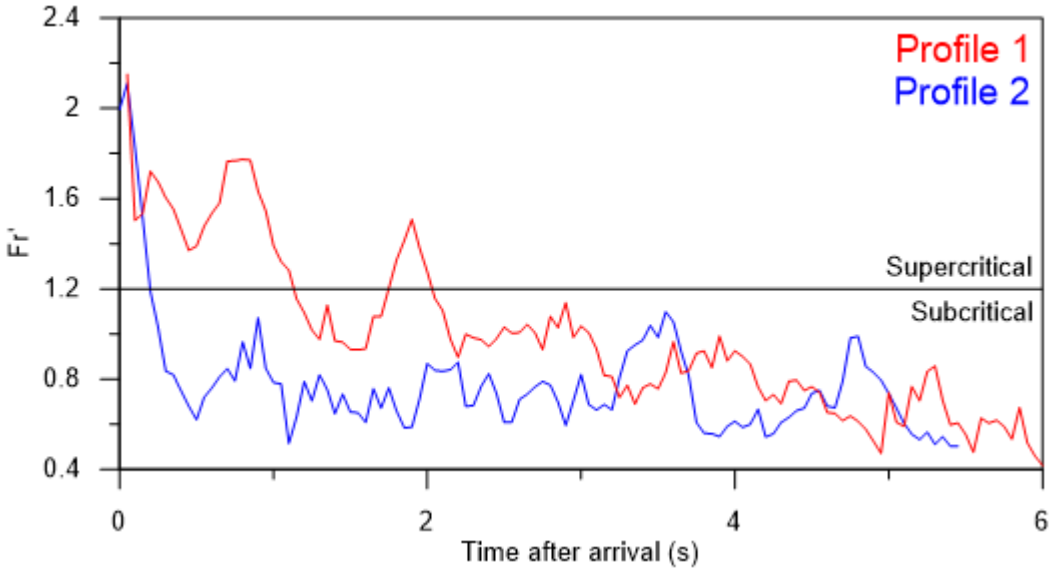

Figure 4.5: Time series of the Densimetric Froude number Fr' for Experiment M at Profiles 1 and 2. The black line at Fr' = 1.2 corresponds to the delimitation between supercritical and subcritical regimes.

The perturbation of the vertical flow structure by the obstacles can also be seen in a comparison of the data of the vertical temperature profiles of Profiles 1 and 2 (Fig. 4.6). This is because of the partial thermal coupling of the volcanic particles with the gas phase and because the majority of the flow's thermal mass is carried by the solid phase:

- Before the obstacle, temperature strongly increases downwards, except for the dilute head and frontal body regions where density is low.
- Behind the obstacle, the lower flow portion occupied by the turbulent wake, is markedly colder than the flow above, due its generally lower density (or low concentration of hot particles).
- This cold wake region only warms slowly due to the progressive sedimentation of hot particles from the gravity current above into the wake.

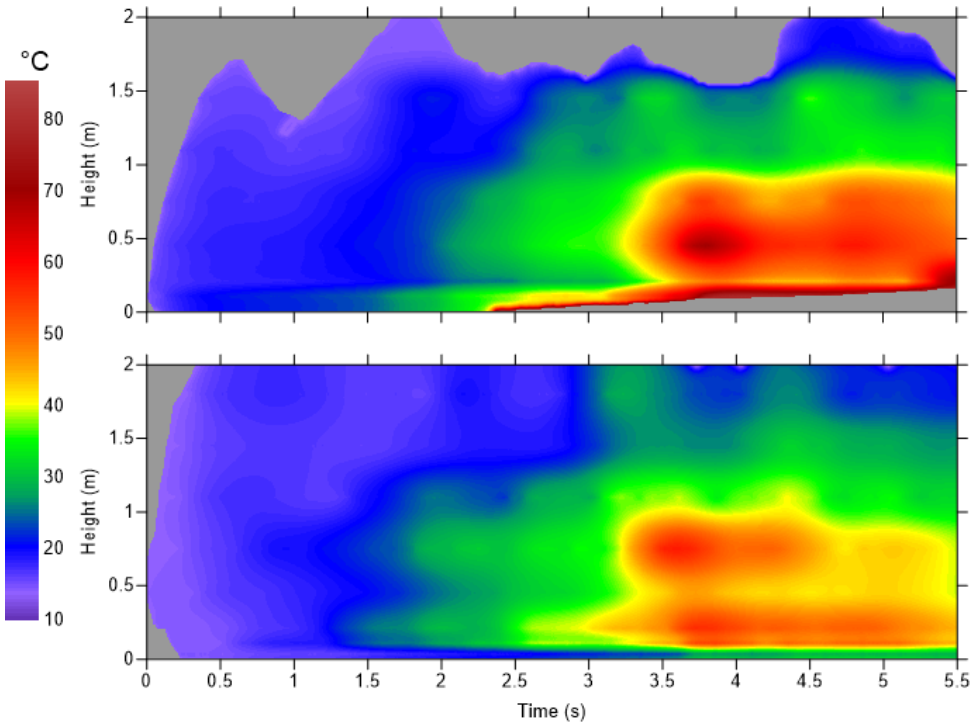

Figure 4.6: Time-resolved temperature plots for the experiment L at (a) Profile 1 and (b) 2. The temperature at the base of the flow after the hill is significantly colder than the flow above during the entire flow propagation.

4.3.3. Flow momentum before and behind the obstacle

The measurements of time-series of flow density and flow velocity in vertical profiles before and after the obstacles lend themselves to compute flow depth- and time-integrated flow momentum $\bar{M}$ as:

$$\bar{M} = \overline{\rho_C} V \overline{U_C} \ , \qquad \text{(Eq. 4.3)}$$

where ρ_c is flow density, V is flow volume, U_C is flow velocity, and overbars denote depth- and time-averages.

A comparison of flow momentum at Profiles 1 and 2 shows strong reductions by 48% for the Experiment S, 72% for Experiment M and 68% at for Experiment L. The main sinks for flow momentum are mass loss by deposition in-between the two control profiles, and pressure drag (also form drag) exerted by the hill onto the flow. Energy dissipation due to friction (also skin drag) exerted by the hill surface onto the overriding gravity current contributes only minor momentum losses.

The large mass of material blocked and accreted at the stoss side of the obstacles accounts for the largest proportion of the momentum loss. The momentum carried by

the dense underflow in the three experiments contributes to c. 47 ± 8% at Profile 1. In order to compare the momentum loss due to pressure drag exerted by the currents onto the (stoss side of the) hill-shaped obstacles, we compute the time- and depth-integrated momentum of only the dilute turbulent parts of the experimental PDCs at Profiles 1 and 2. The reduction in flow momentum of the dilute part of the currents accounts to *c.* 26% for Experiment S, *c.* 38% for Experiment M, and *c.* 46% for Experiment L, and is, thus, positively correlated with the effective dimensions of the obstacles. The data of depth- and time-integrated flow velocity, density and momentum is summarised in Table 4.2.

	Unit	Experiment S		Experiment M		Experiment L	
		Profile 1	Profile 2	Profile 1	Profile 2	Profile 1	Profile 2
Density	kg/m^3	6.32	5.19	6.68	2.63	6.55	2.57
Velocity U	m/s	3.35	2.37	3.16	2.56	2.91	2.51
Bulk momentum	$kg.m.s^{-1}$	59.57	31.15	70.56	19.46	58.56	19.01
Dilute momentum	$kg.m.s^{-1}$	42.14		31.2		35.21	

Table 4.2: Data of density, downslope velocity (U) and momentum at Profiles 1 and 2 for the three experiments. Bulk momentum refers to the momentum of the entire flow, underflow included, while dilute momentum refers to the momentum of the dilute upper part of the flow. At profile 2, no distinction is made because of the thin (<0.01 m) bedload.

4.3.4. PDC propagation over obstacles

In order to better understand the perturbation of the vertical flow structure and momentum losses due to interaction with hill-shaped obstacles better, we interrogated, and analysed high-speed videos of the experimental PDCs through Particle-Image-Velocimetry (PIV). These captured either the entire hill (for the small obstacle) or the lee side of the hills including their crests (for the intermediate and large obstacles). From the PIV data, downslope (U) and orthogonal (V) components of velocity, flow streamlines, as well fields of turbulent fluctuations and turbulent kinetic energy were computed. In the following, we describe and subdivide the processes of PDC-obstacle interaction in four characteristic but highly transient flow phases. These four phases, which are recognised in all three experiments, correspond approximately to the subsequent passages of the head, frontal body, distal body, and tail regions of the experimental PDCs.

Phase 1. During propagation of the gravity current head region across the obstacle, the relatively dilute incoming flow, with depth-averaged densities of *c.* 1.85–2.06 kg m^{-3}, is entirely non-depositional. At the base of the current, a <0.01 m-thick bedload layer of rolling and saltating particles is developed, but there is no dense underflow.

On the stoss side, and similar to normal fluids interacting with a cylinder of sphere, flow streamlines of the impacting lower part of the current strongly converge. This convergence is associated with a strong local acceleration (the static pressure decreases as dynamic pressure increases) that affects the flow up to approximately the height of the obstacle crest. As the head climbs the stoss side, particularly in the case of the intermediate and large obstacles, the basal part of the flow is advected upward and prevents the upper part of the current to cross immediately, leading it to a strong backward rotation.

Behind the hill crest, flow streamlines strongly diverge in the adverse pressure field. This leads to the separation of the turbulent flow boundary layer and detachment of the flow (Fig 4.7a-c). The detachment angle θ, characterized as the angle between the channel slope and point of detachment ($\theta = 90°$ corresponding to the crest), increases during Phase 1 to values up to c. 130°. Before re-attaching at a channel downslope distance from the crest D_R, the separated flow encloses an initially cold volume of ambient air. Strong shear of the basal separated flow with this volume leads to a first spot of turbulence developing on the upper lee side. Over time, and accompanied with sediment entering this dilute volume, this spot grows into a first large clock-wise rotating vortex that propagates downslope in the thus created turbulent wake (Fig. 4.7d). The wake is characterised and can be defined by slow and reversed flow (note negative downstream velocity components U in Figures 4.7d-f).

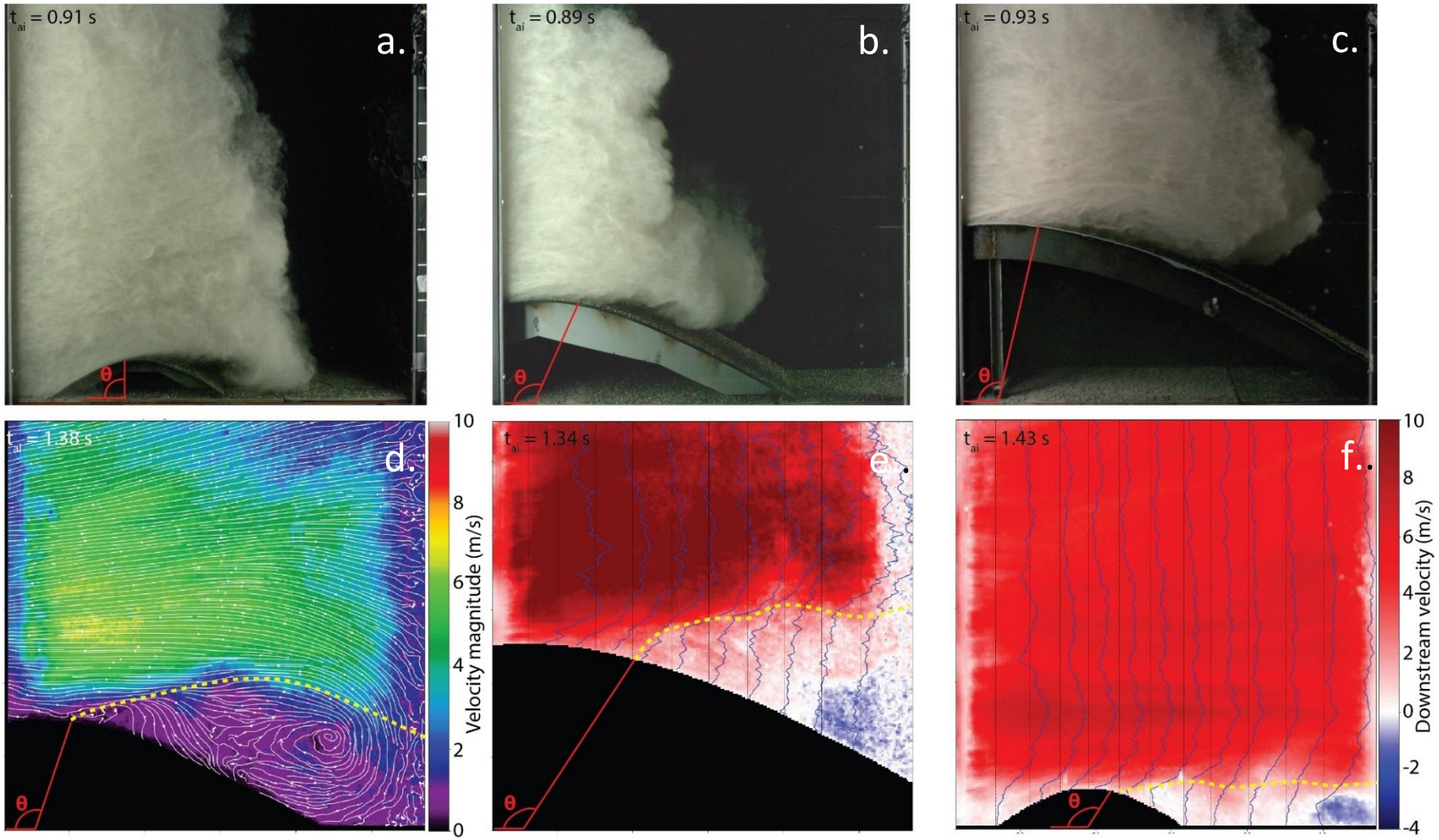

Figure 4.7: Panel showing typical pictures during the propagation of the head (Phase 1). (a-c) Snapshots of the flow jumping across the three obstacles; (d) Velocity magnitude and streamlines of the large rotating vortex created in the wake of Experiment M. The low-velocity wake is delimited by a yellow dashed line. (e) Downstream velocity component U at the large obstacle showing strong velocity in the upper flow and negative velocities in the lee side evidencing the backflow; (f) Downstream velocity in Experiment S showing the migration of the vortex downstream (evidenced by negative velocities).

Phase 2. The passage of the frontal body region is associated with an increase in flow density to *c.* 3.63 – 7.81 kg m^{-3} (Fig. 4.4). The thickness of the bedload layer is generally increasing up to a few centimetres and comprises stages of transport of rolling and saltation alternating with times of mobile, dense, granular sand-waves that start climbing the stoss side. Overall, the experimental PDCs remain mostly non-depositional, although thin stratified deposits are slowly emplaced on the stoss side of the hills.

On the stoss side, the converging and accelerating flow is associated with a strong compression of the denser basal gas-particle mixture flow. This compression is seen in the flare up and escaping upwards of gas bubbles and streaks of fine ash from the compressed flow region (Fig. 4.8a). The lowermost up to c. 0.03 m (for the small hill) and up to c. 0.2 m (for the large hill) region of converging and accelerating flow forms a distinct jet-like structure (Fig. 4.8b). This 'jet' forms the base of the detaching flow behind the crest towards the turbulent wake below and is clearly visible in plots of the downstream (U) and orthogonal (V) components of velocity and graphs of velocity magnitude (Figures 4.8b-e).

After detachment, velocities in the now progressively diverging jet are increasing with obstacle size and reach values of up to 10 m s^{-1} in experiment L. In the region of the detached flow above the jet, flow velocities take values of up to 16 m.s^{-1}. The presence of the relatively dense and fast-moving jet-like structure appears to shield the turbulent wake from particles sedimenting through it from the detached flow into the wake. However, over time the jet diverges and diffuses downstream, which is also accompanied by strong sediment from above loading it. The jet alternatively collapses and finger-like instabilities protrude vertically downwards into the wake (Fig. 4.8f). During the times of the jet diffusing or collapsing, strong sedimentation of ash-rich material into the wake occurs. The formation and collapse of the jet features occurs periodically. In experiment S, three jets were counted, which are associated with velocities of up to c. 5 m s^{-1}. In experiment M, five phases of jet formation and collapse show maximum jet velocities of up to c. 8 m s^{-1}; while for experiment L we counted only two prolonged jet phases with the largest velocities of c. 10 m s^{-1}. At least for the large obstacle, these velocity values are significantly higher than velocity maxima in the incoming flow and characterize local compressible dynamics of the flow.

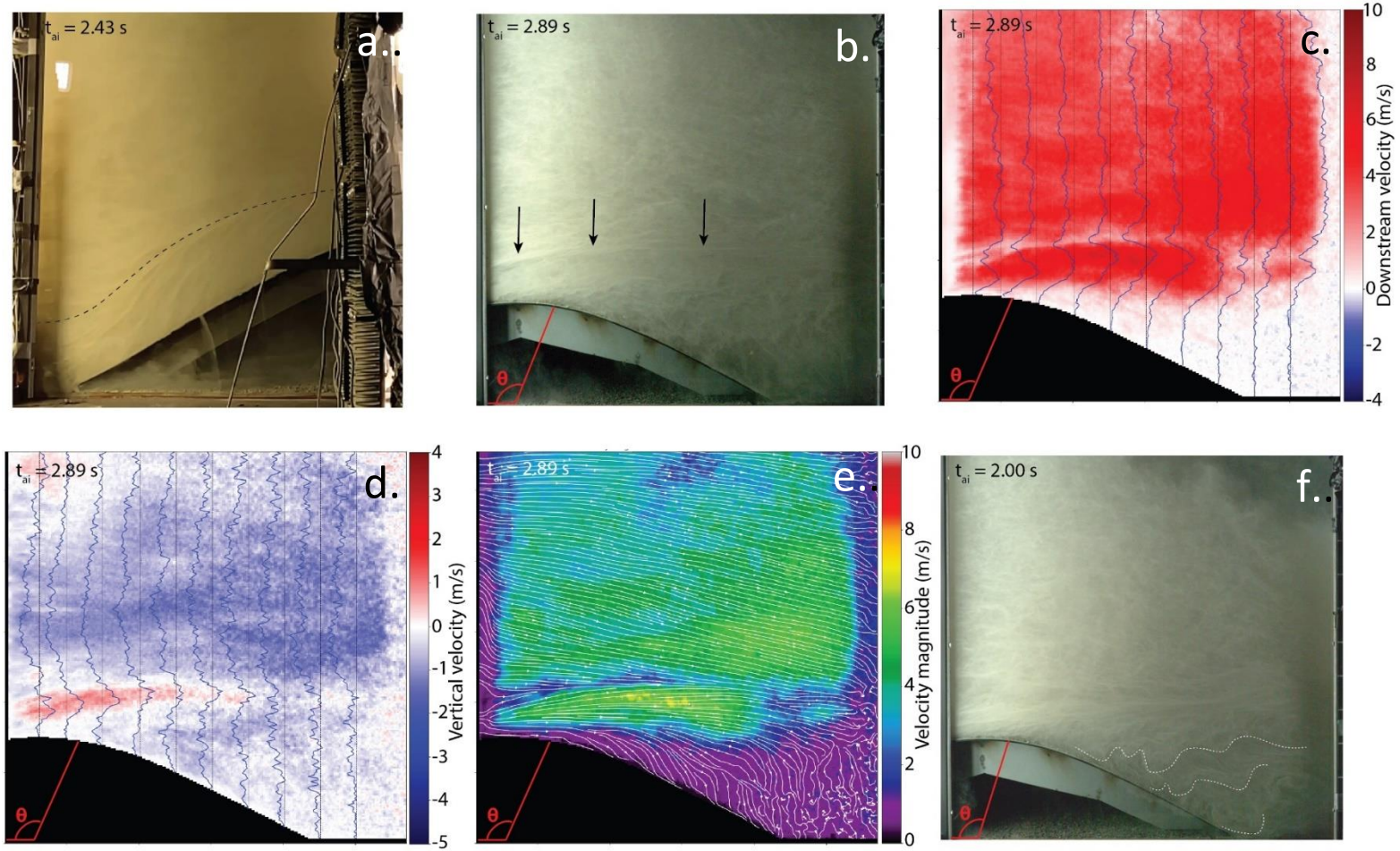

Figure 4.8: Panel showing typical pictures during the propagation of the early body (Phase 2). (a) Snapshot of vertical flares on the stoss side of the large obstacle showing the formation of gas-escape layer (bordered by dashed line) as the flow compresses and accelerates; (b-e) Respectively: snapshot, U component, V component and velocity magnitude with streamlines of a typical well-developed jet structure above the wake of the intermediate obstacle. Black arrows in (b) point at the top border of the jet structure. Note the divergence of the streamlines associated with the maximum velocity, the lower velocity in the upper boundary of the jet, and the slow, vertical settling of particles inside the dilute wake. (f) Snapshot of the intermediate obstacle showing finger instabilities (outlined in white dashed line) in the wake at a time when the jet structure is not well developed.

Phase 3. During approximately the second half of the passage of the gravity current body, the depth-integrated density markedly increases to values up to c. 20 kg m^{-3} (Fig. 4.4a).

On the stoss side, the underflow reaches its maximum thickness, and, from c. 3 seconds, rapidly deposits a thick wedge of sediment. The continuing convergence and acceleration of the flow markedly moves (or shoots up) dense flow material (including relatively coarse particles) from the lower wall region of the current and into upper wall and jet regions. Behind the crest, this loading of the detached flow with (coarse and heavy) particles leads to a bending downwards of the detached flow (Fig. 4.9a-c). During this time, rolling and saltating particles as well as thin sand waves start migrating as a poorly-defined bedload over the crest and down the lee slope. This is associated with a strong increase of the detachment angle and decrease of the re-attachment distance and thus a decrease of the cross-sectional area of the turbulent wake (Fig. 4.9a-c). Characteristic for Phase 3, jet-like structures do not form. Instead, the strong disruption of the vertical density and velocity structure is associate with strong sedimentation of particles into the increasingly hotter and denser turbulent wake (Fig. 4.9d).

Phase 4. From c. 5 seconds after flow arrival, the velocity and density of the incoming flow start to decline, marking the passage of the gravity current tail region. This burial of the stoss side slope continues from the previous phase and decreases its effective inclination as well as the effective hill height. As a consequence of the thick deposits, the wall region of the impinging gravity current markedly ceases to converge and accelerate along the increasingly flatter stoss side of the obstacle. At the same time, while the downslope component of the velocity fields decreases, the orthogonal component becomes more dominant. Together with the continuing sedimentation of particles from the upper flow onto the turbulent wake, this leads to a distinct rotation of the velocity streamlines in the detached flow from a previously (channel-) slope-parallel direction (that is c. 6° from the horizontal) to angles similar to the lee slope of the obstacle (Fig. 4.10a-b). This rotation of the flow field creates an increase of the angle of attack of the incoming flow onto the hill, and causes a strong increase of the detachment angle as well as decreases of the re-attachment distance and cross-sectional area of the turbulent wake (Fig. 4.10 and Fig. 4.11c-d). From c.

5.5 – 6 seconds, flow detachment ceases completely and the re-attached gravity current directly moves down the lee slope (Fig. 4.10c).

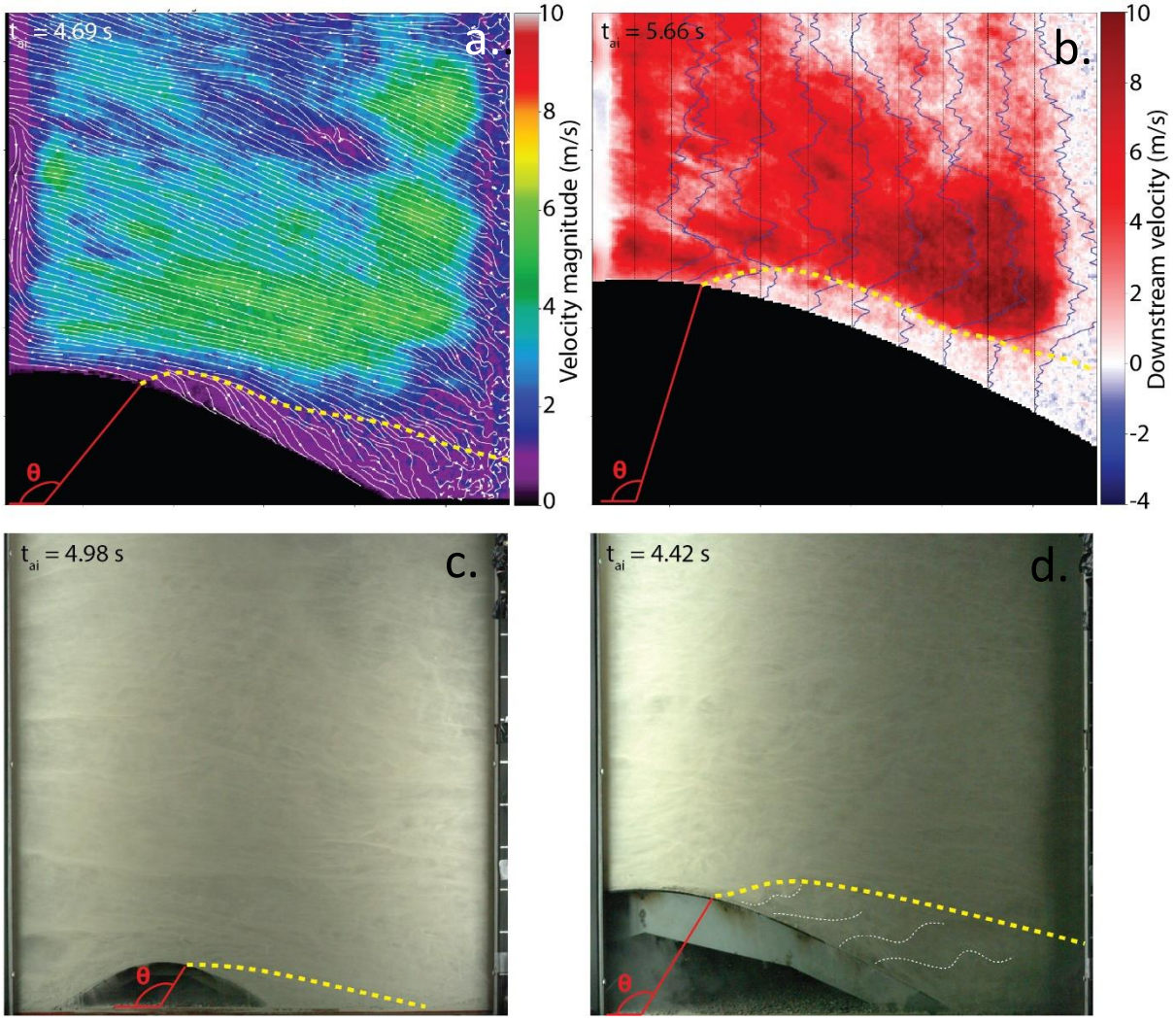

Figure 4.9: Panel showing typical pictures during the propagation of the late body (Phase 3). (a) Velocity magnitude with streamlines during Experiment M showing the intrusion of the upper flow into the wake as the jet structure has disappeared. The wake is delimited by a yellow dashed line. (b) U component on the large obstacle showing a thin wake above which a high-velocity detached flow propagates. (c) Snapshot of Experiment S showing a strongly reduced area of the wake. (d) Snapshot of Experiment M showing sedimentation pulses inside the wake outlined in dashed lines.

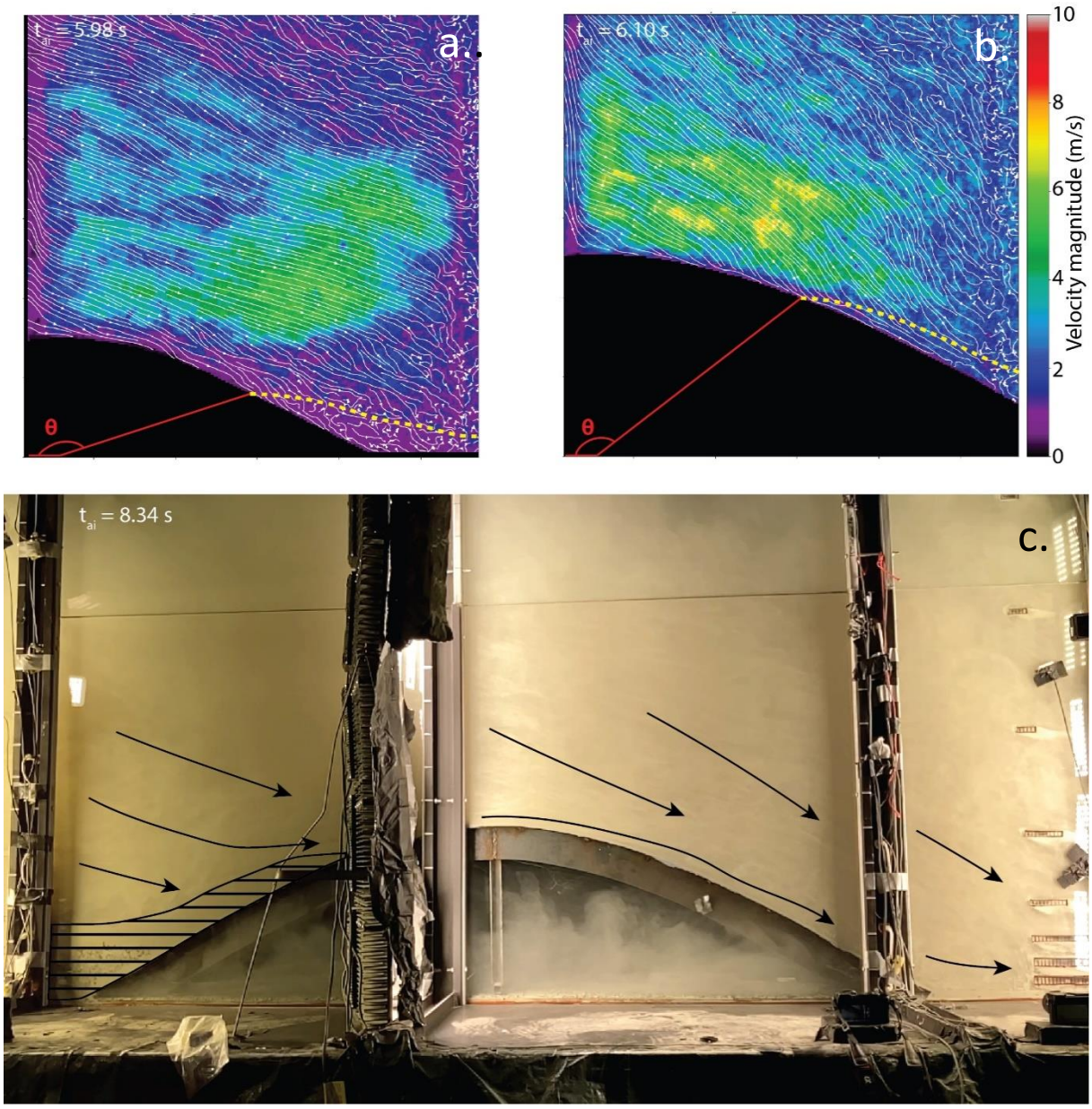

Figure 4.10: Panel showing typical picture of the propagation of the tail (Phase 4) with (a,b) the rotation of the velocity field showing streamlines becoming parallel (experiment M) of steeper (experiment L) than the lee side topography as the wake is about to disappear; and (c) overview snapshot of the large obstacle with stoss side deposits completely built (striated area), as the flows follow the topography without acceleration on the stoss side. The general flow direction is indicated as black arrows.

4.3.5. Geometric characteristics of the turbulent wake

Figure 4.11 characterises the temporal evolution of the turbulent wake that forms in all three experiments behind the hill crests. Time-series of the detachment angle θ, the re-attachment distance D_R and the cross-sectional area A_W of the wake are displayed (Fig. 4.11a). As expected for the highly unsteady high Reynolds number

gravity currents, θ, D_R and A_W show strong turbulent excursions too (Fig. 4.11b-d). Despite this turbulent variability, characteristic pattern of the temporal variations of these three geometric parameters occur in the four subsequent but highly transient flow phases:

- The passages of the dilute PDC heads in Phase 1 are characterized by initial strong increases in θ, D_R and A_W associated with the frontal and central head regions, and their subsequent strong decreases during passage of the rear of the head and frontal body regions (Fig. 4.11b-d).

- At slightly increasing flow density during Phase 2, θ, D_R and A_W alternatingly increase and decrease (Fig. 4.11b-d). These alternations approximately correspond to the formation and collapses of the high-velocity jet-like structures at the base of the detached flow. Markedly, for the intermediate hill, with a crest height similar to the height of the velocity maximum of the incoming flow, the smallest detachment angles were observed. Generally, during Phase 2, θ, D_R and A_W decrease over time.

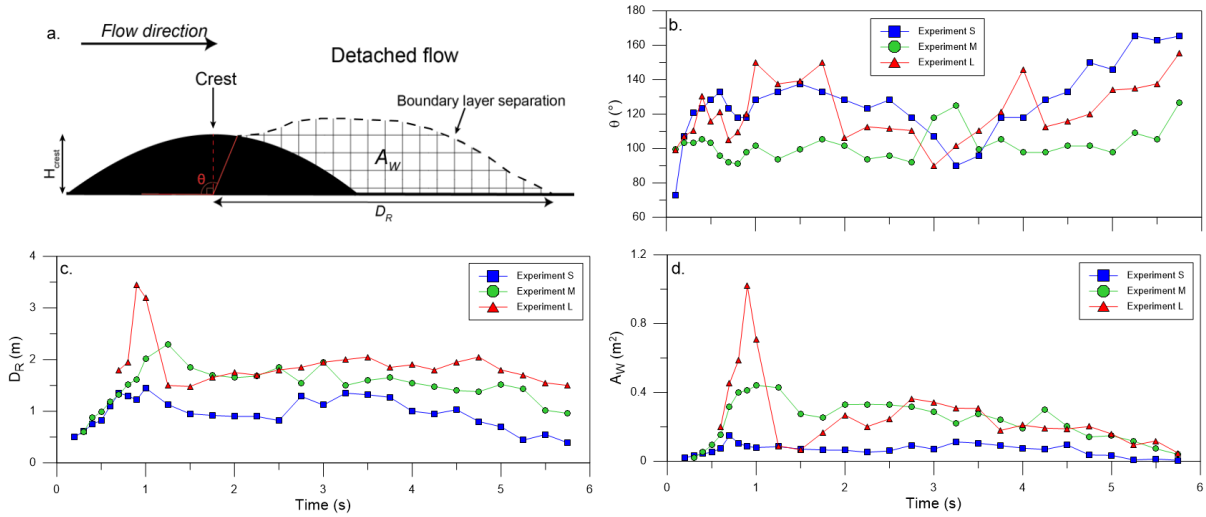

Figure 4.11: (a) Sketch defining the re-attachment distance DR, detachment angle θ and wake area AW. (b-d) Time-variant detachment angle, re-attachment distances and wake area for each experiment. Note the strong decrease in the re-attachment distance and wake area after approximately 5 seconds of propagation.

- With the formation of a dense underflow before the obstacles during Phase 3, the detachment angles increase again, but also show strong fluctuations particularly for experiment L (Fig. 4.11b). This is associated with the largest upward spreading of the detached flow. The re-attachment distance and consequently the wake area, however, remain relatively constant (Fig. 4.11c-d).

- The strong rotation of the flow field in the detached flow behind the crest during Phase 4 (Fig. 4.10) and passage of the significantly more dilute PDC tail region are associated with strong increases of θ, which reach its maximum values (Fig. 4.11b). This is associated with the marked increase of the angle of attack of the PDC immediately above the hilltop and above the lee slope as described above. This 'late' detachment also occurs at a distinctively downwards directed angle. Hence, the re-attachment distance and the wake area strongly decrease during Phase 4 (Fig. 4.11c-d).

4.3.6. Deposit characteristics across hill-shaped obstacles

Figure 4.3e-g shows the deposits across the large obstacle on the stoss side, the lee side and immediately after the hill. The partial blocking of the experimental PDCs on the stoss side and flow detachment on the lee side of the hills are signified by strong asymmetry and different facies of deposits on both sides of the obstacle, which are also depicted in Figures 4.12 and 4.13.

In all the experiment, the same type of deposits are emplaced, described as follows:

- Coarse pumice breccia. This unit extends up to the stoss slope of the obstacle and is strongly blocked (Fig. 4.12e). Its thickness can reach up to c. 0.15 m. It consists of a clast-supported, massive, coarse pumice layer with a lapilli content up to c. 50 wt% and a median grainsize of up to c. 2 mm (-0.95 Φ) rapidly emplaced through granular-fluid avalanche. The breccia can also be more matrix-supported as it transitions to the massive bed unit.
- Massive bed unit. This massive, poorly-sorted unit usually extends up to the stoss slope of the obstacle and is blocked before the crest (i.e. 3.3 m), excepted in the case of the Experiment S where it is emplaced to distances up to c. 6.5 m from the impact zone. This unit is usually divided in two to three beds with thicknesses up to c. 0.1 m (Fig 4.12b) emplaced during rapid sedimentation of thick granular-fluid avalanches forming shifting sand-waves (Brosch and Lube 2020). Faint variations are

visible locally in the deposit, with the presence of more lithic-rich beds and degassing pipes (Fig. 4.12b). The average median grainsize for this unit is c. 313 μm (1.68 Φ).

- Stratified bed unit. This unit extends from the source up to c. 14.5 m. It consists of thinly stratified and cross-stratified beds of coarse to very fine ash with an average median grainsize of 143 μm (2.81 Φ) and a thickness of up to 20 mm. It is usually emplaced on top of the massive bed unit from rolling and saltating bedload. It is also present at the base of the deposits on the stoss slope of the obstacle, draping the topography (Fig. 4.12b). Behind the hill, the base of this unit is less stratified and intercalated with coarse pumice clasts, becoming strongly poorly sorted.

- Lapilli cover unit. This unit extends up to c. 20.5 m from the impact zone and consists of individual pumice clasts (2-16 mm diameter), partially indenting the stratified unit, that have been rolling and saltating in the late stages of the flow. Locally, these clasts can show impact craters and rolling tracks upstream of them, as well as crescent micro-dunes on their sides surrounding a lower-deposition zone immediately downstream of them.

- Laminated unit. This unit is present on top of the sequence and covers the entire deposit footprint. It consists of a thin (< 2 mm) unit of laminated very fine ash with an average median grainsize of 39.5 μm (4.66 Φ). It covers the lapilli clasts underneath of a fine dusting that is emplaced from the phoenix cloud up to several minutes after the flow ends. In addition, behind the obstacles, a very thin (< 1 mm), laminated fine-ash unit is located at the base of the sequence.

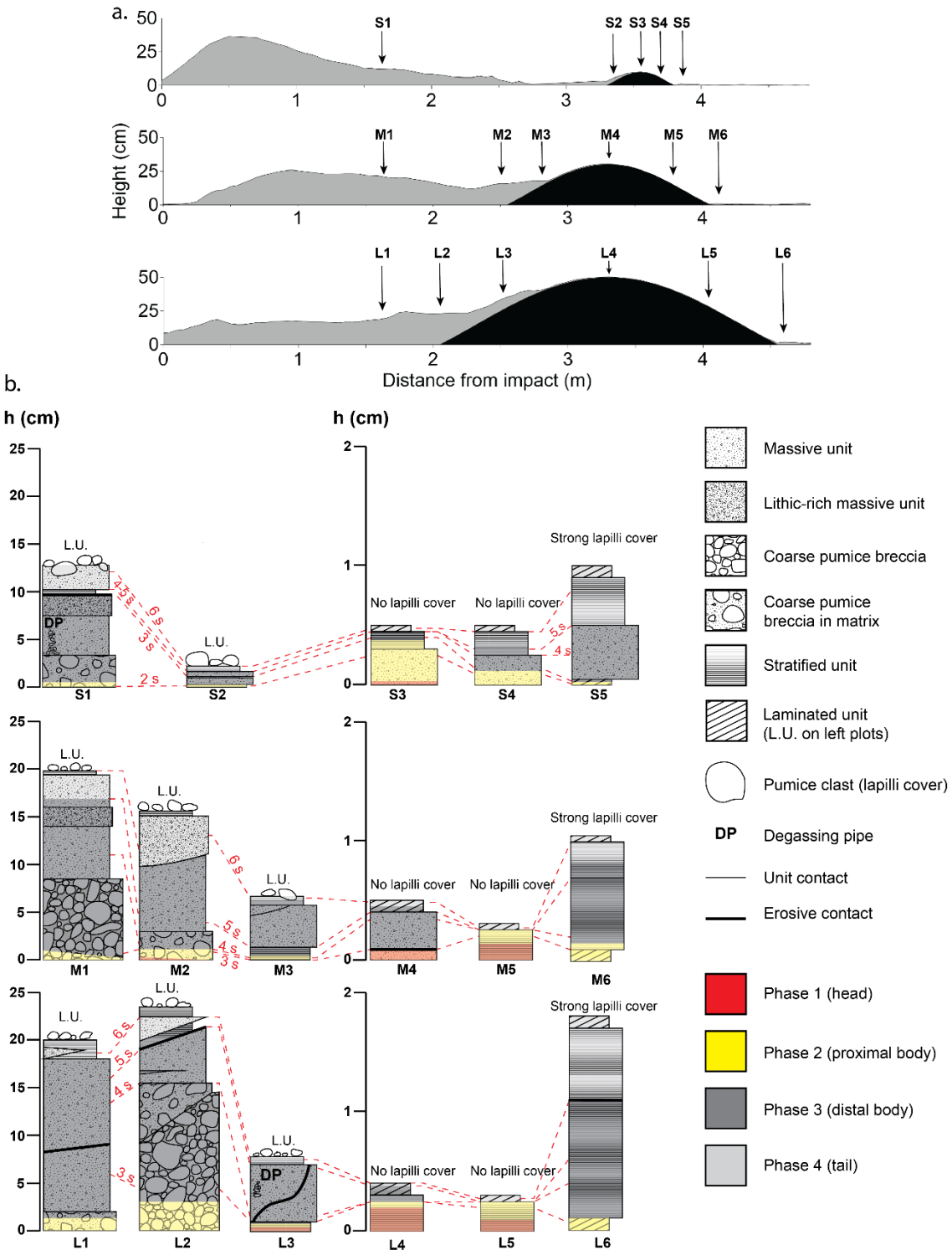

Figure 4.12: (a) Thickness of the deposits in the first 4.8 m of the channel. The initial dune becomes longer and flatter with increasing obstacle size. Labelled arrows point at the location where the stratigraphic logs are shown. (b) Stratigraphic logs for the three experiments located between Profile 1 and the end of the obstacle, showing different unit facies and features, isochrones of deposition, and deposition phases. At Profile 1 and immediately before the hill, the logs follow a typical sequence of roughly Coarse breccia – Massive Unit – Stratified unit – Lapilli cover – Laminated unit (not represented because too thin). On the stoss side of the hill, a stratified unit is also present at the base of the sequence. From the crest onward, deposits are significantly thinner. No lapilli cover is present on the crest and lee side. After the hill, lapilli clasts intrude the entire sequence.

The geometry of the deposits before the obstacles is worth noting, as the initial dune becomes flatter and longer with increasing obstacle size (Fig. 4.12a).

At Profile 1, despite a thinner section in Experiment S, the deposits are relatively similar regardless of the obstacle. The coarse pumice breccia is located at the base and is topped by the massive unit, followed by the stratified unit, the lapilli cover and finally, the laminated beds (Fig. 4.12b).

In all three experiments, the partial blocking is associated with a sudden increase of the deposit's median particle diameter immediately before the obstacle. This is associated with the blocking of the coarse-grained underflow. For experiment S, deposits on the stoss side are characterised by upstream migrating bedforms of massive beds which are separated by unit boundaries that are sub-parallel to the stoss side slope (Fig. 4.12b and 4.13a). For experiments M and L, blocking of the dense underflow is more complete. On the stoss side, alternating phases of bedload deposition and intense erosion emplace thin, stratified beds that drape the slope during Phases 1 and 2. In Phase 3, thick and dense shifting sand waves of the bedload region transform into coherent underflow that begins to encroach and aggrade onto the stoss side of the hill. This is followed by the rapid deposition of the massive unit partially with stoss-parallel beds (Fig. 4.12b and 4.13b-c). These beds are particularly visible in Experiment L where they were able to climb a significant part of the obstacle up to c. 0.4 m above the channel base. As shown on Figure 4.13, most of the deposition occurs in Phase 3, where the flow density is the highest (Fig. 4.4). This is followed by the formation of regressive dune bedforms in Phase 4 ponding the deposits before the obstacle, increasing their thickness (Fig. 4.13b-c). Then, a rolling and saltating tractional bedload emplaces the stratified unit at the top of the sequence (Fig. 4.12b and 4.13).

Towards the crest and along the lee slope, deposits are significantly thinner, finer-grained and thinly laminated (Fig. 4.12b), as a result of intense erosion and redeposition during the entire flow duration.

Immediately after the obstacles, deposits abruptly become thicker, more coarse-grained and more poorly sorted. This sudden change in grain-size distribution is associated three deposition processes occurring during the passage of the flow: (i) continuous sedimentation of markedly finer-grained ash through suspension-sedimentation in the wake; (ii) instability of the wake causing pulsing finger-like instabilities during Phases 2 and 3; and (iii) saltating and rolling pumice lapilli

transported as a (poorly-defined) bedload across the obstacle rolling down the slope and become stranded at the break in slope in Phases 3 and 4.

Finally, weak tractional deposition of fine ash mantles the deposit across the entire hill.

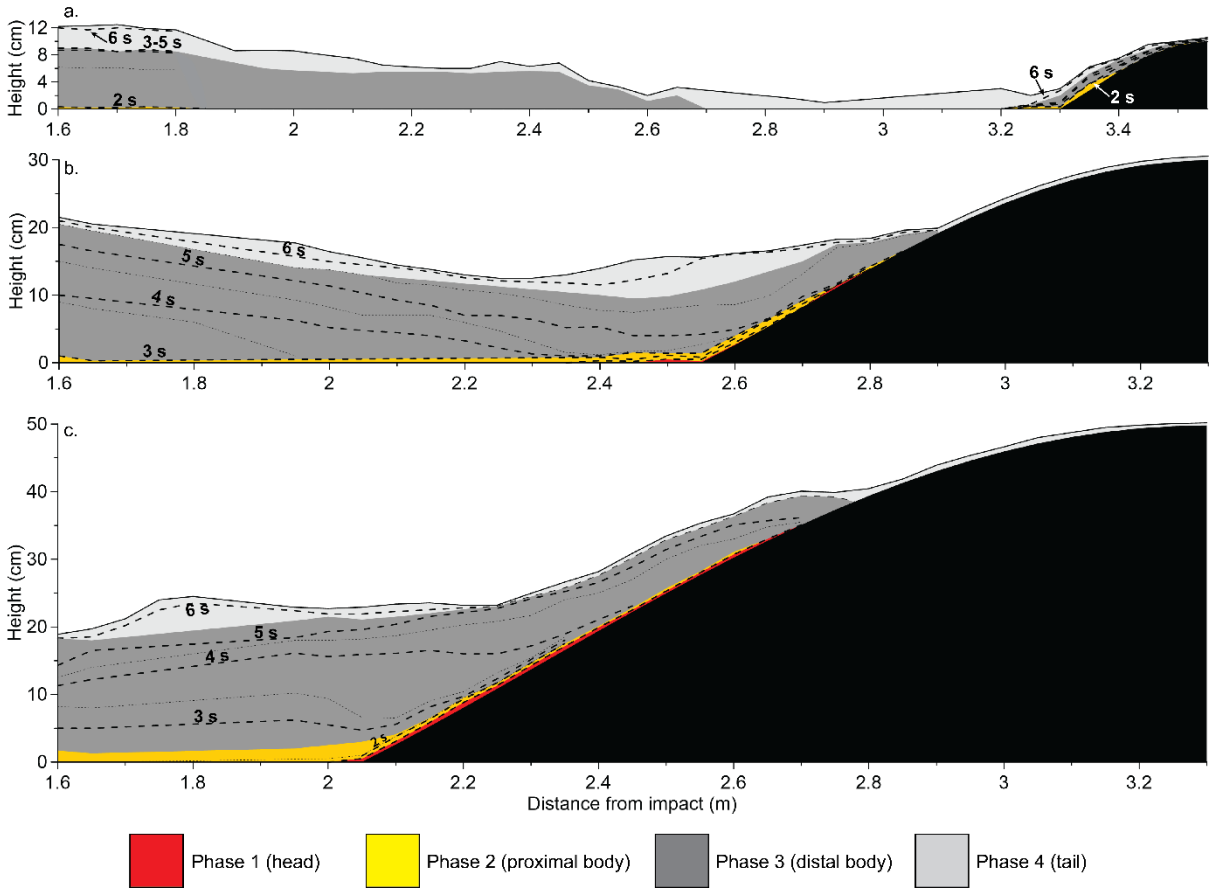

Figure 4.13: Time-resolved deposition of on the stoss side of each obstacle (in black). (a) Small obstacle (b) Intermediate obstacle (c) Large obstacle. Thick and thin dashed lines show isochrones of deposition at 1 and 0.5 second intervals respectively, with t = 0 corresponding to flow arrival at Profile 1. On the small obstacle, slope-parallel, upstream-migrating bedforms are deposited for the entire duration of the flow. On the intermediate and large obstacles, the thick underflow is able to climb the obstacle, before a regressive dune bedform is built and ponds the deposits upstream of the hills.

4.4. Discussion

4.4.1. Variations in flow conditions across the obstacles

In all experiments, blocking of the dense underflow occurs and leads to a strong density and momentum loss. However, the dilute part of the flow can cross the obstacle. In experiment S, deposits on the stoss side are sub-parallel to the topography and show that the bedload is also unhindered by the obstacle. In experiment M and L, thick, massive dune bedforms are deposited, partly able to climb the slope, with the formation of a regressive dune ponding the deposits upstream, showing the strong stranding of both the underflow and the bedload.

The proportion of the flow interacting with the hill is compressed and accelerated when moving up the ridge and up in the gravitational field. This differs from previous energy conservation models from kinetic to potential energy suggesting that flows decelerate by climbing obstacles (Sparks 1976; Malin and Sheridan 1982). These models were used to estimate initial velocities of pre-historic flows such as the parent flow of the Taupō Ignimbrite in dense (Wilson 1985) and dilute (Dade and Huppert 1996) hypotheses. Instead, our observations show that the flow compresses and accelerates, transporting (coarse-grained and concentrated) flow material from the lower portion of the density stratified flow into upper flow regions higher than the crest (Fig. 4.14). This advection effect strongly increases by increasing the obstacle dimensions and causes a reduction of the mass blocked before the crest from 90 % of the initial mass in experiment S to 80 % in experiment L. Together with the development of a dilute turbulent wake, this leads to the formation of an unstable vertical density stratification behind the obstacle. After flow re-attachment, the vertical density stratification needs to redevelop. This will take longer for larger obstacles because particles have been advected into higher flow regions.

In experiment S, the flow does not accelerate significantly and loses c. 30 % of its initial time- and height-integrated velocity after the hill. The underflow is blocked before the obstacle, but the bedload is largely unhindered. Hence, density remains high. In experiment M, the underflow and the bedload are effectively blocked by the obstacle, but the dilute part accelerates. Hence, the flow conserves its velocity better (c. 17 % loss), but density strongly decreases by c. 60 %. In experiment L, the acceleration is

strong and the flow only loses c. 10 % of its initial time- and depth-integrated velocity. The dense underflow is blocked but material from the saltating bedload and the dilute flow is well accelerated and advected into high proportions of the flow. Hence, the density loss is similar to that of experiment M despite the larger wake.

Flow thickening, density loss and deceleration after the crest induce that obstacles have a strong control on the Densimetric Froude Number Fr'. After analysing Fr' across the three obstacles, we observed that flows do not become supercritical upon crossing the hills but stay strongly subcritical. In that the case, our experimental PDCs are therefore comparable to low-velocity, high-energy flows passing over small ridges reproduced by Woods et al. (1998). However, because density could not be measured on the crest of the obstacle, we could not collect information of Fr' at this location. It is possible that after strongly accelerating on the stoss slope and before detaching and thickening, the flows may have transitioned into a short phase under a critical or supercritical regime.

Unlike uncompressible flows with water as a fluid phase, PDCs do not create hydraulic jumps on the lee side because of flow detachment and expansion, strongly increasing their thickness. In addition, no backward travelling bore (Alexander and Morris 1994; Woods et al. 1998) was observed during the experiments, which leads us to believe that reflected bores may only be present in Boussinesq flows, where the density contrast between the flow and the atmosphere is low (<10%), such as turbidity currents. In gas flows, the compressibility of the fluid phase prevents the formation of such structures and the entire dilute flow crosses the hill. However, the formation of a regressive dune bedform before the obstacle could indicate the presence of a similar feature in the dense underflow, which could cause valley filling and overflowing.

4.4.2. Strongly time-variant processes

The mechanisms allowing PDCs to cross topographic obstacles have mostly been described as single processes for the entire duration of the flow with no time distinctions according to the different parts of the current (Sulpizio et al. 2008; Brown and Branney 2013; Gardner et al. 2018). However, as flow dynamics are strongly time-variant, different parts of the flow having different physical properties interact in

different ways with topographic obstacles. This distinction was recently introduced by Guinn et al. (2022) on Mount Saint Helens, who proposed that while the head was jumping over the hills, the body was more ground-hugging, destroying partly or totally the trees that were left standing. Only in the most distal parts of the flow propagation (over 70 % of the whole runout) would the dynamic pressure in the flow body have decreased enough to only burn the trees without toppling them (Guinn et al. 2022).

In Figure 4.14, the similarities in the time-variant interactions of PDCs with obstacles are sketched in the four different phases for all three obstacles. The proximal part of the body is dilute enough to detach and “fly” over the lee side in Phases 1 and 2. However, the late stage of the body shows a strong density increase that disturbs the boundary layer separation in the lee sides of hills in Phase 3. The dense detached flow, loaded with particles conveyed from the base of the stratified flow, pushes on the wake, reducing its re-attachment distance and its area with time.

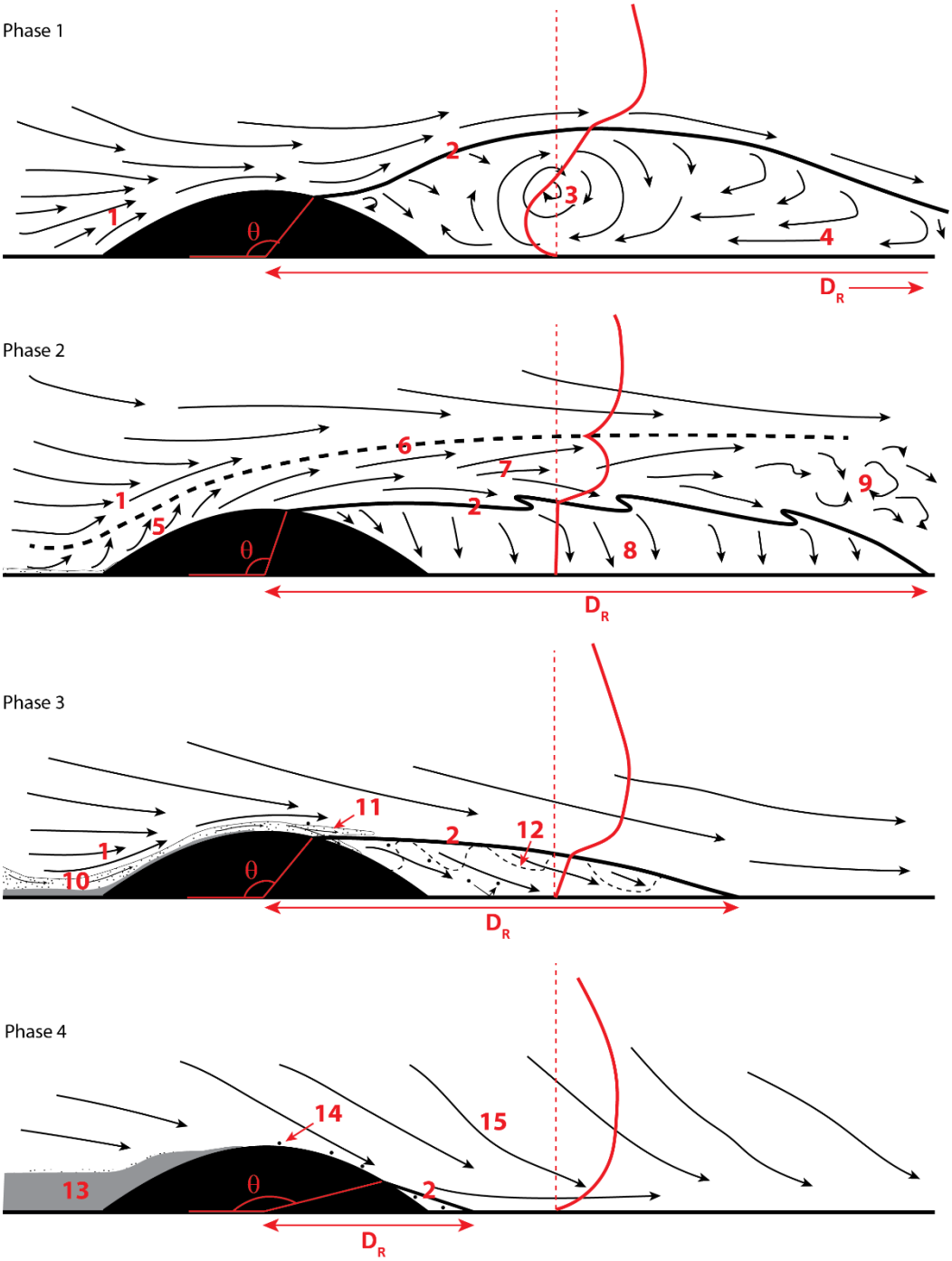

Figure 4.14: Sketch of the time-variant propagation of the experimental PDCs across the obstacles depicting the processes happening for all sizes of obstacles. The arrows show typical streamlines and flow direction. A typical streamwise velocity profile after the obstacle is shown in red, where the vertical dotted red line shows U = 0. θ: detachment angle; D_R: re-attachment distance from the crest; (1) flow compression and acceleration on the stoss side; (2) boundary layer separating the wake below and the detached flow above; (3) rotating vortex inside the wake; (4) backflows; (5) compression forms a gas-escape layer on the stoss side with strong upward velocities, leading to the formation of a jet structure above the lee side; (6) upper limit of the jet structure with lower velocities; (7) diverging streamlines in the high velocity jet; (8) slow settling of particles; (9) strong turbulences inside the jet as the flow re-attaches; (10) dense bedload partially able to climb the stoss side; (11) the bedload separates with a part flowing down the lee slope and a part ejected in the detached flow, increasing its density and pushing on the boundary layer separation; (12) finger-like instabilities enhancing sedimentation inside the wake; (13) thick, massive deposits on the stoss side from the blocked underflow; (14) rolling pumice down the lee slope; (15) strong rotation of the streamlines leading to the disappearance of the wake as the flow follows the lee side topography.

4.4.3. Model for momentum loss during PDCs-obstacle interactions

The obstacles used in our experiments were shaped as hills found around real-world volcanoes. Sulpizio et al. (2008) interpreted the massive, coarse-grained deposits on the stoss side of an obstacle as evidence for flow deceleration and momentum loss. In numerical simulations, Doronzo et al. (2010) also highlighted increasing thickness of deposits and sediment flux on the stoss side of obstacles and interpreted them as a drop in velocity leading to increasing density and rapid suspension-sedimentation. However, field studies on bluff obstacles have revealed that despite the mass loss, PDCs were able to maintain their momentum (Jeon et al. 2011), suggesting that form drag is more responsible for blocking than friction and deceleration. In the experiments, the dilute upper region of the flow is compressed and accelerated. Even the underflow is able to partially climb the obstacle (though without crossing), showing that there is no immediate flow deceleration when PDC interacts with obstacles. Instead, they accelerate, highlighting the importance of flow compression on the stoss side which likely affects the energy conversion from kinetic to potential. The increasing density is rather caused by increasing incoming mass during Phase 3. Finally, the massive underflow is largely blocked by form drag, rather than by deceleration or friction.

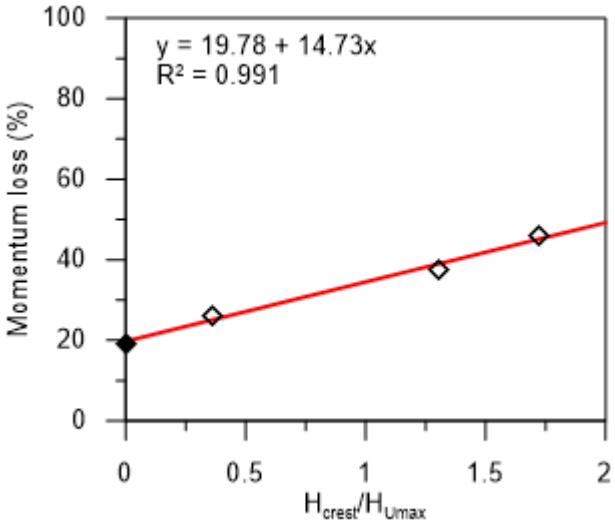

Figure 4.15: Momentum loss of the dilute part of the flow against the ratio of heights of the obstacle over the velocity maximum of the incoming flow (H_{max}/H_{Umax}). The data align well on a linear fit depicted as a red curve and suggest that total blocking with 100 % momentum loss happens from a height ratio of 5.45. Note that momentum still decreases without obstacles (closed point at x=0, data from Brosch and Lube 2020) as density and velocity decrease with distance.

However, even when considering only the dilute upper region of the flow without the bedload and despite compression and acceleration, momentum still decreases

after the obstacles (Table 4.2). This shows that the drag does not only affect the dense underflow.

The dimension of the obstacle in the flow path needs to be characterized as a given hill may be considered a small or a large obstacle depending on the incoming flow thickness. The height ratio (H_R) is the ratio of the crest height of the obstacle over the time-integrated height of the velocity maximum (H_{crest}/H_{Umax}) and depicts how large is the obstacle compared to the flow boundary layer thickness. In Figure 4.15, we plotted the momentum loss of the dilute part of the PDCs (above the bedload) against the height ratio. The data suggest that the momentum loss of a dilute PDC is linearly correlated to the height ratio, which can be empirically expressed by a best fit as:

$$\overline{\Delta M} = 19.78 + 14.73 \frac{H_{crest}}{H_{Umax}} \qquad \text{(Eq. 4.4)}$$

where $\overline{\Delta M}$ is the difference in time- and depth-averaged flow momentum before and after the obstacle in percent. This fit suggests that obstacles that are 5.45 times higher than the height of the velocity maximum lead to 100% momentum loss (complete blocking of the flow). In our experiments, this condition of complete flow blocking would require a hill crest height of c. 1.63 m. Andrews and Manga (2011) found that a dilute PDC cannot cross an obstacle that is higher than approximately 1.5 times the flow thickness. This result is in close agreement with our experimental findings and Eq. 4, where the time-averaged thickness of the body of our experimental PDCs at Profile 1 (before the obstacle) is c. 1.1 m.

In the following sections, we will test this simple conceptual model with real-world examples.

4.4.4. Case study: the 1980 Mount Saint Helens lateral blast

Here, we study a Northeast-oriented topographic profile of Mount Saint Helens (Fig. 4.16a), where the lateral blast travelled across three obstacles and kept propagating up to 19 km from the vent. The initial height of the velocity maximum is estimated at 250 m (Moore and Rice 1984; Esposti Ongaro et al. 2012).

As the flow reaches Johnston Ridge (365 m high), the height ratio is 1.46. Applying Eq. 4.4 to these parameters, the bulk momentum loss of the PDC across the ridge would amount to c. 41 %. After the ridge, in the valley of South Coldwater Creek, the position of the maximum velocity is lifted up to c. 700 m above the ground (Esposti Ongaro et al. 2012). This upward shift in the height of the velocity maximum is similar to our observations at Profile 2 after the obstacle. Therefore, the height of the maximum velocity becomes significantly higher than Coldwater Ridge, although this second obstacle has a larger absolute elevation (426 m high): the height ratio is only 0.61, leading to a momentum loss of c. 30 %. After this obstacle, the height of the velocity maximum stays at a similar altitude, and is only c. 600 m above the ground (Esposti Ongaro et al. 2012). The third obstacle (Minnie Ridge) is only 634 m high (height ratio of 1.09) and causes a momentum reduction of c. 35 %. After these three obstacles, the flow has lost c. 73 % of its initial momentum, and the height of the velocity maximum is now around 250 m above the ground, as topography remains high in altitude. This low-energy flow propagates approximately 5 more kilometres on a gentle downslope before lifting off. This application suggests that despite crossing multiple obstacles, PDCs conserve their momentum, which can explain the reason behind their long runout, even on rough topography.

The application of Eq. 4.4 on successive ridges however needs to be carried out with caution, especially if the flow has not re-attached yet after the first ridge, which could lead to different flow-obstacle interactions.

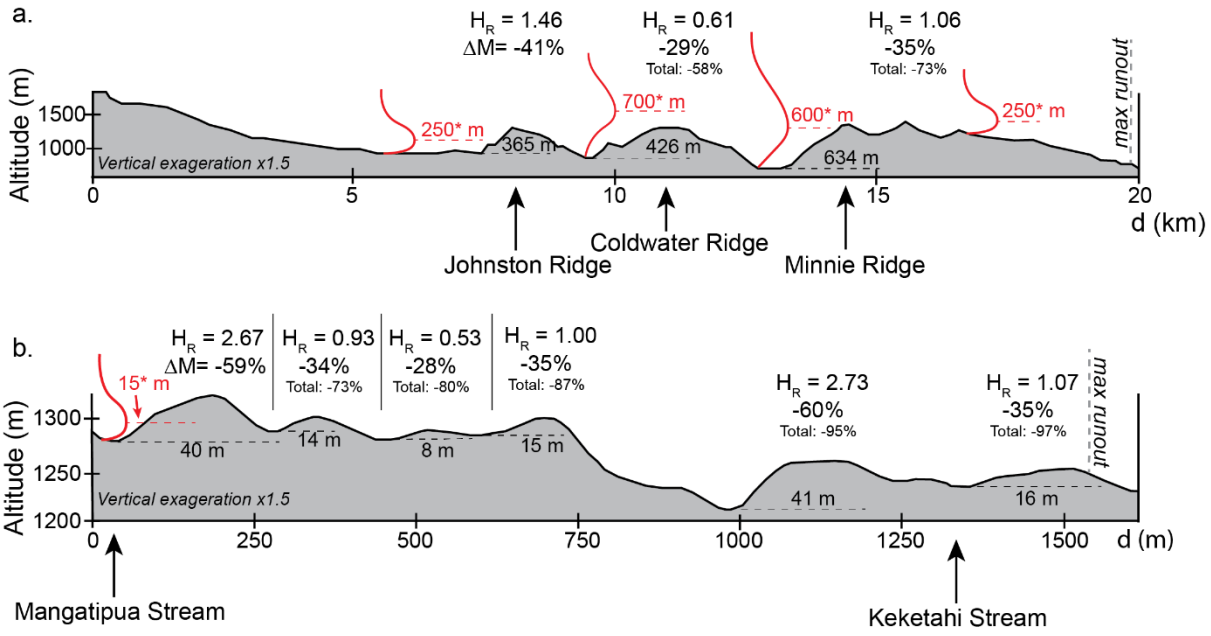

Figure 4.16: Topographic profiles in the flow direction for (a) Mount Saint Helens and (b) Te Maari. The heights of the obstacles above their base (black dotted line) are indicated in black. The red curves show typical velocity profile, and the red number indicates the height of the velocity maximum above the base (*: data extracted from Esposti-Ongaro et al. (2012), Lube et al. (2014), Cerminara et al. (2021)). The height ratios (H_R) of the obstacles are shown above each hill, along with the momentum loss (ΔM) created by the hill. In the case of Te Maari, the variations in the heights of the maximum velocity are not known.

4.4.5. Case study: the 2012 Te Maari lateral blast

The blast-like PDC generated during the 2012 Te Maari eruption (New Zealand) was able to cross a series of several ridges roughly perpendicular to the flow direction (Breard et al. 2015). Before the first ridge, the flow thickness was estimated to c. 80 m with the presence of a sharp delimitation of fine ash deposits against the cliffs (Lube et al. 2014). According to Cerminara et al. (2021), the ratio of the e-folding height of the PDC over the height of the maximum velocity is constant and takes a value of 5.3, indicating that the height H_{Umax} of the maximum velocity for the Te Maari blast was located at c. 15 m above the base. Assuming that the flow re-attached before encountering the next obstacle, the height ratio and the momentum loss can be calculated for each of these ridges (Fig. 4.16b). The critical blocking height where the entire flow momentum is lost and the PDC is fully blocked can be estimated at c. 82 m, indicating that none of these 8-41 m high ridges would have been able to block the obstacle.

The first obstacle, which is located approximately 1000 m from the source, is a large 40 m high ridge with a Height Ratio H_R of 2.67. Following Eq. 4.4, the flow has lost almost 60 % of its initial momentum upon crossing this first obstacle. After the fourth ridge, the flow has lost c. 87 % of its initial momentum, and from this position onwards, trees are not uprooted or broken, but only show burning of leaves with thin <1 cm deposits (Breard et al. 2015). Eventually, as the flow kept progressing across the fifth and the sixth ridge, the momentum loss was too important, reaching 97 % of the initial flow momentum, and the flow stopped.

4.4.6. Interpretations of sedimentation

Mechanisms of emplacement

Topographic obstacles have a strong influence on local transport and deposition mechanisms. The geometry of the deposits before the hill gets increasingly longer and flatter with increasing obstacle size. This unique feature has never been observed before in PELE experiments without obstacles. Therefore, we strongly suspect that their presence is responsible for this varying geometry, suggesting that obstacles do have an impact on upstream sedimentation, notably through the emplacement of regressive bedforms. Variations in depositional features are also linked to the different flow phases.

The blocking of the dense underflow into a coarse breccia or massive unit allows a continuous burying of the obstacle and reduction of its absolute height. This effect strongly affects the flow and wake dynamics, as well as the sedimentation immediately downstream of the hill.

Stratified deposits are emplaced with tractional transport of a bedload through rolling and saltation. This type of unit is usually found above a massive unit, as it is emplaced in the late stages of the flow when its energy decreases. While this type of transport also occurs in the proximal body of the flow, it is hardly depositional because of the high energy of the flow. This is also the case in our experiment before the obstacle. However, on the stoss slope of the hill, stratified deposits intercalated with coarse pumice clasts are found at the base of the sequence, and were deposited by the proximal flow body (Phase 2), and sometimes even the head (Phase 1). We

interpret this feature as the initiation of the partial blocking of the flow by the obstacle through form drag.

On the lee side, deposits are very thin and thinly stratified and are mostly stemming from the head or the proximal body. Strong erosion and redeposition occurring on the lee side during the entirety of the flow is responsible for the deposition of this unit.

After the obstacle, a very thin laminated unit is found at the base of the sequence. It is emplaced from vertical sedimentation pulses dusting the base of the channel in the first seconds of the wake dynamics before the arrival of the dense body of the flow. On top of this fine layer, stratified units are emplaced in the phases 3 and 4. The arrival of denser material crossing the obstacle allows the development of a poorly defined tractional bedload that falls from the detached as finger-like instabilities and allows impacts, saltation and rolling. There, deposits are emplaced with a stronger vertical component, or lower shear. This generates poorly stratified basal, more massive deposits than the upper part of the sequence. Later, as the flow loses energy and the stoss side of the hill is progressively buried, streamlines begin to follow the topography and the flow does not detach well anymore. The top of the sequence after the obstacle becomes significantly more stratified with the sedimentation of a purely tractional bedload.

Comparison between experimental and real-world PDCs

Figure 4.17 shows the comparison between the experimental deposits and deposits of the 232 AD Taupō Ignimbrite (New Zealand). This particular obstacle is located proximally (c. 13 km) from the inferred vent in a northern direction.

Deposits across this obstacle are strongly asymmetric. Similar asymmetry of deposits and layering were observed across other topographic obstacles, typically in Mount Saint Helens, USA (Bursik et al. 1998) and Salina Island, Italy (Sulpizio et al. 2008). These field deposits increase our confidence in our experimental observations and in the similarity between the processes of transport and deposition occurring in the real-world and in PELE.

At the inset of the obstacle, deposits show very coarse clasts similar to the coarse pumice breccia from the experiments (Fig. 4.17). On the stoss side, deposits progressively become thinner, but still show massive, poorly sorted facies resembling the massive unit of the experiments.

From the crest onwards, deposits start showing some layering. The ignimbrite is strongly stratified with coarse pumice lenses intercalated between finer-grained layers. On the lee side, previous eruption units were completely eroded, and no ground layer is deposited at the base of the ignimbrite, showing a strongly erosive parent flow. This is very similar to the thinly laminated unit found on the lee side of the experimental obstacles.

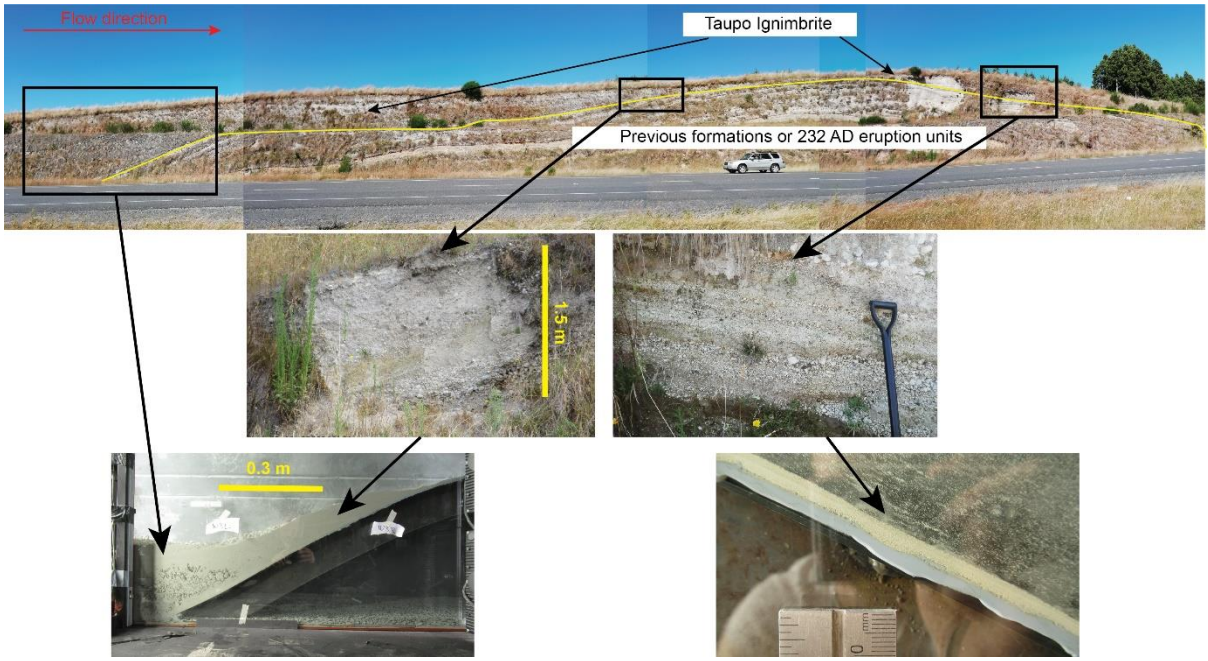

Figure 4.17: Comparison between experimental deposits and real-world deposits from the 232 AD Taupō Ignimbrite, showing a similar asymmetric geometry between the stoss and lee sides, and the same facies of deposits.

4.5. Conclusions

The situation of dynamically and kinematically scaled PDCs encountering ridge-shaped obstacles of variable sizes was studied in large-scale experiments. The flow dynamics around the obstacles were characterized through measurements of flow velocity, temperature, density and deposit structure. The findings of this study are as follows:

- The interactions of experimental PDCs with topographic obstacles are strongly time-variant. Four transient phases of flow-topography interaction occur and are

associated with the time-variant vertical velocity and density structure of the gravity current.

- On the stoss side of the ridges, the flow locally compresses and accelerates strongly despite the conversion of kinetic to potential energy. This effect leads to the advection of material from the base of the flow back into the upper flow regions and increases with increasing obstacle size.
- After the crest, the flow separates and creates an unstable stratification with the formation of a cold, slow, relatively dilute turbulent wake below a hotter, faster, denser detached flow.
- In the case of small obstacles, the bedload is largely unhindered by the hill and massive deposits can be found on each side of the obstacle. On the stoss side, deposits show an aggrading structure with beds sub-parallel to the slope.
- In the case of larger obstacles, the dense underflow is blocked on the stoss side and deposits show facies such as thick pumice breccia and massive units, which can partially climb the obstacle. The formation of an anti-dune ponding and thickening the deposits is also noticeable.
- After the obstacle, vertical settling of fine ash leads to the deposition of a thin, thinly laminated layer at the base of the sequence. A poorly stratified unit is also deposited from a low-shear tractional bedload.
- A momentum analysis of the experimental PDCs suggests that dilute flows cannot cross obstacles that are 5.45 times higher than the height of their velocity maximum. This result is in good agreement with previous analogue PDC experiments of talc powder and air (Andrews and Manga 2011). The momentum loss is linearly related to the ratio of the height of the hill and the height of the velocity maximum of the incoming flow.
- With increasing size, obstacles reduce the momentum despite accelerations, even when considering only the dilute part of the flow. This suggests that the form drag created by the obstacle is strongly acting on the flow and needs further investigation.

4.6. Supplementary materials

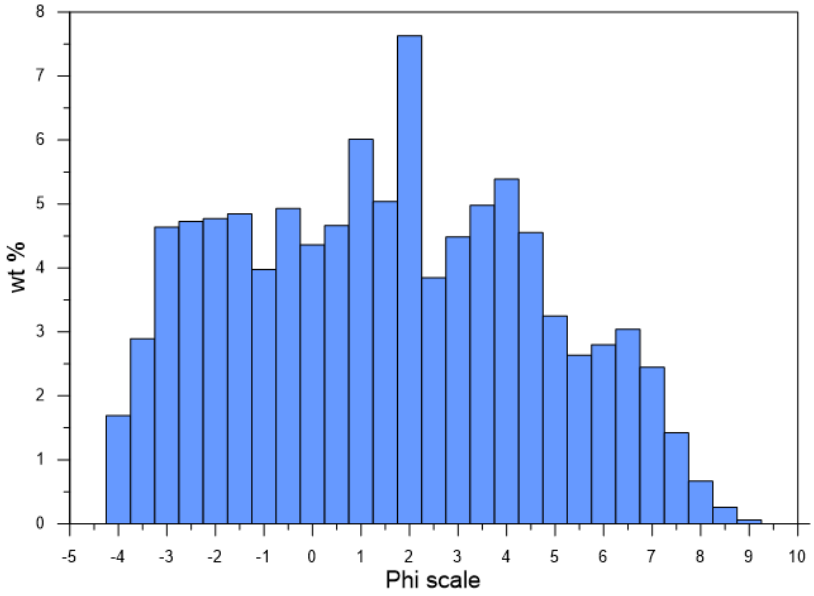

Supplementary material 4.1: Grainsize distribution of the mixture used for the three experiments

Supplementary videos are available at the following address:

https://drive.google.com/drive/folders/1FjtDvSlajUmxNk6lDid5QC_JilHXYPt2?usp=sharing

Supplementary material 4.2: video of the lee side of the intermediate obstacle across the entire flow propagation. The video was recorded at 1000 frame per second (fps) and is played at 30 fps, but the quality here had to be downgraded for file size purposes.

Supplementary material 4.3: video of the lee side of the intermediate obstacle across the entire flow propagation in the downstream (U) velocity field, with velocity profiles every 0.1 m showing inflexion at the boundary layer separation.

Supplementary material 4.4: video of the lee side of the intermediate obstacle across the entire flow propagation in the vertical (V) velocity field, with velocity profiles. Positive values show upward velocities, and negative values show a downward trend.

Supplementary material 4.5: video of the lee side of the intermediate obstacle across the entire flow propagation in the Magnitude velocity field, with streamlines of flow direction.

5. Characteristics of the detachment of dilute pyroclastic density currents behind obstacles: an experimental study

L. Corna, J. Jones, G. Lube, E. Brosch, D. Uhle

Abstract

Dilute pyroclastic density currents (PDCs) produced during explosive eruptions are able to cross topographic obstacles with ease. The observation of areas of low PDC damage on the lee sides of hills suggests that a possible safe zone could exist behind obstacles. Here, we synthesized PDCs in three large-scale experiments with topographic obstacles of the same drag coefficient, but different sizes compared to the thickness of the boundary layer of the incoming flow. We analysed the characteristics of the turbulent wake formed behind the obstacles and suggest a model that allows estimating its dimensions and characteristics behind a given obstacle.

Previous studies envisaged the flow field across obstacles following ballistic trajectories. Our experiments show that PDCs detaching from obstacles do not follow ballistic trajectories which, when used in calculations, under-estimate the wake dimensions. Other processes must occur inside the detached flow to explain these characteristics. We show that the wake geometry is governed by a balance between the drag force exerted by the obstacle onto the flow and a lift force inside the wake. The lift force arises due a vertical gradient in static pressure from the wake into the detached flow. For similar conditions of the incoming flow, the scaled cross-sectional area and the scaled downstream length of the wake are inversely proportional to the obstacle size. This behaviour is explained by an inverse relationship between the ratio of lift over drag forces and the size of the obstacle relative to the flow size. This ratio decreases with obstacle size, and smaller obstacles create larger lift forces due to a strong vertical gradient in static pressure.

The experimental data suggest that the re-attachment distance of a flow behind a ridge-shaped obstacle is related to the ridge height relative to the thickness of the flow,

and can thus be estimated as a power law relationship. However, the area underneath the detached PDC should not be regarded as a ‘safe zone’. Particularly for conditions of obstacles that are smaller than the thickness of the PDC wall region, strong sedimentation from the detached flow into the turbulent wake, which induce a large lift force, cause flow densities that can be up to five times larger than that of the detached flow above. High concentration of hot particles associated with these large densities correspond to high risks of suffocation and burning.

5.1. Introduction

Pyroclastic Density Currents (PDCs) are destructive particle-laden gas flows produced during violent volcanic eruptions with the ability to climb topographic obstacles. This intriguing behaviour has been documented for different sizes of obstacles and flows, from low-volume PDCs climbing several ridges before stopping (e.g. Cronin et al. 2013; Komorowski et al. 2013; Lube et al. 2014; Breard et al. 2015), to larger-volume flows toppling entire mountain ranges (e.g. Fisher et al. 1993; Gardner et al. 2007; Cas et al. 2011). The high velocities and particle concentrations of PDCs result in dynamic pressures (Brosch et al. 2021) of tens to hundreds of kPa and are responsible for damages caused to buildings (Baxter et al. 2005) or trees (Clarke and Voight 2000; Jenkins et al. 2013; Brand et al. 2014). However, on the lee side of hills, patches of scorched but still standing trees can remain (Kelfoun et al. 2000; Gardner et al. 2018), suggesting that when climbing and cresting obstacles, mechanisms occur inside these flows allowing the relative preservation of vegetation.

Experiments on dry granular avalanches showed that upon encountering obstacles, the granular flows detach following ballistic trajectories (Hákonardóttir et al. 2003; Naaim-Bouvet et al. 2004; Chung et al. 2019) and re-attach at a distance controlled by the flow velocity and the relative height of the obstacle compared to the flow thickness (Hákonardóttir et al. 2003). This behaviour, which was modelled as a viscous jet, could explain the existence of spared areas below the ballistic curve. More recently, Gardner et al. (2018) applied the ballistic model to the 1980 Mount Saint Helens blast. In this case, ballistic trajectories overestimated the extent of the documented standing tree patches (that is the assumed re-attachment distance for the

flow). They argued that entrainment of ambient air at the base of the detached flow accounts for this discrepancy. This model was later refined by Guinn et al. (2022) who suggested that only the flow head was propagating ballistically over the lee sides, while the body remained attached. The dynamic pressure of the body would be low enough to preserve tree patches on the lee side of obstacles only in distal reaches of the runout.

Flow detachment due to the adverse pressure gradients around a solid body is known to occur in fluid flows and is responsible for the formation of turbulent wakes behind the solid body (Simpson 1989). The area of the turbulent wake scales with the drag force exerted by the solid body onto the flow (Achenbach 1972; Mehta 1985), and therefore to the drag coefficient of the obstacle. In case of spheres or cylinders, the detachment angle scales non-linearly with the Reynolds Number and becomes greater than 90 degrees for fully turbulent flows (Mehta 1985; Cao and Tamura 2020). Inside the turbulent wake, several vortices develop, grow in size and propagate downstream (e.g. Cao and Tamura 2020). Ma et al. (2000) define the wake as the region approximately fifty diameters downstream of a cylinder, the “near-wake” as the region up to ten diameters behind the cylinder, and finally the “very near wake” up to three diameters.

This research aims at providing new information towards the re-attachment distance, wake area and static pressures inside the wakes generated behind obstacles in the path of PDCs. Is it possible to predict the dimensions of a wake formed behind a given obstacle in the path of a PDC of known starting conditions? Would this wake create a “safe zone” partially protected from these destructive flows? And can field characteristics about the wake dimensions (such as standing tree patches) provide information about the PDC flow conditions (i.e. velocity, density, dynamic pressure)?

5.2. Experimental setup

Three large-scale experiments were run in the Pyroclastic flow Eruption Large-scale Experiment (PELE) setup (Lube et al. 2015). PELE allows the reproduction of kinematically scaled PDCs in a controlled environment, with over 200 samplers,

sensors and cameras along the 30 m runout. It is divided into four sections: (1) a hopper containing a heating system and storing the material, located 7 m above the experimental channel; (2) a heatproof shroud in which the mixture falls and expands by entraining air; (3) a fully instrumented, 6° inclined, 14.2 m long channel with steel walls on one side and glass walls on the other, allowing the visualisation of the internal dynamics of the experimental PDCs; (4) a 16 m-long unconfined runout region. For these experiments, 200 kg of natural ignimbrite deposits from the 232 AD Taupō Eruption were used. The mixture contains particles ranging from 2 μm to 16 mm, with c. 26.5 wt% of fine ash (<63 μm), a median diameter of 1.2Φ (435 μm) and a sorting coefficient of σ = 3.2 Φ (109 μm).

After an initial weeklong heating at 100°C in an oven, the mixture was placed in the hopper and heated at 120°C for three days to remove residual moisture. During the experiment, a trigger signal allowed the synchronisation of all sensors and cameras and opened the trap doors of the hopper. The mixture expanded and impacted the channel, creating a pyroclastic current propagating down the slope.

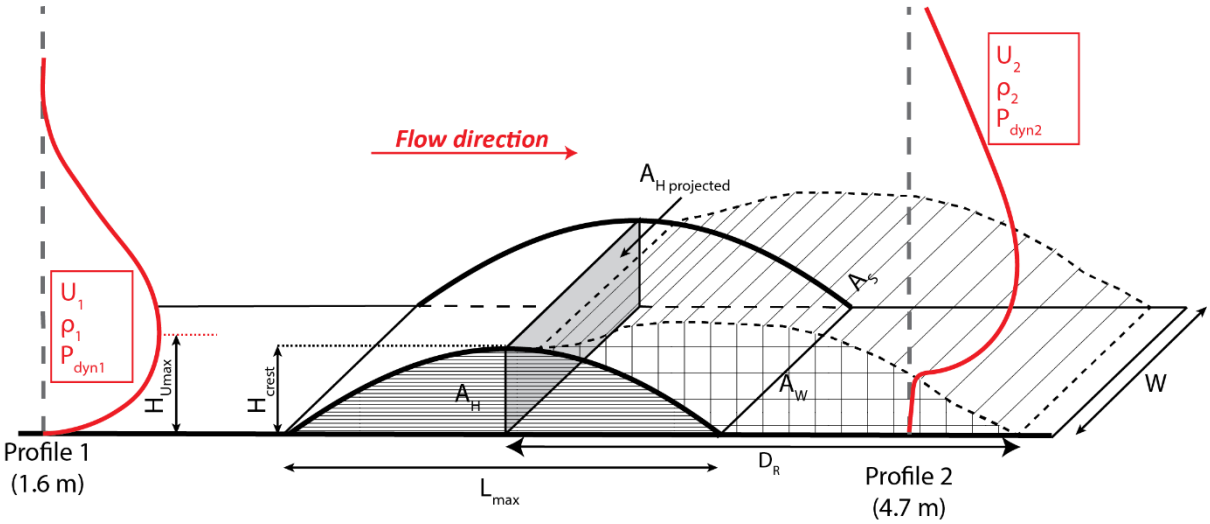

Figure 5.1: Sketch of the setup and employed terms. The red curves show schematic vertical velocity profiles of flow velocity before and after the obstacles. H_{Umax} is the height of the velocity maximum before the obstacle, H_{crest} is the height of the hill at the crest, W the width of the hill, L_{max} the length of the hill, D_R the reattachment distance from the crest, A_H the hill cross-sectional area, $A_{Hprojected}$ the hill projected area perpendicular to the flow direction, A_W the wake area, A_S the wake surface area. U, ρ and P_{dyn} are the time- and depth-averaged velocity, density and dynamic pressures. The subscripts "1" and "2" refer to Profiles 1 and 2 respectively (1.6 m and 4.7 m from the impact).

Hill-shaped obstacles were placed inside the channel. They were designed using average slope angles and aspect ratios (H_{crest}/L_{max}) of real-world obstacles located around the volcanoes Merapi (Indonesia), Tongariro (New Zealand), Mount Saint

Helens (USA) and Bandai (Japan). The general demi-shape of the hill from the crest is given by:

$$H = H_{crest} - \left[\frac{H_{crest}}{\left(\frac{L_{max}}{2}\right)^2}\right] * L^2 \qquad \text{(Eq. 5.1)}$$

with H the height of the hill at a distance L from the crest, H_{crest} the crest height, and L_{max} the maximum length of the obstacle. The aspect ratio is equal to 0.2. At the sides, the hills deviate from the concave shape given by the demi-shape of Eq. 5.1 and merge to a constant slope angle of 21°. Three obstacles of this shape but different sizes were built for each of the three experiments. The height of the obstacles, H_{crest}, were chosen in relationship to the time-averaged height of the velocity maximum (H_{Umax}) of the experimental PDCs before the obstacle. In the experimental flows in PELE, H_{Umax} is located c. 0.3 m from the channel base. Obstacles were designed to span a range of possible scenarios: smaller than H_{Umax} (0.1 m), similar to H_{Umax} (0.3 m) and larger than H_{Umax} (0.5 m). Table 5.1 summarizes the obstacles geometry, using the abbreviations depicted in Figure 5.1. Obstacles were placed in the proximal section of the channel with a crest at c. 3.3 m from the impact zone. The positioning of these obstacles allowed a non-obstructed view with high-speed cameras of the processes occurring on the lee side (downstream side) of the obstacles.

	Formula	Unit	Small	Intermediate	Large
H_{crest}		m	0.1	0.3	0.5
L_{max}		m	0.5	1.5	2.5
H_R	h_{crest}/h_{Umax}		0.39	1.17	1.62
A_H		m^2	0.03	0.28	0.77
$A_{H\ projected}$	$W*h_{crest}$	m^2	0.05	0.15	0.25
D_R (average)		m	0.96	1.49	1.88
$D_{R\ scaled}$ (average)	D_R/h_{crest}		9.62	4.96	3.77
A_W (average)		m^2	0.07	0.24	0.24
A_W scaled (average)	A_W/A_H		2.17	0.84	0.31
A_S (average)		m^2	0.46	0.79	0.89

Table 5.1: Geometric characteristic of the obstacles and the wake generated in their lee side.

Flow velocities were measured along vertical profiles before (1.6 m) and after (4.7 m) the obstacle (named Profiles 1 and 2 respectively), as well as across the lee side of the hills using six high-resolution, high-speed cameras at 1000 frames per second. The videos were analysed through Particle Image Velocimetry in order to extract

velocities, streamlines and turbulence intensity. Flow sediment samplers on the window side collected particles inside the flow and were recorded at 60 fps. The volume of particles deposited in the samplers associated with the measured velocities allowed the calculations of flow densities (Brosch and Lube 2020) before and after the obstacle. Measurements of temperature and flow grainsize were also performed at multiple locations across the entire runout.

As a note for the rest of this article, the three experiments are called S, M and L and refer to the Small, Medium and Large obstacle.

5.3. Results

5.3.1. Energy balance

At Profile 1, the experimental PDCs are characterized by time- and depth-integrated density and velocity of c. 6.5 kg/m^3 and c. 3.27 m.s^{-1}, respectively. Their Reynolds numbers reach 10^6, and a comparison of dimensionless groups in natural PDCs and the experimental gravity currents show a good overlap (Burgisser et al. 2005) summarized in supplementary materials. At the stoss side of the obstacles, the flows compress and accelerate. Downstream from the crest, the flows detach from the obstacle at a detachment angle θ of c. 120° (90° corresponding to the crest) and re-attach after the obstacle at a distance D_R (Fig. 5.1). The zone below the detachment corresponds to the turbulent wake created by the flow detachment and is initially characterized by lower velocities, densities and temperatures than those in the detached flow above. Because of the unsteady and transient nature of the experimental PDCs and due to deposit accretion in front of the obstacle, the locations of the flow detachment and re-attachment vary in time.

In all three experiments, the experimental PDCs approaching the obstacles are comprised of a 0.01-0.1 m thick, dense, non-turbulent underflow and a 0.7-2 m thick, dilute turbulent upper part. The underflow becomes blocked by the obstacles and only the turbulent flow propagates over them. Considering only the dilute proportions of the

flow (i.e. without the underflow), energy conservation across the obstacle between Profiles 1 and 2 can be approximated as:

$$Estored_1 + Ekinetic_1 + Epotential_1 = Estored_2 + Ekinetic_2 + Epotential_2 + Eloss_{1,2} \quad \text{(Eq. 5.2)}$$

where the subscripts 1 and 2 refer to Profiles 1 and 2 (1.6 m and 4.7 m from the impact zone respectively), and 1,2 refers to the average between these profiles.

The stored energy can be expressed as static pressure, the kinetic energy as dynamic pressure, and the potential energy relates to the height of the flow. The loss can be expressed as form drag, relating to the interaction of the flow with the obstacle. The friction loss, or skin drag, is considered negligible. Hence, written in the energy density form of the Bernoulli equation:

$$\frac{1}{2}\rho_1 gZ + \frac{1}{2}\rho_1 U_1^2 + \rho_1 g\left(h_{channel,1} + h_{COM,1}\right) = \frac{1}{2}\rho_2 gZ + \frac{1}{2}\rho_2 U_2^2 + \rho_2 g\left(h_{channel,2} + h_{COM,2}\right) + C_D \frac{\overline{\rho_{1,2}}\,\overline{U_{1,2}^2}}{2} \quad \text{(Eq. 5.3)}$$

where ρ is the flow depth- and time-averaged density, Z the averaged thickness of the body of the flow (that is c. 1.1 m), g the acceleration of gravity, U is the time- and depth-integrated velocity, $h_{channel}$ the height of the base of the inclined channel at a specific location, h_{COM} the average height of the centre of mass of the flow above the channel base (hence the height above and below which sits half of the time- and depth-integrated flow mass), and C_D is the drag coefficient averaged over depth and time. Here, the static pressure term is halved to express the average static pressure of the flow.

The terms of this equation were calculated and allowed the determination of the drag coefficient C_D of the obstacles. The calculated drag coefficient C_D is similar for the three obstacles, as expected for hills having the same shape, and takes a value of c. 0.7. From these calculations, the drag force (F_D) applied by each obstacle on the flow was estimated with:

$$F_D = C_D A_{Hprojected} \frac{\overline{\rho_{1,2}}\,\overline{U_{1,2}^2}}{2} = A_{Hprojected} \Delta P_{loss,1-2} \quad \text{(Eq. 5.4)}$$

Where $\Delta P_{loss1\text{-}2}$ in the difference in the total pressure between Profiles 1 and 2. For the three experiments, the drag force exerted by the obstacle takes values of 1.94, 2.76 and 6.60 N for the small, intermediate and large obstacles respectively. The results are summarized in Table 5.2.

	Formula	Unit	Small		Intermediate		Large	
			Profile 1	Profile 2	Profile 1	Profile 2	Profile 1	Profile 2
Static pressure (P_s)	$0.5*\rho*g*Z$	Pa	21.88	23.18	17.41	15.91	22.16	16.4
Dynamic pressure (P_{dyn})	$0.5*\rho*U^2$	Pa	50.65	22.51	24.63	13.82	32.14	28.51
Potential energy (P_{pot})	$\rho*g*(h_{channel}+h_{COM})$	Pa	57.09	45.21	42.61	36.51	54.62	37.61
Energy density loss ($\Delta P_{1\text{-}2}$)	$\sum Energy,1-\sum Energy,2$	Pa	38.72		18.41		26.4	
C_D	$\frac{2.\Delta P_{1-2}}{\rho U^2}$		0.71		0.7		0.74	
F_D	$A_{H\ projected}\Delta P_{1\text{-}2}$	N	1.94		2.76		6.6	

Table 5.2: Energy densities at Profiles 1 and 2, calculated from Eq. 5.2. These pressures allowed the calculations of the drag coefficient C_D and the drag force F_D. C_D takes a similar value for all three experiments. F_D is increasing with increasing obstacle size.

5.3.2. Wake generation behind topographic obstacles

The interactions of the flows with the obstacles are energetic, time-variant processes. In all three experiments, four characteristic phases were recognized. These phases correspond approximately to the subsequent passings of the density current head, proximal body, distal body and tail regions over the obstacles.

In the first phase, the flow head climbs and crest the obstacles. It re-attaches after enveloping a large volume of ambient air, leading to the formation of a large rotating vortex. D_R and A_W strongly increase while the vortex propagates downstream, before decreasing again during passage of the rear of the head. In the second phase, the unstable boundary layer separation leads to the formation of an alternatively thickening and collapsing jet-like structure at the base of the detached flow. This jet structure is characterized by high velocities, densities and turbulence intensity, and shields the wake from the flow above. D_R and A_W alternatively increase and decrease during this phase. In phase 3, although the flow becomes markedly denser and the detachment angle θ increases, D_R and A_W keep a relatively constant value. Eventually,

in the last phase, the velocity field rotates and streamlines become sub-parallel to the lee side slope: flow detachment occurs at very large angles θ, leading to a subsequent strong reduction of D_R and A_W. Figure 5.2 depict the re-attachment distance and the wake area for each experiment against time. Strong variations are visible on these plots, corresponding to the variations described according to the different flow phases. In general, D_R and A_W are increasing with increasing obstacle size (Fig 5.2a and 5.2c). However, the non-dimensional re-attachment distance D_R/H_{crest} and the non-dimensional wake area A_W/A_H decrease with increasing hill size (Fig 5.2b and 5.2d). In other words, the larger the obstacle, the smaller the relative size of the wake created.

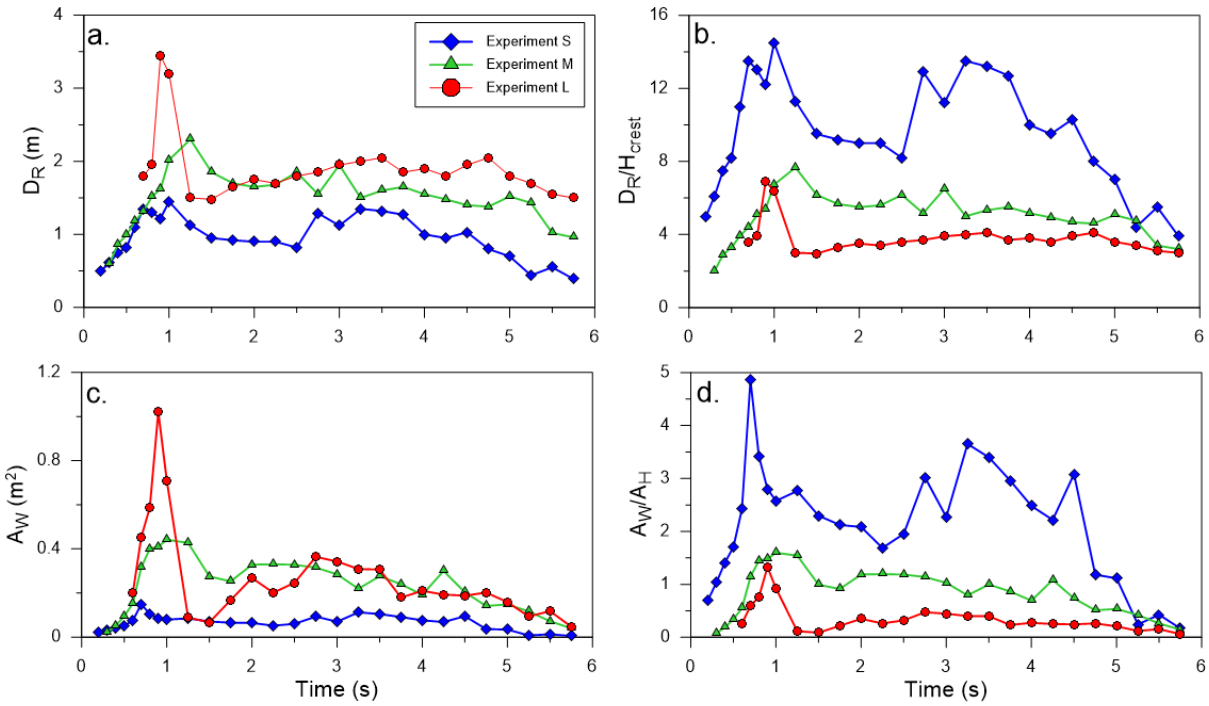

Figure 5.2: Re-attachment distance (D_R) and wake area (A_W) against time. (a & c) original values showing that the wake dimensions are increasing when increasing the size of the hill. (b & d) scaled values compared to the obstacle, showing that small obstacles produce a comparatively larger wake than a large obstacle.

Gardner et al. (2018) suggested that the PDCs behind obstacles were following a ballistic trajectory. In order to estimate the re-attachment distance and wake area behind obstacles, time-resolved ballistic trajectories were calculated for all three experiments with:

$$y = H + x.\tan(\alpha) - \frac{g^*}{2U_{detach}\cos(\alpha)^2}x^2 \quad \text{(Eq. 5.5)}$$

Where y and x are the vertical and horizontal coordinates, H is the height of the obstacle at the launching point, α is the initial launching angle and U_{detach} is the time-resolved, depth-averaged velocity of the flow above the detachment point. Here, because the flow densities are higher than twice the atmosphere density, the gravitational acceleration is corrected with $g^* = g\sqrt{\frac{\rho_c - \rho_a}{\rho_c + \rho_a}}$ (Gröbelbauer et al. 1993; Kelfoun et al. 2000; Gardner et al. 2018), where ρ_c and ρ_a describe the flow and the atmosphere density respectively.

To check if ballistic trajectories describe the characteristics of the detached flow, we tested a range of ballistic scenarios. This included systematic variation of:

- The detachment point, using the crest position or the location of the observed time-resolved detachment point behind the crest.

- The initial trajectory angle α from variably steep angles defined by the stoss side of the obstacle (i.e. 15° to the horizontal plane), channel-parallel angles (i.e. -6°), or the inclination of streamlines of the detached flow that were observed (typically varies between -5 and -16°).

- The detachment velocity U_{detach} for which we tested depth-integrated velocities of the flow above the detachment point and local velocities in the basal part of the detached flow.

In general, re-attachment distances, wake areas and wake shapes modelled as ballistic trajectories do not describe the observed flow pattern.

When using a detachment point at the crest and an initial trajectory angle of the stoss slope as tested by Gardner et al. (2018), re-attachment distances and wake areas strongly exceed measured values. Indeed, the rotation of streamlines in the last phase of the flow strongly reduces the real wake area, suggesting that the streamline angles should be considered instead of any slope angle.

All other tested combinations of ballistic trajectories strongly underestimate the re-attachment distance and the area of the turbulent wake. Particularly for the case of the small and intermediate obstacle, the deviation between observed and modelled wake areas and re-attachment distances is large. The closest agreement between modelled

and observed wake dimensions are obtained for the largest obstacle and for the scenario of the detachment point defined by the observed detachment point, using the depth-integrated velocity of the flow above the detachment point, and the trajectory angle defined by local flow streamlines.

This latter case is depicted in Figure 5.3, where we compare the calculated and measured re-attachment distance and wake area. Ballistics mostly under-estimate the real values except in the flow head.

In experiment L, the strong acceleration of the flow on the stoss side leads to depth-integrated velocities above the detachment point up to c. 9.4 $m.s^{-1}$ (Fig 5.3a). These high velocities are sufficient for the ballistic equation (Eq. 5.5) to provide a close prediction to the measured D_R (Fig 5.3b-c). The average ratio between the ballistic and the measured re-attachment distance takes a value of 0.94. However, the ballistic trajectory is somewhat lower than the real shape of the wake (Fig 5.3b and 5.3d), and the wake area of ballistics is generally significantly smaller than the real wake area.

For experiments S and M, the flow is not accelerated as much as for experiment L, and the ballistic prediction strongly under-estimates both the re-attachment distance and the wake area (Fig 3c-d).

These results suggest that the wake dimensions are not well modelled by ballistic trajectories, and therefore not controlled by velocity or streamline angles (at least in the first three phases). Instead, flows over the obstacle generate a lift force which extends the re-attachment distance. How this lift force is generated and maintained and how its relationship to the components of the $\Delta P_{loss,1-2}$ term is defined require further investigation. The most likely place to start is to look at density and static pressure inside the wake.

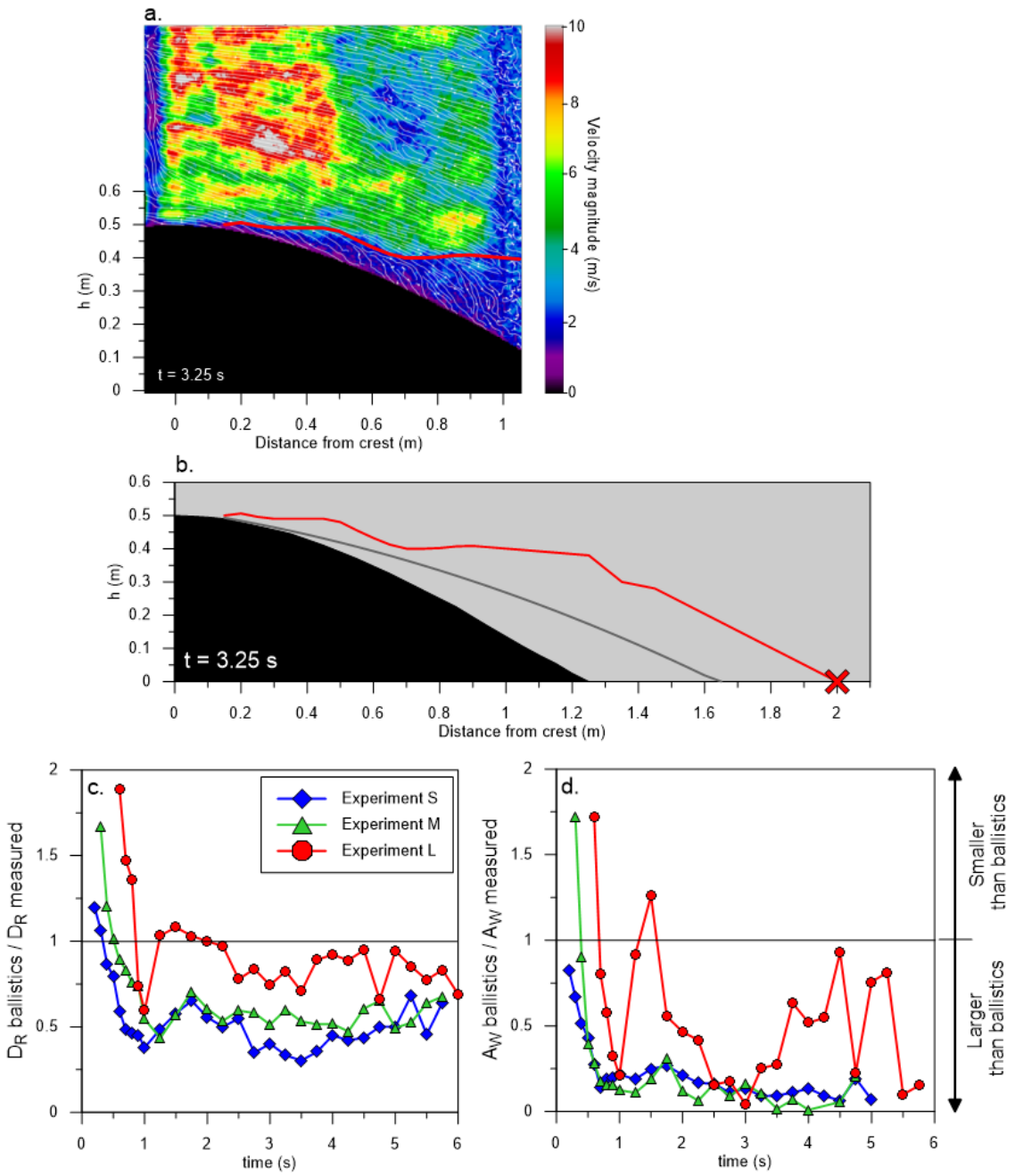

Figure 5.3: Values determined with ballistic models compared with real measurements of the wake for the situation using the real detachment point, the depth-integrated velocity above the detachment point, and the basal streamline angle. (a) Snapshot of the flow in experiment L at t=3.25 s from arrival at the crest in the velocity magnitude field with streamlines. The red curve represents the mapping of the wake area. Note the sharp delineation between the wake low velocities (1-2 m/s) and the high velocities exceeding 10 m/s above. (b) Typical difference between the measured wake trajectory (red curve) and the ballistic trajectory (grey curve) at t=3.25 s from arrival. The red cross corresponds to the measured re-attachment distance. The measured re-attachment distance and wake area are larger than the ballistic estimations. (c) Comparison between the re-attachment distances computed with ballistics and measured. The measured distance is larger than the computed for the small and intermediate obstacles, but takes similar values for the large obstacle. (d) Comparison between the wake areas, showing that ballistics are strongly under-estimating the measured wake, even in the large experiment. Ballistic calculations also produce trajectories smaller than the obstacle in late stages of the current, hence creating negative wake areas, which are here not plotted.

5.3.3. Forces supporting the wake

In the three experiments, the depth-integrated wake densities decrease with increasing obstacle size by up to two orders of magnitude (Fig 5.4a), with densities as high as c. 130 kg/m^3 in the wake of the small obstacle, and as low as c. 1.5 kg/m^3 in the wake of the large obstacle. On average, wake densities decrease from c. 30.3 kg/m^3 in experiment S down to 7.5 kg/m^3 in experiment L. These values suggest that assuming all particles suspended, static pressure is higher in the wake of experiment S and lower in the wake of experiment L.

The relative static pressure difference between the wake and the detached flow above it controls the lift force. Here, this is not a quantity that is directly measured inside the flow, therefore, it needs to be estimated from the measured time-dependant densities and wake thickness. Since ballistic trajectories are a function of gravity, the aforementioned difference in re-attachment distances induces that the lift force reduces the effect of gravity. Kinematic equations allow us to estimate that:

$$\left(\frac{D_{R\,measured}}{D_{R\,ballistic}}\right)^2 = \frac{g}{g-a} = \frac{\rho g Z}{\rho g Z - \rho a Z} \qquad \text{(Eq. 5.6)}$$

where a is the reduction in acceleration due to the uplift provided by the static pressure inside the wake and ρ in the time- and depth-integrated flow density at Profile 2. Rearranging provides the actual static pressure differential (ΔP_{Swake}) between the wake and the detached flow as:

$$\Delta P_{S\,wake} = \rho a Z = \rho g Z \left(1 - \left(\frac{D_{R\,ballistic}}{D_{R\,measured}}\right)^2\right) \qquad \text{(Eq. 5.7)}$$

Averaged values of the static pressure differential are c. 24, 11 and 2 Pa for the wakes of experiments S, M and L respectively (Fig. 5.4b), as suggested by the increasing density in the wake with smaller obstacle size. From the calculation of the static pressure differential, the lift force in the three experiments is obtained with:

$$F_{lift} = A_S . \Delta P_{S\,wake} \qquad \text{(Eq. 5.8)}$$

Figure 5.4c shows the lift force against time for the three experiments. The lift force maintaining the wake is inversely proportional to the size of the obstacle. On average, it takes values of c. 11 N, 8 N and 3 N for experiments S, M and L respectively. In experiment L, the lift force can be negative, and is therefore enhancing the effect of gravity instead of countering it. This correspond to periods where the wake measured is smaller than ballistic estimation (Fig. 5.3a).

In Figure 5.4d, the lift force is compared to the drag force exerted by the obstacle. On average, the force ratio decreases with increasing obstacle dimensions from 5.79 in experiment S, to 2.86 in experiment M and 0.42 in experiment L. In experiment L, the lift force is generally smaller than the drag force and therefore does not take a significant role in the wake stability. These results would suggest that although the drag is responsible for the wake generation, the lift force, and therefore the wake density, is the main factor controlling the wake stability and thickness across the flow duration. Therefore, when the force ratio is negative in experiment L, this suggests that the “lift” is acting with gravity, countering the drag and reducing the wake dimensions.

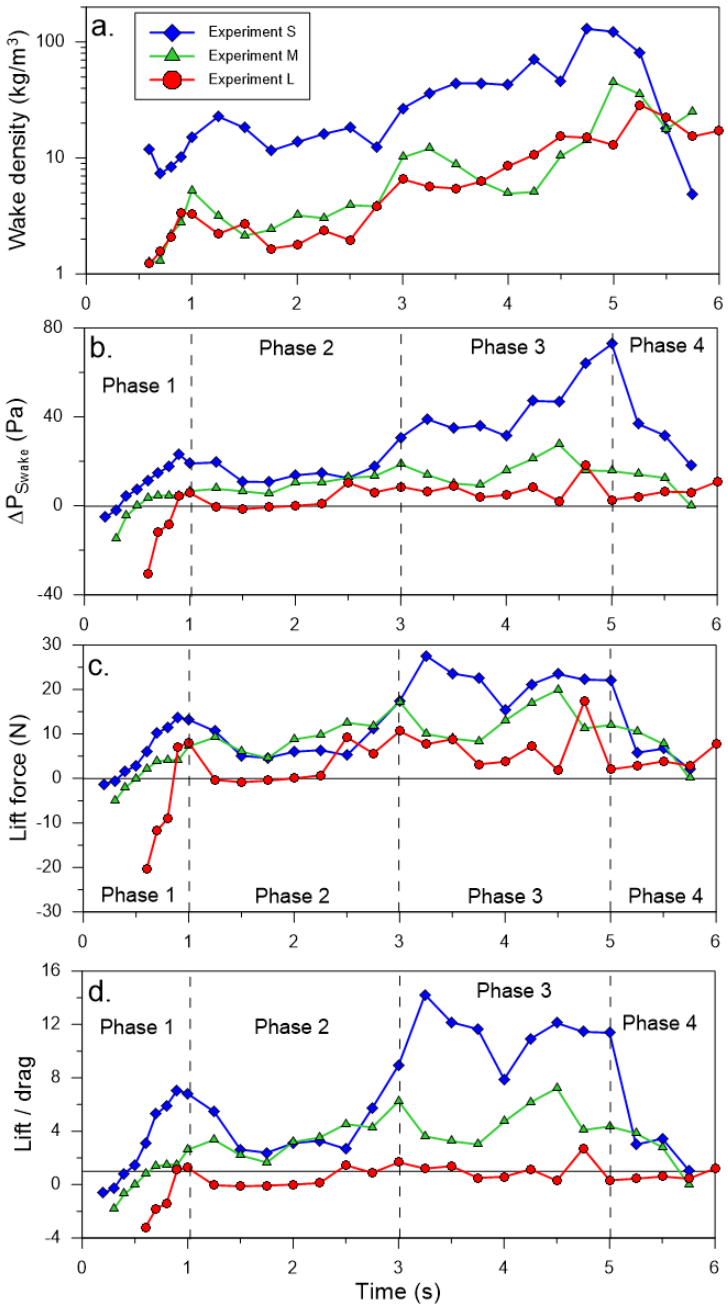

Figure 5.4: Properties of the wakes generated behind the obstacles against time. (a) Particle density inside the wake, showing increasing density with time and with decreasing size of the obstacle. (b) Static pressure difference between the wake and the flow above, showing higher pressures by decreasing the obstacle size. In experiment L, the difference even becomes negative, showing that the flow above pushes down on the wake efficiently. The four phases of interactions between the flow and the hill are well visible with transitions at c. 1s, c. 3 s and c. 5s from flow front arrival at the crest. (c) Lift force of the wake. Averaged values of the lift force show that the wake behind the large hill has the lowest lift force of c. 2.71 N. When the lift force is negative, it is enhancing gravity instead of countering it. (d) Force ratio between the lift and the drag force, showing the dominance of the lift force to maintain the wake aloft in experiment S and M. In experiment L, the lift force is generally smaller than the drag force. Again, the four phases of interactions are well delimited.

The four phases of flow-obstacle interaction are well visible in the variations of static pressure differential, lift force and force ratio over the duration of the gravity current (Fig. 5.4b-d).

- In the head (up to c. 1s), the static pressure increases in the wake. The lift force increases up to c. 14 N in experiment S because of the rotating vortex in the wake, lifting the detached flow and strongly increasing the wake surface area (A_S). The lift force then starts decreasing in the rear of the head.
- In the second phase (c. 1 to 3 s), the static pressure difference is low and relatively constant as the flow is dilute. The wake surface area is decreasing with D_R, and the lift force is therefore relatively low. In experiment L, it can even be negative and enhances gravity. In these cases, the force ratio between the lift and the drag is also negative and shows that the drag is actually countered by the lift.
- Typically, in the third phase of propagation (from c. 3 s), as density suddenly increases, the upper flow above the wake starts pushing down on the wake and bending the boundary layer separation. This effect, associated with bedload flowing over the crest down the slope, introduces more particles inside the wake, increasing its density. The pressure exerted by the flow above is counter-balanced by increasing the static pressure inside the wake. The lift strongly increases in this phase and decrease with increasing obstacle size, from c. 13.6 N in experiment S down to c. 1.8 N in experiment L. A similar pattern is visible in the force ratio, where the lift is c. 11 times higher than the drag in experiment S, and similar to it in experiment L.
- From c. 5 s, in the last phase of interaction, the flow density and velocity decrease and the velocity field rotates, becoming sub-parallel to the lee slope. The drag strongly decreases and the wake progressively disappears. Decreasing static pressure difference and wake surface area subsequently decrease the lift force, which cannot maintain the wake anymore.

The above force analysis shows that for these three flows with similar initial conditions, a clear link exists between the height of the obstacle and the forces in the wake. It is therefore worth speculating whether a similar relationship independent of flow conditions exists. A geometric analysis is proposed in the following, looking only

at the relationship between the re-attachment distance, the height of the obstacle and the height of the maximum velocity of the incoming flow.

5.3.4. Geometric analysis

Because the dimensions of the wake are inversely proportional to the size of the obstacles (Fig 5.2), the relative height of the obstacle compared to the flow must play a role on the wake re-attachment distance and area, as suggested by Hákonardóttir et al. (2003). This non-dimensional height is called the height ratio (H_R) and is defined with:

$$H_R = \frac{H_{crest}}{H_{Umax}} \qquad \text{(Eq. 5.9)}$$

The height ratio depicts the relative thickness of the height of the velocity maximum H_{Umax} of the incoming flow (which can be linked to the total thickness of the flow) compared to the obstacle, hence describing the importance of the obstacle in the flow path. A small height ratio describes an obstacle that is small compared to the flow, and vice-versa.

The height ratio and re-attachment distance compared to the obstacle height are calculated at regular time intervals over the entire flow passage for each experiment and averaged in Fig. 5.5a. The points show a power trend with a best fit power law of the form:

$$D_R = H_{crest} * 5.42{H_R}^{-0.61} \qquad \text{(Eq. 5.10)}$$

From the re-attachment distance, the wake area can be estimated. Figure 5.5b shows data of the scaled wake area against the scaled re-attachment distance. Here, the scaled values are used to account for the reduction of the wake dimensions with increasing obstacle size. With an intercept at 0, the wake area can be approximated by the following squared relationship:

$$A_W = A_H * 0.02 * \left(\frac{D_R}{H_{crest}}\right)^2 \qquad \text{(Eq. 5.11)}$$

Equations 5.10 and 5.11 describe the dimensions of the wake according to the obstacle and flow geometry, but do not take into account the initial flow density, velocity and therefore dynamic pressure.

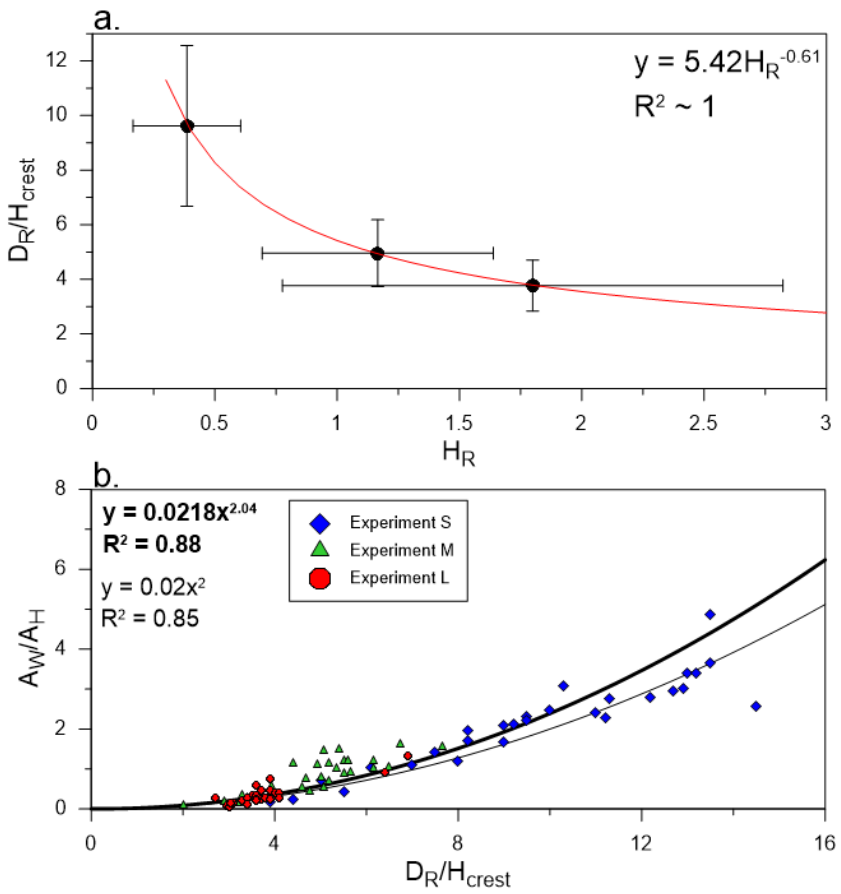

Figure 5.5: (a) Estimation of the re-attachment distance compared to the obstacle height against the height ratio. The three points correspond to the three experiments and are averages over the entire flow duration with c. 30 measurements per experiment. The error bars corresponds to 1 standard deviation and show well the dispersion of the data over a power law shown as the red curve and annotated in the top right corner. (b) Wake area against re-attachment distance, with scaled values to allow a better comparison between the obstacles. The best fit is shown as a bold curve and equation in the top left corner, and simplified as a squared relationship on a thinner curve and equation.

5.4. Discussion

5.4.1. Hazards associated with the wake

The experiments showed that small obstacles exert a low drag force on the flow, which tends to form a small wake. However, over time, both particles transported by bedload over the crest and particles sedimenting from the detached flow into the wake bedload induce a strong increase in wake density with time. As density increases, so does temperature inside the wake as particles carry most of flow's thermal energy. Elevated static pressure allow a high lift during most of the flow propagation. The lift force pushes up the wake and increases its dimensions, making the wake large comparatively to the size of the obstacle.

On the other hand, in the case of a large obstacle, the drag force and the absolute wake dimensions are high. Particles advected back into the flow are highly accelerated and are ejected downstream, mostly travelling above and beyond the generated wake. This effect reduces density and static pressure inside the wake, and therefore, reduces the lift force. Furthermore, the lift force is not high compared to the drag force. Therefore, the wake area is not increased by the lift, and the relative size of the wake is smaller than for smaller obstacles. In some periods, the static pressure differential is negative, showing that the flow above efficiently pushes down on the wake. Hence, the lift force becomes negative and acts with gravity instead of against it. This effect counters the drag and reduces the wake area even more.

In summary, wakes generated behind small obstacles are comparatively larger, but more dangerous because of their high particle load and high temperatures, which can cause suffocation (Baxter 1990; Baxter et al. 1998; Dellino et al. 2021) and fatal burns (Baxter et al. 2017). However, wakes generated behind large obstacle are smaller, but have lower densities and temperatures, hence becoming potentially more "survivable".

5.4.2. Field estimations

In the following, we test the geometric model developed in this study against data from two PDC eruptions. The results of this test are summarized in Table 5.3. A drag coefficient of 0.7 was used on hills having similar shapes and aspect ratios than the experimental obstacles.

Te Maari

The blast-like PDC generated by the 2012 Te Maari eruption travelled c. 2500 m from its source over a succession of seven ridges roughly perpendicular to the flow direction (Breard et al. 2015). Patches of preserved vegetation behind ridge crests were documented after the eruption and are clearly visible in satellite images. Behind the first 40 m high ridge, a patch of undamaged vegetation and distinctly thinner PDC deposits extend to a distance of c. 122 m after the crest. At this position, an approximate flow thickness of c. 80 m was estimated from the elevation of a sharp trail of fine ash deposited by the PDC against sub-vertical lava flow cliffs (Lube et al. 2014). Following the work of Cerminara et al. (2021), the ratio of the e-folding height of the PDC over the thickness of the wall region is approximately constant and takes a value of 5.3. This indicates an approximate height of the velocity maximum to be located c. 15 m above the ground. This suggests that the obstacle was large compared to the flow, with a height ratio of 2.67 (Eq. 5.9). Eq. 5.10 gives a re-attachment distance of 119 m from the crest, which closely matches the measured extend of the tree patch. The wake cross-sectional area is estimated at 1267 m^2 with Eq. 5.11. Figure 5.6a shows the cross section of the hill with the incoming velocity profile, the extent of the tree patch, the calculated re-attachment distance and wake area.

Mount Saint Helens

During the 1980 eruption, the lateral blast propagated for c. 20 km from the source, unhindered by topography (Fisher 1990), leaving patches of trees standing in the lee side of obstacles, generally in the most distal parts of the current (Mullineaux and Lipman 1981; Gardner et al. 2018; Guinn et al. 2022). Gardner et al. (2018) proposed a model of ballistics trajectories corrected with a downward expansion of the front ingesting air. Before this correction, the ballistic equation over-estimated the re-attachment distance of the flow compared to the extent of mapped tree patches. The

observations made in PELE are opposite to theirs, with calculations based on ballistic trajectories under-estimating the re-attachment distance. The reason behind this difference may sit in the simplified model of a triangle-shaped hill used by Gardner et al. (2018). This geometry introduces a positive initial angle α with a detachment at the crest and does not account for lower angles of obstacles near the crest, flow streamlines with negative angles, or turbulent drag causing flow detachment after the crest. Guinn et al. (2022) suggested a revised model where only the head would jump over the obstacle, while the body of the flow would hug topography. Time-resolved interactions between the flow and the obstacles are indeed non negligible. Tree patches would likely record the minimum re-attachment distance after an obstacle, but the observation made in the experiments show that this minimum value of D_R usually occurs towards the end of the current. The head and the body may re-attach further than recorded by tree patches.

On an eastern transect, we tested the large ridge separating Bean Creek and Clearwater Creek, where the crest is located 14 km from the vent. Before the ridge, the thickness of the boundary layer is estimated at c. 400 m above the ground (Esposti Ongaro et al. 2012). The ridge peaks 540 m above its base, hence having a height ratio of 1.35 (Eq. 5.9). Figure 5.6b shows a sketch of the estimated wake dimensions, with D_R located on average 2437 m from the crest (Eq. 5.10), and a wake area of c. 431,000 m^2 (Eq. 5.11). Interestingly, the tree patch mapped at this location by Gardner et al. (2018) extends up to 2200 m from the crest. Hence the results of the empirical model are here close to the reality with a relative error of c. 8 % between the reality and the estimation suggested by Eq. 5.10.

	Unit	MSH - Ridge between Bean and Clearwater Creeks	Te Maari - first hill
h_{crest}	m	540	40
h_{Umax}	m	400*	15*
h_R		1.35	2.67
A_H	m^2	1,058,097	7,144
$A_{H\ projected}$	m^2	2,700,000	20,000
W	m	5,000	500
$D_{R\ scaled}$		4.51	2.98
D_R calculated	m	2,437	119
D_R mapped	m	2200*	122
A_W	m^2	431,069	1,267
$A_{W\ scaled}$		0.407	0.18
Sources		Esposti-Ongaro et al. (2012), Gardner et al. (2018)	Lube et al. (2014), Cerminara et al. (2021)

Table 5.3: Data of the model based on Equations 5.10 and 5.11 applied on different hills around Mount Saint Helens (MSH, USA) and Te Maari (New Zealand) with a drag coefficient of 0.7. The upper block of data represents the parameters for the model. The lower block of data shows the results. The star symbol * represents the values extracted from the source articles.

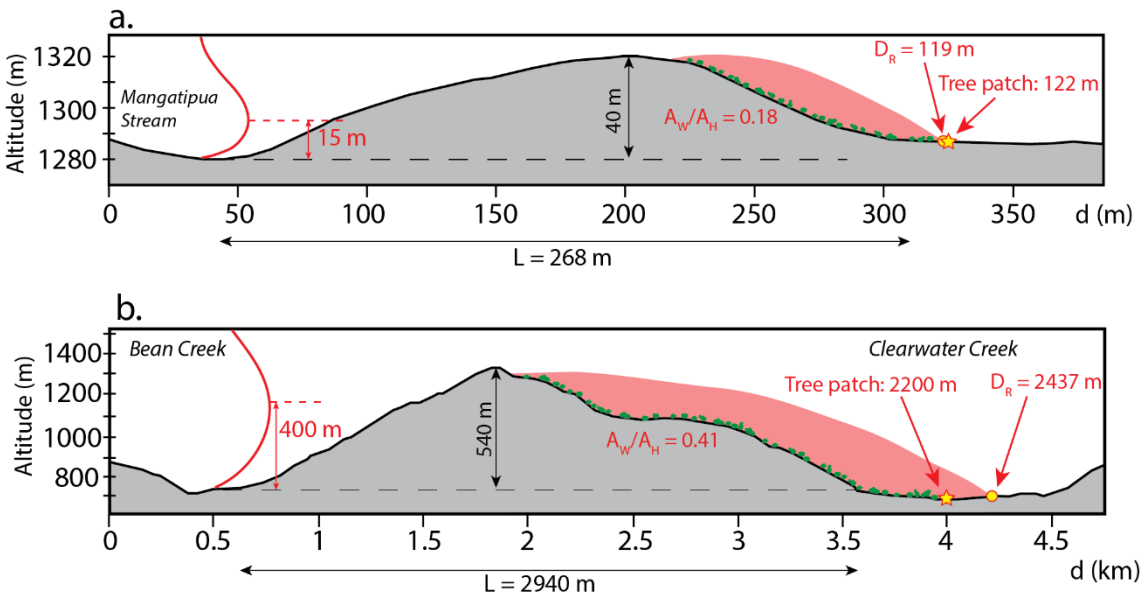

Figure 5.6: Cross-sections of a hill engulfed by blasts at (a) Te Maari, Tongariro, New Zealand, and (b) Mount Saint Helens, USA. On each sketch, the incoming initial velocity profile is drawn on the left with height of the velocity maximum extracted from Esposti Ongaro et al. (2012), or calculated from Lube et al. (2014) and Cerminara et al. (2021). The green pattern on the lee sides represents relatively preserved vegetation, the yellow star the extent of tree patches, and the yellow circle the re-attachment distance calculated from the geometric model of this study. The red shaded area behind the hill corresponds to the wake area. (a) The first hill in the path of the blast generated by the Te Maari eruption has a height ratio of 2.67. A tree patch of preserved vegetation is mapped on the lee side and extends up to 122 m from the crest. Eq. 5.10 and 5.11 allow the calculation of a re-attachment distance reaching 119 m from the crest, with a small wake compared to the obstacle. (b) At Mount Saint Helens, the hill located between Bean and Clearwater Creeks is relatively distant from the source, but shows a large patch of preserved vegetation extending up to c. 2200 m from the crest (Gardner et al. 2018). The calculations of re-attachment distance is close to the mapped patch with D_R of 2437 m.

5.4.3. Limits

In the model proposed here, the wake area and re-attachment distance are only calculated from the obstacle geometry and the flow thickness, but initial velocity and density do not seem to have an effect on the wake area. This model was built based on the three experiments. A larger dataset would be necessary to confirm the power trend calculated in Figure 5.4 and the absence of role of the flow initial conditions (excepted its thickness). Experiments could be run with the same obstacles and different starting conditions to determine if the re-attachment distance and wake area remain the same regardless of flow velocity and density. Alternatively, the obstacles could be placed further down the channel where velocities and densities have decreased. Very large obstacles with a height ratio of 3-5 would also be relevant to confirm or deny this model.

This model allows the calculation of D_R and A_W in nature assuming a given obstacle and height of the velocity maximum. However, it does not allow the calculations of the static pressure differential inside the wake that could be generated by this natural obstacle, and therefore the lift force inside it.

5.5. Conclusions

Large-scale experiments of PDCs were performed with three obstacles of different dimensions in the flow path. The obstacles generated a wake behind them with low velocities. As the obstacles become larger, density and temperature in the wake decrease, and the dimensions of the wake become small compared to the size of the hill. Interestingly, ballistic trajectories do not seem to model the wake, strongly under-estimating its re-attachment distances and area. This suggests that a supplementary lift force must be responsible for increasing the wake dimensions. The lift force calculated in the experiments inversely scales to the obstacle height and varies with the different phases of interactions between the flow and the obstacle. Interestingly, the lift force is up to c. 14 times larger than the drag force and seems more important in maintaining the wake aloft. A geometrical analysis allows an empirical estimation of

the re-attachment distance behind an obstacle controlled by the height ratio between the hill and the boundary layer thickness of the incoming flow.

For small obstacles, the drag force is low and generates an initially small wake. However, particles advected on the stoss side are not well accelerated and tend to sediment quickly and fall inside the wake. The flow loses its energy, and the wake becomes very dense, which allows a high lift force. The wake becomes significantly large compared to the size of the hill as gravity is strongly countered. However, for large obstacles, particles are ejected at high velocities above the wake and travel above it: the wake is relatively cold and dilute. Even though the drag force is higher, the lift force is low and the wake area becomes comparatively smaller. This latter effect can reduce the wake area even more when the lift force acts together with gravity instead of countering it.

The geometric estimations of the re-attachment distance and wake areas allowed the construction of a model that can be applied on the field. This model was tested on several real world examples and gave values in close agreements with the mapped patches of preserved vegetation. More experiments would however be necessary to test this model with different initial conditions and/or different obstacles.

5.6. Supplementary materials

Scaling parameters	*Symbol*	*Unit*	*PELE experiment with obstacles*	*Nature*
Particle size	δ	mm	0.002 - 16	0.002 - 1000
Velocity	U	m/s	3 - 12	10 - 200
Density	ρ	kg/m^3	1 - 15	
Reynolds	Re	-	10^5 - 10^7	10^6-10^9
Richardson	Ri	-	0.5 - 4	0 - 10
Thermal Ri	Ri_T	-	0.003 - 0.7	0 - 5
Densimetric Froude	Fr'	-	0.6 - 15	~ 1
Stokes	S_T	-	10^{-3} - 10^1	10^{-3} - 10^7
Stability	Σ_T	-	10^{-2} - 10^1	10^{-6} - 10^9
Rouse	Pn	-	1 - 20	10^{-3} - 10^2

Supplementary material 5.1: Scaling table comparing the dimensionless numbers between the three experiments and nature. Data in nature extracted from Burgisser et al. 2005 and Choux and Druitt 2002.

6. Effects of hill-shaped terrain on the runout and hazard characteristics of pyroclastic density currents

L. Corna, G. Lube, E. Brosch, D. Uhle, J. Ardo, J. Jones

Abstract

Pyroclastic Density Currents (PDCs) are hot, fast-moving gas-particle clouds flowing down volcanoes. They can propagate unhindered across topographic obstacles, potentially impacting areas that may not have been previously considered in hazard planning. Because internal measurements of real-world PDCs are hardly possible, we performed here a series of large-scale experiments looking at the interactions of PDCs with hill-shaped obstacles of varying size, focusing on the consequences on the flow dynamics up to a 30 m final runout.

A wake with relatively low densities, velocities and temperatures is formed immediately behind the obstacle and increases in size according to the obstacle dimensions. The wake creates an initially unstable stratification with a hot, dense, fast-moving flow above a cold, dilute, slow wake. Up to c. 50 % of the initial momentum is lost after the hill as density and velocity decrease.

Variations in flow density, velocity and deposit characteristics occur up to half of the final flow runout. Afterwards, flow dynamics, deposits and final runout distances are remarkably similar for all obstacle scenarios. This implies that topography and momentum loss have little consequences on downstream hazard impacts and that processes countering them are present. We suggest that small obstacles do not affect flow propagation downstream. However, large obstacles have the ability to transport particles from lower flow regions back into the main flow. The density strongly decreases immediately behind the hill because of the blocking of the underflow on the stoss side and the generation of a large dilute wake. The density ratio is however maintained for long distances in a hotter flow. On the other hand, internal energy pulses visible as density discontinuities propagate unhindered by the obstacle. They

reach the slow flow head and are responsible for strong and sudden accelerations, leading to similar final runouts.

6.1. Introduction

Pyroclastic Density Currents (PDCs) are produced during explosive volcanic eruptions and consist of hot, gas-particle multiphase mixtures travelling at high speed down a volcano (Druitt 1998; Branney and Kokelaar 2002). PDCs are the most lethal volcanic phenomena excluding tsunamis and famines (Baxter 1990), responsible for killing tens of thousands of people since 1783 (Tanguy et al. 1998). Hazards associated with PDCs include high dynamic pressures up to hundreds of kPa enhancing destruction of structures (Valentine 1998; Baxter et al. 2005; Brand et al. 2014; Esposti Ongaro et al. 2012; Brosch et al. 2021), fine ash content leading to suffocation (Baxter 1990; Hincks et al. 2006; Dellino et al. 2021), and temperatures reaching 200 to 500°C responsible for most of their lethality (Voight and Davis 2000; Mastrolorenzo et al. 2001; Loughlin et al. 2002; McClelland et al. 2004; Hudspith et al. 2010; Baxter et al. 2017; Giordano et al. 2018). Furthermore, PDCs have the ability to cross significant topographic obstacles, making it challenging to predict their hazard footprint (e.g. Risica et al. 2022). Understanding the effects of topographic obstacles on the downstream flow and hazard dynamics of PDCs is essential to inform qualitative hazard modelling approaches and hazard mitigation practices.

Several studies have addressed the ability of PDCs to climb topographic obstacles through field study (e.g. Wilson 1985; Fisher et al. 1993; Burgisser 2005; Sulpizio et al. 2008; Cas et al. 2011; Breard et al. 2015), numerical approaches (e.g. Doronzo et al. 2010; Kelfoun and Gueugneau 2022), analogue (Alexander and Morris 1994; Woods et al. 1998; Bursik and Woods 2000; Oshaghi et al. 2013; Abhari et al. 2018; Wilson et al. 2018) and large-scale experiments (Andrews and Manga 2011; Andrews 2014).

Four main parameters are to consider regarding the consequences of an obstacle in the path of a PDC:

- (1) T*he extent of the final runout*. Fisher (1990) proposed that the runout distance was affected by hilly terrain especially when the ridge of the obstacles is perpendicular to the flow path. However, more recent studies showed that only the flow head (and therefore its thickness, density and temperature) controls the flow runout, and that obstacles in the flow path do not affect these parameters which are rather controlled by the initial flow mass (Andrews and Manga 2011) and discharge rates (Roche et al. 2021; Roche et al. 2022).
- (2) *The scale of downstream dynamic pressures*. Direct measurements of dynamic pressures are too dangerous to be done in-situ, but the study of tree damage allowed characterisation of very high dynamic pressure up to 39.7 kPa on the stoss side of ridges during the 1980 Mount Saint Helens eruption (Clarke and Voight 2000). Guinn et al. (2022) also suggested that hills could protect trees in their lee side during the passage of the head, but that the flow body would be more ground-hugging, with lower dynamic pressures still able to strip the vegetation.
- (3) *Flow density and fine ash content*. In numerical experiments, Doronzo et al. (2010) noted turbulent mixing of particles downstream of the obstacles. This mixing of particles after the hill could be enhanced as the flow re-attaches to the ground, elutriating fines in the dilute surge and reinforcing it (Kelfoun and Gueugneau 2022). Deposits of the flows may reflect how the conditions of emplacement change after an obstacle, but no consensus has been reached so far. In water-tank experiments, Bursik and Woods (2000) noted that deposit were unchanged behind small ridges, while Alexander and Morris (1994) suggested that obstacles were reducing the thickness and extent of deposits downstream of obstacles.
- (4) *Flow temperature downstream of the hill.* Flow temperatures were modelled at Vesuvius and showed higher downstream temperatures when the flow were initially encountering an obstacle (Todesco et al. 2002).

However, because no direct observations have been done inside PDCs, there is still a gap in our current knowledge. How do all these parameters link together? How do obstacles of varying size influence them? How do the deposits formed behind obstacles relate to the dynamics of PDC-hill interaction? Here, we performed a series of three large-scale experiments with hill-shaped obstacles in the flow path. We kept the shape of the obstacle similar but increased their heights relatively to the height of

the velocity maximum of the flows. We interrogate the changes in flow structure, grainsize, velocity and temperature after encountering the obstacle and how these parameters vary for different obstacle heights.

After introducing the general characteristics of the flows and the strong local changes occurring immediately after the hills in the flow structure, we describe the flows until the end of the runout. We start by focusing on the flow front kinematics, followed by internal flow characteristics such as density, forces, grainsize and temperature. Energy spectra are analysed at multiple positions of the setup regarding specific kinetic energy and temperature. Finally, we describe the resulting deposits characteristics after the different obstacles. The results of the experimental study are discussed in the context of hazard impacts near volcanoes.

6.2. Methods

6.2.1. PELE setup and materials

The experimental flows were performed in the eruption simulator PELE (Lube et al. 2015). PELE is divided in four main structures depicted in Fig. 6.1:

- The hopper: a 0.7 m^3 reservoir placed at 7 m high, with a heating system and trap doors opening at the experiment trigger, releasing the mixture.
- The shroud: a shrouded vertical section of heatproof clothe connecting the hopper with a flow channel. Upon hopper opening, the mixture falls, accelerates through the shrouded section and dilutes through entrainment of ambient air. It also channelizes the mixture into the channel.
- The confined runout: a 14.2 m long instrumented channel with wall height from 1.8 m to 0.6 m. One side is a steel wall, the other side is a glass wall allowing visualisation of the experimental PDCs internal processes. The channel has a 6° angle until 11.7 m and is horizontal afterwards. The channel base is covered with a 2 cm thick layer of greywacke pebbles with particle diameter ranging from 4-8 mm. They are glued onto the base (and onto obstacles) to prevent their erosion, then loosely placed from 5 m (Fig. 6.1). For a natural PDC with

a thickness of c. 500 m, these pebbles scale to a natural surface roughness of c. 1 m that represents boulders and shrub in the path of PDCs.

- The unconfined runout: an additional 16 m long non-channelized, horizontal runout on concrete in an outdoor section.

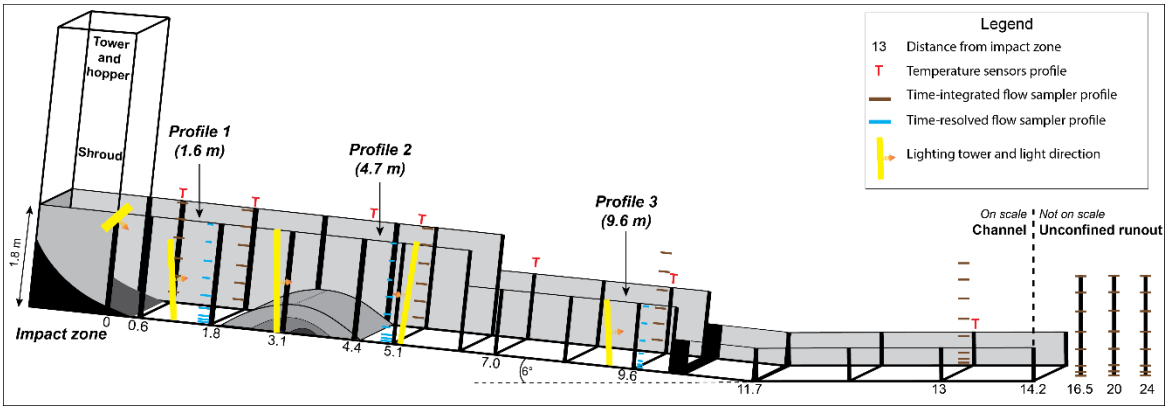

Figure 6.1: Sketch of the PELE setup, showing the channel with the three main Profiles 1, 2 and 3, as well as the three obstacles.

During the experiment, the mixture is dropped from the hopper, expands as it falls and, upon impact, blasts into the channel before continuing for an additional 16 m in an external unconfined runout (Fig. 6.1-2). Table 6.1 compares the non-dimensional numbers calculated in the experiments to those estimated in natural PDCs. The good scaling of the experiments is highlighted with a Reynolds number reaching 2×10^6 and the Stokes Number of 10^{-2} – 10^0 showing a wide range of feedback between the particles and the gas phase.

Scaling parameters	*Symbol*	*Unit*	*PELE experiment with obstacles*	*Nature*
Particle size	δ	mm	0.002 - 16	0.002 - 1000
Velocity	U	m/s	3 - 12	10 - 200
Density	ρ	kg/m^3	1 - 15	
Reynolds	Re	-	10^5 - 10^7	10^6-10^9
Richardson	Ri	-	0.5 - 4	0 - 10
Thermal Ri	Ri_T	-	0.003 - 0.7	0 - 5
Densimetric Froude	Fr'	-	0.6 - 15	~ 1
Stokes	S_T	-	10^{-3} - 10^1	10^{-3} - 10^7
Stability	Σ_T	-	10^{-2} - 10^1	10^{-6} - 10^9
Rouse	Pn	-	1 - 20	10^{-3} - 10^2

Table 6.1: scaling parameters comparing non-dimensional numbers between the experiments and nature. Real-world data is extracted from Burgisser et al. (2005) and Choux and Druitt (2002).

For these three experiments, we used a mixture of 200 kg of pumice and ash from the 232 AD Taupō Ignimbrite (New-Zealand) sampled 17 km North-east from the inferred vent (Wilson 1985). The mixture has a median grainsize D_{50} of 1.24Φ, a sorting coefficient σ of 3.22Φ, and a high content of fine ash with particle diameter smaller than 63 μm (26.5 wt%). The mixture grainsize distribution is shown in Supplementary materials. After sampling, the mixture was heated at 100°C during a week before being placed in the hopper during three more days at 120°C to remove residual moisture.

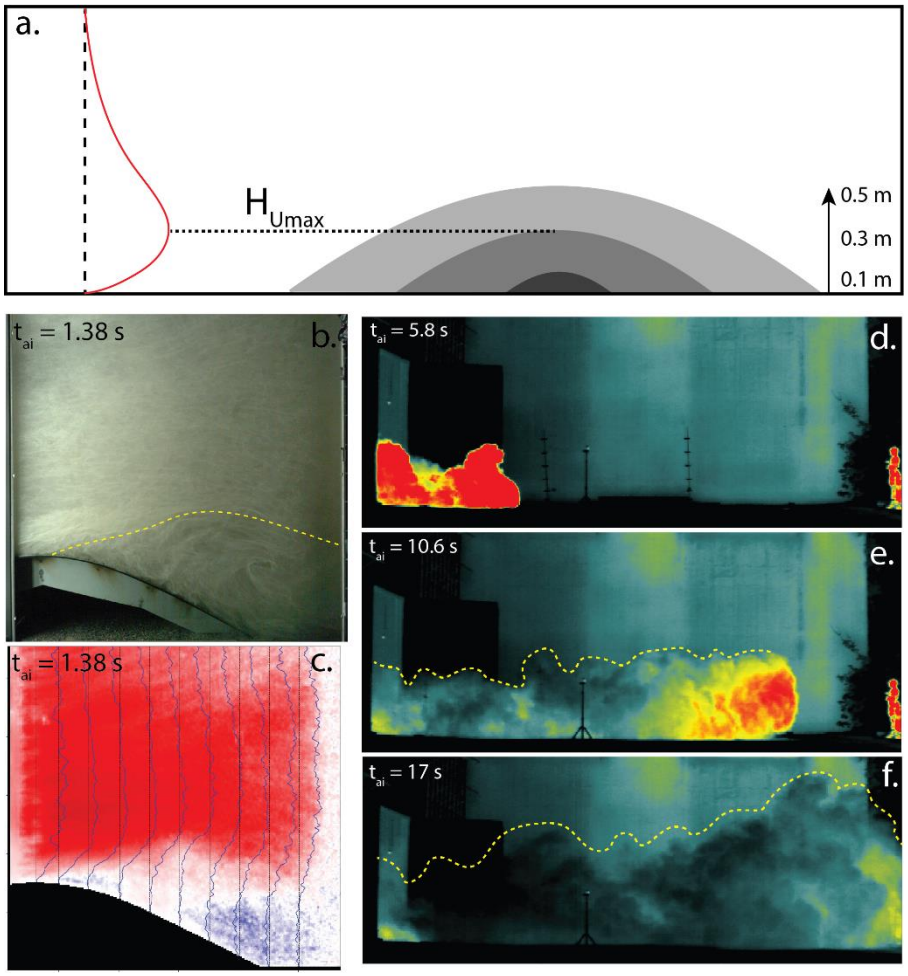

Figure 6.2: Overview of the experiments and the scaling of the obstacles. (a) sketch comparing a typical vertical velocity profile in dilute PDCs with the three obstacles and their associated heights. (b) snapshot of the flow separating over the intermediate obstacle with the formation of a cold, dilute, rotating vortex underneath a hotter, denser upper flow at 1.38 s after impact. The dashed yellow line marks the boundary layer separation between the wake and the upper flow. (c) Snapshot of the same frame looking at the downstream velocity component (noted U). Note the thick backflow in the wake as the vortex is formed (shown in blue colours for negative velocity). An inflexion point in the velocity profiles delimits the wake. (d-e-f) same flow in the unconfined, horizontal, distal runout viewed by the thermal infrared camera at three different times after impact, showing the progression of (d) a hot, shallow flow into (e) lower temperatures with a hot head near buoyancy reversal, into (f) a fully buoyant, thick, cold flow. Dashed yellow lines mark the flow shapes. A 170 cm tall person is on the right-hand side of the image for scale.

PELE is equipped with over 200 sensors, samplers and cameras for each experiment, positioned at distances from the impact zone of 0.6, 1.8, 3.2-4.8, 7, 9.6, 13, 16.5, 20 and 24 m (Fig. 6.1). These locations measure a combination of time-variant temperatures, velocities and particle concentrations of the flow. Three main profiles positioned at 1.6, 4.7 and 9.6 m (and named Profiles 1 to 3) are defined to characterize the flow dynamics before and after the obstacles (Fig.6.1). Profiles 1 and 2 flank the obstacles to define flow characteristics before and after the hill. Profile 3 is a medial to distal position to characterise the flow downstream.

The following equipment was used across the setup. Thermal sensors (TC Direct 410-345 Type K) with a sampling rate of 70 Hz were installed in the channel as vertical profiles from 3.5 cm to 1.8 m above the base. In the unconfined section, the flows were recorded with an infrared thermal camera Infratec VarioCAM at 50 frames per second (Fig 6.2). An array of 22 cameras recorded the flow propagation along the entire setup with speeds of 30 to 240 fps. High-resolution, high-speed cameras recording at 1000 fps were deployed at (1) Profiles 1 to 3 and (2) across the entire window length showing the lee side (downstream side) of the obstacles between 3.2 and 4.4 m. They recorded the internal flow dynamics and velocities were analysed through particle-image-velocimetry using PIVlab (Thielicke and Stamhuis 2014). Time-resolved flow concentrations were calculated at Profiles 1 to 3 by recording the filling of glass sampling tubes on the window following the methods detailed in Brosch and Lube (2020). In order to ensure synchronization of all the sensors and cameras, a trigger signal was implemented at the experiment trigger.

Time-integrated flow mass and grainsize were collected from flow tube samplers at 8 different profiles and heights of 6 to 180 cm above the channel base (21 to 180 cm for the four most proximal profiles). Deposits were sampled with a 15 cm diameter core in the centre of the channel over the first 5 metres where bed roughness was glued. From 5.5 m after impact, aluminium trays of known area were placed at 1.5 m interval. From 14.5 m after impact, trays were emplaced at 3 m interval.

6.2.2. Obstacle design and position

All three experiments have the same starting conditions and hill-shaped obstacles were placed inside the channel. The obstacles have the same shape and only their size vary between each experiment. Digital Elevation Models were used to estimate an average shape of hills in the flow paths of real-world volcanoes like Merapi (Indonesia), Mount Saint Helens (USA), Tongariro (New-Zealand) and Bandai (Japan). The shape was estimated to mimic the geometry of natural obstacles based on their aspect ratio (defined by the ratio of the height over the length of the obstacle) and slope angles. The demi-shape of the obstacles was then estimated using:

$$H = H_{crest} - \left[\frac{H_{crest}}{\left(\frac{L_{max}}{2}\right)^2}\right] * L^2 \qquad \text{(Eq. 6.1)}$$

with H the height of the obstacle at a distance L from the crest, H_{crest} the maximum height of the obstacle at the crest, L_{max} the total length of the obstacle. The aspect ratio is 0.2 and the initial slope was corrected to an angle of 21°.

The desired heights were chosen according to the height of the velocity maximum (H_{Umax}) in the flows at Profile 1. In PELE the averaged H_{Umax} is located approximately 0.3 m above the channel base. Hence, as depicted in Figure 2a, the height at the crest is lower than the velocity maximum for the small obstacle (0.1 m), similar for the intermediate (0.3 m) and higher for the large (0.5 m). The time-integrated ratio of the height of the obstacle over the time-integrated height of the velocity maximum (H_{crest}/H_{Umax}) is here called the height ratio and describes how large is an obstacle compared to the flow. The small obstacle has a height ratio of 0.36, the intermediate obstacle has a height ratio of 1.3, and finally, the large obstacle has a height ratio of 1.72.

The obstacles were placed according to three criteria: (1) the position of the crest needed to be similar; (2) the gravity current structure and vertical density stratification needed to be fully developed upon reaching the beginning of the obstacle and (3) the obstacle needed to be placed in the proximal section of the channel (<5 m) to maximise the length of observations of the resulting flow downstream. Their crests were placed 3.3 m from the impact (Fig. 6.1). The small obstacle was shifted slightly downstream, with a crest at 3.55 m from the impact, so that the entirety of the obstacle would be visible by the same camera without significant changes in the overall flow dynamics upon the arrival at the hill.

For purposes of simplification, in the following, the experiments are called Experiments S, M or L (standing for Small, Medium and Large).

6.2.3. Sampling and laboratory methods

The time-integrated flow samplers were carefully removed from the channel and weighted to calculate the total mass of particles at different heights of the flow. Afterwards, grainsize distributions were obtained through a combination of dry sieving

at half-phi intervals and Laser Particle Analysis. Statistical characteristics such as median and sorting coefficient were calculated using GRADISTATS (Blott and Pye 2001) with the method of Folk and Ward (1957).

Deposits thickness were measured at 5 cm intervals up to 5 m from the impact zone. Deposit mass and mass per area were measured from the trays and core samples aforementioned. After sampling and mass measurements, deposit grainsize distributions were obtained through a combination of wet sieving at half-phi intervals and Laser Particle Analysis.

6.2.4. Flow densities

At positions Profiles 1, 2 and 3, time- and height-resolved densities are calculated from recorded velocities and time-resolved filling of material in samplers (Brosch and Lube 2020). In order to estimate flow densities in the unconfined flow path where neither high-speed cameras nor time-resolved samplers were present, we assumed that only the flow head was depositional. The flow head density was then calculated as:

$$\rho_C = \frac{m_{a(T)} + m_C}{V} \quad \text{(Eq. 6.2)}$$

with ρ_C the flow density, $m_{a(T)}$ the mass of air at the temperature T in the volume V of the head, and m_C the mass of particles in the head, hence the integrated cumulative mass of particles not yet deposited.

6.3. Results

6.3.1. General flow characteristics

Upon impact, the flow expands and is blasted into the channel. It rapidly develops a gravity current structure, comprising a 1-2 m thick head travelling at c. 5.5 m/s, followed by a shallow c. 1.1 m thick body. Inside the current, solid shear with the bed roughness and free shear with the air leads to the formation of a power-Gaussian

velocity profile. The height of the velocity maximum is located at c. 0.27 m. The maximum velocity ranges on average between 5 and 6 m/s at Profile 1. At Profile 1, the time- and depth-integrated flow particle concentration (Cf_{full}) is c. 0.35 vol%, corresponding to a density (ρf_{full}) of c. 6.5 kg/m^3 and a density ratio of the flow density over the density of the ambient air of around 5. A thick (up to 0.1 m), slow moving (c. 1 m/s), dense (up to c. 500 kg/m^3) underflow develops at the base of the current from c. 3 s. This flow is overridden by a dilute surge with particle concentrations Cf_{dilute} of c. 0.14 vol%, corresponding to a density ρf_{dilute} of c. 3.4 kg/m^3. At profile 1, the time- and depth-integrated momentum is approximately evenly split between the slow underflow carrying most of the mass and the fast-moving dilute surge.

The flow propagates downstream and encounter the obstacle where it compresses and accelerates on the stoss side. It detaches after the crest and re-attaches further downstream, leading to the formation of a turbulent wake underneath the detached flow. All three flows keep propagating downstream with velocity and density generally decreasing. However, the density ratio with the atmosphere remains high for most of the propagation and flows are non-Boussinesq (density difference between flow and atmosphere >10 %) until c. 23-25 m from impact. Eventually, the flows become buoyant and lift off at c. 28 m from the impact.

Deposition of the entire PDC takes around 20 s, but the phoenix cloud sedimentation can last several minutes after the end of the propagation. The resulting deposits decrease in thickness with distance, with strong changes around the obstacles. Before the obstacle, a large regressive dune up to c. 0.4 m thick is formed. Its geometry becomes flatter when increasing the size of the obstacles. Partial blocking occurs on the stoss side of the hill, forming thick, massive, poorly sorted deposits. Most of the mass is blocked before the crest of the obstacles: 90% for experiment S, 85 % for experiment M, and 80 % for experiment L. Downstream from the crest, the deposits thins from centimetric down to sub-millimetric values in the most distal locations.

6.3.2. Changes in vertical flow structure across the obstacles

At Profile 1, the flows are strongly density stratified with time-integrated particle concentrations as low as 10^{-4} vol% in the dilute surge and reaching up to 22 vol% in the dense underflow (Fig. 6.2a-c).

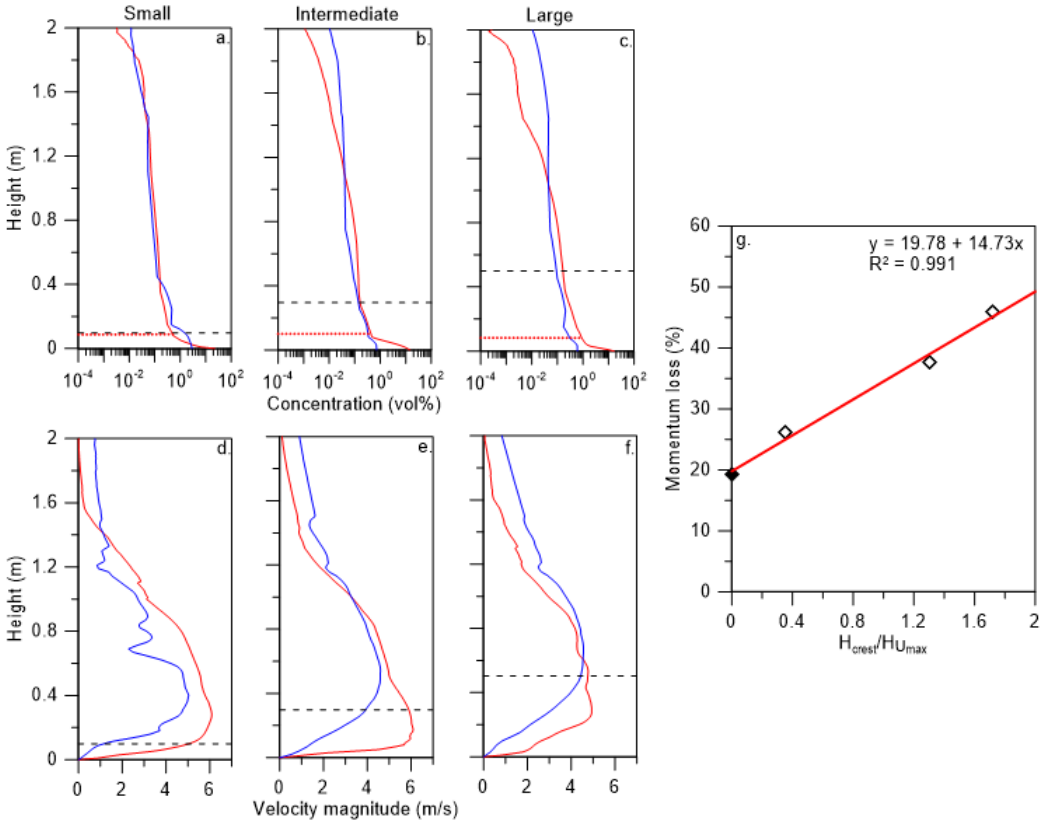

Figure 6.3: Flow characteristics between the Profiles 1 and 2. (a-b-c) time-integrated concentration profiles at Profile 1 (red curve) and 2 (blue curve) for each experiment, showing that upper flow regions >1.1 m become loaded in particles after the intermediate and large obstacles. The red dashed line depicts the maximum bedload thickness. The black dashed line represents the hill height. (d-e-f) time-integrated velocity profile showing a general upward shift in the maximum velocity after the obstacle. (g) momentum loss between Profile 1 and 2 for the three experiments (open symbols) against the height of the obstacle normalised to the height of the maximum velocity. The closed symbol on the vertical axis represents a no-obstacle experiment run by Brosch et Lube (2020). The momentum loss is linearly correlated to the obstacle height (red curve).

Upon encountering the obstacles, the slow underflow is stranded on the stoss side and the fully dilute turbulent upper flow region is also partially blocked.

At Profile 2, the flows are increasingly disturbed with increasing obstacle height because of the formation of the turbulent dilute wake behind the obstacles. In experiment S, time- and depth-integrated concentration Cf_{full} remains high to c. 0.26 vol% (5.19 kg/m^3). However, in experiments M and L, Cf_{full} decreases down to c. 0.09

vol% (2.63 and 2.57 kg/m^3 respectively). Particle concentration in the upper flow regions (i.e. h > 1.1 m above the base) are markedly higher than for Profile 1 (Fig. 6.3a-c), showing an unstable density stratification. Similarly, velocity profiles are also disturbed by the hills. The height of the velocity maximum shifted upward to 0.4, 0.55 and 0.68 m above the base for experiments S, M and L respectively. The maximum velocity has also decreased down to 4-5 m/s (Fig. 6.3d-f). Finally, in all the experiments, the shear at the base of the flow is significantly lower than in Profile 1.

Measurements of flow velocities and concentrations allows the calculation of the depth- and time-integrated momentum $\bar{M}$ as:

$$\bar{M} = \overline{\rho_C} V \overline{U_C} \quad \text{(Eq. 6.3)}$$

with ρ_C the flow density, U_C the flow velocity, V the flow volume. The volume is calculated as the product of the channel width, the flow thickness and U_C.

Considering only the dilute proportion of the flow, the time- and depth-integrated momentum shows strong loss from 25 to 50 % with increasing obstacle size (Fig. 6.3g). The data is plotted against the height ratio of each obstacle. In Figure 6.3g, an extra data point was added for a case with no obstacle (height ratio of 0) calculated from Brosch and Lube (2020). The momentum loss and the height ratio are positively correlated and well fitted by a linear equation of the form:

$$\bar{M}_{loss} = 19.78 \left(\frac{H_{crest}}{H_{Umax}}\right) + 14.73 \quad \text{(Eq. 6.4)}$$

6.3.3. Flow front kinematics

The density contrast with the ambient air is the main driving force for the current downstream of the obstacle. Therefore, the combination of density and momentum loss would suggest that experiment S propagates further than experiment M and L. To check this hypothesis, the position of the flow front was mapped at time intervals of 50 to 500 ms along the entire flow propagation using overview cameras recording at 30-120 fps. Flow front velocities were then calculated.

Figure 6.4a shows the position of the flow front against time for all three experiments on linear scales. Before the obstacle, the flow front position is identical for all three experiments at the same time after impact. After c. 0.4 s, the gravity

currents reach Profile 1 with flow front velocities of c. 5.0 m/s. After the crest, experiments M and L show a significant delay compared to experiment S. However, the three flows reach their maximum runout at approximately the same time. Figures 6.4b show the same data broken up into single plots for each experiment, on a log-log scale.

Data of the position (and velocity) of the flow front against time can be subdivided into three main kinematic regimes of different constant deceleration rates:

In regime 1, characterising the flow from impact until the obstacle, the front is strongly decelerating. On log-log scales, data of distance against time fall onto lines of slope 1. This regime is equivalent to the inertial regime of non-Boussinesq gas-particle gravity currents defined by Brosch et al. (2022).

Regime 2 characterizes the flow from behind the obstacle and to a distance of c. 28 m. Distance-time data on log-log scales fall onto lines of slope 2/3. This regime corresponds to the inertia-buoyancy regime of Brosch et al. (2022).

Regime 3 occurs from c. 28 m onwards. The flow front decelerates more strongly with distance against time on log-log scales, falling onto lines of slope 1/5. Brosch et al. (2022) identified this regime as a regime where inertial forces and drag forces are balanced.

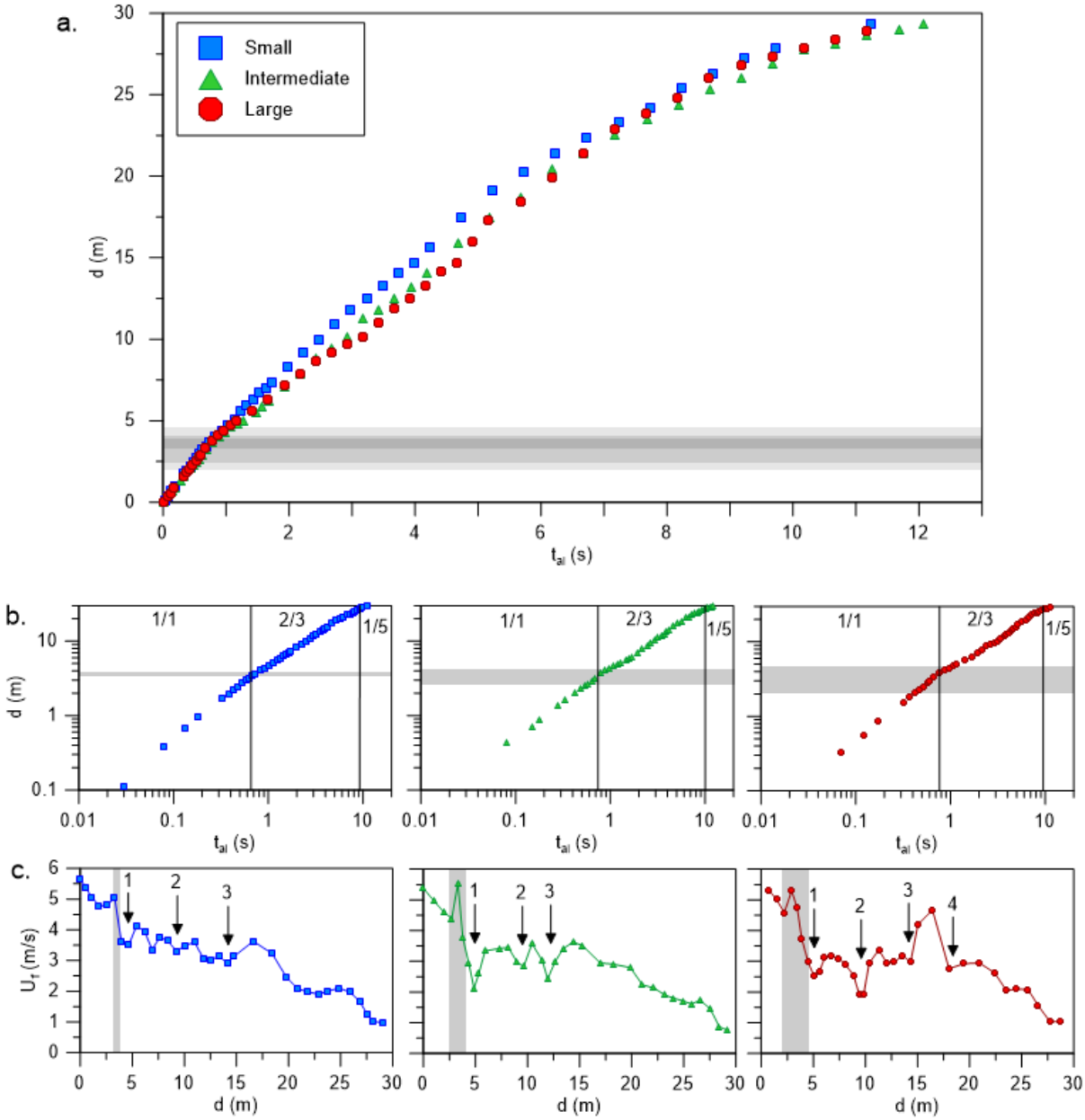

Figure 6.4: Kinematics of the flow front for each experiment. The shaded areas mark the obstacles. (a) Position of the flow front for each experiment compared with time on a linear scale. While the three datasets are comparable before the obstacles, decelerations of the flow front are visible immediately after the crest and are increasingly stronger with obstacle size. Experiment L becomes significantly delayed compared to experiments S and M. However, the three flows reach the same distance at similar times. (b) Same dataset showing each experiment separately on log-log scales, where deceleration and acceleration are strongly visible. The black lines represent the changes in flow regime with general slopes of 1, 2/3 and 1/5. (c) Flow front velocity with distance after impact. Note the strong acceleration of the flow upon reaching the stoss side, followed by a deceleration that becomes stronger with larger obstacles. Acceleration peaks are visibly disrupting the deceleration after the hill and become stronger with increasing obstacle size. They are numbered 1-4.

This general trend of deceleration is however interrupted by short-lived accelerations (Fig 6.4c) in the first two regimes. The first acceleration occurs on the stoss slope of the obstacles, and is the strongest in experiment M, with velocities

increasing from 4.4 to 5.5 m/s. As the flows detach, expand and ingest a large volume of air during the wake formation, they strongly decelerate from c. 5 m/s down to c. 2 m/s. This strong deceleration occurs immediately before the second regime. In experiment S, velocity decreases relatively steadily during the second regime. However, from c. 5 m onward, three small acceleration peaks are visible (Fig 6.4c) with velocity increases up to 0.7 m/s. In experiment M, three peaks are markedly more visible and correspond to velocity increases up to 1.2 m/s. No acceleration occurs after c. 15 m from the impact. In experiment L, the four peaks are very strong, with velocity increases up to 1.7 m/s. The sudden and brief acceleration peaks are present until c. 21 m from the impact. The initiations of the accelerations of the second regime are numbered in each individual plot of Figure 6.4c.

Taking a closer look at the times when these acceleration peaks occur, we notice energy pulses inside the flows travelling downstream as density discontinuities. These discontinuities are visible through their bow-shaped density contrast with the surrounding flow as described by Brosch et al. (2021). They also coincide with sudden increases and decreases in temperature of 1 to 5K and lasting between c. 0.05 and 0.25 s. A typical peak is shown in Figure 6.5b and shows a sharp temperature increase of 5K followed by a cooling during a time interval of 0.25 s. Thus, the visual mapping and the temperature data can both be used to compile a detailed distance-time dataset of 12-14 density discontinuities in each experiment up to 20 m from the impact zone.

Figure 6.5a shows the distance-time plot of the flow front and the 14 density discontinuities of experiment L on a linear scale. Before the obstacle, the velocity of the discontinuities is markedly constant with an average of 6.45 m/s. A notable feature of the density discontinuities is their ability to travel across the obstacle without significant changes in their velocity. At Profile 2 in experiment L, the density discontinuities have an average velocity of 6.2 m/s. Their velocity only slightly decrease to c. 6 m/s at Profile 3. Therefore, the density discontinuities travel faster than the head and their arrival in the frontal part of the flow coincides with the acceleration peaks previously described.

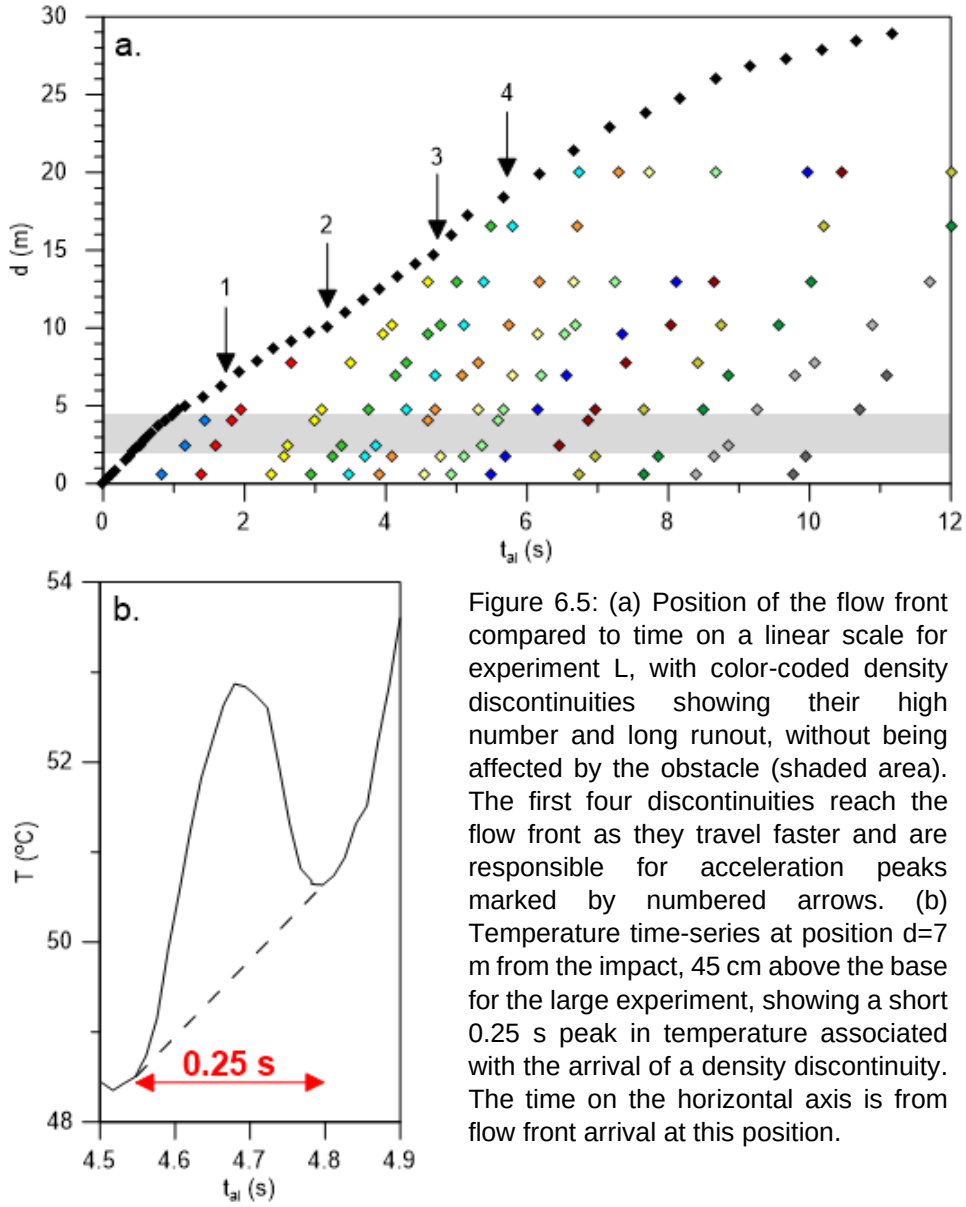

Figure 6.5: (a) Position of the flow front compared to time on a linear scale for experiment L, with color-coded density discontinuities showing their high number and long runout, without being affected by the obstacle (shaded area). The first four discontinuities reach the flow front as they travel faster and are responsible for acceleration peaks marked by numbered arrows. (b) Temperature time-series at position d=7 m from the impact, 45 cm above the base for the large experiment, showing a short 0.25 s peak in temperature associated with the arrival of a density discontinuity. The time on the horizontal axis is from flow front arrival at this position.

6.3.4. Effects of the obstacle on flow properties

These fast-moving flows show differences in their propagation immediately after the obstacles, which are likely affecting flow geometry and internal properties.

The head thickness shows strong variations across the entire propagation, alternatively thickening and thinning and showing similar trends for all the experiments (Fig 6.6a).

The flows have a high density ratio with the ambient air up to 5.4 at Profile 1. This characteristic defines the flows as non-Boussinesq currents because the density difference between the flow and the ambient air is over 10% up to c. 23-25 m from the

impact. Figures 6.6a-c show the head thickness, density and densimetric Froude Number (Fr') of the three flows across distance. The densimetric Froude Number is calculated in the non-Boussinesq approximation. Hence,

$$Fr' = \frac{U_f}{\sqrt{g'.h.\cos(\alpha)}} \quad \text{(Eq. 6.5)}$$

with U_f the flow front velocity, g' the reduced gravity, h the height of the flow head and α the slope of the channel in degrees. The reduced gravity g' in the non-Boussinesq situation is defined as $g' = g\left(\frac{\rho_c - \rho_a}{\rho_c}\right)$ with ρ_a the air density and ρ_c the flow density (Burgisser et al. 2005). The flow densities decrease on a power law decay with distance (Fig 6.6b) as the flows deposit particles and ingest air. However, significant differences appear between experiment S and the two others. In experiment S, flow density only slightly decreases after the obstacle from 6.32 to 5.19 kg/m^3, corresponding to a density ratio of 4. The strongest decrease in density occurs between Profile 2 and 11.4 m, where it reaches 1.95 kg/m^3. In experiments M and L, the densities at Profile 2 have significantly decreased from c. 6.5 kg/m^3 down to c. 2.6 kg/m^3, corresponding to a density ratio of 2. However, this density ratio stays relatively constant until Profile 3. There, density has decreased only down to 2.1 kg/m^3 in experiment M, and stayed approximately constant in experiment L. From Profile 3 onward, all three experimental flows show very similar density decays. They all become neutrally buoyant from c. 28 m from the impact.

In Fig. 6.6d-f, we compare the inertial (F_I), buoyancy (F_B) and drag forces (F_D) in the flow and defined as:

$$F_I = \rho_C {U_f}^2 h\, W \quad \text{(Eq. 6.6)}$$

$$F_B = \rho_C g' h^2\, W \quad \text{(Eq. 6.7)}$$

$$F_D = \frac{1}{2}\rho_a {U_f}^2 W h C_D \quad \text{(Eq. 6.8)}$$

where W is the width of the flow and C_D the drag coefficient of the flow front. The flows are initially dominated by inertial forces and are subcritical with Fr' taking values of 0.9 – 1. Immediately after the obstacles at Profile 2, as velocity decreases and the flows

become thicker, they become dominated by buoyancy forces and even more subcritical (Fr' between 0.7 and 0.8). Inertial forces become dominant again between c. 8 and 12 m from impacts and the flows become supercritical with Fr'>1.2. As the flows propagate in the unconfined section, the drag forces increase, but do not become higher than the inertial forces which remains dominant until the complete runout. This strong inertia is in agreement with relatively high velocities measured until the end of the propagation (U_f > 2 m/s until c. 23-26 m from impact, Fig 4c).

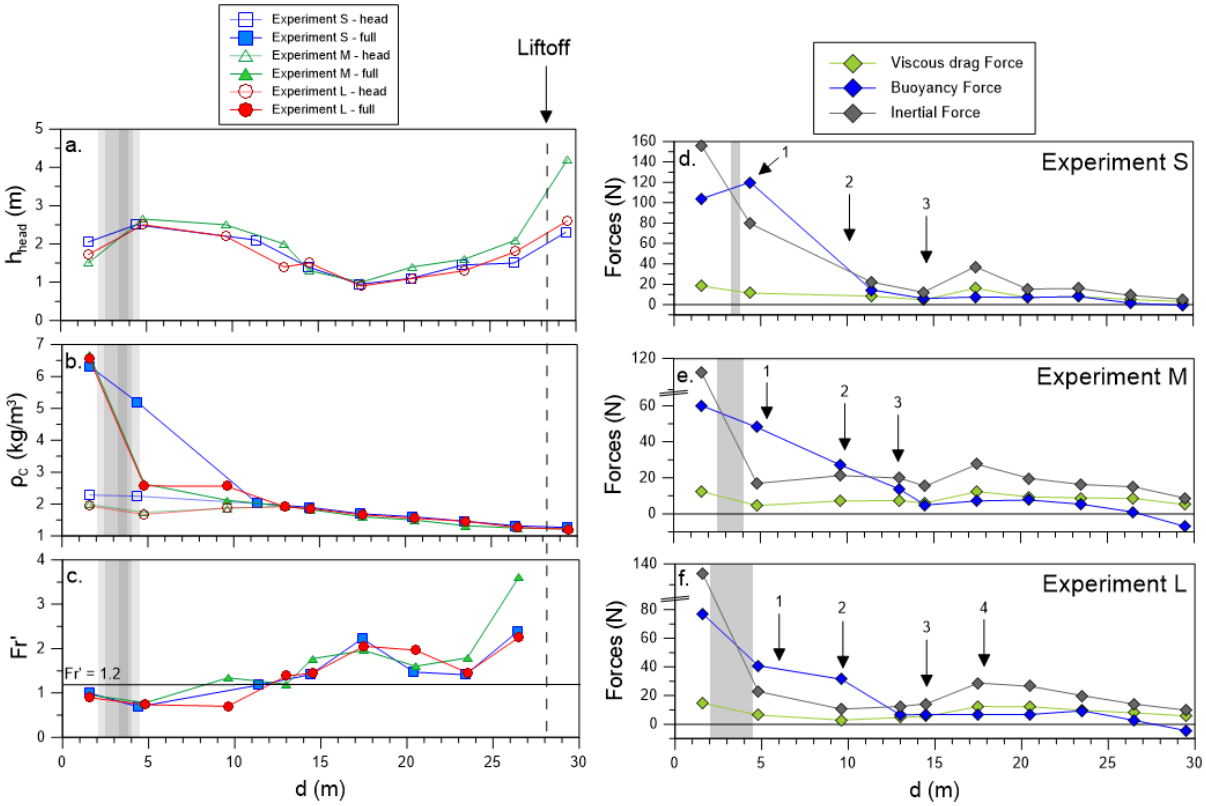

Figure 6.6: Head thickness, density, densimetric Froude number and force balance against distance for the three experiments. The shaded areas correspond to the obstacles. (a) Head thickness shows an initial increase after the obstacle and stays constant until c. 10 m from impact. The flow head becomes thinner especially when exiting the channel (14.2 m from impact), and thick again as the flow expands and ingest more air before lifting off. (b) Data for flow density for each experiment. Note the strong density decrease for experiments L and M at Profile 2, occurring significantly earlier than for experiment S. However, all the flows have the same density from Profile 3. (c) Data for the densimetric Froude number. The flows are initially sub-critical, and become more sub-critical after the obstacle, allowing density discontinuities to reach the flow front. (d-e-f) Force balance of Inertial, Buoyancy and Viscous drag forces for the three experiments, showing that Inertial forces are dominant throughout the entire runout, except after the obstacles where Buoyancy forces are dominant. Numbers corresponding to the accelerations marking the arrival of density discontinuities in the head are plotted.

The propagation of the gravity current can be subdivided into regimes that vary in duration with different obstacle sizes. These regimes correspond to those established previously with flow front velocity.

Regime 1: Defined by a high density ratio with the ambient air (ρ_c/ρ_a>4). There, the flow thickness is low and increasing. Inertial forces are dominant, and the velocity decreases (excepted on the stoss side). This regime extends until the crest of the obstacles.

Regime 2a: Defined when buoyancy forces are dominant, and Fr'<1.2. This regime occurs immediately behind the crest as the flow detaches and expands. There, the flow velocity strongly decreases but shows acceleration peaks caused by density discontinuities propagating unhindered and reaching the slowing subcritical flow front. The head thickness is high and relatively constant. The density ratio is between 4 and 1.7. Density strongly decreases for experiment S in this phase. However, the strongest density loss already occurred across the hill for experiments M and L and from Profiles 2 to 3, their density ratio stays relatively constant. This regime extends from the crest down to 8m, 11m and 12m for experiments S, M and L respectively.

Regime 2b: As the head thickness starts decreasing again, inertial forces become dominant again, and the flows become supercritical (Fr'>1.2). Velocity still shows accelerations caused by density discontinuities especially in experiment L. The density ratio is comprised between 1.7 and 1.35 and is similar for the three experiments. This regime extends between 8 and 17m experiment S; 11 and 15m for experiment M; 12 and 17m for experiment L.

Regime 2c: Defined from the moment the drag force becomes higher than the buoyancy force. There, the velocity strongly decreases as the density discontinuities barely reach the front and do not cause accelerations anymore. The density ratio keeps decreasing between 1.35 and 1. This regime extends up to 28 m from the impact for all three experiments.

Regime 3: Defined by buoyancy reversal and $\rho_c<\rho_a$ (density ratio <1). There the flow thickness keeps increasing up to 4 m, while its velocity is very low (<1m/s) and strongly decreasing (slope of 1/5 in the log-log plots of Fig.6.4b).

We now interrogate the variations in flow grainsize between the three flows. Figure 6.7 shows the time- and depth-averaged flow grainsize distribution at five different profiles along the channel and the unconfined section. Despite the variations in flow density, the grainsize distributions are remarkably similar for all three experiments (Fig 6.7). The flows become better sorted and see an enrichment in fines with distance, with median grainsizes ranging from c. 3.91Φ (67 μm) at Profile 1 up to c. 5.56Φ (22

μm) in the most distal location 24 m from the impact. At Profile 1, the flows are very poorly sorted; the distribution is polymodal and coarse-skewed because of the dense underflow propagating at the base of the current. At Profile 2, behind the obstacles, the grainsize distribution of the flows becomes unimodal but still shows the presence of lapilli inside the flows. At Profile 3, the flow grainsize is unimodal and particles carried by the flow only consist only of grains smaller than 250 μm. At 20 m, the distribution shifts with two modes at 4.5Φ (44 μm) and 6.5Φ (11 μm) as the flows enter Regime 2c and slow down, depositing coarse and medium ash clasts. From that point onward, only very fine ash stay in suspension inside the flow. The grainsize distributions become unimodal again with a main mode at 6.5Φ in the most distal parts of the runout.

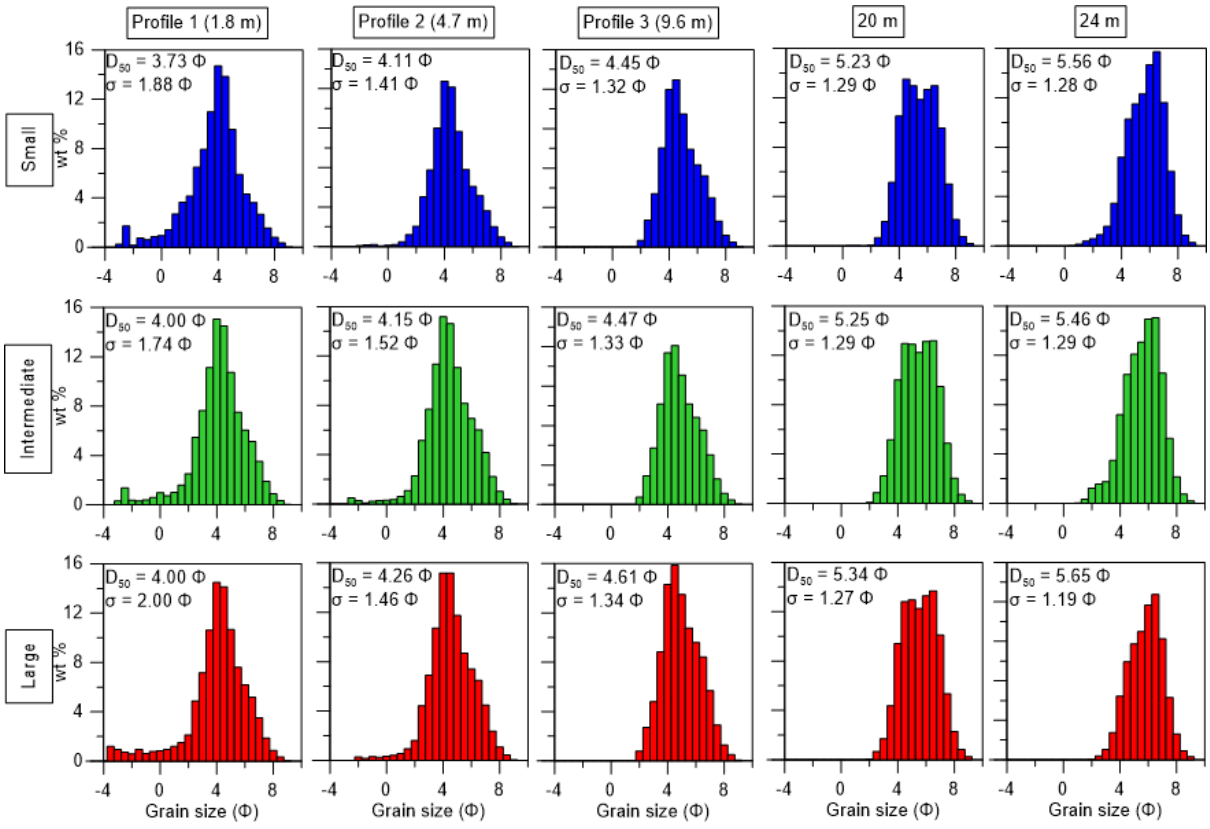

Figure 6.7: Depth- and time-integrated flow grainsize at five different locations, showing remarkably similar distributions for all the experiments. The flows become progressively finer grained and better sorted as they propagate downstream. Experiment L shows slightly finer flow grainsize.

In general, the flow grainsize distributions are surprisingly similar regardless of the obstacle size. A slight enrichment in fines is however notable by increasing obstacle size (Fig. 6.7). This difference is marked from Profile 2 down to 20 m from the impact,

where experiment L is finer-grained than the others. The sorting coefficient is however similar, showing that the range of particle size is comparable, but the mass of fines increases. This is particularly visible at Profile 3 (Fig. 6.7).

6.3.5. Flow temperature

We analysed the variations in temperature over the entire flow propagations. Because the three experiments were run over a period of more than two months, ambient temperatures were different. In order to compare the temperatures of each experiment, we used the temperature differences (ΔT) between the flows and the atmosphere. Figure 6.8 compares the ΔT of the three experimental flows at five different times after the impact.

Initially, all the flows have similar ΔT, which confirms that they have comparable temperature characteristics. After 3 seconds, a hot body intrudes the flows. In experiment S, this hot body overcomes the obstacle and propagates further downstream. However, it is partially blocked by the intermediate and large obstacles. Significantly cold wakes are visible in the lee side of the hills.

At 9 seconds, the proximal regressive dune shows the highest temperatures. In experiment S, most of the heat is contained to medial distances <15 m, forming a thermally buoyant plume (up to 21 K above ambient) around 10 m after the impact zone. The head is only moderately hot, c. 10 K above the ambient air. At the same time for experiment M, the flow seems colder after the obstacle (up to 16 K above ambient). However, the heat propagates far after the obstacle, feeding the hot head (Fig. 6.3d-f) with a ΔT of 13 K. For experiment L, the temperature downstream of the obstacle is markedly the highest, with ΔT up to 24 K above the ambient in medial distances (<15 m), showing efficient heat propagation after the obstacle. The head is also hotter, with a temperature difference of 15 K with the ambient air.

After 20 seconds, the three flows show similar ΔT, although experiment L is still the hottest, with ΔT up to 10 K at Profile 3, and 12 K at the 13 m profile.

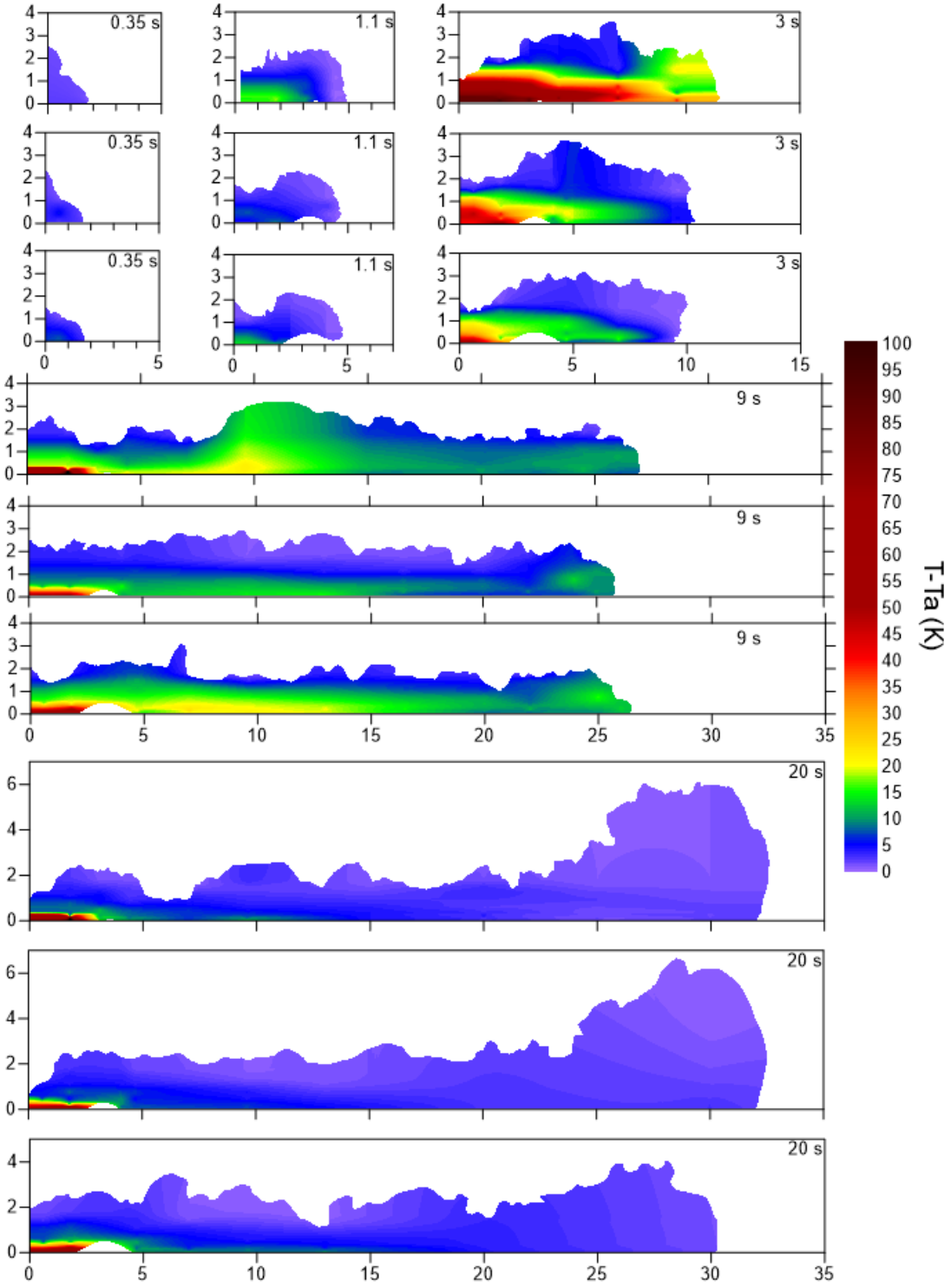

Figure 6.8: Difference of temperature compared to the ambient atmosphere inside cross-sectional contours of the flows, at 5 selected times after the impact for all three experiments. The obstacles are represented by the white shape before 5 m. Note that the small obstacle is too small to be clearly visible.

6.3.6. Energy spectra

Brosch et al. (2021) proposed a fitting power-gaussian mean velocity profile modified from Cantero-Chinchilla et al. (2015), and calculated the turbulence fluctuations as the difference between the measured and mean velocity. Brosch et al. (2022, in press) recently showed that most of the flow energy and dynamic pressure in dilute PDCs is focussed into large-scale coherent turbulence structures and fast-travelling density discontinuities. In the following, we analyse Fourier spectra of specific kinetic energy and temperature to investigate how large-scale coherent structures and density discontinuities are influenced by the hill-shaped obstacles.

The high resolution of the velocity data allows the calculation of specific kinetic energy E_K of the turbulence fluctuation in the downstream component (U') defined as:

$$E_K = \frac{1}{2}U'(z,t)^2 \qquad \text{(Eq. 6.9)}$$

A constant height z was chosen at c. 45 cm above the base to avoid the influence of the wakes for experiments S and M. For experiment L, because the hill is higher, we chose the analysis at z = 75 cm above the base. The power gaussian mean velocity profile however cannot be computed in case of flow detachment because of the low shear in the wake preventing a good fit. In these cases, a mean velocity time-series was calculated at the height of the maximum velocity with a third order polynomial suggested by Cerminara et al. (2021).

We computed the Fourier frequency spectra for specific kinetic energy, as well as for the high-resolution temperature data series. Both parameters followed the Kolmogorov energy cascade and showed energy peaks at similar frequencies. Figure 6.9a-b show a comparison between the Fourier spectra from temperature time series and from specific kinetic energy for experiment L at Profile 1. The three main energy peaks at the top of the energy cascade are located at 1.006 Hz (dark blue band), 1.15 Hz (light blue band) and c. 1.7 Hz (red band) for both parameters. In turbulent flows, the frequency f of turbulence can be expressed with the Strouhal Number (Str):

$$Str = \frac{fL}{U} \qquad \text{(Eq. 6.10)}$$

with L and U the typical lengths and velocity scales. In these experiments, the characteristic length scale is established by the thickness of the flow body (i.e. 1.1 m at Profile 1) and the averaged velocity U_{body} represents the typical velocity scale (c. 3.84 m/s at profile 1 for experiment L). Using the frequency of 1.006 Hz determined

by the Fourier analysis, the Strouhal number takes a value of 0.29, which is very close to the critical value 0.3 at high Reynolds Number (>10^5) that can predict the most energetic turbulent structures. This can explain the 1.006 Hz peak as the frequency of the large-scale coherent structures inside the flow. Solving Eq. 6.10 with the theoretical Str = 0.3, L = 1 m (corresponding to the thickness of the body without the underflow), and U = 3.85 (averaged velocity of the dilute surge), we obtain f = 1.16 Hz. This result suggests the second peak in the Fourier spectra corresponds to the energy of the large-scale coherent structures before the arrival of the dense underflow.

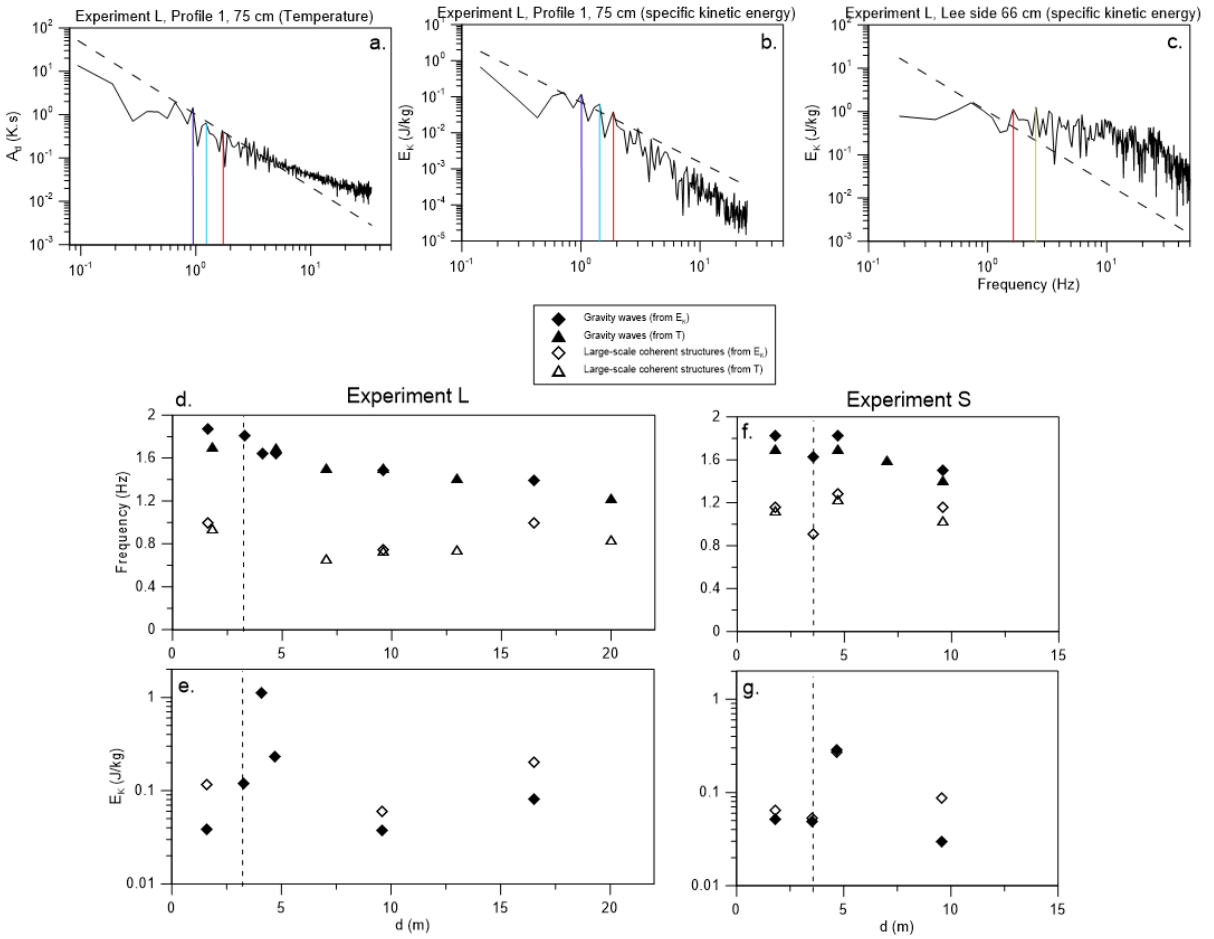

Figure 6.9: Fourier spectra, frequencies and energy values associated with density discontinuities and large-scale coherent structures for experiment L. Values are taken 75 cm above the channel base at most positions, except over the lee side at the height of the maximum velocity (66 cm above channel base). (a-b-c) Fourier spectra for temperature time series or specific kinetic energies at Profile 1 and over the lee side. The spectra follow the Kolmogorov Cascade (dashed curve) and show energy peaks associated with density discontinuities at c. 1.7-1.9 Hz (red line) and large-scale coherent structures at c. 1Hz (blue lines). Over the lee side, a peak associated with vortex shedding is visible at 2.54 Hz (yellow line). (d) Frequency of density discontinuities (closed symbols) and large-scale coherent structures (open symbols) plotted against distance for both temperature time series (triangles) and specific kinetic energy (diamonds) in experiments S and L. The black dashed line is the obstacle crest. (e) Specific kinetic energy plotted against distance for experiments S and L. Both density discontinuities and large-scale coherent structures see an energy peak above the obstacle, decrease after the hill, and increase again after an acceleration when the flow exits the channel.

Following the argument of Brosch et al. (2021), we can calculate the theoretical velocity c of the third energy peak as:

$$c = \frac{f_{max} U_{body}}{f} \qquad \text{(Eq. 6.11)}$$

With f_{max} the frequency of the third energy peak (1.7 Hz) and f the frequency of the first energy peak (1.006 Hz). The theoretical velocity c is c = 6.489 m/s, which is closely related to the averaged velocity of density discontinuities at Profile 1 (6.45 m/s), showing that this third energy peak is related to their propagation.

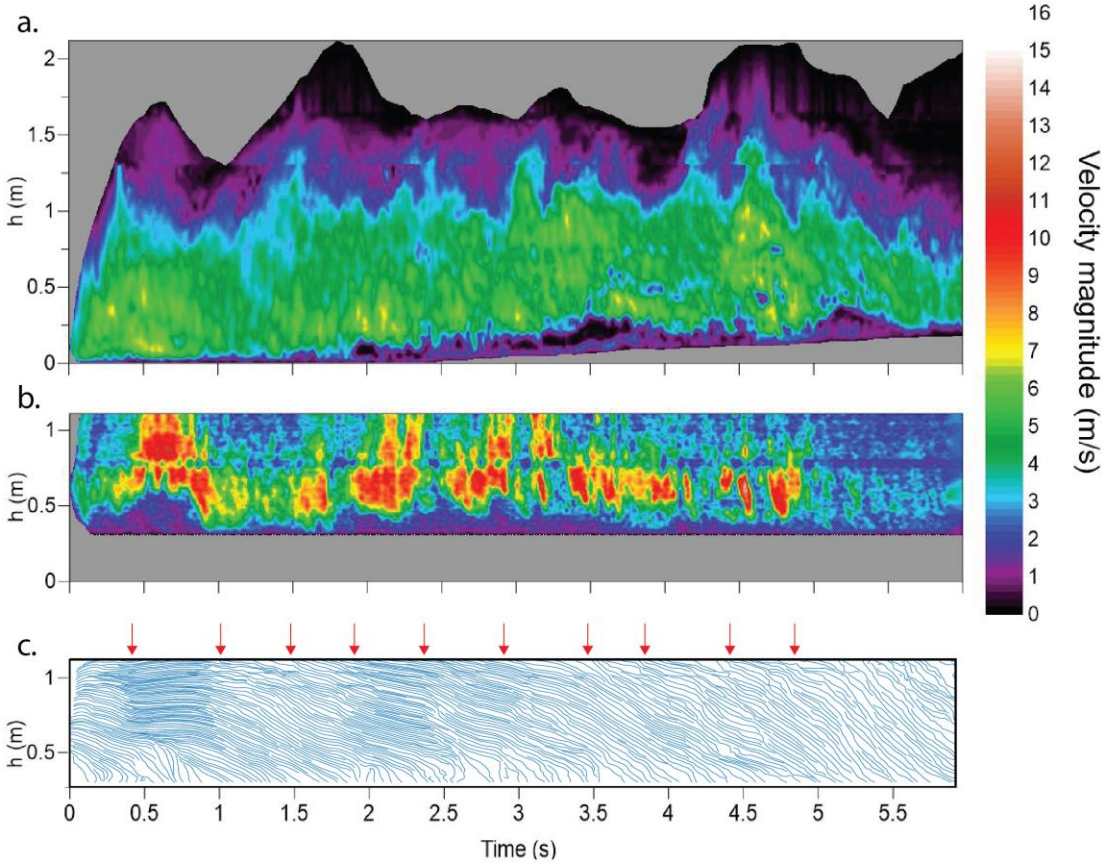

Figure 6.10: Time-height plots of experiment L. (a) Velocity magnitude at Profile 1 showing velocities peaking at c. 7 m/s. The grey area at the base corresponds to the deposits building. (b) Velocity magnitude over the lee side, showing strong accelerations of the flow as it has crossed the obstacle, with velocities up to 16 m/s. The low-velocity wake is visible at the bottom of the plot. The grey areas corresponds to the obstacle height at that location. (c) Streamlines over the lee side showing flow direction mostly downward, and the rotation of the velocity field from c. 5 s onward. Abrupt changes in the streamlines direction and density are pointed by red arrows above the plot and are interpreted as vortex shedding.

Figure 6.9c shows the energy spectra of specific kinetic energy in the lee side of the large obstacle and highlights two main energy peaks at 1.65 Hz (red band) and 2.55 Hz (yellow band). A similar approach allows us to determine that the peak at 1.65 Hz is also related to the propagation of density discontinuities on the lee side of the hill. Using Eq. 6.10, we use U as the time averaged velocity of the dilute surge at Profile 1 up to the height of the hill (3.81 m/s), and L as the hill height H_{crest} subtracting the averaged thickness of the underflow (L = 0.45 m). These two values represent the effective velocity and length scales for vortex shedding and produce a theoretical frequency of 2.54 Hz, which is closely related to the yellow peak of Figure 6.9c. The vortex shedding is visible in a time-height plot of streamlines as sharp changes in their direction or density, as plotted in Figure 6.10c. The structure of these vortices, travelling at the interface of the wake, suggests that they are more similar to arch vortices (Cao and Tamura 2020) and not von Kármán vortex street (Manhart 1998) as the flow does not go around the obstacle. Interestingly, the only peak in lower frequencies is related to the length of the data series and therefore is not accounted, suggesting that large-scale coherent structure may have disappeared above the lee side of the hill as there is no shear with the substrate to generate them.

We analysed the Fourier spectra at different distances for the most extreme case of experiments S and L. The results, shown in Figures 6.9d-e are as follow.

In the experiment L, the frequencies of density discontinuities steadily decrease along the flow runout from 1.87 Hz at the Input location down to 1.23 Hz after 20 m of runout, with no apparent influence of the obstacle (Fig 6.9d). Large-scale coherent structures are not visible in Fourier spectra when the flow is detached. Newly formed large-scale coherent structures appear at 7 m with significantly lower frequencies of 0.66 Hz than before the obstacle. However, as the flow thins and accelerates upon exiting the channel, the frequency of large-scale coherent structures shows a temporary increase up to 1 Hz, before slowing down again with frequencies of 0.84 Hz at 20 m from the impact. Figure 6.9e shows the downstream variation of specific kinetic energy associated with the frequencies of large-scale coherent structures and density discontinuities. Interestingly, although the frequency of density discontinuities is relatively unchanged across the hill, their energy strongly increases from 0.038 J/kg at Profile 1 to 1.13 J/kg over the lee side. These high energies coincide with the strong acceleration of the flow, reaching velocities up to 16 m/s over the lee side (Fig. 6.10a-

b). The energies for both density discontinuities and large-scale coherent structures is the lowest in medial distances with values of 0.037 and 0.06 J/kg respectively. Another short increase in energy occurs when the flow exits the channel and accelerates again (Fig 6.9e).

In experiment S, the frequencies associated with density discontinuities seem to decrease at a similar rate than in experiment L, from 1.82 Hz at Profile 1 to 1.5 Hz at Profile 3 (Fig. 6.9d). A peak in specific kinetic energy at Profile 2 is also present but lower than experiment L, increasing from 0.05 J/kg to 0.29 J/kg. Large-scale coherent structures do not seem to be inhibited and are visible in the spectra at Profile 2 with high energies of 0.27 J/kg close to that of density discontinuities. At Profile 3, frequencies and energies both decrease for density discontinuities and large-scale coherent structures (Fig. 6.9d-e).

6.3.7. Deposit characteristics

After analysis of the flows and their differences, we focus here on the characteristics of the deposits, which should encrypt the flow dynamics and how they were affected by the hills.

Deposit thickness vary between 0.4 m and sub-millimetric, generally decreasing with distance approximately following a power law decay. The mass per area (MpA) reaches values up to c. 190 kg/m^2 at Profile 1. Upon crossing the obstacles, deposit thickness and MpA rapidly decrease down to c. 1 kg/m^2 on the crest (Fig 6.11a) in experiment M. The lee side of the obstacle shows very thin, thinly laminated deposits and the MpA decreases below 1 kg/m^2. Immediately after the obstacle, the mass suddenly increases again up to c. 3.8 kg/m^2 (in experiment L). Finally, after the obstacles, the deposit thickness and MpA decrease normally following a power law decay.

However, down to c. 15 m after impact, the deposited mass is systematically larger by increasing the size of the hill (Fig 6.11a). Typically, at 8.5 m from the impact, experiment S has deposited 1.37 kg/m^2, while experiment M has deposited 1.63 kg/m^2 and experiment L 1.88 kg/m^2. From 20 m onwards, the deposited mass is similar for all experiments and decreases down to c. 0.027 kg/m^2 at 26.5 m from the impact.

Figure 6.11b shows the deposit median diameter (D_{50}) for all three experiments with distance. At Profile 1, D_{50} is very similar to the initial mixture (star symbol on the y-axis in Fig. 11b). Immediately before the obstacles, the deposits are very rich in coarse particles and very poorly sorted with D_{50} reaching -1.83 Φ (3550 μm), showing the stranding of the dense, coarse-rich underflow on the stoss side. Across all the obstacles, the deposits rapidly become finer grained, with median grainsize decreasing to 3.9 Φ in experiment L (66.9 μm). Immediately behind the obstacles, there is a strong enrichment in coarse particles again (67.4, 71.6 and 73.6 wt% of lapilli clasts for experiments S, M and L). Deposits at this location present strongly bimodal distributions with the coarsest median diameter and the worst sorting coefficient σ of the entire deposition area (D_{50} is on average at -2.67 Φ and σ at 3.38 Φ). After the obstacles, deposits become constantly finer grained with distance (Fig 11b) and their grainsizes are remarkably similar regardless of the obstacle size, though small variations occur. They are also coarser with increasing hill height up to 15 m from the impact zone. Typically, at 8.5 m from impact, D_{50} is 4.2, 4.1 and 3.9 Φ for experiments S, M and L respectively. This trend changes between 15 and 23 m from impact, where experiment L shows the finest deposits. However, there is no systematic correlation between the grainsize and the obstacle size anymore. Eventually, from c. 23 m from impact, the deposit median grainsize becomes similar for all three experiments.

In summary, deposits are thick and have a similar distribution before the obstacle. They rapidly thin and get finer across the hill. Immediately after the obstacle, thicker deposits are emplaced with a high proportion of lapilli clasts. After the obstacles, deposits become progressively thinner and finer grained with distance. Deposit characteristics (thickness, mass per area and grainsize) are remarkably similar for all three experiments. However, up to 15 m from the impact, by increasing obstacle size, deposits are slightly thicker and coarser. After 15-20 m from impact, all three experiments show extremely similar median grainsize and thicknesses.

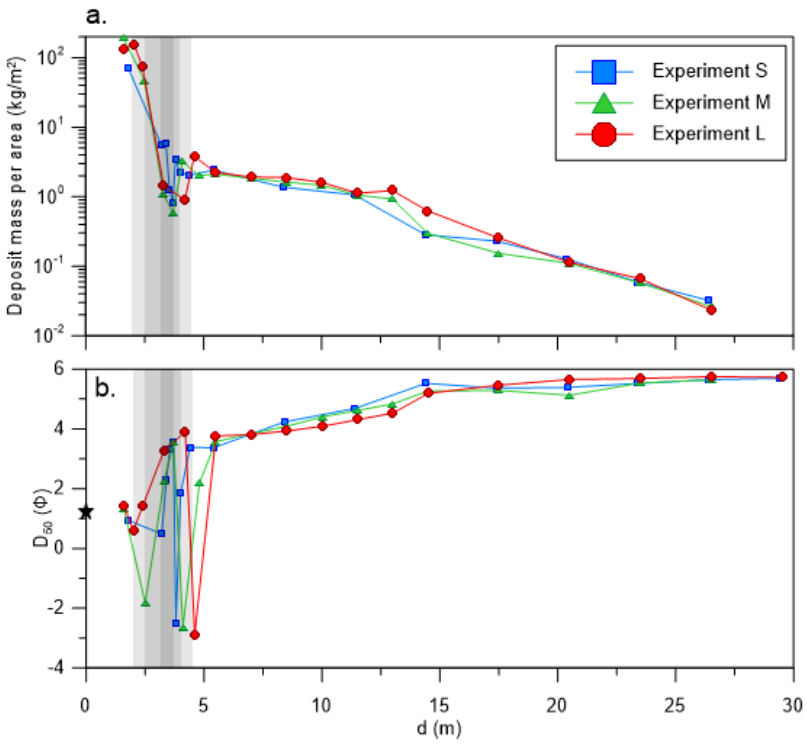

Figure 6.11: Deposit grainsize information across distance for all experiments. (a) Deposit mass per area showing a general decrease of mass with distance. After the obstacles up to 17 m, more mass is deposited when increasing the hill size. (b) Median of the deposits. Deposits get finer across the obstacles and show a sudden coarsening immediately after it, as coarse lapilli roll down the slope and are dumped in the wedge. When increasing obstacle size, deposits are coarser grained up to c. 15 m, and finer grained for the rest of the runout. The star symbol on the vertical axis corresponds to the median of the initial mixture.

6.4. Discussion

Topographic obstacles are responsible for loss of the PDC momentum because of the high resistance, or drag, exerted on the flow (Fisher 1990). The experiments showed that this loss increases with increasing obstacle size. Another important difference reported by our experiment resides in the strong decrease in density immediately after the intermediate and large obstacles, but not after the small obstacle. The density ratio between the flow and the atmosphere is the main driving force of the propagation of the gravity current. Therefore, the most intuitive thinking is to expect that a flow encountering a small obstacle would have the longest runout and the thickest, coarsest deposits.

However, regardless of the obstacle dimensions, the experimental PDCs all reach the final runout and buoyancy reversal at the same time. The explanation of this behaviour resides in in the strong compression and acceleration of the flow on the stoss side of the hills. This phenomenon is responsible for the advection of material from lower flow regions into upper flow regions. The higher the obstacle, the further upwards basal flow material is advected. This effect counter-intuitively decreases the mass blocked before the crest when increasing the obstacle size and loads the flows with higher concentrations of particles after the hills. For small obstacles, this phenomenon is not efficient because particles sediment again quickly after the obstacle. However, for larger obstacles, particles are transferred back into the upper flow. Fine particles couple well with the gas phase, staying in suspension for a long time. Coarser clasts either (1) roll down the lee slope and accumulate at the end of the hill or (2) are ejected and redeposited in medial distances <15 m from the impact. Deposits in this zone are therefore slightly thicker and present a slightly fines-depleted facies visible in the field across rough topography (Fisher 1990). This process balances the density loss after large obstacles and maintains a high density ratio with the atmosphere to values similar to flows with no or small obstacles for the rest of the propagation.

This fines-rich flow is increasingly more dangerous as the higher particle load significantly increases suffocation hazards (Baxter 1990; Dellino et al. 2021) and long-term respiratory diseases (Hincks et al. 2006). At the same time, the hazard associated with blocks rolling down the lee slope significantly increases at the end of the obstacle, potentially causing increased destruction on buildings (e.g. Baxter et al. 2005).

Compression and acceleration also amplify the energy of density discontinuities travelling inside the flow without changing their frequency. As the flow front decelerates, the density discontinuities travel unhindered and reach the head, compensating for the momentum loss and propelling the flows downstream further than expected. These periodic, sudden accelerations allow the flows to reach similar runouts regardless of the size of the obstacle. Together with the thinning of the head, they also allow inertial forces to be dominant for most of the flow propagation.

Because density discontinuities are associated with internal gravity waves carrying the highest dynamic pressures (Brosch et al. 2021), these results pose a

major issue toward hazard assessment of PDCs interacting with topographic obstacles. Not only do the number and frequency of density discontinuities remain unchanged, but their destructive power strongly increases in the vicinity of these hills.

Comparing the runout of these three experiments to other experiments previously run in PELE, a striking time difference is noticed, namely the surge flows performed by Brosch et al. (2021) reach the end of the runout significantly later than these experiments (15.5 s instead of c. 11 s). This is very likely due to the smaller mass used for their experiments (120 kg) and the lower density contrast. This is in agreement with Andrews and Manga (2011) who suggested that the final runout is controlled by flow density and thickness, but not by the presence or absence of topographic obstacles.

Upon encountering the obstacles, most of the underflow or bedload remains blocked on the stoss side of the obstacles, therefore creating a hot dune that concentrates most of the heat. Furthermore, the wake immediately behind the obstacle remains colder during most of the flow duration. This is explained by the detachment of the flow after the crest and the ingestion of cold ambient air, along with the strong reduction on particles density in the wake.

These two processes are stronger with increasing size of the obstacles, and therefore one could expect that larger obstacles will reduce the likelihood of fire hazards downstream. However, the advection of material from the base of the flow back into upper flow regions by the obstacles loads the flow with suspended fine particles carrying thermal energy. As the fines content remain high, so does the temperature downstream of the obstacle. This process was previously described in numerical simulations on Mt. Vesuvius (Todesco et al. 2002) and induces serious, long-term hazards in regions thought to be protected from heat because of ridges.

6.5. Conclusions

A series of large-scale experiments was performed looking into the interactions of PDCs with hill-shaped topographic obstacles of varying size. Partial flow blocking caused a loss of momentum ranging from 25 to 50% after the obstacles with increasing

obstacle size. Flow velocity, concentration and temperatures are strongly affected in the immediate vicinity of the hill, with changes becoming larger with increasing obstacle size. The partial blocking of the flow was compensated by an increasingly strong compression and acceleration of the flows on the stoss side, which conveyed particles from the base back into the flow. This process caused the flows downstream of the obstacles to become increasingly loaded with hot particles. As density discontinuities travel unaffected, or even amplified by the obstacle regardless of its size, they propagate to the flow front and cause brief, sudden accelerations, allowing runout distances longer than expected. These findings explain why PDCs, and particularly dilute PDCs, can travel relatively unhindered by topographic obstacles. Furthermore, this research raises the caution that topographic obstacles may not reduce but instead increase hazards impacts through increasing likelihood of impacts such as burns, suffocation and destruction with unchanged final distances. These results demonstrate that PDC hazard models should account for the compressibility of these turbulent gas-particles flows to allow realistic forecasts of runout and hazard potential.

6.6. Supplementary materials

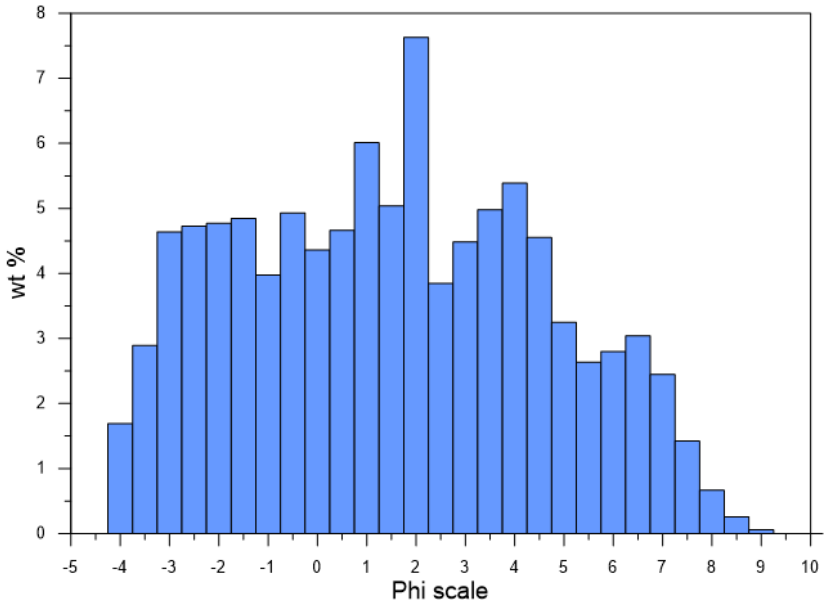

Supplementary material 6.1: initial grainsize distribution of the mixture used for the experiments.

7. - Conclusions

This chapter reviews the main findings of the thesis and synthesizes them to answer the three main questions driving this research. The chapter also concludes with a list of limitations and offers perspectives for future research in the field of PDCs, whether they encounter obstacles or not.

7.1. Synthesis

This PhD research was focused on the interaction of Pyroclastic Density Currents with topographic obstacles. Previous studies described the flow-obstacles interactions of the two end-members of PDCs (dense and dilute). Analogue experiments on granular flow avalanches (e.g. Hákonardóttir et al. 2003; Naaim-Bouvet et al. 2004; Viroulet et al. 2017; Chung et al. 2019) and fully turbulent, fully dilute flows (e.g. Andrews and Manga 2011) were previously reproduced in the laboratory, and experiments in water tanks have also been carried out (e.g. Alexander and Morris 1994; Woods et al. 1998; Oshaghi et al. 2013; Nasr-Azadani and Meiburg 2014). While these studies captured important characteristics of dry granular flows and compositional gravity currents interacting with topographic obstacles, the processes that occur in situations where a spectrum between dense and dilute flow coexists, such as PDCs, remains poorly understood. The absence of direct observations of natural PDCs interacting with topographic obstacles motivated this research.

Large-scale experiments were used to reproduce kinematically scaled PDCs and synthesize their dynamics around hill-shaped obstacles. Three obstacle sizes were used to visualize the interactions of PDCs with small, intermediate and large hills and the differences they involve. The research was guided by three main research questions:

- (1) What are the physical processes governing the interactions of PDCs with topographic obstacles?
- (2) Can topographic obstacles modify the internal flow and deposition behaviour of PDCs? How is this reflected in their deposits?

- (3) What are the consequences of the interaction of PDCs with topographic obstacles on their runout and hazard behaviour?

7.1.1. Physical processes of PDC-obstacle interactions

The flows generated during these experiments have an initial density contrast with the atmosphere of c. 5, and a velocity of c. 3.4 m/s. They are bi-partite, comprising (1) a 0.01 – 0.1 m thick, slow, laminar, dense bedload where particles are moving through saltation and rolling or through thick granular-fluid underflows (Brosch and Lube 2020); and (2) a c. 0.7 – 2 m thick, fast-moving, turbulent, more dilute flow above in which particles are suspended. The gravity currents cross the obstacles and detach after the crest at an angle of c. 120° with the channel base (where 90° represents the crest). The flows generate a turbulent wake beneath the detached flow and re-attach further downstream. Eventually, the flows reach a final runout of c. 30 m from the impact zone.

The experiments revealed strongly time-variant processes occurring in PDC-obstacle interaction linked to the flow structure of a head, a proximal body, a distal body and a tail. Four phases of interaction were described in all three experiments, with similar durations. However, the larger the obstacles, the larger and more pronounced were these phases. A series of transient processes were documented during the propagation of the experimental PDCs across the hill, and are summarized in Figure 7.1, notably:

(1) During propagation of the PDC head, the flow detaches from the hill and re-attaches further downstream. This leads to the formation of a dilute turbulent wake underneath the detached flow. In the wake, strong shear between backward flow motion and the detached flow generates vortices that grow and migrate downstream. The flow stratification behind the obstacles is unstable due to the appearance of a dilute, slow, cold wake below a denser, faster, hotter flow. The head sees the largest wake dimensions (re-attachment distance and wake area) before a strong decrease in its rear.

(2) During propagation of the increasingly denser PDC body across the obstacle, the basal flow region compresses and accelerates during interaction with the

stoss side of the obstacle. This leads to the formation of gas-escape structures in the compressed basal flow. The acceleration of the basal flow on the stoss side is characterized by the formation of decimetre-thick, distinctive jet-like structure at the base of the detached flow. This jet shows high velocities, densities and turbulence intensity and prevents sedimentation of particles from the detached flow above into the turbulent wake below. Jet structures appear periodically, and their disappearance is associated with strong sedimentation from the detached flow into the wake through finger-like instabilities.

(3) As the flow density strongly increases in the later part of the body, sedimentation strongly increases on the stoss side. This leads to blocking of the dense underflow and deposition of a thick, massive, poorly sorted dune bedform. The increase in flow density affects the detached flow which becomes denser and charged with (coarse-grained) particles that had previously sedimented into the wall region and which become re-suspended into higher flow levels. In this phase, jet structures disappear, and the detachment bends downwards, reducing the wake dimensions. Inside the wake, sedimentation is enhanced and density and temperature increase. Denser bedload also propagate across the hill and down the lee slope.

(4) Eventually, towards the end of the flow, density and velocity start declining. The vertical component of the flow becomes more dominant, and the entire flow field rotates from slope-parallel angles to angles approaching that of the lee side. This is associated with a now thick wedge of deposits on the stoss side, reducing the effective hill height and therefore the compression and acceleration. These two effects, flow field rotation and stoss side sedimentation, strongly increase the angle of detachment as the flow streamlines become more ground-hugging. The wake dimensions strongly decrease. Saltation and rolling on the lee slope build laminated deposits behind the obstacles.

Time-variance in PDC-obstacle interaction should be considered for future research as different parts of the flow have different physical properties. This is important in the consideration of flow density, which is not uniform throughout the gravity current, but rather increases from approximately half of the propagation. On the stoss side of obstacles, the thick, massive deposits may not be formed through friction and flow deceleration, but rather through form drag blocking the late-stage flow

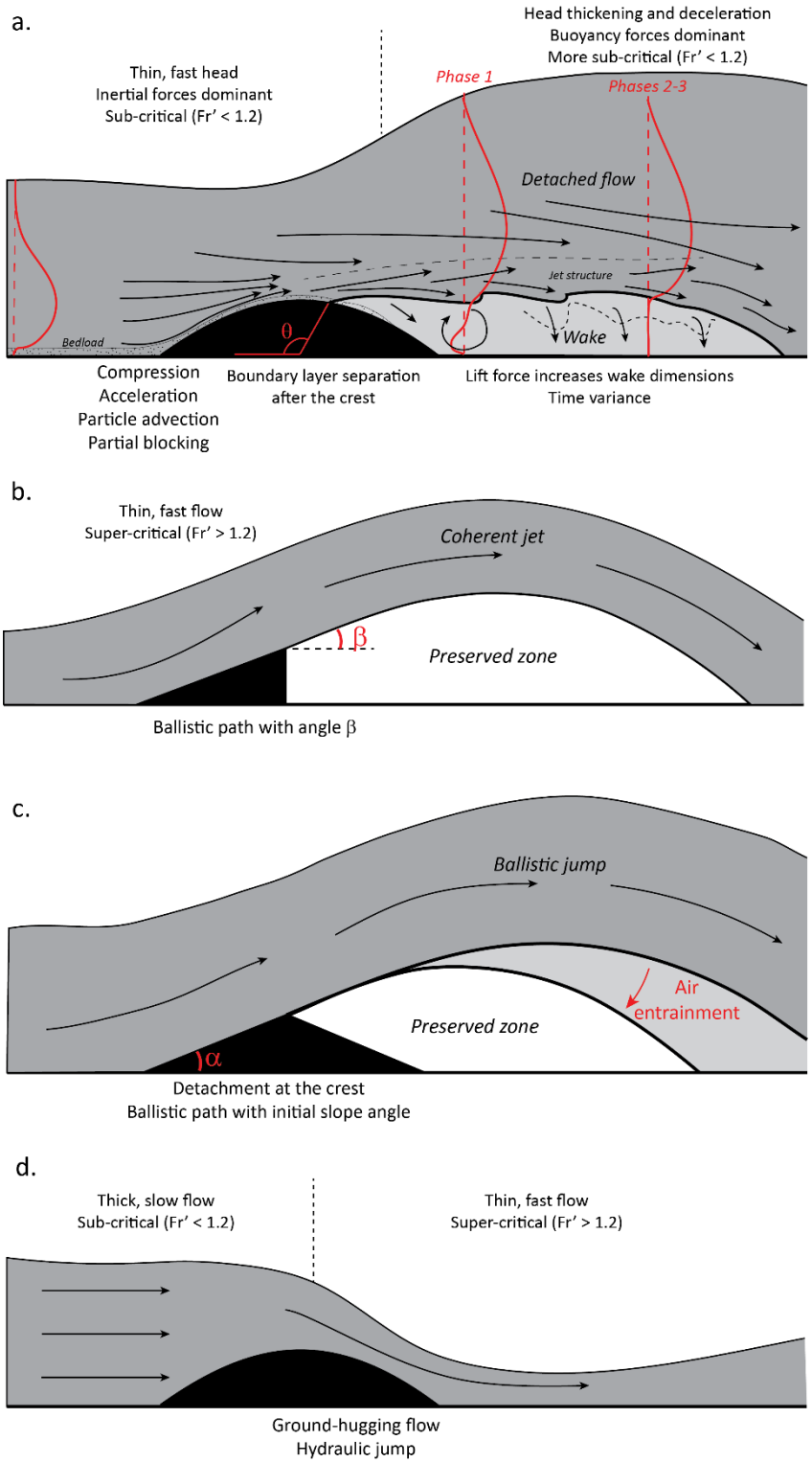

Figure 7.1: Sketch comparing the model developed in this thesis with other models previously described. Black arrows describe the main streamlines of the flow. (a) Model developed in this thesis, showing complex time-variant interaction, compression and acceleration on the stoss side, boundary layer separation. Flows are sub-critical before the hill and become more sub-critical after it. Velocity profiles are shown in red before and after the obstacle for Phase 1 and Phases 2-3. (b) Model by Hákonardóttir et al. (2003) on super-critical dry granular flows, where the flows form a coherent jet with a ballistic trajectory using the detachment angle with the horizontal plane. (c) Model by Gardner et al. (2018) where the flow follows ballistic paths taking the slope angle of a triangle-shaped obstacle. (d) Model by Woods et al. (1998) where the sub-critical flow does not detach and becomes super-critical after the hill, forming a hydraulic jump.

with high mass flux and densities. On the lee side, this increasing density leads to the progressive disappearance of the wake. Hence, if a large safe zone existed behind a hill when the flow front detached and travelled above it, its dimensions rapidly decrease in the rear of the head, and it eventually disappears in the latest stages of the flow.

Because the flows accelerate, up to doubling their initial velocity in the case of large obstacles, this suggests that the massive deposits on the stoss side are formed through form drag and partial blocking, and not from deceleration of the flow. Hence, the mass blocked on the stoss side accounts for most of the momentum loss. However, comparing the momentum loss of only the dilute proportion of the flow (i.e. without the dense underflow) reveals that it is positively and linearly correlated to the size of the obstacle (Eq. 4.3). Extrapolating this linear relationship suggests that total flow blocking (i.e 100 % momentum loss) occurs for obstacles that are approximately 5.45 times higher than the height of the velocity maximum of the flow. With the conditions under which the experiments were carried out in the PELE setup, this condition would occur for a crest height of c. 1.63 m. Considering the thickness of the flow body at c. 1.1 m, this crest height corresponds approximately to 1.5 times the flow thickness. This is in close agreement with the experimental results of Andrews and Manga (2011), for gas-particle gravity currents propagating across wall-shaped obstacles.

This result suggests that the pressure drag created by the obstacle strongly affects even the dilute proportions of the flows and should also affect the turbulent wake behind the hill. The characteristics of the wake generated were therefore investigated in order to understand its dynamics and the mechanisms allowing it to be maintained during most of the gravity current.

This research revealed that the wake is not controlled by any ballistic trajectory as previously suggested by models of dense granular avalanches (e.g. Hákonardóttir et al. 2003; Naaim-Bouvet et al. 2004; Chung et al. 2019) or applied models using tree patches in Mount Saint Helens (Gardner et al. 2018) shown in Figure 7.1b-c. This is evidenced by several observations: (1) the detachment of the flow does not occur at the crest of the hill but after it; (2) even for the scenario modelling the detached flow paths as ballistic trajectories from the observed detachment point and its associated

depth-integrated velocity and basal streamline angles, the modelled re-attachment distance and the area of the wake highly under-estimate the measured values (Fig. 5.3).

Instead, the detachment of the flow is modelled by turbulent boundary layer separation which explains high detachment angles (Mehta 1985) and the presence of vortices at the interface and inside the wake (Cao and Tamura 2020). The wake dimensions are therefore strongly linked to the shape of the obstacles, represented by the drag coefficient. The drag coefficient is the same for all three obstacles. By increasing the size of the obstacle, the drag force increases, and the absolute dimensions of the wake increase too.

However, the size of the wake is inversely proportional to the size of the obstacles: a large obstacle creates a relatively small wake while a small obstacle creates a relatively large wake compared to the hill (Fig. 5.2). This suggest that a lift force counter-balances gravity and controls the wake dimensions. This lift force is controlled by the static pressure difference between the wake and the detached flow above, and therefore by the wake density.

A consequence of the compression and acceleration on stoss side of the hills resides in the aforementioned advection of particles at the base of the flow back into higher flow regions when encountering obstacles. Dense and coarse flow material from the base of the flow is conveyed upward higher than the crest and into the detached flow. By increasing the size of the hill, the proportion of the flow that is accelerated and conveyed upward increases too. The advection of this material has strong consequences on the wake dynamics immediately after the hill.

For small obstacles, this effect is limited because particles do not cross the height of the velocity maximum and sediment again quickly. The wake is small because of the low drag force, but it is loaded with hot particles. The lift force is therefore very high and pushes the wake upward, making it very large compared to the obstacle. The conservation of density and velocity across the hill leads to a low momentum loss. For large obstacles, the high drag force is responsible for large absolute dimensions of the wake. However, particles are advected back into significantly higher regions of the flow and well accelerated above the wake. The generated wake is more dilute and colder, because particles rather travel above it (instead of sedimenting into it). This more unstable flow stratification strongly reduces the lift force, which does not significantly push the wake upward and can even reduce its size by acting in the same

direction of gravity instead of against it. The flow sees a strong deceleration following the hill, which, associated with the strong density loss, leads to a significant loss of momentum.

Previous thinking suggested the presence of a safe zone behind obstacles as evidenced by the preservation of tree patches in the lee side of hills (Kelfoun et al. 2000; Komorowski et al. 2013; Gardner et al. 2018; Guinn et al. 2022). The findings of this research put more complexity to this. Even in the wakes behind obstacles, real-world flows are still extremely dangerous because of high densities and temperatures. This is particularly the case behind small obstacles, even though the wake is large compared to the hill.

7.1.2. Consequences of flow-obstacle interaction

Due to increasing loss of momentum and flow density with increasing obstacle size, a logical hypothesis would state that flows encountering large obstacles do not travel as far as flows encountering small obstacles. An intriguing characteristic observed in this research resides in the fact that this is not the case (Fig. 6.4). The three experimental flows reach similar final runout distances in similar times, suggesting other processes countering the momentum loss across the obstacles and the smaller density difference between the flow and the ambient air after larger obstacles.

The experimental PDCs encounter the obstacles as subcritical flows with a densimetric Froude number below 1.2. Immediately after the obstacle crest, the currents strongly decelerate and become even more subcritical and dominated by buoyancy forces (Fig. 6.6). This is different from the gravity current model of Woods et al. (1998), where sub-critical gravity currents become super-critical downstream (Fig. 7.1d). Downstream of the obstacle, strong and sudden accelerations of the slow flow front occur. These accelerations get stronger behind large obstacles than behind small obstacles. They allow the delayed flow front of larger obstacles to propagate further than expected and reach similar distances at similar times for all three experiments. Interestingly, these accelerations match with the arrival at the front of internal gravity waves visible as density discontinuities and recorded as brief temperature peaks. These density discontinuities travel at high velocity inside the flow

and are unhindered by the obstacles, conserving their velocity and frequency across them regardless of their size. These brief but strong accelerations behind obstacles may need attention for hazard mitigation, particularly in the case of large obstacles.

Fourier spectra of specific kinetic energy across the obstacles allow the visualisation of strong energy peaks immediately behind the crest corresponding to these density discontinuities (Fig. 6.9). As the flow becomes compressed and accelerated on the stoss side of the obstacles, their energy associated with the density discontinuities increase significantly. However, large-scale coherent structures present before the obstacle may disappear in the detached flow, as there is no basal shear to generate them, before re-appearing downstream of the obstacle where the flow has re-attached. Interestingly, Fourier spectra also point out the presence of energy peaks associated with vortex shedding in the lee side of obstacles, which supports boundary layer separation mechanisms, and not ballistic trajectories.

Time- and depth-integrated density is the largest after the small obstacle because the form drag is lower, which explains why this flow has a great driving force. However, the density strongly decreases after the intermediate and large obstacles. The fine particles that are accelerated and advected on the stoss side of the hills become well coupled with the gas phase, while the coarse particles are ejected and redeposited downstream. Therefore, after the small obstacles, deposition is strong and the density decreases strongly. By contrast, after larger obstacles, fines stay suspended, and the density contrast remains relatively constant (Fig. 6.6b). Sufficiently downstream of the obstacles, flow density approaches similar values for all three obstacles, and the flows become positively buoyant at similar runout distances.

This effect influences how thermal energy is advected downstream. The flow temperature is hotter after the large obstacle and is well transferred downstream in the flow head. In contrast, after the small obstacle, temperature is colder and less well advected into the flow front (Fig. 6.8).

Figure 7.2 shows a sketch of the differences between flow propagation over a small and a large obstacle. The effect of flow compression and acceleration on the stoss side is shown. This phenomena has consequences up to the end of the runout, where fast-moving density discontinuities reach the slow flow front and cause sudden, accelerations. Hazards associated downstream of obstacles are also increasing with

increasing hill size. The suspension of fines and the long-lasting density contrast increases risks of suffocation while the heat carried by these particles increases burning hazards.

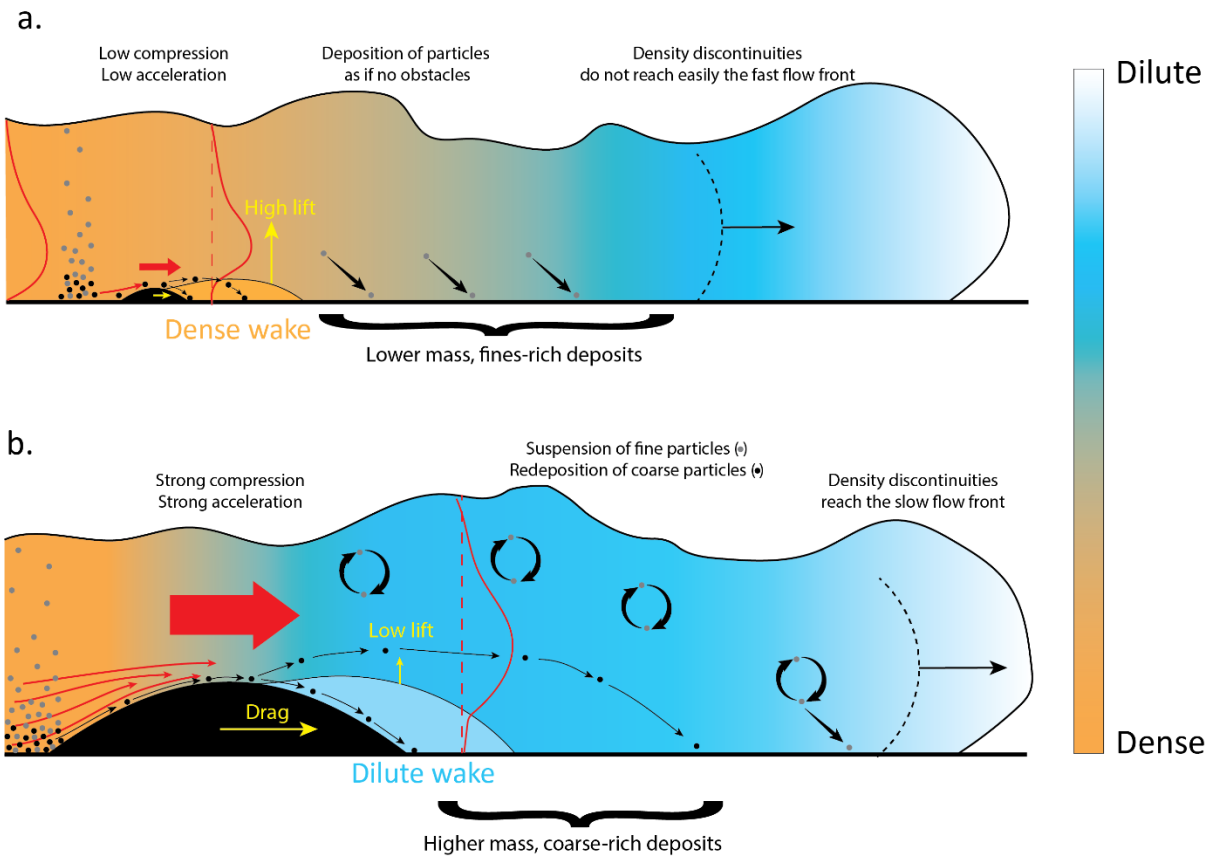

Figure 7.2: Sketch showing the difference in PDC-obstacle interactions with varying obstacle size and the consequences of this interaction downstream. The red arrows reprensent the compression of the flow on the stoss side and the acceleration. Typical velocity profiles are inserted before and after the obstacles as a red curve. Black and grey symbols represent coarse and fine particles respectively. Flow density is represented by the filling colour, with orange as the highest density and white as the lowest. After a small obstacle, density remains high but keeps decreasing. After a large obstacle, density decreases rapidly, but remains constant for long durations as fines are well suspended. The wakes are also coloured accordingly. The wake behind the small obstacle is dense and creates a strong lift force. The wake behind the large obstacle is more dilute and create a lower lift force.

7.1.3. Real-world application

The flows created for this research were dynamically and kinematically scaled to real-world PDCs. Therefore, real-world examples were tested for an application of these models.

The acceleration and compression on the stoss side of hills have important implications regarding the transfer from kinetic to potential energy. It suggests that compression of the flow is non negligible and should be accounted for when estimating the energy conversion. Previous gravity current models used obstacles and the conversion of kinetic to potential energies to estimate the velocity of pre-historic flows such as the parent flow that emplaced the 232 AD Taupō Ignimbrite. Very high initial velocities were found, up to 300 m/s for dense flows (Wilson 1985) and 250 m/s for fully dilute turbulent flows (Dade and Huppert 1996). These velocities are likely over-estimated as simple energy conversion model may not hold to estimate velocities of PDCs. Instead, when considering compression and acceleration of the flows on the stoss side of obstacles, the initial velocity of this parent flow may be significantly lower.

Tree patches are a good proxy to estimate the average re-attachment distance of a PDC behind an obstacle. In order to predict the possible re-attachment distance behind a known obstacle, a geometrical model linking the height of the obstacle compared to the flow and the re-attachment distance was developed. The average re-attachment distance from the crest follows an empirical power trend against the height ratio (Eq. 5.10 and Fig 5.5). Although more data would be required to confirm this model, it was able to accurately predict the re-attachment distances behind obstacles for the blast and blast-like surges of Mount Saint Helens 1980 (USA) and Te Maari 2012 (New Zealand), respectively. However, unless direct measurements of density are made inside a real-world flow, the lift force pushing up the boundary layer separation cannot be calculated with this model. Nevertheless, it is worth pointing out that the wakes behind obstacles should not be considered as a safe zone. Real-world flows are extremely dangerous and the particle density and temperatures in the wake would not be survivable, particularly behind small obstacles (see Chapter 5 of this thesis).

Finally, it was shown that the flows after a small obstacle have a high density contrast with the atmosphere and do not lose a lot of momentum. On the other hand, the flows after a large obstacle show significantly lower density contrast with the atmosphere and a strong momentum loss. Yet, the flow runout and distal densities are remarkably similar regardless of the obstacle dimensions. Two phenomena are responsible: (1) density discontinuities gaining energy and not decelerating on the stoss side of the obstacle due to compressible effects of PDC-obstacle interaction,

and (2) good coupling of fine particles with the gas phase. Whether this occurs in real-world flows or not remains to be shown.

Transport and deposition processes were analysed in detail across topographic obstacles. The variability in depositional features is explained through the variability in flow processes during its propagation described as flow phases. Figure 7.3 shows a sketch summarizing the sedimentation processes occurring across topographic obstacles. On the stoss side, coarse pumice breccia and massive units are emplaced through partial blocking of the dense underflow. A regressive bedform then ponds the deposits. On the lee side, thinner, layered deposits are visible with strong erosive features. Fine ash layers are emplaced through suspension sedimentation and sedimentation pulses in the wake. Coarser layers are deposited through migration of parts of the rolling and saltating bedload over the crest and down the slope. After the hill, the combination of these processes is the strongest as coarse clasts roll down the lee slope and are stranded at the break-in-slope, forming very poorly sorted deposits.

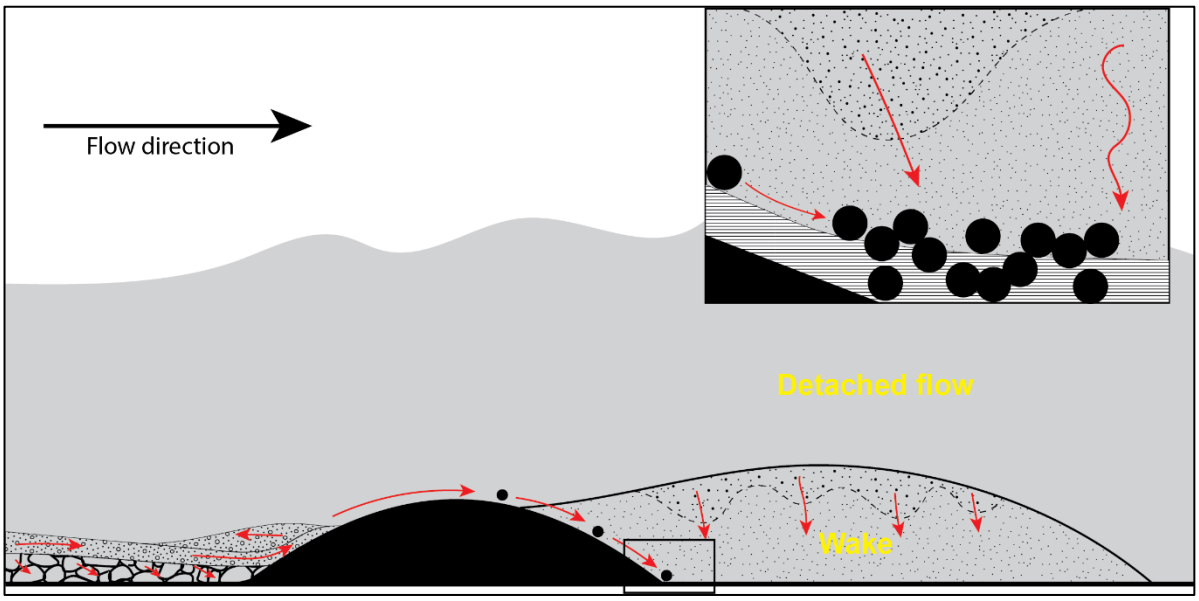

Figure 7.3: Sketch of the sedimentation processes occurring across topographic obstacles. On the stoss side, advection, partial blocking and regressive sedimentation occur. On the lee side and after the hill, rolling and saltating bedload, suspension sedimentation and sedimentation though pulses in finger-like instabilities occur.

This model can explain facies variations in real-world deposits of PDCs across topographic obstacles. Similar depositional features than the experiments are visible, notably regarding thickness and facies variations (e.g. Wilson 1985; Bursik et al. 1998;

Sulpizio et al. 2008). These findings can improve the understanding of sedimentation of real PDCs and help with the interpretation of deposits.

7.2. Limitations of the study

The results of this research need to be considered with attention to the following limits:

- Because each of these experiments takes months to prepare and analyse, they were carefully carried out to obtain the best possible results, but could not be repeated. Hence, only three experiments are considered here. More experiments would be needed to reinforce the dataset.
- Although similar processes are likely to occur in distal locations with lower energy, the experimental results proposed in this research are more applicable for proximal obstacles. Similarly, because of the disturbances created by the obstacle, the model is more applicable for an isolated ridge, or for the first ridge of a succession of obstacles. Future experiments and/or numerical studies should explore how the here described processes change when PDCs cross a succession of ridges.
- Ridges are comparable to the obstacles used in the experiments. However, a standing peak may not reproduce the described interactions in a similar way, because part of the flow may be deflected on the sides of the hill (e.g. Valentine 1987; Alexander and Morris 1994; Nasr-Azadani and Meiburg 2014). This could possibly disturb the wake dimensions and/or inhibit the downstream effects of the hill as the flow goes around it. However, vortex shedding may be significantly more intense, with von Karman vortex streets such as those described in turbulent flows interacting with hemispheres (e.g. Manhart 1998; Cao and Tamura 2020)

7.3. Perspectives for future research

These limits open the way to possible future works regarding the interactions of PDCs with obstacles, with other bodies, or to characterize their general characteristics. Here, suggestions for future research are presented.

Quantitative dataset of PDC-obstacles interactions

Because of the small number of experiments conducted during this PhD, developing a quantitative dataset would provide the necessary insights to extend the models proposed here. Typical possible experiments include:

- Reproducing experiments with the same conditions and obstacles for repeatability. Alternatively, variable initial flow mass, temperature, grainsize distribution, and/or different positioning of the hills could be possible.
- Experiments with very large obstacles inducing complete or almost complete blocking.
- Experiments with a longer discharge.

Succession of obstacles

In the real world, obstacles near volcanoes are seldom isolated, but consist more of a succession of hills, forming a terrain with alternating topographic highs and lows. Depending on the relative placement of these hills to each other, experiments modelling these terrains could provide new information on ponding of deposits or secondary flows channelizing particles into topographic lows. If the obstacles are close, the generated wake could englobe the next obstacle, or the re-attachment could occur on the stoss slope of the next hill.

Buildings as obstacles

Previously, large-scale experiments provided some insights on the risks associated with dynamic pressures on buildings. However, no experimental study so far has been scaled specifically for the purpose of investigating PDC-building interactions. While impacts of PDCs on human structures have been observed, changes in flow paths and dynamics associated with building interactions remain enigmatic. Such work could improve models of PDCs propagating in urban areas and

increase the resilience and preparedness of high-risk cities such as Auckland, Arequipa or Naples.

Channel bend

One typical behaviour of PDCs resides in their channelisation into valleys. But when these valleys abruptly change direction, PDCs have the ability to overspill (Cronin et al. 2013; Risica et al. 2022). Experiments with changes in channel direction could provide additional information on the conservation of momentum, building of deposits or other processes leading to this behaviour while the rest of the flow follows the channel.

Erosive layer

One idea that was not explored in this research was the introduction of an erosive layer into the channel. Particles changing colours with distance could be spread on the base of the channel (and over an obstacle) to track where erosion happens and where a given particle is redeposited. This research could provide insight into the erosive power of PDCs and ingestion of foreign material.

Variability in roughness

The roughness of the channel was kept constant during these experiments. Introduction of smoother or rougher substrate could provide information on the generation of turbulent structures inside PDCs and how they change according to the roughness.

PDC interactions with a water body

Volcanic tsunamis generated from a PDC entering water have recently raised the attention of scientists, with the notable example of the 2019 Stromboli eruption. Experiments by Bougouin et al. (2020) revealed that the PDC velocity, mass flux and grainsize distribution have major roles into the amplitude of the generated wave. More experiments, potentially with real-world material, could determine the processes behind the formation of these waves, and what conditions, if any, would lead to no tsunamis.

8. References

Abdurachman, EK, J-L Bourdier, and B Voight. 2000. “Nuées Ardentes of 22 November 1994 at Merapi Volcano, Java, Indonesia.” *Journal of Volcanology and Geothermal Research* 100 (1–4): 345–61.

Abhari, Mandana N, Marzieh Iranshahi, Masoud Ghodsian, and Bahar Firoozabadi. 2018. “Experimental Study of Obstacle Effect on Sediment Transport of Turbidity Currents.” *Journal of Hydraulic Research* 56 (5): 618–29.

Achenbach, Elmar. 1972. “Experiments on the Flow Past Spheres at Very High Reynolds Numbers.” *Journal of Fluid Mechanics* 54 (3): 565–75.

Alexander, Jan, and Stephen Morris. 1994. “Observations on Experimental, Nonchannelized, High-Concentration Turbidity Currents and Variations in Deposits around Obstacles.” *Journal of Sedimentary Research* 64 (4a): 899–909.

Allen, JRL. n.d. “1982, Sedimentary Structures: Their Character and Physical Basis, Volume II.” *Developments in Sedimentology* 30: 71009–4.

Altinakar, MS, WH Graf, and EJ Hopfinger. 1996. “Flow Structure in Turbidity Currents.” *Journal of Hydraulic Research* 34 (5): 713–18.

Andrews, Benjamin J. 2014. “Dispersal and Air Entrainment in Unconfined Dilute Pyroclastic Density Currents.” *Bulletin of Volcanology* 76 (9): 1–14.

Andrews, Benjamin J, and Michael Manga. 2011. “Effects of Topography on Pyroclastic Density Current Runout and Formation of Coignimbrites.” *Geology* 39 (12): 1099–1102.

———. 2012. “Experimental Study of Turbulence, Sedimentation, and Coignimbrite Mass Partitioning in Dilute Pyroclastic Density Currents.” *Journal of Volcanology and Geothermal Research* 225: 30–44.

Aramaki, Shigeo. 1984. “Formation of the Aira Caldera, Southern Kyushu,∼ 22,000 Years Ago.” *Journal of Geophysical Research: Solid Earth* 89 (B10): 8485–8501.

Baxter, Peter J. 1990. “Medical Effects of Volcanic Eruptions.” *Bulletin of Volcanology* 52 (7): 532–44.

Baxter, Peter J, Robin Boyle, Paul Cole, Augusto Neri, Robin Spence, and Giulio Zuccaro. 2005. “The Impacts of Pyroclastic Surges on Buildings at the Eruption of the Soufrière Hills Volcano, Montserrat.” *Bulletin of Volcanology* 67 (4): 292–313.

Baxter, Peter J, Susanna Jenkins, Rosadi Seswandhana, Jean-Christophe Komorowski, Ken Dunn, David Purser, Barry Voight, and Ian Shelley. 2017. “Human Survival in Volcanic Eruptions: Thermal Injuries in Pyroclastic Surges, Their Causes, Prognosis and Emergency Management.” *Burns* 43 (5): 1051–69.

Baxter, Peter J, Augusto Neri, and Micol Todesco. 1998. “Physical Modelling and Human Survival in Pyroclastic Flows.” *Natural Hazards* 17 (2): 163–76.

Best, James L. 1988. “Sediment Transport and Bed Morphology at River Channel Confluences.” *Sedimentology* 35 (3): 481–98.

Blott, Simon J, and Kenneth Pye. 2001. “GRADISTAT: A Grain Size Distribution and Statistics Package for the Analysis of Unconsolidated Sediments.” *Earth Surface Processes and Landforms* 26 (11): 1237–48.

Bougouin, Alexis, Raphael Paris, and Olivier Roche. 2020. “Impact of Fluidized Granular Flows into Water: Implications for Tsunamis Generated by Pyroclastic Flows.” *Journal of Geophysical Research: Solid Earth* 125 (5): e2019JB018954.

Brand, Brittany D, Sylvana Bendaña, Stephen Self, and Nicholas Pollock. 2016. “Topographic Controls on Pyroclastic Density Current Dynamics: Insight from 18 May 1980 Deposits at Mount St. Helens, Washington (USA).” *Journal of Volcanology and Geothermal Research* 321: 1–17.

Brand, Brittany D, Darren M Gravley, Amanda B Clarke, Jan M Lindsay, Simon H Bloomberg, Javier Agustin-Flores, and Károly Németh. 2014. “A Combined Field and Numerical Approach to Understanding Dilute Pyroclastic Density Current Dynamics and Hazard Potential: Auckland Volcanic Field, New Zealand.” *Journal of Volcanology and Geothermal Research* 276: 215–32.

Brand, Brittany D, Chelsea Mackaman-Lofland, Nicholas M Pollock, Sylvana Bendaña, Blaine Dawson, and Pamela Wichgers. 2014. “Dynamics of Pyroclastic Density Currents: Conditions That Promote Substrate Erosion and Self-Channelization—Mount St Helens, Washington (USA).” *Journal of Volcanology and Geothermal Research* 276: 189–214.

Branney, Michael J, and Peter Kokelaar. 1992. “A Reappraisal of Ignimbrite Emplacement: Progressive Aggradation and Changes from Particulate to Non-Particulate Flow during Emplacement of High-Grade Ignimbrite.” *Bulletin of Volcanology* 54 (6): 504–20.

———. 1997. “Giant Bed from a Sustained Catastrophic Density Current Flowing over Topography: Acatlan Ignimbrite, Mexico.” *Geology* 25 (2): 115–18.

———. 2002. “Pyroclastic Density Currents and the Sedimentation of Ignimbrites.” In . Geological Society of London.

Breard, ECP, G Lube, SJ Cronin, and GA Valentine. 2015. “Transport and Deposition Processes of the Hydrothermal Blast of the 6 August 2012 Te Maari Eruption, Mt. Tongariro.” *Bulletin of Volcanology* 77 (11): 100.

Breard, Eric Christophe Pascal. 2016. “Dynamics of Pyroclastic Density Currents.” *Massey University, Palmerston North, New Zealand*.

Breard, Eric CP, Josef Dufek, and Gert Lube. 2018. “Enhanced Mobility in Concentrated Pyroclastic Density Currents: An Examination of a Self-fluidization Mechanism.” *Geophysical Research Letters* 45 (2): 654–64.

Breard, Eric CP, Jim R Jones, Luke Fullard, Gert Lube, Clive Davies, and Josef Dufek. 2019. “The Permeability of Volcanic Mixtures—Implications for Pyroclastic Currents.” *Journal of Geophysical Research: Solid Earth*.

Breard, Eric CP, and Gert Lube. 2017. “Inside Pyroclastic Density Currents–Uncovering the Enigmatic Flow Structure and Transport Behaviour in Large-Scale Experiments.” *Earth and Planetary Science Letters* 458: 22–36.

Breard, Eric CP, Gert Lube, Jim R Jones, Josef Dufek, Shane J Cronin, Greg A Valentine, and Anja Moebis. 2016. “Coupling of Turbulent and Non-Turbulent Flow Regimes within Pyroclastic Density Currents.” *Nature Geoscience* 9 (10): 767.

Brodu, Nicolas, Renaud Delannay, Alexandre Valance, and Patrick Richard. 2015. “New Patterns in High-Speed Granular Flows.” *Journal of Fluid Mechanics* 769: 218–28.

Brosch, E, G Lube, T Esposti-Ongaro, M Cerminara, ECP Breard, and E Meiburg. 2022. “Characteristics and Controls of the Runout Behaviour of Non-Boussinesq Particle-Laden Gravity Currents–A Large-Scale Experimental Investigation of Dilute Pyroclastic Density Currents.” *Journal of Volcanology and Geothermal Research*, 107697.

Brosch, Ermanno. 2020. “Inside Pyroclastic Surges-a Characterisation of the Flow Behaviour, Hazard Impact Mechanisms and Sedimentation Processes through Large-Scale Experiments: A Thesis Presented in Partial Fulfilment of the Requirements for the Degree of Doctor of Philosophy in Earth Science at Massey University, Palmerston North, New Zealand.”

Brosch, Ermanno, and Gert Lube. 2020. “Spatiotemporal Sediment Transport and Deposition Processes in Experimental Dilute Pyroclastic Density Currents.” *Journal of Volcanology and Geothermal Research*, 106946.

Brosch, Ermanno, Gert Lube, Matteo Cerminara, Tomaso Esposti-Ongaro, Eric CP Breard, Josef Dufek, Betty Sovilla, and Luke Fullard. 2021. “Destructiveness of Pyroclastic Surges Controlled by Turbulent Fluctuations.” *Nature Communications* 12 (1): 1–12.

Brown, Richard J, and Michael J Branney. 2013. “Internal Flow Variations and Diachronous Sedimentation within Extensive, Sustained, Density-Stratified Pyroclastic Density Currents

Flowing down Gentle Slopes, as Revealed by the Internal Architectures of Ignimbrites on Tenerife." *Bulletin of Volcanology* 75 (7): 1–24.
Burgisser, Alain. 2005. "Physical Volcanology of the 2,050 BP Caldera-Forming Eruption of Okmok Volcano, Alaska." *Bulletin of Volcanology* 67 (6): 497–525.
Burgisser, Alain, and George W Bergantz. 2002. "Reconciling Pyroclastic Flow and Surge: The Multiphase Physics of Pyroclastic Density Currents." *Earth and Planetary Science Letters* 202 (2): 405–18.
Burgisser, Alain, George W Bergantz, and Robert E Breidenthal. 2005. "Addressing Complexity in Laboratory Experiments: The Scaling of Dilute Multiphase Flows in Magmatic Systems." *Journal of Volcanology and Geothermal Research* 141 (3–4): 245–65.
Bursik, Marcus I, Andrei V Kurbatov, Michael F Sheridan, and Andrew W Woods. 1998. "Transport and Deposition in the May 18, 1980, Mount St. Helens Blast Flow." *Geology* 26 (2): 155–58.
Bursik, Marcus I, and Andrew W Woods. 2000. "The Effects of Topography on Sedimentation from Particle-Laden Turbulent Density Currents." *Journal of Sedimentary Research* 70 (1): 53–63.
Calder, ES, PD Cole, WB Dade, TH Druitt, RP Hoblitt, HE Huppert, L Ritchie, RSJ Sparks, and SR Young. 1999. "Mobility of Pyroclastic Flows and Surges at the Soufriere Hills Volcano, Montserrat." *Geophysical Research Letters* 26 (5): 537–40.
Cantero-Chinchilla, Francisco Nicolás, Subhasish Dey, Oscar Castro-Orgaz, and Sk Zeeshan Ali. 2015. "Hydrodynamic Analysis of Fully Developed Turbidity Currents over Plane Beds Based on Self-preserving Velocity and Concentration Distributions." *Journal of Geophysical Research: Earth Surface* 120 (10): 2176–99.
Cao, Yong, and Tetsuro Tamura. 2020. "Large-Eddy Simulation Study of Reynolds Number Effects on the Flow around a Wall-Mounted Hemisphere in a Boundary Layer." *Physics of Fluids* 32 (2): 025109.
Capra, L, JL Macías, A Cortés, N Dávila, R Saucedo, S Osorio-Ocampo, JL Arce, JC Gavilanes-Ruiz, P Corona-Chávez, and L García-Sánchez. 2016. "Preliminary Report on the July 10–11, 2015 Eruption at Volcán de Colima: Pyroclastic Density Currents with Exceptional Runouts and Volume." *Journal of Volcanology and Geothermal Research* 310: 39–49.
Cas, Ray AF, Heather MN Wright, Christopher B Folkes, Chiara Lesti, Massimiliano Porreca, Guido Giordano, and Jose G Viramonte. 2011. "The Flow Dynamics of an Extremely Large Volume Pyroclastic Flow, the 2.08-Ma Cerro Galán Ignimbrite, NW Argentina, and Comparison with Other Flow Types." *Bulletin of Volcanology* 73 (10): 1583–1609.
Cerminara, Matteo, Ermanno Brosch, and Gert Lube. 2021. "A Theoretical Framework and the Experimental Dataset for Benchmarking Numerical Models of Dilute Pyroclastic Density Currents." *ArXiv Preprint ArXiv:2106.14057*.
Chédeville, Corentin, and Olivier Roche. 2015. "Influence of Slope Angle on Pore Pressure Generation and Kinematics of Pyroclastic Flows: Insights from Laboratory Experiments." *Bulletin of Volcanology* 77 (11): 1–13.
Choux, CM, and TH Druitt. 2002. "Analogue Study of Particle Segregation in Pyroclastic Density Currents, with Implications for the Emplacement Mechanisms of Large Ignimbrites." *Sedimentology* 49 (5): 907–28.
Chung, YC, CW Wu, CY Kuo, and SS Hsiau. 2019. "A Rapid Granular Chute Avalanche Impinging on a Small Fixed Obstacle: DEM Modeling, Experimental Validation and Exploration of Granular Stress." *Applied Mathematical Modelling* 74: 540–68.
Clarke, AB, and B Voight. 2000. "Pyroclastic Current Dynamic Pressure from Aerodynamics of Tree or Pole Blow-Down." *Journal of Volcanology and Geothermal Research* 100 (1–4): 395–412.
Criswell, C William. 1987. "Chronology and Pyroclastic Stratigraphy of the May 18, 1980, Eruption of Mount St. Helens, Washington." *Journal of Geophysical Research: Solid Earth* 92 (B10): 10237–66.
Cronin, Shane J, Gert Lube, Devi S Dayudi, Sri Sumarti, and S Subrandiyo. 2013. "Insights into the October–November 2010 Gunung Merapi Eruption (Central Java, Indonesia) from the

Stratigraphy, Volume and Characteristics of Its Pyroclastic Deposits." *Journal of Volcanology and Geothermal Research* 261: 244–59.
Dade, W Brian, and Herbert E Huppert. 1996. "Emplacement of the Taupo Ignimbrite by a Dilute Turbulent Flow." *Nature* 381 (6582): 509.
Dellino, P, F Dioguardi, B Zimanowski, R Büttner, D Mele, L La Volpe, R Sulpizio, DM Doronzo, I Sonder, and R Bonasia. 2010. "Conduit Flow Experiments Help Constraining the Regime of Explosive Eruptions." *Journal of Geophysical Research: Solid Earth* 115 (B4).
Dellino, Pierfrancesco, Ralf Büttner, Fabio Dioguardi, Domenico M Doronzo, Luigi La Volpe, Daniela Mele, Ingo Sonder, Roberto Sulpizio, and Bernd Zimanowski. 2010. "Experimental Evidence Links Volcanic Particle Characteristics to Pyroclastic Flow Hazard." *Earth and Planetary Science Letters* 295 (1–2): 314–20.
Dellino, Pierfrancesco, Fabio Dioguardi, Roberto Isaia, Roberto Sulpizio, and Daniela Mele. 2021. "The Impact of Pyroclastic Density Currents Duration on Humans: The Case of the AD 79 Eruption of Vesuvius." *Scientific Reports* 11 (1): 1–9.
Dellino, Pierfrancesco, Daniela Mele, Roberto Sulpizio, Luigi La Volpe, and Giuseppe Braia. 2008. "A Method for the Calculation of the Impact Parameters of Dilute Pyroclastic Density Currents Based on Deposit Particle Characteristics." *Journal of Geophysical Research: Solid Earth* 113 (B7).
Dellino, Pierfrancesco, Bernd Zimanowski, Ralf Büttner, Luigi La Volpe, Daniela Mele, and Roberto Sulpizio. 2007. "Large-scale Experiments on the Mechanics of Pyroclastic Flows: Design, Engineering, and First Results." *Journal of Geophysical Research: Solid Earth* 112 (B4).
Doronzo, Domenico M, and Pierfrancesco Dellino. 2013. "Hydraulics of Subaqueous Ash Flows as Deduced from Their Deposits: 2. Water Entrainment, Sedimentation, and Deposition, with Implications on Pyroclastic Density Current Deposit Emplacement." *Journal of Volcanology and Geothermal Research* 258: 176–86.
Doronzo, Domenico M, Greg A Valentine, Pierfrancesco Dellino, and Marco D de Tullio. 2010. "Numerical Analysis of the Effect of Topography on Deposition from Dilute Pyroclastic Density Currents." *Earth and Planetary Science Letters* 300 (1–2): 164–73.
Doronzo, Domenico Maria, and Pierfrancesco Dellino. 2010. "A Fluid Dynamic Model of Volcaniclastic Turbidity Currents Based on the Similarity with the Lower Part of Dilute Pyroclastic Density Currents: Evaluation of the Ash Dispersal from Ash Turbidites." *Journal of Volcanology and Geothermal Research* 191 (3–4): 193–204.
Douillet, Guilhem Amin, Daniel Alejandro Pacheco, Ulrich Kueppers, Jean Letort, Ève Tsang-Hin-Sun, Jorge Bustillos, Minard Hall, Patricio Ramón, and Donald B Dingwell. 2013. "Dune Bedforms Produced by Dilute Pyroclastic Density Currents from the August 2006 Eruption of Tungurahua Volcano, Ecuador." *Bulletin of Volcanology* 75 (11): 1–20.
Douillet, Guilhem Amin, Ève Tsang-Hin-Sun, Ulrich Kueppers, Jean Letort, Daniel Alejandro Pacheco, Fabian Goldstein, Felix Von Aulock, Yan Lavallée, Jonathan Bruce Hanson, and Jorge Bustillos. 2013. "Sedimentology and Geomorphology of the Deposits from the August 2006 Pyroclastic Density Currents at Tungurahua Volcano, Ecuador." *Bulletin of Volcanology* 75 (11): 1–21.
Druitt, TH. 1992. "Emplacement of the 18 May 1980 Lateral Blast Deposit ENE of Mount St. Helens, Washington." *Bulletin of Volcanology* 54 (7): 554–72.
———. 1998. "Pyroclastic Density Currents." *Geological Society, London, Special Publications* 145 (1): 145–82.
Druitt, TH, and RSJ Sparks. 1984. "On the Formation of Calderas during Ignimbrite Eruptions." *Nature* 310 (5979): 679.
Druitt, Tim. 1996. "Turbulent Times at Taupo." *Nature* 381 (6582): 476.
Esposti Ongaro, T, AB Clarke, Barry Voight, A Neri, and Christina Widiwijayanti. 2012. "Multiphase Flow Dynamics of Pyroclastic Density Currents during the May 18, 1980 Lateral Blast of Mount St. Helens." *Journal of Geophysical Research: Solid Earth* 117 (B6).

Farizan, Ahmadreza, Sina Yaghoubi, Bahar Firoozabadi, and Hossein Afshin. 2019. “Effect of an Obstacle on the Depositional Behaviour of Turbidity Currents.” *Journal of Hydraulic Research* 57 (1): 75–89.

Fisher, Richard V. 1990. “Transport and Deposition of a Pyroclastic Surge across an Area of High Relief: The 18 May 1980 Eruption of Mount St. Helens, Washington.” *Geological Society of America Bulletin* 102 (8): 1038–54.

Fisher, Richard V, Giovanni Orsi, Michael Ort, and Grant Heiken. 1993. “Mobility of a Large-Volume Pyroclastic Flow—Emplacement of the Campanian Ignimbrite, Italy.” *Journal of Volcanology and Geothermal Research* 56 (3): 205–20.

Folk, Robert Louis, and William C Ward. 1957. “Brazos River Bar [Texas]; a Study in the Significance of Grain Size Parameters.” *Journal of Sedimentary Research* 27 (1): 3–26.

Freundt, Armin, and Hans-Ulrich Schmincke. 1985. “Lithic-Enriched Segregation Bodies in Pyroclastic Flow Deposits of Laacher See Volcano (East Eifel, Germany).” *Journal of Volcanology and Geothermal Research* 25 (3–4): 193–224.

García, Marcelo H. 1993. “Hydraulic Jumps in Sediment-Driven Bottom Currents.” *Journal of Hydraulic Engineering* 119 (10): 1094–1117.

Gardner, James E, Alain Burgisser, and Pete Stelling. 2007. “Eruption and Deposition of the Fisher Tuff (Alaska): Evidence for the Evolution of Pyroclastic Flows.” *The Journal of Geology* 115 (4): 417–35.

Gardner, James E, Caroline Nazworth, Mark A Helper, and Benjamin J Andrews. 2018. “Inferring the Nature of Pyroclastic Density Currents from Tree Damage: The 18 May 1980 Blast Surge of Mount St. Helens, USA.” *Geology* 46 (9): 795–98.

Giordano, G, E Zanella, M Trolese, C Baffioni, A Vona, Chiara Caricchi, AA De Benedetti, S Corrado, C Romano, and R Sulpizio. 2018. “Thermal Interactions of the AD79 Vesuvius Pyroclastic Density Currents and Their Deposits at Villa Dei Papiri (Herculaneum Archaeological Site, Italy).” *Earth and Planetary Science Letters* 490: 180–92.

Giordano, Guido. 1998. “The Effect of Paleotopography on Lithic Distribution and Facies Associations of Small Volume Ignimbrites: The WTT Cupa (Roccamonfina Volcano, Italy).” *Journal of Volcanology and Geothermal Research* 87 (1–4): 255–73.

Goodarzi, Danial, Kaveh Sookhak Lari, Ehsan Khavasi, and Soroush Abolfathi. 2020. “Large Eddy Simulation of Turbidity Currents in a Narrow Channel with Different Obstacle Configurations.” *Scientific Reports* 10 (1): 1–16.

Gröbelbauer, HP, TK Fanneløp, and RE Britter. 1993. “The Propagation of Intrusion Fronts of High Density Ratios.” *Journal of Fluid Mechanics* 250: 669–87.

Gueugneau, Valentin, Karim Kelfoun, and Timothy Druitt. 2019. “Investigation of Surge-Derived Pyroclastic Flow Formation by Numerical Modelling of the 25 June 1997 Dome Collapse at Soufrière Hills Volcano, Montserrat.” *Bulletin of Volcanology* 81 (4): 25.

Guinn, Nicole K, James E Gardner, and Mark A Helper. 2022. “Dynamic Pressure Evolution within the 18 May 1980 Mount St. Helens Pyroclastic Density Current: Evidence from Tree Damage.” *Bulletin of Volcanology* 84 (4): 1–12.

Gurioli, L, Elena Zanella, MT Pareschi, and Roberto Lanza. 2007. “Influences of Urban Fabric on Pyroclastic Density Currents at Pompeii (Italy): 1. Flow Direction and Deposition.” *Journal of Geophysical Research: Solid Earth* 112 (B5).

Gurioli, Lucia, Raffaello Cioni, Alessandro Sbrana, and Elena Zanella. 2002. “Transport and Deposition of Pyroclastic Density Currents over an Inhabited Area: The Deposits of the AD 79 Eruption of Vesuvius at Herculaneum, Italy.” *Sedimentology* 49 (5): 929–53.

Gurioli, Lucia, R Sulpizio, R Cioni, Alessandro Sbrana, Roberto Santacroce, W Luperini, and D Andronico. 2010. “Pyroclastic Flow Hazard Assessment at Somma–Vesuvius Based on the Geological Record.” *Bulletin of Volcanology* 72 (9): 1021–38.

Hákonardóttir, Kristín Martha, Andrew J Hogg, Jenny Batey, and Andrew W Woods. 2003. “Flying Avalanches.” *Geophysical Research Letters* 30 (23).

Hincks, Thea K, WP Aspinall, Peter J Baxter, Alison Searl, RSJ Sparks, and G Woo. 2006. “Long Term Exposure to Respirable Volcanic Ash on Montserrat: A Time Series Simulation.” *Bulletin of Volcanology* 68 (3): 266–84.

Hoblitt, RICHARD P, CD Miller, and JW Vallance. 1981. “Origin and Stratigraphy of the Deposit Produced by the May 18 Directed Blast.” In *The 1980 Eruptions of Mount St. Helens, Washington*, 1250:401–19. US Government Printing Office Washington, DC.

Hudspith, Victoria A, Andrew C Scott, Colin JN Wilson, and Margaret E Collinson. 2010. “Charring of Woods by Volcanic Processes: An Example from the Taupo Ignimbrite, New Zealand.” *Palaeogeography, Palaeoclimatology, Palaeoecology* 291 (1–2): 40–51.

Jenkins, S, J-C Komorowski, PJ Baxter, R Spence, A Picquout, and F Lavigne. 2013. “The Merapi 2010 Eruption: An Interdisciplinary Impact Assessment Methodology for Studying Pyroclastic Density Current Dynamics.” *Journal of Volcanology and Geothermal Research* 261: 316–29.

Jeon, Yong Mun, Chang Woo Kwon, and Young Kwan Sohn. 2011. “Deposition from Pyroclastic Surges Partially Blocked by a Topographic Obstacle: An Example from the Ilchulbong Tuff Cone, Jeju Island, Korea.” *Geosciences Journal* 15 (2): 121–30.

Kelfoun, K, F Legros, and A Gourgaud. 2000. “A Statistical Study of Trees Damaged by the 22 November 1994 Eruption of Merapi Volcano (Java, Indonesia): Relationships between Ash-Cloud Surges and Block-and-Ash Flows.” *Journal of Volcanology and Geothermal Research* 100 (1–4): 379–93.

Kelfoun, Karim, and Valentin Gueugneau. 2022. “A Unifying Model for Pyroclastic Surge Genesis and Pyroclastic Flow Fluidization.” *Geophysical Research Letters*, e2021GL096517.

Kieffer, Susan Werner, and Bradford Sturtevant. 1988. “Erosional Furrows Formed during the Lateral Blast at Mount St. Helens, May 18, 1980.” *Journal of Geophysical Research: Solid Earth* 93 (B12): 14793–816.

Komorowski, Jean-Christophe, Susanna Jenkins, Peter J Baxter, Adrien Picquout, Franck Lavigne, Sylvain Charbonnier, Ralf Gertisser, Katie Preece, Noer Cholik, and Agus Budi-Santoso. 2013. “Paroxysmal Dome Explosion during the Merapi 2010 Eruption: Processes and Facies Relationships of Associated High-Energy Pyroclastic Density Currents.” *Journal of Volcanology and Geothermal Research* 261: 260–94.

Lee, Hong-Yuan, and Wei-Sheng Yu. 1997. “Experimental Study of Reservoir Turbidity Current.” *Journal of Hydraulic Engineering* 123 (6): 520–28.

Legros, F, and K Kelfoun. 2000. “On the Ability of Pyroclastic Flows to Scale Topographic Obstacles.” *Journal of Volcanology and Geothermal Research* 98 (1–4): 235–41.

Legros, François, Karim Kelfoun, and Joan Martí. 2000. “The Influence of Conduit Geometry on the Dynamics of Caldera-Forming Eruptions.” *Earth and Planetary Science Letters* 179 (1): 53–61.

Loughlin, SC, ES Calder, Amanda Clarke, PD Cole, R Luckett, MT Mangan, DM Pyle, RSJ Sparks, B Voight, and RB Watts. 2002. “Pyroclastic Flows and Surges Generated by the 25 June 1997 Dome Collapse, Soufrière Hills Volcano, Montserrat.” *Geological Society, London, Memoirs* 21 (1): 191–209.

Lovering, Thomas Seward. 1957. “Halogen-Acid Alteration of Ash at Fumarole No. 1, Valley of Ten Thousand Smokes, Alaska.” *Geological Society of America Bulletin* 68 (12): 1585–1604.

Lube, G, ECP Breard, SJ Cronin, and J Jones. 2015. “Synthesizing Large-scale Pyroclastic Flows: Experimental Design, Scaling, and First Results from PELE.” *Journal of Geophysical Research: Solid Earth* 120 (3): 1487–1502.

Lube, Gert, Eric CP Breard, Shane J Cronin, Jonathan N Procter, Marco Brenna, Anja Moebis, Natalia Pardo, Robert B Stewart, Arthur Jolly, and Nicolas Fournier. 2014. “Dynamics of Surges Generated by Hydrothermal Blasts during the 6 August 2012 Te Maari Eruption, Mt. Tongariro, New Zealand.” *Journal of Volcanology and Geothermal Research* 286: 348–66.

Lube, Gert, Eric CP Breard, Tomaso Esposti-Ongaro, Josef Dufek, and Brittany Brand. 2020. “Multiphase Flow Behaviour and Hazard Prediction of Pyroclastic Density Currents.” *Nature Reviews Earth & Environment* 1 (7): 348–65.

Lube, Gert, Eric CP Breard, Jim Jones, Luke Fullard, Josef Dufek, Shane J Cronin, and Ting Wang. 2019. “Generation of Air Lubrication within Pyroclastic Density Currents.” *Nature Geoscience*, 1.

Lube, Gert, Shane J Cronin, Thomas Platz, Armin Freundt, Jonathan N Procter, Cargill Henderson, and Michael F Sheridan. 2007. “Flow and Deposition of Pyroclastic Granular Flows: A Type Example from the 1975 Ngauruhoe Eruption, New Zealand.” *Journal of Volcanology and Geothermal Research* 161 (3): 165–86.

Lube, Gert, Shane J Cronin, and Jean-Claude Thouret. 2011. “Kinematic Characteristics of Pyroclastic Density Currents at Merapi and Controls on Their Avulsion from Natural and Engineered Channels.” *GSA Bulletin* 123 (5–6): 1127–40.

Lucas, Antoine, Anne Mangeney, and Jean Paul Ampuero. 2014. “Frictional Velocity-Weakening in Landslides on Earth and on Other Planetary Bodies.” *Nature Communications* 5: 3417.

Ma, X, G-S Karamanos, and GE Karniadakis. 2000. “Dynamics and Low-Dimensionality of a Turbulent near Wake.” *Journal of Fluid Mechanics* 410: 29–65.

Macıas, JL, JM Espındola, M Bursik, and MF Sheridan. 1998. “Development of Lithic-Breccias in the 1982 Pyroclastic Flow Deposits of El Chichon Volcano, Mexico.” *Journal of Volcanology and Geothermal Research* 83 (3–4): 173–96.

Malin, Michael C, and Michael F Sheridan. 1982. “Computer-Assisted Mapping of Pyroclastic Surges.” *Science* 217 (4560): 637–40.

Manhart, Michael. 1998. “Vortex Shedding from a Hemisphere in a Turbulent Boundary Layer.” *Theoretical and Computational Fluid Dynamics* 12 (1): 1–28.

Mastrolorenzo, Giuseppe, Pier P Petrone, Mario Pagano, Alberto Incoronato, Peter J Baxter, Antonio Canzanella, and Luciano Fattore. 2001. “Herculaneum Victims of Vesuvius in AD 79.” *Nature* 410 (6830): 769–70.

McClelland, Elizabeth, Colin JN Wilson, and Leon Bardot. 2004. “Palaeotemperature Determinations for the 1.8-Ka Taupo Ignimbrite, New Zealand, and Implications for the Emplacement History of a High-Velocity Pyroclastic Flow.” *Bulletin of Volcanology* 66 (6): 492–513.

Mehta, Rabindra D. 1985. “Aerodynamics of Sports Balls.” *Annual Review of Fluid Mechanics* 17 (1): 151–89.

Middleton, Gerard V. 1966a. “Experiments on Density and Turbidity Currents: I. Motion of the Head.” *Canadian Journal of Earth Sciences* 3 (4): 523–46.

———. 1966b. “Experiments on Density and Turbidity Currents: II. Uniform Flow of Density Currents.” *Canadian Journal of Earth Sciences* 3 (5): 627–37.

———. 1967. “Experiments on Density and Turbidity Currents: III. Deposition of Sediment.” *Canadian Journal of Earth Sciences* 4 (3): 475–505.

———. 1993. “Sediment Deposition from Turbidity Currents.” *Annual Review of Earth and Planetary Sciences* 21 (1): 89–114.

Moore, JAMES G, and CARL J Rice. 1984. “Chronology and Character of the May 18, 1980, Explosive Eruptions of Mount St. Helens.” *Explosive Volcanism: Inception, Evolution, and Hazards* 10: 133–57.

Moore, JG. 1967. “Base Surge in Recent Volcanic Eruptions.” *Bulletin Volcanologique* 30 (1): 337.

Mullineaux, Donal R, and Peter W Lipman. 1981. *The 1980 Eruptions of Mount St. Helens, Washington*. US Government Printing Office.

Naaim-Bouvet, Florence, Mohamed Naaim, and Thierry Faug. 2004. “Dense and Powder Avalanches: Momentumreduction Generated by a Dam.” *Annals of Glaciology* 38: 373–78.

Nasr-Azadani, Mohamad M, and Eckart Meiburg. 2014. “Influence of Seafloor Topography on the Depositional Behavior of Bi-Disperse Turbidity Currents: A Three-Dimensional, Depth-Resolved Numerical Investigation.” *Environmental Fluid Mechanics* 14 (2): 319–42.

Ogburn, Sarah E, Eliza S Calder, Paul D Cole, and Adam J Stinton. 2014. “The Effect of Topography on Ash-Cloud Surge Generation and Propagation.” *Geological Society, London, Memoirs* 39 (1): 179–94.

Oshaghi, Mohammad Reza, Hossein Afshin, and Bahar Firoozabadi. 2013. “Experimental Investigation of the Effect of Obstacles on the Behavior of Turbidity Currents.” *Canadian Journal of Civil Engineering* 40 (4): 343–52.

Parker, Gary, M Garcia, Y Fukushima, and Wrn Yu. 1987. “Experiments on Turbidity Currents over an Erodible Bed.” *Journal of Hydraulic Research* 25 (1): 123–47.

Pollock, Nicholas M, Brittany D Brand, Peter J Rowley, Damiano Sarocchi, and Roberto Sulpizio. 2019. “Inferring Pyroclastic Density Current Flow Conditions Using Syn-Depositional Sedimentary Structures.” *Bulletin of Volcanology* 81 (8): 46.

Prosser, Ian P, Ian D Rutherfurd, Jon M Olley, William J Young, Peter J Wallbrink, and Chris J Moran. 2001. “Large-Scale Patterns of Erosion and Sediment Transport in River Networks, with Examples from Australia.” *Marine and Freshwater Research* 52 (1): 81–99.

Risica, Gilda, Mauro Rosi, Marco Pistolesi, Fabio Speranza, and Michael J Branney. 2022. “Deposit-Derived Block-and-Ash Flows: The Hazard Posed by Perched Temporary Tephra Accumulations on Volcanoes; 2018 Fuego Disaster, Guatemala.” *Journal of Geophysical Research: Solid Earth* 127 (6): e2021JB023699.

Roche, Olivier. 2012. “Depositional Processes and Gas Pore Pressure in Pyroclastic Flows: An Experimental Perspective.” *Bulletin of Volcanology* 74 (8): 1807–20.

Roche, Olivier, Nourddine Azzaoui, and Arnaud Guillin. 2021. “Discharge Rate of Explosive Volcanic Eruption Controls Runout Distance of Pyroclastic Density Currents.” *Earth and Planetary Science Letters* 568: 117017.

Roche, Olivier, David C Buesch, and Greg A Valentine. 2016. “Slow-Moving and Far-Travelled Dense Pyroclastic Flows during the Peach Spring Super-Eruption.” *Nature Communications* 7 (1): 1–8.

Roche, Olivier, and Timothy H Druitt. 2001. “Onset of Caldera Collapse during Ignimbrite Eruptions.” *Earth and Planetary Science Letters* 191 (3–4): 191–202.

Roche, Olivier, Christopher D Henry, Nourddine Azzaoui, and Arnaud Guillin. 2022. “Long-Runout Pyroclastic Density Currents: Analysis and Implications.” *Geology*.

Roche, Olivier, Siet van den Wildenberg, Alexandre Valance, Renaud Delannay, Anne Mangeney, Lucas Corna, and Thierry Latchimy. 2021. “Experimental Assessment of the Effective Friction at the Base of Granular Chute Flows on a Smooth Incline.” *Physical Review E* 103 (4): 042905.

Rowley, Pete J, Olivier Roche, Timothy H Druitt, and Ray Cas. 2014. “Experimental Study of Dense Pyroclastic Density Currents Using Sustained, Gas-Fluidized Granular Flows.” *Bulletin of Volcanology* 76 (9): 1–13.

Savitzky, Abraham, and Marcel JE Golay. 1964. “Smoothing and Differentiation of Data by Simplified Least Squares Procedures.” *Analytical Chemistry* 36 (8): 1627–39.

Scarpati, Claudio, Paul Cole, and Annamaria Perrotta. 1993. “The Neapolitan Yellow Tuff—a Large Volume Multiphase Eruption from Campi Flegrei, Southern Italy.” *Bulletin of Volcanology* 55 (5): 343–56.

SCHMINCKE, HANS-ULRICH, Richard V Fisher, and Aaron C Waters. 1973. “Antidune and Chute and Pool Structures in the Base Surge Deposits of the Laacher See Area, Germany.” *Sedimentology* 20 (4): 553–74.

Schneider, Jean-Luc, Anthony Le Ruyet, Frank Chanier, Christophe Buret, Jacky Ferrière, Jean-Noël Proust, and Jean-Baptiste Rosseel. 2001. “Primary or Secondary Distal Volcaniclastic Turbidites: How to Make the Distinction? An Example from the Miocene of New Zealand (Mahia Peninsula, North Island).” *Sedimentary Geology* 145 (1–2): 1–22.

Sher, Diana, and Andrew W Woods. 2017. “Experiments on Mixing in Pyroclastic Density Currents Generated from Short-Lived Volcanic Explosions.” *Earth and Planetary Science Letters* 467: 138–48.

Sigurdsson, Haraldur, Steven Carey, Charles Mandeville, and Sutikno Bronto. 1991. “Pyroclastic Flows of the 1883 Krakatau Eruption.” *Eos, Transactions American Geophysical Union* 72 (36): 377–81.

Sigurdsson, Haraldur, Stanford Cashdollar, and Stephen RJ Sparks. 1982. “The Eruption of Vesuvius in AD 79: Reconstruction from Historical and Volcanological Evidence.” *American Journal of Archaeology*, 39–51.

Simpson, Roger L. 1989. “Turbulent Boundary-Layer Separation.” *Annual Review of Fluid Mechanics* 21 (1): 205–32.

Sparks, R Stephen J. 1976. “Grain Size Variations in Ignimbrites and Implications for the Transport of Pyroclastic Flows.” *Sedimentology* 23 (2): 147–88.

Sparks, RSJ, Lionel Wilson, and George Hulme. 1978. “Theoretical Modeling of the Generation, Movement, and Emplacement of Pyroclastic Flows by Column Collapse.” *Journal of Geophysical Research: Solid Earth* 83 (B4): 1727–39.

Sulpizio, Roberto, Rosanna De Rosa, and Paola Donato. 2008. “The Influence of Variable Topography on the Depositional Behaviour of Pyroclastic Density Currents: The Examples of the Upper Pollara Eruption (Salina Island, Southern Italy).” *Journal of Volcanology and Geothermal Research* 175 (3): 367–85.

Sulpizio, Roberto, P Dellino, DM Doronzo, and D Sarocchi. 2014. “Pyroclastic Density Currents: State of the Art and Perspectives.” *Journal of Volcanology and Geothermal Research* 283: 36–65.

Takarada, Shinji, and Hideo Hoshizumi. 2020. “Distribution and Eruptive Volume of Aso-4 Pyroclastic Density Current and Tephra Fall Deposits, Japan: A M8 Super-Eruption.” *Frontiers in Earth Science* 8: 170.

Tanguy, J-C, Ch Ribière, A Scarth, and WS Tjetjep. 1998. “Victims from Volcanic Eruptions: A Revised Database.” *Bulletin of Volcanology* 60 (2): 137–44.

Tanguy, Jean-Claude. 1994. “The 1902–1905 Eruptions of Montagne Pelée, Martinique: Anatomy and Retrospection.” *Journal of Volcanology and Geothermal Research* 60 (2): 87–107.

Thielicke, William, and Eize Stamhuis. 2014. “PIVlab–towards User-Friendly, Affordable and Accurate Digital Particle Image Velocimetry in MATLAB.” *Journal of Open Research Software* 2 (1).

Todesco, M, A Neri, T Esposti Ongaro, P Papale, G Macedonio, Roberto Santacroce, and A Longo. 2002. “Pyroclastic Flow Hazard Assessment at Vesuvius (Italy) by Using Numerical Modeling. I. Large-Scale Dynamics.” *Bulletin of Volcanology* 64 (3): 155–77.

Trofimovs, Jessica, R STEPHEN JOHN SPARKS, and Peter J Talling. 2008. “Anatomy of a Submarine Pyroclastic Flow and Associated Turbidity Current: July 2003 Dome Collapse, Soufrière Hills Volcano, Montserrat, West Indies.” *Sedimentology* 55 (3): 617–34.

Valentine, Greg A. 1987. “Stratified Flow in Pyroclastic Surges.” *Bulletin of Volcanology* 49 (4): 616–30.

———. 1998. “Damage to Structures by Pyroclastic Flows and Surges, Inferred from Nuclear Weapons Effects.” *Journal of Volcanology and Geothermal Research* 87 (1–4): 117–40.

Valentine, Greg A, David C Buesch, and Richard V Fisher. 1989. “Basal Layered Deposits of the Peach Springs Tuff, Northwestern Arizona, USA.” *Bulletin of Volcanology* 51 (6): 395–414.

Viroulet, Sylvain, JL Baker, AN Edwards, C Gjaltema Johnson, C Gjaltema, P Clavel, and JMNT Gray. 2017. “Multiple Solutions for Granular Flow over a Smooth Two-Dimensional Bump.” *Journal of Fluid Mechanics* 815: 77–116.

Voight, B, and MJ Davis. 2000. “Emplacement Temperatures of the November 22, 1994 Nuée Ardente Deposits, Merapi Volcano, Java.” *Journal of Volcanology and Geothermal Research* 100 (1–4): 371–77.

Walker, George PL. 1983. “Ignimbrite Types and Ignimbrite Problems.” *Journal of Volcanology and Geothermal Research* 17 (1–4): 65–88.

———. 1985. “Origin of Coarse Lithic Breccias near Ignimbrite Source Vents.” *Journal of Volcanology and Geothermal Research* 25 (1–2): 157–71.

Walker, GPL, and CJN Wilson. 1983. “Lateral Variations in the Taupo Ignimbrite.” *Journal of Volcanology and Geothermal Research* 18 (1–4): 117–33.

Waters, Aaron C, and Richard V Fisher. 1971. “Base Surges and Their Deposits: Capelinhos and Taal Volcanoes.” *Journal of Geophysical Research* 76 (23): 5596–5614.

White, James DL. 2000. “Subaqueous Eruption-Fed Density Currents and Their Deposits.” *Precambrian Research* 101 (2–4): 87–109.
Whiteford, Linda M, and Graham A Tobin. 2009. “If the Pyroclastic Flow Doesn’t Kill You, the Recovery Will: Cascading Impacts of Mt. Tungurahua’s Eruptions in Rural Ecuador.” *The Political Economy of Hazards and Disasters. Lanham, MD: Altamira*, 155–78.
Wilson, CJN. 1997. “Emplacement of Taupo Ignimbrite.” *Nature* 385 (6614): 306.
Wilson, Colin James Ness. 1985. “The Taupo Eruption, New Zealand. II. The Taupo Ignimbrite.” *Philosophical Transactions of the Royal Society of London. Series A, Mathematical and Physical Sciences* 314 (1529): 229–310.
Wilson, Richard I, Heide Friedrich, and Craig Stevens. 2018. “Flow Structure of Unconfined Turbidity Currents Interacting with an Obstacle.” *Environmental Fluid Mechanics* 18 (6): 1571–94.
Wohletz, KH. 1998. “Pyroclastic Surges and Two-Phase Compressible Flows.” *From Magma to Tephra*, 247–312.
Wohletz, KH, and Michael F Sheridan. 1979. “A Model of Pyroclastic Surge.” *Geol Soc Am Spec Pap* 180: 177–94.
Woods, Andrew W, Marcus I Bursik, and Andrei V Kurbatov. 1998. “The Interaction of Ash Flows with Ridges.” *Bulletin of Volcanology* 60 (1): 38–51.
Yamamoto, Takahiro, Yoichi Nakamura, and Harry Glicken. 1999. “Pyroclastic Density Current from the 1888 Phreatic Eruption of Bandai Volcano, NE Japan.” *Journal of Volcanology and Geothermal Research* 90 (3–4): 191–207.
Yamamoto, Takahiro, Shinji Takarada, and Shigeru Suto. 1993. “Pyroclastic Flows from the 1991 Eruption of Unzen Volcano, Japan.” *Bulletin of Volcanology* 55 (3): 166–75.

9. Appendix

Appendix A – Supplementary data sheets

Data sheets are available at the following address, along with videos of Supplementary materials 4.2 to 4.5.

https://drive.google.com/drive/folders/1FjtDvSlajUmxNk6lDid5QC_JilHXYPt2?usp=share_link

Appendix B: DRC 16 forms

DRC 16

MASSEY UNIVERSITY
UNIVERSITY OF NEW ZEALAND
GRADUATE RESEARCH SCHOOL

STATEMENT OF CONTRIBUTION
DOCTORATE WITH PUBLICATIONS/MANUSCRIPTS

We, the candidate and the candidate's Primary Supervisor, certify that all co-authors have consented to their work being included in the thesis and they have accepted the candidate's contribution as indicated below in the *Statement of Originality*.

Name of candidate:	Lucas Raphael Pierre Corna
Name/title of Primary Supervisor:	Gert Lube
In which chapter is the manuscript /published work:	4

Please select one of the following three options:

○ The manuscript/published work is published or in press

- Please provide the full reference of the Research Output:

○ The manuscript is currently under review for publication – please indicate:

- The name of the journal:
- The percentage of the manuscript/published work that was contributed by the candidate:
- Describe the contribution that the candidate has made to the manuscript/published work:

◉ It is intended that the manuscript will be published, but it has not yet been submitted to a journal

Candidate's Signature:	Digitally signed by Lucas Corna
Date:	21-Nov-2022
Primary Supervisor's Signature:	Gert Lube Digitally signed by Gert Lube Date: 2022.11.05 06:26:15 +13'00'
Date:	21-Nov-2022

This form should appear at the end of each thesis chapter/section/appendix submitted as a manuscript/ publication or collected as an appendix at the end of the thesis.

GRS Version 5 – 13 December 2019
DRC 19/09/10

DRC 16

MASSEY UNIVERSITY
UNIVERSITY OF NEW ZEALAND
GRADUATE RESEARCH SCHOOL

STATEMENT OF CONTRIBUTION
DOCTORATE WITH PUBLICATIONS/MANUSCRIPTS

We, the candidate and the candidate's Primary Supervisor, certify that all co-authors have consented to their work being included in the thesis and they have accepted the candidate's contribution as indicated below in the *Statement of Originality*.

Name of candidate:	Lucas Raphael Pierre Corna
Name/title of Primary Supervisor:	Gert Lube
In which chapter is the manuscript /published work:	5

Please select one of the following three options:

○ The manuscript/published work is published or in press

- Please provide the full reference of the Research Output:

○ The manuscript is currently under review for publication – please indicate:

- The name of the journal:
- The percentage of the manuscript/published work that was contributed by the candidate:
- Describe the contribution that the candidate has made to the manuscript/published work:

◉ It is intended that the manuscript will be published, but it has not yet been submitted to a journal

Candidate's Signature:	Digitally signed by Lucas Corna
Date:	21-Nov-2022
Primary Supervisor's Signature:	Gert Lube Digitally signed by Gert Lube Date: 2022.11.06 06:27:12 +13'00'
Date:	21-Nov-2022

This form should appear at the end of each thesis chapter/section/appendix submitted as a manuscript/ publication or collected as an appendix at the end of the thesis.

GRS Version 5 – 13 December 2019
DRC 19/09/10

DRC 16

MASSEY UNIVERSITY
UNIVERSITY OF NEW ZEALAND
GRADUATE RESEARCH SCHOOL

STATEMENT OF CONTRIBUTION
DOCTORATE WITH PUBLICATIONS/MANUSCRIPTS

We, the candidate and the candidate's Primary Supervisor, certify that all co-authors have consented to their work being included in the thesis and they have accepted the candidate's contribution as indicated below in the *Statement of Originality*.

Name of candidate:	Lucas Raphael Pierre Corna
Name/title of Primary Supervisor:	Gert Lube
In which chapter is the manuscript /published work:	6

Please select one of the following three options:

○ The manuscript/published work is published or in press

- Please provide the full reference of the Research Output:

○ The manuscript is currently under review for publication – please indicate:

- The name of the journal:
- The percentage of the manuscript/published work that was contributed by the candidate:
- Describe the contribution that the candidate has made to the manuscript/published work:

◉ It is intended that the manuscript will be published, but it has not yet been submitted to a journal

Candidate's Signature:	Digitally signed by Lucas Corna
Date:	21-Nov-2022
Primary Supervisor's Signature:	Gert Lube Digitally signed by Gert Lube Date: 2022.11.06 06:28:02 +13'00'
Date:	21-Nov-2022

This form should appear at the end of each thesis chapter/section/appendix submitted as a manuscript/ publication or collected as an appendix at the end of the thesis.

GRS Version 5 – 13 December 2019
DRC 19/09/10